



The University of Queensland

# Validation of a CFD Solver for Hypersonic Flows

A THESIS SUBMITTED FOR THE DEGREE OF  
MASTER OF PHILOSOPHY  
AT THE UNIVERSITY OF QUEENSLAND IN SEPTEMBER 2005

BY

MICHAEL CHARLES ELFORD, B.E. (MECHANICAL AND SPACE)  
DIVISION OF MECHANICAL ENGINEERING  
SCHOOL OF ENGINEERING

Principal Supervisor: *Dr Peter Jacobs*  
Associate Supervisor: *Prof Richard Morgan*



© Copyright 2005  
by  
Michael Charles Elford



I hereby declare that this submission is my own work and to the best of my knowledge it contains no material previously published or written by another person, nor material which to a substantial extent has been accepted for the award of any other degree or diploma at UQ or any other educational institution, except where due acknowledgement is made in the thesis. Any contribution made to the research by colleagues, with whom I have worked at UQ or elsewhere, during my candidature, is fully acknowledged.

I also declare that the intellectual content of this thesis is the product of my own work, except to the extent that assistance from others in the project's design and conception or in style, presentation and linguistic expression is acknowledged.

Michael Charles Elford  
(Author)

Dr Peter Jacobs  
(Principal Supervisor)





To my father for his foresight to teach me computers, my boss and friend Chris for his patience and to the crew of ST-107 who never returned home

---

<sup>1</sup>Image obtained from the NASA Image Exchange ([nix.nasa.gov](http://nix.nasa.gov)).



---

## Acknowledgments

---

Completing a research degree part time can become an insurmountable task without the right support and guidance. I would therefore like to express gratitude to my supervisor Dr Peter Jacobs and my former boss Dr Chris Gourlay for their continued support and patience over the past four years. To my lovely wife Karen I thank her for her understanding and support. I would also like to extend thanks to Prof. Richard Morgan for his advice in the area of hypersonics and Rowan Gollan for his help in matters involving L<sup>A</sup>T<sub>E</sub>X formatting. Lastly I would like to thank Alice Miller of CUBRC for her help in tracking down many elusive journal papers and to Prof. Hans Hornung of CALTEC for sending information express from overseas.



---

# Abstract

---

In this thesis the validation of a computational fluid dynamics (CFD) code against published experimental data and alternative CFD results is explored. Six case studies are presented with flow speeds ranging from mid supersonic to hypersonic. The studies include complex compressible flow phenomena such as the interaction of shockwaves with boundary layers, vortices and other shockwaves. Two of the six validation cases also consider complex thermodynamic behaviour such as vibrational and chemical nonequilibrium. The problems chosen are limited in scope to flows which are planar or axisymmetric and remain laminar throughout the region of flow studied. This allows the studies to focus on simulating the fundamental behaviour of the flow without the added complication of turbulence or the need for large scale computing facilities. The problems which arose during the validation studies and a background to why they occurred and, wherever possible, strategies to avoid their occurrence are discussed. General modelling strategies in compressible CFD are also discussed. In this thesis the software suite CFD-FASTRAN is used to construct and analyse the CFD models. The material presented in this thesis is however general such that users of similar packages should find the thesis beneficial.



---

# Contents

---

<b>Originality Statement</b>	<b>iii</b>
<b>Dedication</b>	<b>v</b>
<b>Acknowledgments</b>	<b>vii</b>
<b>Abstract</b>	<b>ix</b>
<b>Table of Contents</b>	<b>xi</b>
<b>List of Figures</b>	<b>xv</b>
<b>List of Tables</b>	<b>xix</b>
<b>Nomenclature</b>	<b>xxi</b>
<b>1 Introduction</b>	<b>1</b>
1.1 In Pursuit of Speed: A Century of Powered Flight	1
1.2 Origins of Simulation	4
1.3 Layout of a CFD Model	5
1.4 Validation Studies	10
1.5 Precision versus Correctness	11
1.6 The CFD-FASTRAN Software Package	12
1.7 Thesis Aims and Objectives	14
<b>2 High Temperature Gas Dynamics</b>	<b>19</b>
2.1 Behaviour of High Temperature Air	19
2.2 Modes of Internal Energy	20
2.3 Chemical Reactions in Air	23
2.4 Frozen, Equilibrium and Nonequilibrium Flow	25
2.5 Summary of High Temperature Effects	26
2.6 Continuity of Flow	27

<b>3</b>	<b>Methodology of Modelling</b>	<b>31</b>
3.1	Stages of Analysis	31
3.2	Grid Design Methodology	33
3.2.1	Structured Grids	33
3.2.2	Unstructured Grids	35
3.2.3	Structured versus Unstructured - The Great Debate	36
3.2.4	Grid Smoothing in Structured Grids	39
3.2.5	Grid Biasing in Structured Grids	39
3.2.6	Capturing Viscous Effects	41
3.2.7	Shockwave - Boundary Layer Interaction	42
3.3	Model Setup and Solution	46
3.3.1	Modelling Choices and Assumptions	46
3.3.2	Model Setup	46
3.3.3	Boundary Conditions	47
3.3.4	Initial Conditions	51
3.4	Overview of the Solution Process	52
3.4.1	Solver Approach	52
3.4.2	Flux Calculators	53
3.4.3	Flux Limiters	55
3.4.4	Integration in Time	58
3.4.5	When solutions become unstable	59
3.4.6	Convergence and Residuals	63
3.4.7	Grid Dependence	64
3.5	Processing Results Data	68
3.5.1	General Visualisation Tools	70
3.5.2	Special Visualisation Techniques for Supersonic Flow	75
<b>4</b>	<b>Validation Studies</b>	<b>79</b>
4.1	Shock Focusing in a Parabolic Reflector	82
4.1.1	Problem Overview	82
4.1.2	Key Features	82
4.1.3	Assumptions	83
4.1.4	Grid Setup, Boundary Conditions and Initial Conditions	83
4.1.5	Solution Setup	83
4.1.6	Results and Comparisons	84
4.2	Shock Diffraction Over a 43° Cone	89
4.2.1	Problem Overview	89
4.2.2	Key Features	89
4.2.3	Assumptions	89
4.2.4	Grid Setup, Boundary Conditions and Initial Conditions	90

4.2.5	Solution Setup . . . . .	90
4.2.6	Results and Comparisons . . . . .	91
4.2.7	Grid Convergence . . . . .	102
4.3	Shock Diffraction Over a Cylinder . . . . .	104
4.3.1	Problem Overview . . . . .	104
4.3.2	Key Features . . . . .	104
4.3.3	Assumptions . . . . .	105
4.3.4	Grid Setup, Boundary Conditions and Initial Conditions . . . . .	105
4.3.5	Solution Setup . . . . .	107
4.3.6	Results and Comparisons . . . . .	107
4.4	Shock Diffraction Over a Half Diamond . . . . .	117
4.4.1	Problem Overview . . . . .	117
4.4.2	Key Features . . . . .	117
4.4.3	Assumptions . . . . .	118
4.4.4	Grid Setup, Boundary Conditions and Initial Conditions . . . . .	118
4.4.5	Solution Setup . . . . .	119
4.4.6	Results and Comparisons . . . . .	120
4.4.7	Grid Convergence . . . . .	129
4.5	Hypersonic Flow Over a Sharp Double Cone . . . . .	131
4.5.1	Problem Overview . . . . .	131
4.5.2	Key Features . . . . .	132
4.5.3	Assumptions . . . . .	133
4.5.4	Grid Setup, Boundary Conditions and Initial Conditions . . . . .	133
4.5.5	Solution Setup . . . . .	135
4.5.6	Results and Comparisons . . . . .	135
4.5.7	Grid Convergence . . . . .	148
4.6	Hypersonic Flow over a Sphere . . . . .	150
4.6.1	Problem Overview . . . . .	150
4.6.2	Key Features . . . . .	150
4.6.3	Assumptions . . . . .	151
4.6.4	Grid Setup, Boundary Conditions and Initial Conditions . . . . .	151
4.6.5	Solution Setup . . . . .	154
4.6.6	Results and Comparisons . . . . .	156
<b>5</b>	<b>Conclusions . . . . .</b>	<b>167</b>
5.1	Suggestions for Future Study . . . . .	168
<b>A</b>	<b>Review of Equations . . . . .</b>	<b>171</b>
A.1	Conservation Equations . . . . .	172
A.2	Equations of State . . . . .	174

A.3 Diffusion and Transport Properties . . . . .	179
A.4 Thermochemical Source Terms . . . . .	184
<b>B Simulation Results in Video Format . . . . .</b>	<b>187</b>
<b>Bibliography . . . . .</b>	<b>195</b>

---

## List of Figures

---

1.1	The Bell X-1 research plane (left) and pilot William “Pete” Knight beside the NASA X-15 research plane (right). . . . .	2
1.2	The SpaceShipOne Suborbital Plane . . . . .	4
1.3	Streamlines of flow generated from a CFD simulation of the shuttle and external fuel tank. . . . .	6
1.4	Example of geometry and grid setup a for CFD analysis. . . . .	7
1.5	Examples of flow symmetry. . . . .	9
1.6	Prediction of the temperature field. . . . .	12
1.7	Prediction of surface temperature. . . . .	13
2.1	Temperature ratio across a normal shock in equilibrium air [7]. . . . .	21
2.2	Visualisation of the modes of internal energy. . . . .	22
2.3	Composition of equilibrium air versus temperature at one atmosphere [7]. . . . .	24
2.4	Velocity-altitude map with superimposed regions of vibrational excitation, dissociation and ionisation [7]. . . . .	27
3.1	Stages of analysis within the CFD-FASTRAN system. . . . .	33
3.2	Axisymmetric cartesian grid of the pathfinder shape. . . . .	34
3.3	Single curvilinear block containing 50 cells. . . . .	35
3.4	Adaptive gridding applied to a simulation of supersonic flow over a ramp deflection in a duct. . . . .	37
3.5	Structured and unstructured axisymmetric grids for the pathfinder shape inside the X3 expansion tube. . . . .	38
3.6	Examples of grid smoothing in structured grids. . . . .	39
3.7	Orthogonal smoothing applied to a multi-block grid for flow over a double wedge. . . . .	40
3.8	Even and uneven biasing. . . . .	40
3.9	Examples of one-way grid biasing. . . . .	41
3.10	Examples of symmetric grid biasing. . . . .	41
3.11	X-T diagram for the sealed tube. . . . .	43
3.12	Schematic showing a typical form of shock boundary layer interaction. . . . .	43
3.13	Near wall velocity profiles for the initial value problem. . . . .	44

3.14	Shock boundary layer interaction in the initial value problem. . . . .	45
3.15	Left and right states for the evaluation of flux. . . . .	53
3.16	Numerical Schlieren image showing spurious waves. . . . .	55
3.17	Effects of limiters on the linear convection of a square wave [30]. . . . .	57
3.18	Comparison of some common flux limiters. . . . .	57
3.19	Example of the effects of using different flux calculators. . . . .	61
3.20	Failure in the reconstruction of a planar shockwave through odd-even de- coupling. . . . .	62
3.21	Failure in the reconstruction of a bow shockwave through the carbuncle phenomenon. . . . .	62
3.22	Convergence for a supersonic aerofoil at 1 km/s. . . . .	66
3.23	Change in pressure with grid refinement. . . . .	67
3.24	Supersonic flow over a ramp deflection: different ways of visualising the density field. . . . .	69
3.25	Visualisation techniques in CFD-VIEW. . . . .	74
3.26	Effect of the maximum gradient in Schlieren images. . . . .	77
4.1	Experimental setup of Izumi et al. . . . .	83
4.2	Multi-block grid for Case 1. . . . .	84
4.3	Focusing of a planar shock: Izumi et al. experimental Schlieren (top half), CFD-FASTRAN numerical Schlieren (bottom half). . . . .	87
4.4	Focusing of a planar shock: Izumi et al. numerical isopycnics (top half), CFD-FASTRAN numerical isopycnics (bottom half). . . . .	88
4.5	Multi-block grid for Case 2. . . . .	91
4.6	Comparison between MB-CNS laminar simulation (top half) and CFD- FASTRAN laminar simulation (bottom half), $X_s = 5$ mm. . . . .	94
4.7	Comparison between MB-CNS laminar simulation (top half) and CFD- FASTRAN laminar simulation (bottom half), $X_s = 10$ mm. . . . .	95
4.8	Comparison between MB-CNS laminar simulation (top half) and CFD- FASTRAN laminar simulation (bottom half), $X_s = 15$ mm. . . . .	96
4.9	Comparison between MB-CNS laminar simulation (top half) and CFD- FASTRAN laminar simulation (bottom half), $X_s = 20$ mm. . . . .	97
4.10	Comparison of MB-CNS and CFD-FASTRAN: pressure along the cone. . .	98
4.11	Comparison of MB-CNS and CFD-FASTRAN: heat flux along the cone. . .	99
4.12	Comparison of MB-CNS and CFD-FASTRAN: skin friction along the cone. .	100
4.13	Origins of secondary peak in skin friction. . . . .	101
4.14	Pressure results for the full, half and quarter models. . . . .	103
4.15	Multi-block grid for Case 3. . . . .	106
4.16	Comparison between experiment (top half) and CFD-FASTRAN laminar simulation (bottom half), frame 1 and frame 2. . . . .	110

4.17	Comparison between experiment (top half) and CFD-FASTRAN laminar simulation (bottom half), frame 3. . . . .	111
4.18	Comparison between MB-CNS laminar simulation (top half) and CFD-FASTRAN laminar simulation (bottom half), frames 1 and 2. . . . .	113
4.19	Streamlines and flooded contours of speed for laminar and inviscid solution at $80 \mu\text{s}$ ( $68 \mu\text{s}$ after initial impact of shock on cylinder). . . . .	115
4.20	Plots of flow speed on radial lines at $80 \mu\text{s}$ ( $68 \mu\text{s}$ after initial impact of shock on cylinder). . . . .	115
4.21	Laminar CFD-FASTRAN simulation (top half) and inviscid CFD-FASTRAN simulation (bottom half), frames 1, 2 and 3. . . . .	116
4.22	Multi-block grid for Case 4. . . . .	119
4.23	Shock diffraction over a half diamond: isopycnics computed at different stages of diffraction. . . . .	122
4.24	Comparison between experimental interferogram (top) and CFD-FASTRAN numerical interferogram (bottom). . . . .	124
4.25	Comparison of CFD-FASTRAN results to CFD results from Quirk (left) and Glass et al. (right) . . . . .	125
4.26	Comparison between numerical Schlieren images from CFD-FASTRAN results: laminar simulation (top half), inviscid simulation (bottom half). . .	126
4.27	Streamlines and contours of speed for the CFD-FASTRAN laminar solution (top half) and inviscid solution (bottom half). . . . .	127
4.28	Close up view of the shock boundary layer interaction region of the CFD-FASTRAN solution: Schlieren image with superimposed velocity vectors (red). . . . .	128
4.29	Pressure results for the full, half and quarter models. . . . .	130
4.30	Sharp double cone model used by Holden et al. . . . .	132
4.31	Multi-block grid for Case 5. . . . .	134
4.32	CFD-FASTRAN: Mach contours for the sharp double cone model. . . . .	136
4.33	Streamlines and contours of flow speed for the sharp double cone model (closeup view). . . . .	136
4.34	CFD-FASTRAN: Isobars and isopycnics for the sharp double cone model. .	137
4.35	CFD-FASTRAN: Temperature and vibrational temperature contours for the sharp double cone model. . . . .	138
4.36	Experimental results from Holden et al. for CUBRC run 7. . . . .	139
4.37	Pressure contours in the separated flow region: CFD-FASTRAN NS simulation (top) and Moss DSMC simulation (bottom). The CFD-FASTRAN contour range has been truncated to the same scale as Moss's results. . . .	142
4.38	Comparison between CFD-FASTRAN simulation and experimental data from Holden et al. . . . .	143

4.39	DSMC results from Moss using the DSMC code “DS2V” [28]. . . . .	144
4.40	DSMC results from Markelov et al. using the DSMC code “SMILE”. . . . .	144
4.41	DSMC results from Boyd. . . . .	145
4.42	NS results from Candler. . . . .	145
4.43	Comparison between experimental Schlieren image and numerical isopycnics.	146
4.44	Comparison of pressure contours for the CFD-FASTRAN laminar simulation (top half) and inviscid simulation (bottom half). . . . .	147
4.45	Pressure results for the full, half and quarter models. . . . .	149
4.46	Original and reduced grids with isobars from the original grid. . . . .	152
4.47	Multi-block grid for Case 6. . . . .	153
4.48	Contours of temperature for different freestream vibrational temperatures.	157
4.49	Comparison of an interferogram from Shot 491 (top half) with isopycnics from the chemically reacting CFD-FASTRAN simulation (bottom half). . . . .	158
4.50	Comparison of results for the CFD-FASTRAN perfect gas simulation (top half) and chemically reacting simulation (bottom half). . . . .	159
4.51	Contours of species mass fraction and vibrational temperature for the chemically reacting CFD-FASTRAN simulation. . . . .	160
4.52	Species mass fractions along the stagnation streamline (centerline). . . . .	161
4.53	Correlation of stagnation Stanton number ( $St_s$ ) and the freestream Reynolds number $Re_\infty$ for experiment, CFD and theory (reproduction of fig. 4.7 from Wen). . . . .	164
4.54	Heat flux distribution for Shot 471 (reproduction of fig. 4.29 from Wen). . . . .	164
4.55	Predictions of heat flux distribution across the sphere for Shot 491. . . . .	165
5.1	Hollow cylinder extended flare (HCEF) model. . . . .	170
5.2	25° - 60° blunt double cone model. . . . .	170

---

## List of Tables

---

1.1	Examples of alternative high speed NS solvers. . . . .	15
1.2	Abbreviations for several high speed NS solvers. . . . .	15
2.1	Thermodynamic properties for calorically perfect air. . . . .	20
2.2	Typical number of collisions needed to reach equilibrium. . . . .	25
2.3	Collision diameters for some common gases [72]. . . . .	29
3.1	Thermal boundary conditions for different subtypes of wall. . . . .	48
3.2	Formulations for some common flux limiters. . . . .	56
4.1	Description of validation cases. . . . .	80
4.2	Setup of validation cases. . . . .	81
4.3	Boundary conditions for Case 1. . . . .	84
4.4	Initial conditions for Case 1. . . . .	84
4.5	Estimation of flow time for each experimental image. . . . .	85
4.6	Boundary conditions for Case 2A. . . . .	91
4.7	Boundary conditions for Case 2B. . . . .	92
4.8	Initial conditions for Case 2A and 2B. . . . .	92
4.9	Boundary conditions for Case 3A and 3B. . . . .	106
4.10	Initial conditions for Case 3A and 3B. . . . .	107
4.11	Estimation of flow time for each experimental image. . . . .	107
4.12	Boundary conditions for Case 4A and 4B. . . . .	119
4.13	Initial conditions for Case 4A and 4B. . . . .	119
4.14	Boundary conditions for Case 5A and 5B. . . . .	134
4.15	Initial conditions for Case 5A and 5B. . . . .	134
4.16	Boundary conditions for Case 6A and 6B. . . . .	153
4.17	Initial conditions for Case 6A and 6B. . . . .	153
4.18	Freestream species concentrations for Case 6B. . . . .	154
4.19	Park-1 reaction scheme for air . . . . .	155
4.20	Sensitivity of the solution to freestream vibrational temperature. . . . .	157
4.21	Estimation of the heat transfer constant for a 4" sphere. . . . .	162
A.1	Constants for the vibrational relaxation time equation. . . . .	186

B.1 Listing of files included on Appendix B CD. . . . .	188
---	-----

---

# Nomenclature

---

## Greek

$\alpha'$	Concentration power of the forward reaction
$\alpha''$	Concentration power of the backwards reaction
$\beta$	Oblique shockwave angle
$\Delta h_{f,T_{\text{ref}}}^0$	Enthalpy of formation at reference temperature
$\Delta T$	Time step
$\Delta$	Cell size, general increment
$\delta$	Distance normal to the wall between the wall and the cell center adjacent to the wall
$\eta$	Exponential in the Arrhenius chemical rate equation
$\gamma$	Ratio of specific heats ( $C_P/C_V$ )
$\kappa$	Thermal conductivity, user defined parameter in the Osher-C limiter formulation
$\kappa_{\text{int}}$	Internal energy conductivity
$\lambda$	Mean free path
$\mu$	Absolute viscosity
$\nabla$	Gradient operator
$\nu'$	Stoichiometric coefficient of the forward reaction
$\nu''$	Stoichiometric coefficient of the backwards reaction
$\nu^{(m)}$	$m^{\text{th}}$ vibrational quantum number
$\omega$	Source of energy due to chemical reactions

$\Omega_\mu$	Viscosity collision integral
$\omega_{\text{int}}$	Source of energy obtained from an imbalance between E and $E_{\text{int}}$
$\Omega_{D_{ij}}$	Diffusion collision integral
$\Psi$	Flux limiter function
$\rho$	Density
$\sigma$	Stefan Boltzmann constant = $5.6697 \times 10^{-8} \frac{w}{m^2 K^4}$ , Collision diameter of a molecule
$\tau_f$	Time taken for a particle to traverse through a region of flow
$\tau_w$	Wall shear stress (skin friction)
$\tau_{chem}$	Characteristic time taken to complete a chemical reaction
$\tau_{ij}$	Shear stress tensor
$\tau_{vib}$	Characteristic time taken to transfer vibrational energy
$\theta$	Wedge angle
$\Theta_V^{(m)}$	$m^{th}$ characteristic vibrational temperature
$\varepsilon$	Total number of molecular rotational degrees of freedom
$\varepsilon_{\text{user}}$	User defined emissivity
$D_{ij}$	Binary diffusion coefficient

## Dimensionless Numbers

Kn	Knudsen Number
M	Mach Number
Pr	Prandtl Number
Re	Reynolds Number
Sc	Schmidt Number

## Roman

$[\mathcal{X}]$	Molar concentration
$[Y]$	Mass fraction

$\hbar$	Plank's constant = $6.622 \times 10^{-23} \frac{kg}{m^2 \cdot s^2}$
$\mathbf{v}$	Velocity vector
$\mathcal{M}$	Molecular weight
$\tilde{G}^0$	Gibbs free energy at reference pressure
$E_a$	Activation energy term in the Arrhenius chemical rate equation
$K_b$	Backwards reaction rate
$K_{eq}$	Equilibrium reaction rate
$K_f$	Forwards reaction rate
$a$	Speed of sound
$c$	Cell local speed of sound
$C_P$	Specific heat at constant pressure
$C_V$	Specific heat at constant volume
$C_{V,el}$	Electronic component of specific heat at constant volume
$C_{V,rot}$	Rotational component of specific heat at constant volume
$C_{V,trans}$	Translational component of specific heat at constant volume
$C_{V,vib}$	Vibrational component of specific heat at constant volume
CFL	User defined multiple of the CFL number
$E_t$	Total energy per unit volume
$e_t$	Total energy per unit mass
$E_{int}$	Total molecular internal energy per unit volume
$e_{int}$	Total molecular internal energy per unit mass
$e_{el}$	Electronic internal energy
$e_{rot}$	Rotational internal energy
$e_{trans}$	Translational internal energy
$e_{vib}$	Vibrational internal energy
$h$	Sensible enthalpy

I	Intensity of light
J	Mass diffusivity
K	Rate constant
k	Boltzmann's Constant = $1.381 \times 10^{-23} \frac{J}{K}$
M	Mach number
$M_{Shock}$	Shockwave Mach number
N	Number of cells in a model, Total number of characteristic vibrational temperatures of a molecule
n	Total number of species in a mixture
P	Pressure
q	Heat flux, a primitive variable
$q_{int}$	Internal energy conductivity
$q_{user}$	User defined heat flux
R	Specific gas constant ( $C_P - C_V$ ), Total number of reactions
r	Ratio of gradients across an interface
$R_U$	Universal gas constant = $8314 \frac{J}{kg \cdot molK}$
S	Constant in the Arrhenius chemical rate equation
S	Entropy
T	Temperature
t	Time
$T_c$	Cell center temperature adjacent to the wall
$T_{int}$	Internal temperature (combined vibrational and electronic temperature)
$T_{ref}$	Reference temperature
$T_{user}$	User defined temperature
$T_{vib}$	Vibrational temperature
$T_{wall}$	Temperature at the wall

u	Velocity component
V	Volume
x	Coordinate direction
Y	Distance from a wall, normal to the wall
Y+	Normalised distance from a wall, normal to the wall
Z	Frequency of molecular collisions

## Superscript

*	Equilibrium value
(m)	m <sup>th</sup> quantum number or characteristic vibrational temperature

## Subscript

∞	Freestream value
0	Stagnation value
atm	Atmospheres
eq	Equilibrium
j	the j <sup>th</sup> direction
r	Reaction r, belonging to species r
s	Belonging to species s

## Acronyms

ACIS	American Committee for Interoperable Systems
AIAA	American Institute for Aeronautics and Astronautics
ASCI	Accelerated Strategic Computing Initiative
AUSM	Advection Upwind Splitting Method
BMP	Bitmap
CAD	Computer Aided Design
CALTEC	California Institute of Technology
CFD	Computational Fluid Dynamics

CFDRC	CFD Research Corporation
CFL	Courant-Friedrichs-Lewy
CUBRC	Calspan - University of Buffalo Research Center
DSMC	Direct Simulation Monte Carlo
DTF	Data Transfer Facility
FDS	Flux Difference Splitting
FVS	Flux Vector Splitting
GGD	Grid and Geometry Definition
GUI	Graphical User Interface
ICASE	Institute for Computer Applications in Science and Engineering
IGES	Initial Graphics Exchange Specification
JFM	Journal of Fluid Mechanics
JPEG	Joint Photography Expert Group
LENS	Large Energy National Shock
MDICE	Multi-Disciplinary Computing Interface
MPEG	Moving Pictures Expert Group
NASA	National Aeronautics and Space Administration
NS	Navier-Stokes
RANS	Reynolds Averaged Navier-Stokes
SDC	Sharp Double Cone
SST	Shear Stress Transport
TFI	Trans-Finite Interpolation

# Introduction

---

This section aims to first provide the reader with a preliminary discussion of the topics upon which this thesis is based. Having established the necessary background, the aims of the thesis are then presented.

## 1.1 In Pursuit of Speed: A Century of Powered Flight

On December 17, 1903, brothers Orville and Wilbur Wright demonstrated to the world that powered flight was possible. Orville piloted the world's first heavier than air plane, named the Kitty Hawk, for duration of just twelve seconds. Their achievement was the result of years of dedicated research into the flow of air around wings using a wind tunnel which they designed, built and operated themselves. In the century that followed the advancements in the field of powered flight have been nothing less than astonishing. These advancements were made possible through the scientists and engineers who, following in the footsteps of the Wright brothers, worked to improve the speed, efficiency and reliability of aircraft designs. A large part of this research has been directed towards the area of fluid dynamics. This area of research is important because a thorough understanding of the airflow around a vehicle in flight is required to predict the forces which act on that vehicle during flight. An understanding of these forces as they vary with the direction of the aircraft allows some degree of control over the aircraft to be imposed.

Over the next few decades, the speed of aircraft increased rapidly but researchers realised a limit was approaching. Prior to 1947 all manned aircraft operated at speeds below the speed of sound (subsonic). Researchers had for decades prior developed theories and made predictions for faster than sound (supersonic) aircraft but it was not until October 14, 1947 that humans were propelled beyond the speed of sound. On this day Chuck Yeager took the Bell X-1 research plane (shown in Figure 1.1) to a maximum speed of Mach 1.06 at an altitude of just over 13 km. Unlike the propeller driven Kitty Hawk, the X-1 plane was powered by the combustion of liquid fuel and Oxygen in a rocket chamber located at the rear of the plane. To reach the speed of sound, the X-1 plane was first carried to an altitude of 7.6 km by a B-29 bomber plane. Once at altitude, the X-1 was released from

the undercarriage of the B-29 and its rockets were fired when a safe distance was reached.

The X plane research program continued with further funding from the US Government and by December 12, 1953 Yeager had flown to a top speed of over Mach 2 in the X-1A, a newer version of the X1 research plane. Yeager was not however the first person to claim this record with Scott Crossfire achieving Mach 2 in a D-558-2 Skyrocket just hours before Yeager's flight. The next milestone was set by Milburn Apt who surpassed the Mach 3 barrier in September 1956. Milton reached a top speed of Mach 3.2 at an altitude of 20 km when in command of the Bell X-2 research plane. Tragically, Milton was not familiar with the plane and failed to slow the plane sufficiently whilst turning. The turn caused the plane to flip backwards and Milton was unable to separate from the escape capsule before impacting the ground. March 7, 1961 saw Major Robert White pilot the more modern NASA X-15 research plane to a top speed of Mach 4.43 at an altitude of 23.6 km. Robert then proceeded to break his own record on two occasions. Firstly on June 23, travelling to Mach 5.27 at an altitude of 32.8 km and again on September 11 of that year when he reached a speed of Mach 6 at an altitude of 31 km. Robert did not however claim the final speed record. This record belongs to William "Pete" Knight who flew the X-15 to a maximum speed of Mach 6.7 at an altitude of 31.1 km on October 3, 1967. William is shown below in Figure 1.1 beside the NASA X-15 research plane (photos courtesy of National Air and Space Museum (left) and NASA (right)).

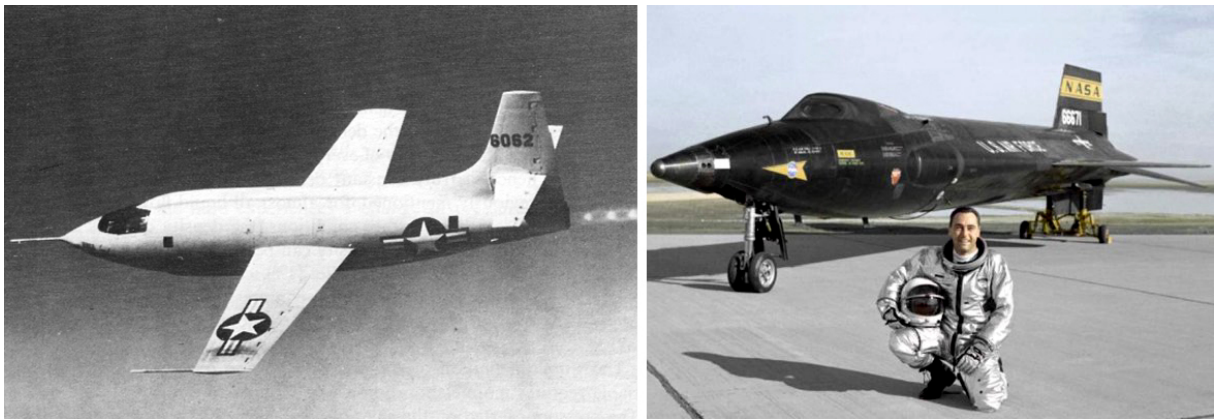


Figure 1.1: The Bell X-1 research plane (left) and pilot William "Pete" Knight beside the NASA X-15 research plane (right).

By this time researchers began to encounter challenges in the design of their planes. The main problem was the amount of heat generated when travelling at such high speeds. The X-15 skin, composed of a specially designed chrome nickel alloy termed Inconel-X, was exposed to temperatures of several thousand degrees causing it to weaken and in some cases even melt. The kinetic energy due to the difference in speed between the aircraft and the air was converted into heat which was absorbed by the metal skin of the aircraft. The boundary layer which formed along the skin of the aircraft contained a large gradient

of air velocity resulting in considerable skin friction. Also, complex interactions between shockwaves and boundary layers resulted in unexpected hotspots on the surface of the aircraft. These localised hotspots were responsible for nearly severing a portion of the X-15 plane from the main body during flight. The X-15 research program is considered one of the most successful projects of its time. Several books are available on the program [47], [42], [75].

The term Hypersonic is used to describe speeds at which the aforementioned thermal effects begin to become significant. Whilst the transition from subsonic to supersonic flow is rapid and marked by the sudden onset of shockwaves, the transition from supersonic to hypersonic flow is gradual. This gradual transition means that an exact definition of hypersonic flow is hard to quantify, but as a rule of thumb researchers generally consider Mach numbers over 5.0 as hypersonic. Researchers of the X plane used hypersonic wind tunnels as the main means of predicting the performance of their designs. The flux of mass and energy required to sustain a stream of hypersonic flow is enormous so hypersonic wind tunnels can only provide a brief burst (in the order of milliseconds) of flow<sup>1</sup>. Researchers were initially reluctant to conclude that their tests provided any useful data. Fortunately, the test data was validated and hypersonic tunnels are still widely used to research hypersonics today despite the handicap of small test times.

The United States was not the only nation to design and test equipment capable of travelling at hypersonic speeds. Soviet cosmonaut Yuri Gagarin became the first person to orbit the Earth on April 12, 1961. In doing so Yuri is also credited with being the first person to travel at hypersonic speeds, having beaten Robert White to the record by just over two months. In the years that followed, political tension between the United States and the Soviet Union led to a showdown of technology that ended abruptly on July 20, 1969. On this day Americans Neil Armstrong and Edwin “Buzz” Aldrin walked on the surface of the moon.

At the time of writing, just over one century has elapsed since the Wright brothers first demonstration of powered flight. In that century, the amount of knowledge in the field of aerodynamics and in particular hypersonics has increased dramatically but research is still ongoing today. In 2004, NASA’s robotic space probe Cassini entered orbit around Saturn. The X-43 and X-43A unmanned NASA test planes set new hypersonic records cruising at Mach 6.8 and 9.8 respectively and did so without the use of rocket engines. Perhaps most significant of all, the privately developed craft SpaceShipOne rocketed to an altitude of over 100 km twice within one fortnight. This stunning achievement earned

---

<sup>1</sup>Some facilities exist today which provide a continuous stream of hypersonic flow by reducing the temperature of the test gas. The enthalpy of such flows is not as high as would be seen by the X-15 at top speed and so these facilities still cannot provide equivalent flight conditions.

the designers of the craft the elusive X-Prize, a US\$10 million award, and both pilots were granted astronaut status by the United States government. SpaceShipOne and its mothership the White Knight are the creation of Burt Rutan's company Scaled Composites and funded by billionaire Paul Allen. On a historical note, the flight took place in the Mojave Desert of California, the site where Chuck Yeager first took humankind beyond the speed of sound. The history making SpaceShipOne is shown in Figure 1.2 (photo courtesy of Scaled Composites LLC).



Figure 1.2: The SpaceShipOne Suborbital Plane

## 1.2 Origins of Simulation

Historically, scientists and engineers have taken two approaches to understanding the world around us. The first approach is to consistently reproduce an event under controlled circumstances and measure the outcomes. Such a process is known as experimental analysis. The second is to model the problem of interest by mathematically describing the processes which occur in that problem, this is termed theoretical analysis. Typically experiments were performed in order to validate a theoretical analysis which could then be used to predict scenarios for which there was no experimental results available. By the mid nineteenth century, mathematical models for most physical phenomena had been established. Claude Navier and George Stokes had independently published a set of equations which describe the general motion of a fluid. James Maxwell had discovered a set of equations which describe the coupled effects of electricity and magnetism and similarly a theory describing the relationship between load, deflection and stresses in solid objects was obtained. The problem which faced the scientists, mathematicians and engineers of the time was the sheer complexity of the equations at hand. For the most part, the

equations were in the form of coupled partial differential equations and could only be solved for the simplest of problems where gross simplifications could be made. Most real engineering applications required significant approximations to be made in order for a solution to be obtained.

By the mid twentieth century the concept of digital computing was born. Computers at first were large, occupying entire rooms or even floors of buildings, but when microprocessors came of age computer sizes decreased and the processing and data storage capability of computers dramatically increased. It was around this time that a third form of engineering analysis, numerical analysis, was in its beginnings. Numerical analysis, also known as numerical simulation, refers to techniques which involve the approximation of a domain as many smaller interconnected domains known as cells or elements. The solution for a variable at each cell is written in terms of its neighbouring cells in a way which can be described as a set of simultaneous equations. The equations can then be solved for the variables at each cell. Clearly the processing power of a computer plays a major role in determining the number of cells and the number of variables which can be computed in a reasonable time frame. With the development of modern computing, the requirement for numerical simulation in postgraduate engineering research has grown rapidly. The students of today are often expected to undertake numerical simulation at some point in their thesis, alongside physical experiments and theoretical modelling. Industry has also embraced simulation with many large companies incorporating simulation into their product development cycle. In doing so they can achieve higher levels of quality and reliability whilst reducing the number of prototypes required for testing. In this thesis a subset of numerical analysis known as Computational Fluid Dynamics (CFD) is studied. CFD refers to numerical simulation models which predict the motion of fluids (liquids and gases) and the corresponding transport of quantities such as mass, momentum, and energy within the flow. CFD is now commonplace in the aerospace industry where it is used to better understand the behaviour of aerospace vehicles leading to safer, more efficient designs. An example of a CFD simulation is shown in Figure 1.3. This figure shows calculated streamlines of flow generated from the results of a CFD simulation of the shuttle and attached fuel tank in mid flight (model courtesy of CEI Inc., [www.ensight.com](http://www.ensight.com)).

### 1.3 Layout of a CFD Model

Whilst the concepts behind CFD can be quite complex and abstract, the basic layout of a CFD model is not difficult to comprehend. CFD models require a domain on which the equations of flow will be solved. This domain defines a region of physical space through which the fluid passes and spans a portion of time if the solution is transient. The domain is represented by a grid of cells spatially and the time period is divided into discrete steps.

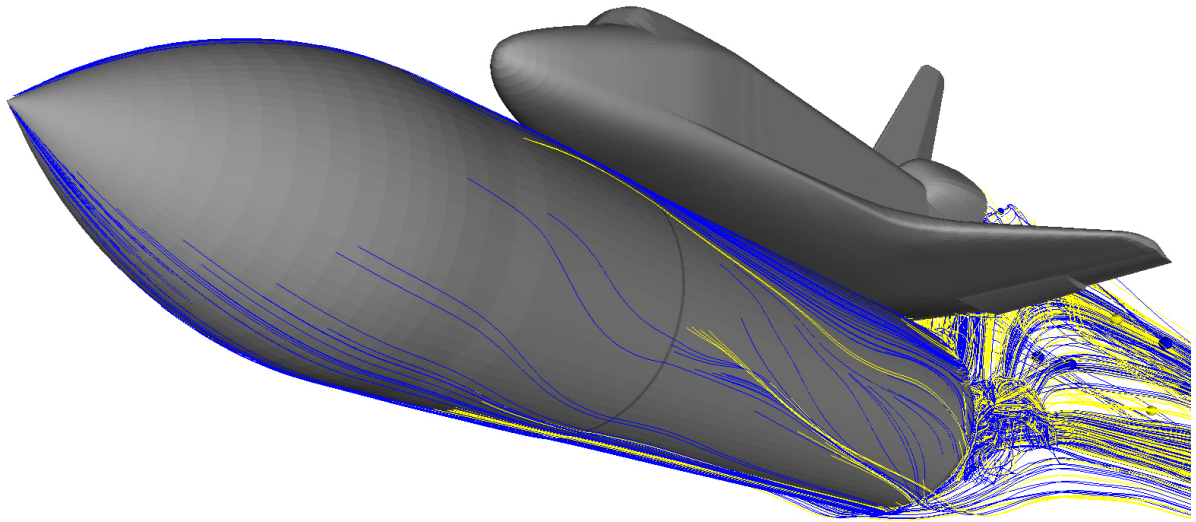


Figure 1.3: Streamlines of flow generated from a CFD simulation of the shuttle and external fuel tank.

Figure 1.4 illustrates a typical setup for a CFD model. This setup depicts an experiment in which the flow over a scale model of a reentry body is studied using an expansion tube, a device which produces hypersonic flow. The scale model of the reentry body is positioned at a slight angle to the freestream flow and a sting is connected to the rear which holds the model in place. Figure 1.4A shows the region of the expansion tube which is of interest to the study. The aeroshell is shown in blue for clarity. Figure 1.4B shows the surrounding volume of gas which is chosen to be analysed. This volume is the domain on which the equations of flow are solved. Note that the volume chosen consists of only one half of the full volume surrounding the reentry body. The symmetric nature of the flow about the centerplane allows the model to be reduced in this way. Figure 1.4C shows one possible way in which the domain can be divided up into a grid of cells. Note that a lesser amount of cells is shown than would typically be needed to adequately resolve the flow detail.

### Simplifying CFD Models

The flow of fluid is generally three dimensional and time varying in nature. Simulations of most practical engineering problems which account for this behaviour can be time consuming to setup. They may also require the power of a supercomputer to solve with sufficient accuracy. Great advantages in solution time and computer resources can be achieved by performing simulations where the CFD model is simplified to less dimensions than are present in the physical world. Steady flows are one such example of simplification. Models of steady flows solve the equations of flow on a domain which is independent of time. In doing so, only one set of results is required. A result for pressure can be

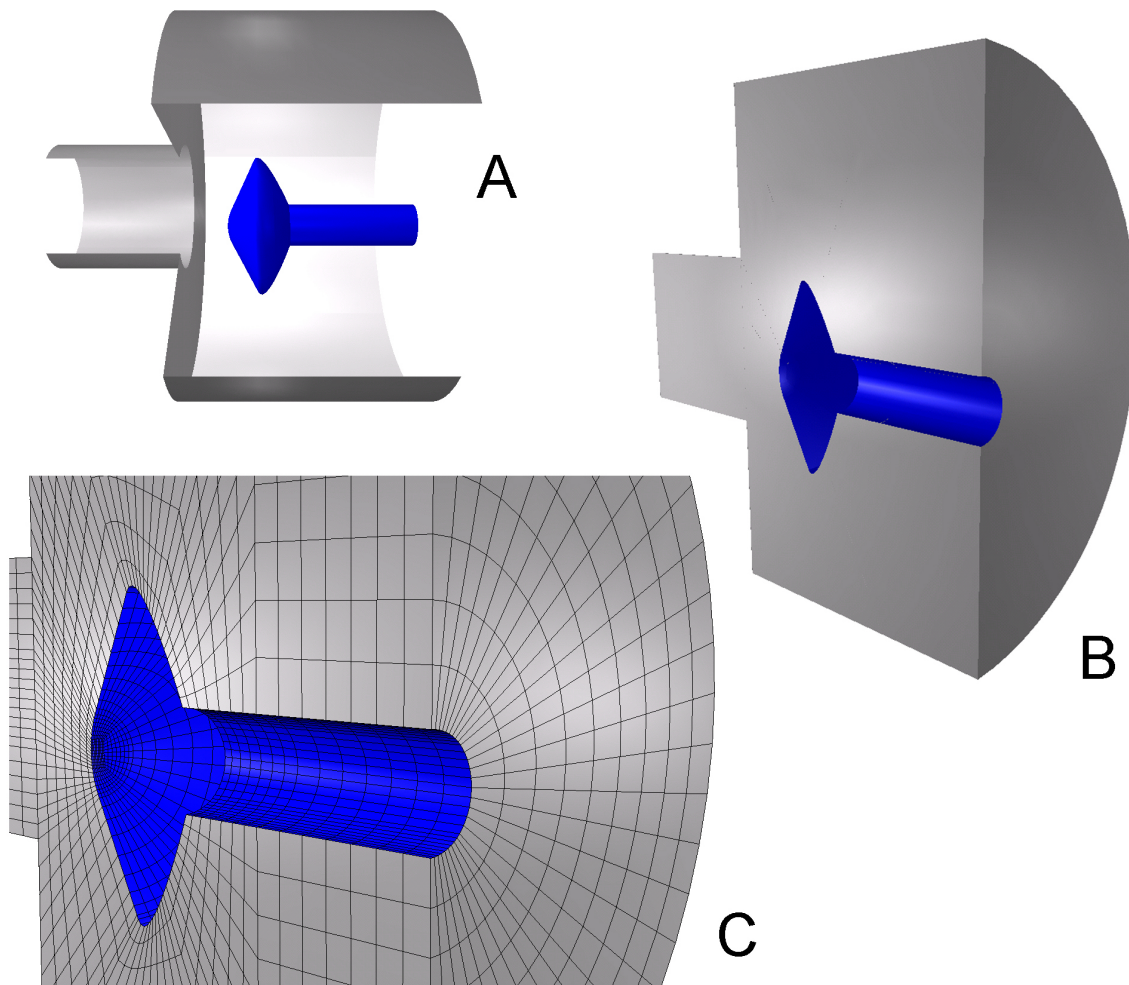


Figure 1.4: Example of geometry and grid setup a for CFD analysis.

displayed as single image for example. For transient flows, the solution must be obtained at various points throughout the time period which is simulated. The pressure must then be shown as an animation or as a series of images.

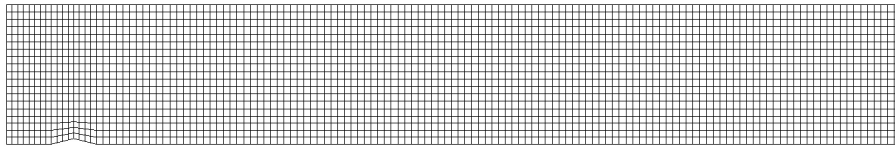
There are also many instances where variations in flow occur mainly in one or two dimensions spatially. In these cases, the computational requirements can also be reduced by limiting the domain of the CFD model to those dimensions where the flow changes are significant. Flows which can be reduced in this way are said to have symmetry. In the validation problems presented in this thesis, all cases assume one or more forms of symmetry. Figure 1.5 shows three examples of symmetry within a flow. In each case a grid is shown alongside an experimental setup. As with Figure 1.4, fewer cells are displayed than would typically be used in a simulation. In each experimental setup a transparent red surface shows how the grid aligns with the experimental model.

Example A contains a small ramp deflection located in a duct. In this example, the

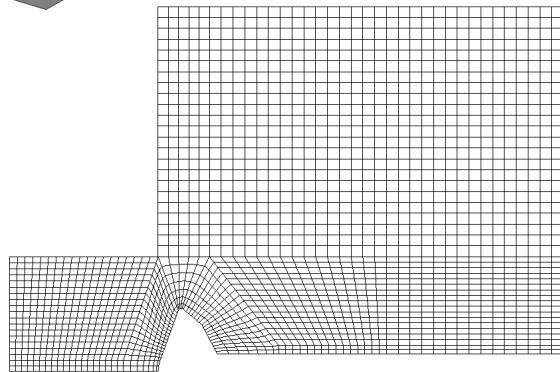
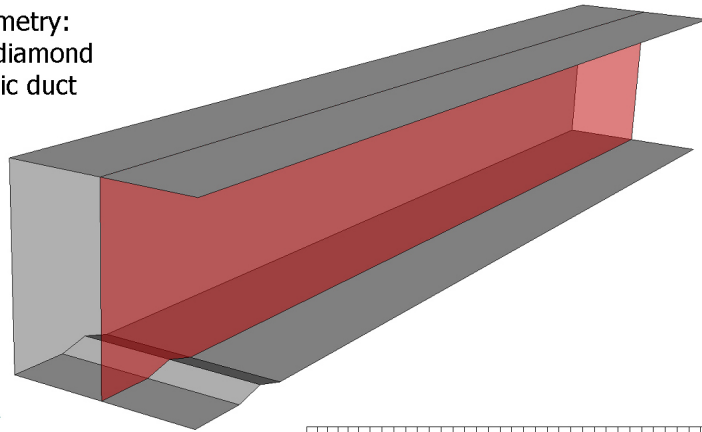
flow is assumed to be planar thereby neglecting any variation across the width of the duct. In reality the vertical walls of the duct will form boundary layers. The boundary layers will cause a variation in flow across the width but the assumption of planar flow will be applicable if the boundary layers do not interact with the core flow.

Example B is of an aeroshell model with an attached sting located inside an expansion tube. In this setup the aeroshell, which is a body of revolution, has its axis aligned with the freestream flow. In this situation the setup can be simplified to an axisymmetric model of flow. An axisymmetric model assumes there is negligible variation in flow along the circumferential direction. If the aeroshell was positioned at an angle to the freestream flow, as with the previous example, the assumption of an axisymmetric model would no longer be valid. If the model was located in a non circular cross section the assumption would also be invalid.

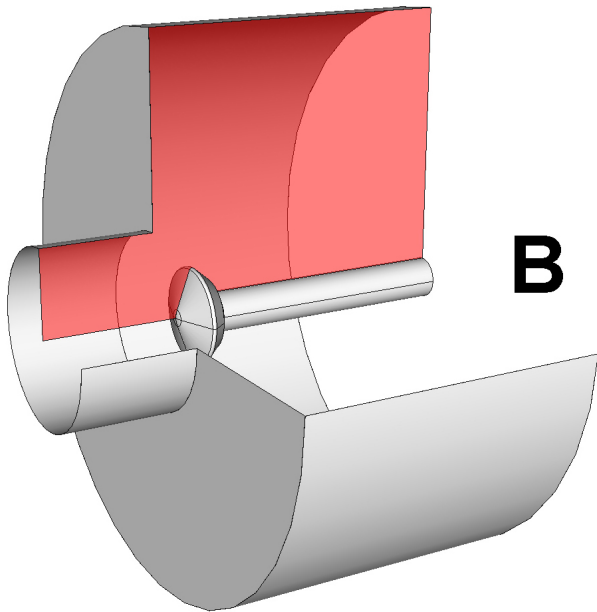
Example C is of a parabolic reflector located in a duct. As with Example A, this setup contains planar symmetry. Unlike Example A, the experiment is a mirror image from top to bottom. This symmetry about the centerline allows the computational domain to be reduced to either the top or bottom half of the experimental setup. Caution should be applied when using this form of symmetry as particular flow conditions can cause asymmetric behaviour. Vortex shedding in the wake region of a flow obstruction is one such example.



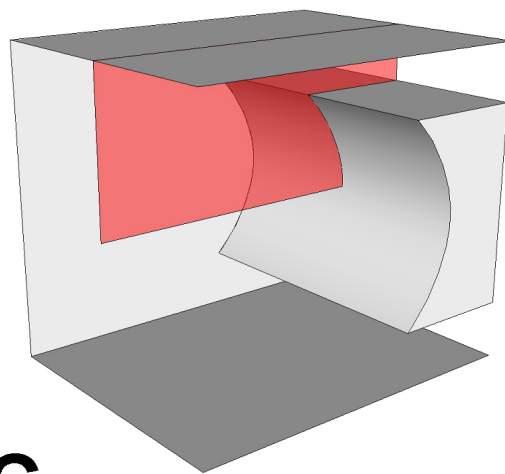
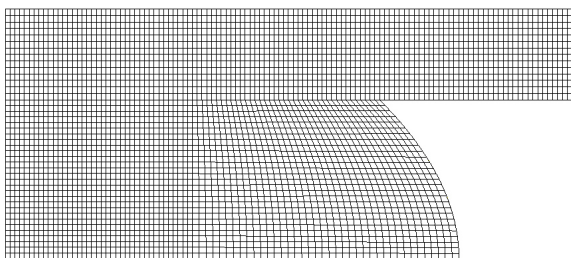
**A** Example of planar symmetry:  
multi-block grid for half diamond  
obstruction in supersonic duct



**B** Example of axisymmetry:  
multi-block grid for pathfinder scale model  
(with sting) at zero angle of attack in the X3  
expansion tube



Example of planar and centerline symmetry:  
multi-block grid for shock focusing on a  
parabolic reflector in a supersonic duct



**C**

Figure 1.5: Examples of flow symmetry.

## 1.4 Validation Studies

With the growing popularity of computer simulation, more of the engineering community has been exposed to the use of computer simulation. Unfortunately adequate tutoring in the field of simulation is not always provided together with the simulation tools. Consequently the tools can sometimes be applied in a less than satisfactory manner. With the powerful desktop computers and mature CFD software that is available today, the capability exists to construct quite complex models which can be solved in a reasonable time frame. Yet despite having highly detailed models, misleading conclusions can easily be drawn if the solver does not embrace all the physics necessary to adequately describe the problem at hand. Boundary conditions must be chosen carefully and located a suitable distance away from the regions of interest otherwise they may influence the solution. Even for a highly detailed model including all the necessary physics, a viscous solution can be fundamentally flawed if the boundary layer is not modelled with sufficient resolution. Such complexity makes validation critical. It is important to validate CFD results with experimental results performed on models of a similar nature. If the pressure, heat transfer or skin friction cannot be reliably predicted on a small test configuration then there is no merit in generating a large model of an entire spacecraft and hoping that the results will be correct. It is important to note that the process of implementing a code on a given model is only a minor aspect to validation. The most important information which is gained from validation studies is the discovery of potential problems and the development of ways to circumvent them or the realisation that the problem is beyond the capabilities of the software being used.

Many papers have been written on the topic of CFD validation. The National Aeronautics and Space Administration (NASA) maintain a comprehensive list of papers which are specific to the validation of hypersonic flows [2]. The American Institute for Aeronautics and Astronautics (AIAA) dedicated a section of their May 1998 journal to hypersonic CFD validation. The section is headed by a paper from Mehta [57] who provides an excellent overview to the topics of CFD validation and verification. In the same section Oberkampf et al. [58] present a useful breakdown of the source of common errors in hypersonic CFD models. Roache [68] provides a glossary of error types and a rigorous technical review on the topic of error detection. In an earlier AIAA paper, Marvin [55] offers a slightly different angle on hypersonic CFD validation, approaching the topic from an experimentalist point of view. More recently Holden et al. [36] discuss the creation of CUBDAT, a database of experimental results aimed at providing a benchmark source of information on hypersonic flows for the purposes of code validation. Case study 5 presented in this thesis is based around results from this database.

## 1.5 Precision versus Correctness

Perhaps the most common question asked by newcomers to the field of simulation is “How do I know if the solution is correct?”. To answer this question the question must first be understood. This is where the concept of precision (or accuracy) versus correctness becomes useful. Consider the following definitions, taken from the Merriam-Webster’s Online Dictionary [3]:

**Precision:** (2) The degree of refinement with which an operation is performed or a measurement stated.

**Correctness:** (2) Conforming to or agreeing with fact, logic, or known truth.

An interpretation of this when applied to simulation might read as follows:

**Precise CFD Solution:** A highly detailed solution to the equations of flow being modelled

**Correct CFD Solution:** A solution which is in agreement with experimental observations or a known solution

Precision and correctness are very separate qualities of a model. For example, it is possible to generate a model of airflow over a cylinder at 500 m/s which assumes an isothermal and incompressible gas. This model can be made very precise but can never be *correct* because compressibility and energy are fundamental to this flow problem. Figure 1.6 shows two solutions from one instant in time of the diffraction of a shockwave over a half diamond. Both models were performed on the same grid. The solution on the left half of the picture includes viscous forces whilst the solution on the right half does not. The solutions are nearly identical except for the detail at the lower left of each image. The laminar solution reveals the significant effects of shock boundary layer interaction. Figure 1.7 shows the temperature distribution along the surface of the model. The difference between the two models is apparent here also, with the laminar model (blue) predicting a higher peak temperature than the inviscid model (green).

The point to be made is that both models are equally precise because they are performed with the same code using the same grid but ultimately only one model reflects the real behaviour of the system. Only one model is *correct* or to put it a better way the laminar model is more correct than the inviscid model, as no model can ever be perfectly correct. In Figure 4.24 a comparison between the aforementioned laminar simulation and a matching experiment is shown. As can be seen, the laminar model agrees well with the experiment. The model is discussed further in Section 4.4.

In essence, precision in a CFD solution implies being able to capture all the details of a given flow down to some finite level of resolution. Precision does not imply that the solution is meaningful in any context. Precision may imply that the solution is a relatively correct answer to the equations being solved but this does not necessarily mean that these equations are suitable for the physical environment being modelled. Only validation through comparison to some form of experimental observations can give a measure of correctness. Those readers interested in this topic may wish to refer to Adams and Askenazi [4] who discuss the concept of Accuracy versus Correctness in a similar context as it applies to modelling structures using finite element analysis.

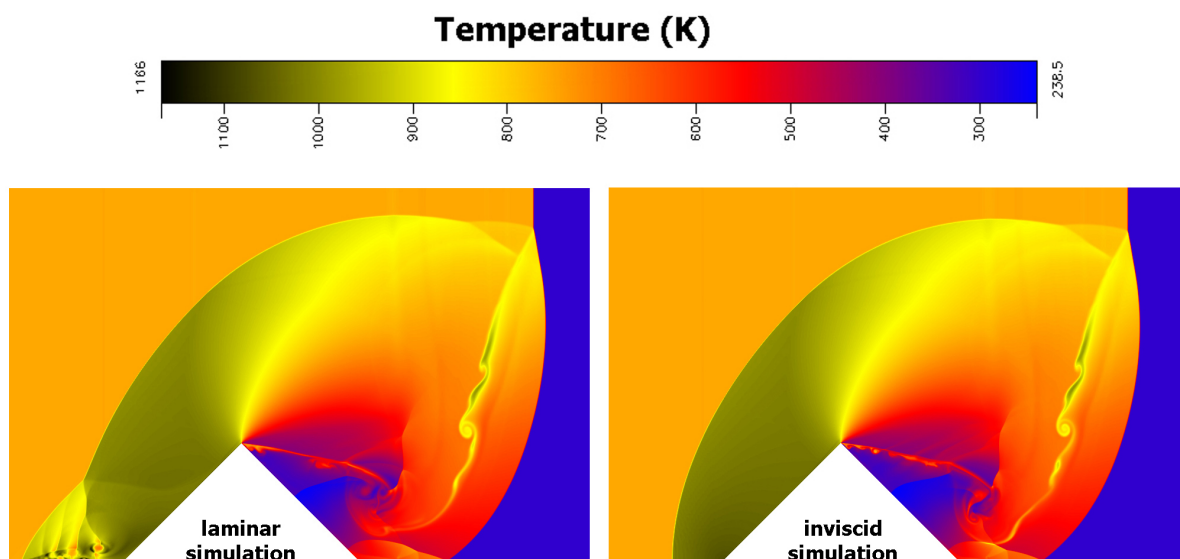


Figure 1.6: Prediction of the temperature field.

## 1.6 The CFD-FASTRAN Software Package

In this thesis a commercial software package known as CFD-FASTRAN is used as a basis for discussion. CFD-FASTRAN is developed and maintained by the CFD Research Corporation (CFDRC), a division of ESI Software. The CFD-FASTRAN package is a complete modelling and analysis system in that it provides tools for model construction, model setup, analysis and results extraction. The package consists of a grid generation environment (CFD-GEOM), a model setup interface (CFD-FASTRAN-GUI), a flow solver (CFD-FASTRAN-SOLVER) and a results extraction package (CFD-VIEW).

The solver uses a finite volume density-based method based on either a Roe's Flux Difference Splitting (FDS) scheme or a Van Leer's Flux Vector Splitting (FVS) scheme for calculating the flux of mass, momentum and energy between cells. An entropy correction

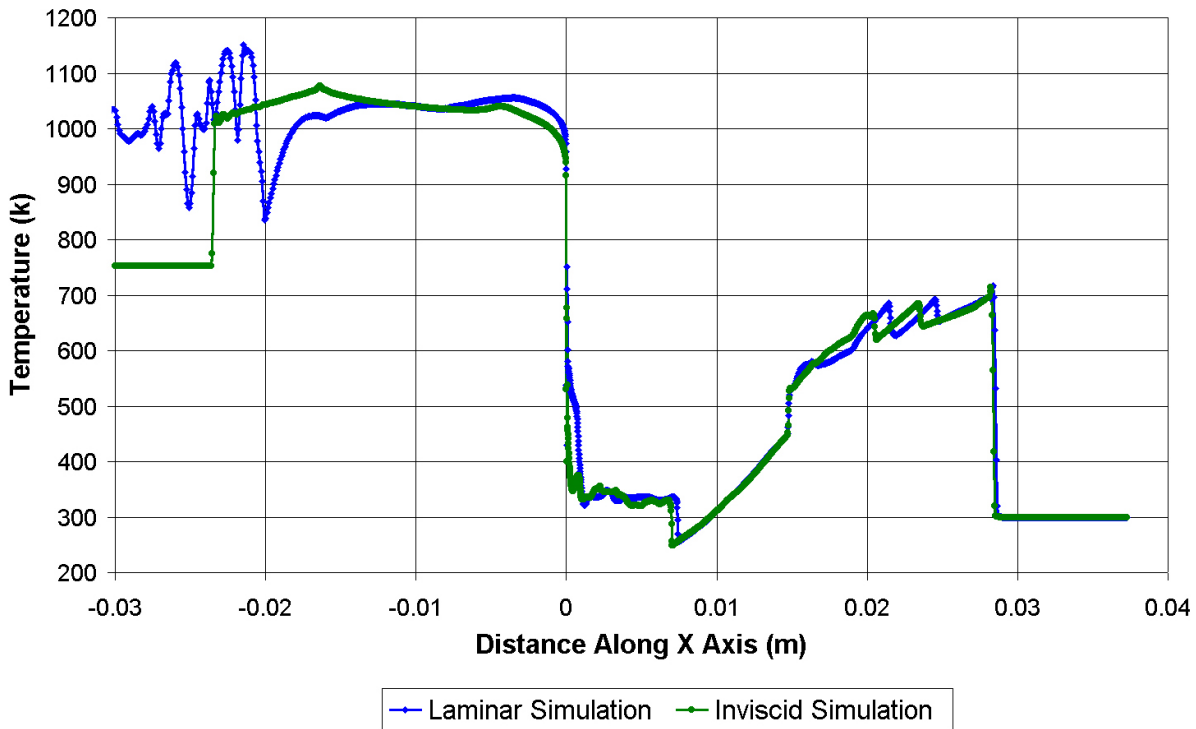


Figure 1.7: Prediction of surface temperature.

is built into the FDS solver to help suppress artificial waves around regions of sonic flow. Details of these numerical schemes can be found in the two volume text *Numerical Computation of Internal and External Flows* [29], [30].

The solver marches in time from an initial condition using either explicit or implicit time integration techniques. The timesteps can be constant across all cells for transient time accurate simulation or vary with each cell for steady flow simulations. Models of flow can be planar, axisymmetric or three dimensional using either a structured multi-block grid or unstructured polyhedral grid<sup>2</sup>. The software has the capability to model ideal, thermally perfect or chemically reacting mixtures of gases. Chemically reacting gases can be treated as being in equilibrium or in nonequilibrium using a modified Arrhenius model for the chemical reaction rate. Flows in vibrational nonequilibrium can be modelled with a two-temperature approach assuming a Landau-Teller rate model for the transfer of vibrational energy. These models are presented in Appendix A. By default the package solves the Navier Stokes equations of flow but the user can solve the reduced Euler set of equations by selecting the inviscid option. For turbulent flows, the software supports a range of RANS schemes such as  $k-\varepsilon$ ,  $k-\omega$ , Baldwin-Lomax, Spalart-Allmaras and the Menter Shear Stress Transport (SST) model.

<sup>2</sup>Not all capability associated with the structured solver is available with the polyhedral solver in CFD-FASTRAN v2004.

CFD-FASTRAN also has extensive capability for moving bodies through the use of overset chimera grids. Motion can be specified in advance or determined within the solution from the summation of pressure on the moving body. CFD-FASTRAN can also be coupled to a structural finite element solver such as Nastran for aeroelastic analysis. This requires use of the **M**ulti-**D**isciplinary **C**omputing **E**nvironment (MDICE) interface. Aeroelasticity as well as moving bodies and turbulent flows are not within the scope of this thesis.

As with all software, CFD-FASTRAN is being continually updated with requests from users. At the time of writing, there are some features which may be desirable when modelling hypersonic flows that are not yet implemented in the CFD-FASTRAN system. The implementation of such features will undoubtedly depend on their demand as well as the time and cost involved in setup. Some relevant features which CFD-FASTRAN v2004 does not support include:

- full consideration of the radiative exchange of energy into and out of the flow<sup>3</sup>
- biasing of dissociation reactions towards the vibrational temperature
- slip wall models for rarefied flow
- capability to model separate internal / vibrational energy equations for each species
- modelling of the electric and magnetic fields generated by a strongly ionised flow
- creation of a boundary condition with a spatial distribution of quantities

The topics in this thesis relate not only to the use of CFD-FASTRAN but also more generally to the use of any finite volume, density-based solver of the Navier-Stokes equations of flow. Examples of other solvers which are written specifically for supersonic and hypersonic flows are shown in Table 1.1. Most of these codes are acronyms and for interest sake their full unabbreviated form is shown in Table 1.2. It should be noted that many of these codes have been developed in the United States and their full use is limited due to export restrictions. Such codes are marked in Table 1.2 with an “(R)” and may not be available for download for non US citizens.

## 1.7 Thesis Aims and Objectives

In the preceding sections, some background to the topics of hypersonics, CFD and validation were discussed. Some fundamental concepts in CFD were presented and the commercial CFD software package, CFD-FASTRAN, was introduced. Reiterating the key points, the structural and thermal loading which acts on a body in hypersonic flight

---

<sup>3</sup>A simple radiation boundary condition is possible which assumes a thermally opaque gas.

Table 1.1: Examples of alternative high speed NS solvers.

solver	type	website	references
VULCAN	NASA(R)	<a href="http://vulcan-cfd.larc.nasa.gov">vulcan-cfd.larc.nasa.gov</a>	[82]
LAURA	NASA(R)		[84]
FUN3D	NASA(R)	<a href="http://fun3d.larc.nasa.gov">fun3d.larc.nasa.gov</a>	
HEFSS	NASA(R)	<a href="http://hefss.larc.nasa.gov">hefss.larc.nasa.gov</a>	
TLNS3D-MB	NASA(R)		[77], [78]
CFL3D	NASA(R)	<a href="http://cfl3d.larc.nasa.gov/Cf13dv6/cf13dv6.html">cfl3d.larc.nasa.gov/Cf13dv6/cf13dv6.html</a>	[46]
GASP	commercial(R)	<a href="http://www.aerosft.com">www.aerosft.com</a>	[5]
GUST	commercial(R)	<a href="http://www.aerosft.com">www.aerosft.com</a>	[6]
PAB3D	commercial(R)	<a href="http://www.asm-usa.com/software/PAB3D/">www.asm-usa.com/software/PAB3D/</a>	
MB-CNS	academic	<a href="http://www.mech.uq.edu.au/cfcfd">www.mech.uq.edu.au/cfcfd</a>	[38], [39]
CLAWPACK	academic	<a href="http://www.amath.washington.edu/~claw/">www.amath.washington.edu/~claw/</a>	[48]
PPM	academic		[19], [10]
DLR- $\mathcal{T}$	research	<a href="http://www.as.go.dlr.de/RF/index.php?page=tau">www.as.go.dlr.de/RF/index.php?page=tau</a>	[25]
elsA	research	<a href="http://elsa.onera.fr/elsA/software/pressoft.html">elsa.onera.fr/elsA/software/pressoft.html</a>	

Table 1.2: Abbreviations for several high speed NS solvers.

VULCAN	<b>V</b> iscous <b>U</b> pwind <b>a</b> lgorithm for <b>C</b> omplex Flow <b>A</b> nalysis
LAURA	<b>L</b> Angley <b>U</b> pwind <b>R</b> elaxation <b>A</b> lgorithm
FUN3D	<b>F</b> ully <b>U</b> nstructured <b>N</b> avier-Stokes <b>T</b> hree <b>D</b> imensional
HEFSS	<b>H</b> igh <b>E</b> nergy <b>F</b> low <b>S</b> olver <b>S</b> ynthesis project
TLNS3D-MB	<b>T</b> hin <b>L</b> ayer <b>N</b> avier <b>S</b> tokes <b>T</b> hree <b>D</b> imensional <b>M</b> ulti <b>B</b> lock
CFL3D	<b>C</b> omputational <b>F</b> luids <b>L</b> aboratory <b>T</b> hree <b>D</b> imensional
GASP	<b>G</b> eneral <b>A</b> erodynamic <b>S</b> imulation <b>P</b> ackage
GUST	<b>G</b> eneral <b>U</b> nstructured <b>S</b> oftware <b>T</b> oolkit
CLAWPACK	<b>C</b> onservation <b>L</b> AW <b>S</b> oftware <b>P</b> ACKage
MB-CNS	<b>M</b> ulti <b>B</b> lock <b>C</b> ompressible <b>N</b> avier- <b>S</b> tokes
PPM	<b>P</b> iecewise <b>P</b> arabolic <b>M</b> ethod code
DLR- $\mathcal{T}$	<b>D</b> eutsches Zentrum für <b>L</b> uft und <b>R</b> aumfahrt - <b>T</b> AU
elsA	<b>e</b> nsemble <b>l</b> ogiciel pour la <b>s</b> imulation en <b>A</b> rodynamique

needs to be understood when designing vehicles which transcend the atmosphere. This information can be obtained by analysing the flow which passes over the vehicle in flight. Analysis can be theoretical, experimental or numerical in form. The numerical analysis of flow is termed computational fluid dynamics (CFD).

CFD models can be sensitive to parameters such as the type of grid used, the positioning of cells within the grid, the boundary and initial conditions imposed on the model,

the mathematical model used to describe the flow and the numerical methods used to solve the mathematical equations. Validation of CFD models to experimental results is therefore a critical step in the process of modelling a flow. Without validating CFD software for problems similar to the model of interest, no confidence can be placed in the results.

Many software codes are currently available for the analysis of fluid flow. Typically each code has strengths and weaknesses and it is unusual for one single CFD code to perform well in all aspects of fluid dynamics. In this thesis the software package CFD-FASTAN has been selected because of its focus on supersonic and hypersonic flows.

Overall this thesis is intended to provide a starting guide and a set of validation exercises for students of hypersonics whose projects require them to undertake some CFD analysis. It was motivated by the poor success that postgraduate students achieved when required to use CFD-FASTAN to analyse hypersonic flow problems as part of their research projects. Whilst CFD-FASTAN could nominally perform the analysis it was not clear how to get it to do the analysis reliably.

The thesis begins with a review of some thermodynamic considerations for high speed flow in Chapter 2. The reader is then guided through some practical advice regarding the construction and solution of typical CFD models for high speed flow in Chapter 3. The application of techniques discussed in this chapter is then demonstrated in Chapter 4 where six validation studies are presented. The validation problems cover a range of supersonic and hypersonic problems including steady and unsteady shockwave interaction, viscous effects and thermochemical nonequilibrium. Chapter 5 then presents a summary of the thesis and recommends some future directions for research into the validation of hypersonic flow models.

The desired outcomes of the thesis are as follows:

- review some of the relevant physics of high temperature gases
- introduce the concepts of CFD modelling
- discuss some options and techniques in grid construction
- discuss setup of a CFD model including boundary conditions and initial conditions
- present an overview of the solution process
- demonstrate some traditional as well as innovative methods for results extraction and presentation.

- validate CFD-FASTRAN against experimental results obtained in ground based hypersonic test facilities.
- run selected models with and without viscosity to highlight the role of viscous effects in high speed flows
- conclude the thesis by summarising the key concepts

Lastly, this thesis assumes the reader has an adequate knowledge in the areas of heat transfer, thermodynamics, physical chemistry, compressible gas dynamics and boundary layer theory. Students not familiar with these topics are advised to review the fundamentals of these topics before continuing. Familiarity with the topic of CFD is not essential but will be beneficial to the reader.



---

# High Temperature Gas Dynamics

---

This chapter introduces some of the concepts involved in the analysis of gas flows that involve high temperatures. When flow at very high speed is brought to a halt, the kinetic energy of the flow is transferred mostly into internal energy. The physical manifestation of this energy is a large increase in temperature. The behaviour of gases at high temperatures is therefore an important aspect to hypersonic flow. This chapter includes a general introduction to the effects present in high temperature air as well as a more detailed discussion on the concepts of internal energy modes, chemical reactions and nonequilibrium flow. Whilst not directly related, a discussion of rarified flow is also included in this chapter. This chapter is based on information presented in Anderson's text "Hypersonics and High Temperature Gas Dynamics" [7].

## 2.1 Behaviour of High Temperature Air

A gas is classed as thermally perfect when the local gas pressure ( $P$ ), temperature ( $T$ ) and density ( $\rho$ ) are related by the ideal gas law:

$$P = \frac{\rho R_U T}{\mathcal{M}}$$

Where  $R_U$  is the universal gas constant and  $\mathcal{M}$  is the molecular weight of the gas. The ratio of the universal gas constant to the molecular weight is known as the specific gas constant ( $R$ ) such that for any given thermally perfect gas:

$$P = \rho R T$$

Where  $R$  is unique to that gas.

The specific heat of a gas at constant pressure ( $C_P$ ) and at constant volume ( $C_V$ ) plays an important role in compressible flows as the specific gas constant can be expressed in terms of these values:

$$R = C_P - C_V$$

and the speed of sound in a gas (a) depends upon the ratio of specific heats ( $\gamma$ ):

$$a = \sqrt{\gamma RT}$$

Where:

$$\gamma = \frac{C_P}{C_V}$$

A calorically perfect gas is a thermally perfect gas for which the specific heats do not vary with temperature. This thermodynamic state is valid in Air given that temperatures are in the range of around 3K to around 600K<sup>1</sup>. As the specific heats are constant in the above range, both R and  $\gamma$  are also constant in this range of temperatures. The properties of calorically perfect air are shown in Table 2.1.

Table 2.1: Thermodynamic properties for calorically perfect air.

specific heat at constant pressure, $C_P$	1004 $\frac{J}{KgK}$
specific heat at constant volume, $C_V$	717 $\frac{J}{KgK}$
ratio of specific heats, $\gamma$	1.4
specific gas constant, R	287 $\frac{J}{KgK}$
molecular weight, $\mathcal{M}$	28.97 $\frac{g}{mol}$

The properties of air, and indeed all gases, at very high temperatures are far more complex than a calorically perfect gas model suggests. Figure 2.1 shows the temperature ratio  $\frac{T_2}{T_1}$  across a normal shock in air versus the pre-shock velocity  $u_1$ . This figure has been reproduced from Anderson [7]. Four curves are shown on the chart. The dashed curve represents a calorically perfect gas whilst the three solid curves represent a chemically reacting gas in equilibrium. The equilibrium gas depends on pressure as well as temperature hence the need for multiple curves. It can be seen from this plot that the error introduced by the assumption of a calorically perfect gas can become large with increasing speed. For example, at 6 km/s, a calorically perfect gas model predicts a temperature ratio of around 90 whereas the more realistic chemically reacting gas model predicts 25 to 35 depending on the pressure. A margin of error this large means that hypervelocity flows of air cannot be adequately modelled using a calorically perfect gas assumption. The proceeding sections discuss some effects which lead to the deviation from calorically perfect behaviour.

## 2.2 Modes of Internal Energy

Molecular internal energy can exist in translational, rotational, vibrational and electronic forms. In room temperature air, the molecules of Nitrogen and Oxygen translate and

<sup>1</sup>Ignoring the condensation of gases from the air and associated vapor states.

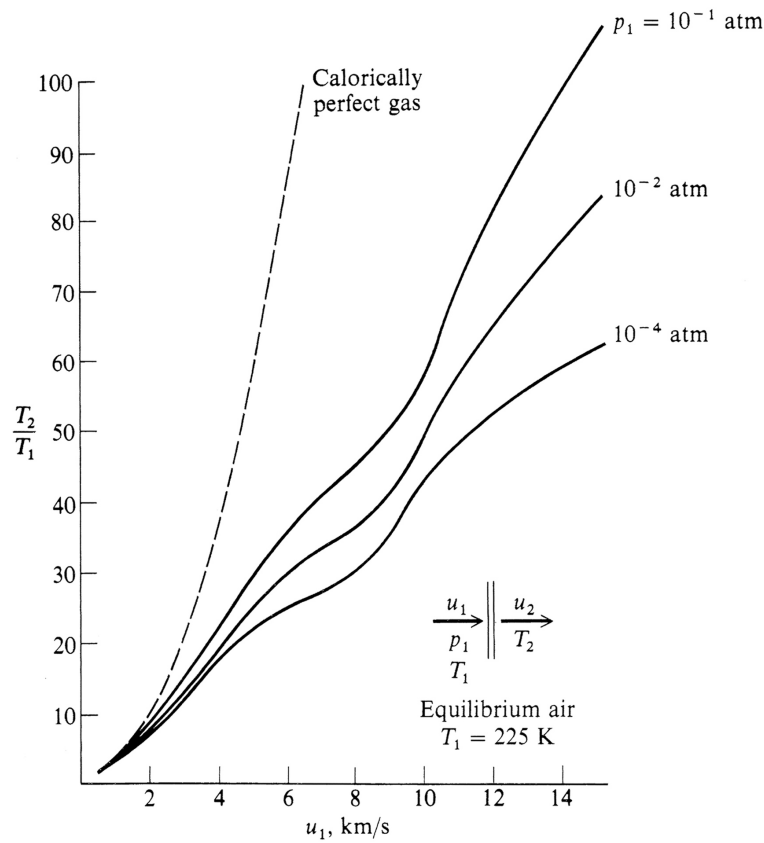


Figure 2.1: Temperature ratio across a normal shock in equilibrium air [7].

rotate as they collide with one another. At this temperature the translational and rotational modes of internal energy are fully excited and the specific heats of air are constant. Below around 1 K only the translational mode of Oxygen and Nitrogen molecules is active. At this temperature the specific heats are less because energy is not absorbed by the rotational mode. The rotational mode is activated above 1 K and is fully excited by 3 K. When air is heated above around 600 K the atoms in Nitrogen and Oxygen molecules begin to vibrate like two balls connected by a stiff spring. When the vibrational mode of internal energy becomes excited, the specific heats increase nonlinearly with temperature. At 500 K, the specific heat at constant pressure is 1004 so raising one kilogram of air to 501 K at constant pressure will take exactly 1004 J of energy. Now consider raising that same kilogram of air from 1500 K to 1501 K. This requires around 1208 J of energy because 204 J of the heat energy will be stored by the molecules as they vibrate toward and away from each other, whilst the remaining 1004 J is stored as random translations and rotations. As temperature is a measure of the translational mode of internal energy the energy requirement to raise the temperature of the gas becomes higher to account for the extra storage in the vibrational mode. Oxygen and Nitrogen molecules can only vibrate towards and away from each other so they are said to have only one vibrational degree of freedom (DOF). A more complex molecule such as Carbon Dioxide can have

multiple vibrational DOF. A monatomic gas such as Helium can never store vibrational energy because the gas is composed of individual atoms. With further heating, the energy with which molecules collide is increased and the vibrational energy of a molecule becomes larger. These two effects lead ultimately to the separation of a molecule into its component atoms. This process is known as dissociation. For air at atmospheric pressure, all of the Oxygen and Nitrogen molecules are in atomic form by 9000 K. At this temperature, the electronic mode of internal energy becomes excited. Electronic internal energy changes occur when electrons jump orbital shells. The transfer of energy in this mode occurs in discrete amounts and so the energy levels possible are quantized (discontinuous). All modes of internal energy are, in fact quantized into discrete energy levels but the translational and rotational modes appear almost continuous. The vibrational energy levels are more quantized but can still in most cases be approximated as continuous. With further heating the electrons can completely separate from their parent atoms. This process is known as ionisation. At temperatures high enough to sustain full ionisation, the gas is considered to have transformed into a plasma state. Figure 2.2 shows one possible visualisation of the different modes of internal energy<sup>2</sup>. The vibrational and electronic energy levels are often quoted in terms of a temperature such as “vibrational temperature” and “electron temperature”. These do not relate to the physical temperature but are simply a measure of the degree of excitement of the corresponding energy levels. CFD-FASTRAN uses a slightly different terminology which is discussed in the following section.

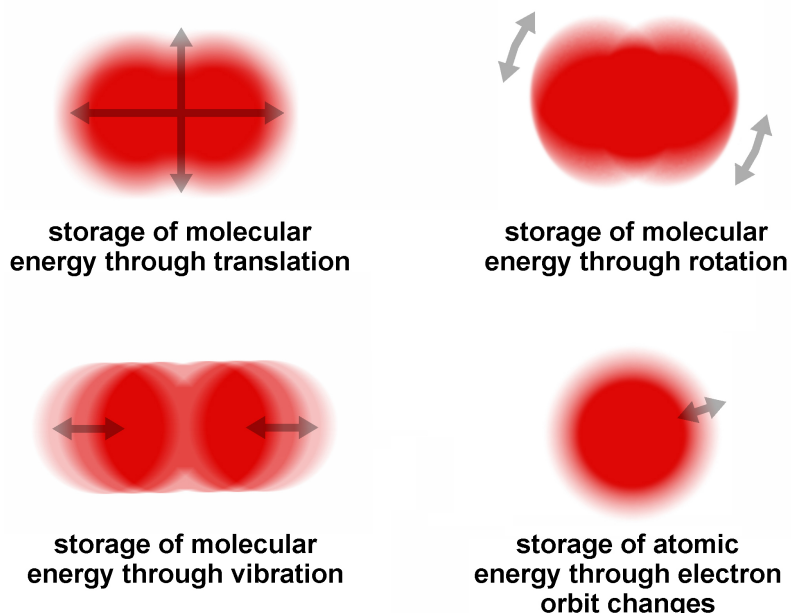


Figure 2.2: Visualisation of the modes of internal energy.

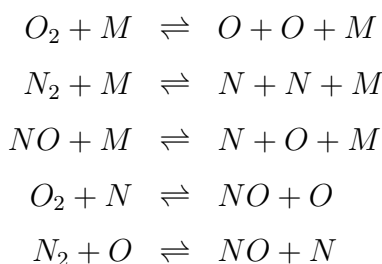
<sup>2</sup>This is an artistic impression only.

### A Note on Internal Temperature

CFD-FASTRAN does not use the term “vibrational temperature” but instead uses the term “internal temperature” or  $T_{\text{INT}}$ . In CFD-FASTRAN, the definition of internal temperature is dependent upon the thermodynamic database chosen. The default curve fit database is suitable for flows where the maximum temperature is below 6,000 K. For this option the internal temperature is a combination of the vibrational and electronic temperatures. The alternative molecular database can be used for flows where the maximum temperature exceeds 6,000 K but the electronic mode of internal energy is neglected. The internal temperature is then equal to the vibrational temperature. Throughout this thesis, the term vibrational temperature is used in lieu of internal temperature as the case studies selected for validation do not involve significant excitation of the electronic mode of internal energy.

## 2.3 Chemical Reactions in Air

For air at 2000 K and atmospheric pressure, the Oxygen molecules begin to dissociate into individual atoms. At 2000 K only a small fraction of the total Oxygen will be dissociated but as the temperature increases, the fraction of dissociated Oxygen also increases. At 5000 K almost all of the Oxygen will be dissociated into individual atoms. A similar process occurs with Nitrogen molecules but the dissociation does not begin, for atmospheric pressure, until around 4000 K and is not complete until around 9000 K. Increasing the pressure generally has the effect of raising these temperature ranges whilst decreasing the pressure has the effect of lowering them. In the presence of atomic Nitrogen and Oxygen, nitric oxide can form. Oxygen molecules will dissociate into Oxygen atoms which may subsequently recombine with other Oxygen atoms to reform an Oxygen molecule or with Nitrogen atoms to form nitric oxide. At atmospheric pressure, nitric oxide is present from about 2000 K - 6000 K with a peak concentration at 3500 K. Figure 2.3 shows the equilibrium molar fraction of each of the above five species ( $O_2$ ,  $N_2$ ,  $N$ ,  $O$  and  $NO$ ) plotted against temperature for a pressure of one atmosphere. This figure is taken from Anderson’s text [7]. Reaction schemes involving these five species have been proposed by Park [60] and Kang et al. [45]. The reaction scheme suggested by Park (commonly referred to as PARK-I) contains the following reactions:



In the above reactions “M” is the collision partner and represents any species which does not take part in the reaction but does effect the reaction rate through its presence. For each different collision partner, a third body efficiency ( $M_{EFF}$ ) is given. A third body efficiency is a multiplying factor on the reaction rate to account for the presence of the collision partner which may retard or accelerate the reaction. Each of the above reactions can occur forwards and backwards and each have corresponding temperature dependent rates. Rate data for this reaction scheme is listed in Section 4.6.5. Ionisation is another process which effects the composition of high temperature air. Of all the above species, nitric oxide requires the lowest temperature to become ionised.  $NO^+$  and  $e^-$  can be found in flows with temperatures below 9000 K. Increasing the temperature beyond 9000 K leads to significant ionisation of all five species and the mixture becomes an electrically charged plasma. The components of air are then  $O_2$ ,  $N_2$ ,  $O$ ,  $N$ ,  $NO$ ,  $NO^+$ ,  $O_2^+$ ,  $N_2^+$ ,  $O^+$ ,  $N^+$  and  $e^-$ . Reaction schemes which account for all eleven species have been suggested by Park [61], [62] as well as Dunn and Kang [21]. The reaction schemes are quite complex, containing up to 49 reactions.

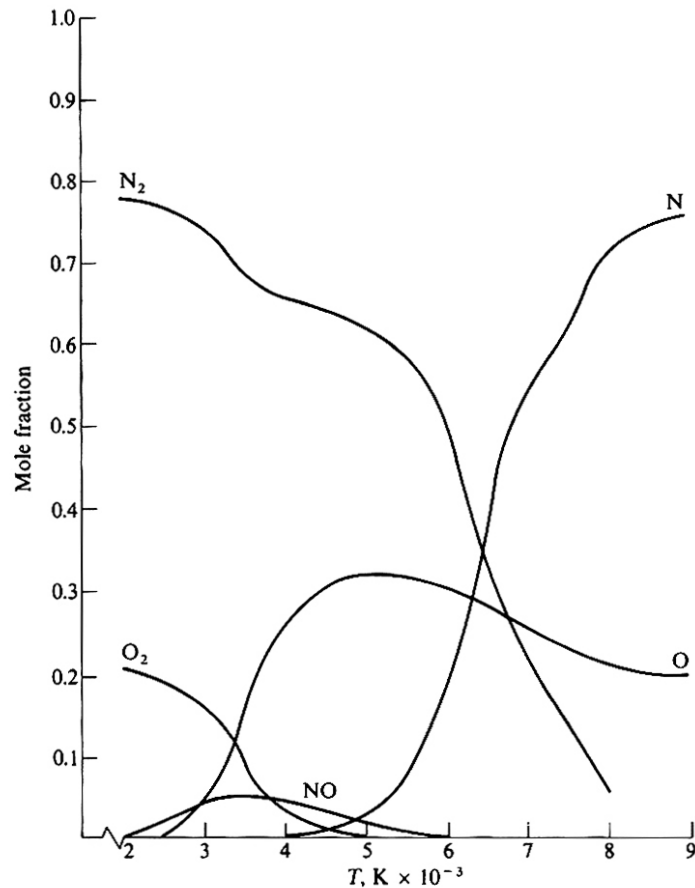


Figure 2.3: Composition of equilibrium air versus temperature at one atmosphere [7].

## 2.4 Frozen, Equilibrium and Nonequilibrium Flow

Internal energy can only be transferred through collisions between molecules or through radiation. Putting aside the complexity of radiation, this means that the transfer of internal energy is essentially dependent on how often molecular collisions occur. The kinetic theory of gases can be used to show that the frequency of molecular collisions ( $Z$ ) is proportional to both the pressure and temperature of a gas in the following manner<sup>3</sup>:

$$Z \propto \frac{P}{\sqrt{T}}$$

Typically, a number of collisions are required to transfer internal energy and there is a finite amount of time between each collision. The exchange of internal energy therefore takes some small amount of time to complete. Because molecules undergoing this transfer of energy travel through the flow at some finite speed, the spatial distribution of flow properties is dependent on the efficiency of internal energy transfer. The typical number of collisions required to transfer internal energy depends on the mode of internal energy being transferred. The typical number of collisions required for the transfer of different internal energy modes for molecules such as Nitrogen and Oxygen is shown in Table 2.2. This information was obtained from the GASP User Manual [5] where the information was collected together from a number of papers. As can be seen from the table, the transfer of vibrational energy is far less efficient than for other modes. For this reason, only transfer of the vibrational mode is generally considered in air because this mode requires significantly more collisions than the more efficient rotational and translational modes. Hydrogen molecules require around 300 collisions to come into rotational equilibrium and so the transfer of this mode may become significant when modelling this gas. At the time of writing, CFD-FASTAN only allows for the transfer of vibrational and electronic energy.

Table 2.2: Typical number of collisions needed to reach equilibrium.

energy mode	collisions required for N <sub>2</sub>	collisions required for O <sub>2</sub>
translational	4 - 5	4 - 5
rotational	9	12
vibrational	~100,000	~100,000

Chemical reactions also take a finite number of collisions to complete. This can be seen behind a strong shockwave in hypersonic flow where the concentration of each chemical species takes a certain distance before approaching an equilibrium value. For both

<sup>3</sup>From [7] Page 475, equation 12.22

internal energy transfer and chemical reactions, the nature of time dependency can be approximated in two ways. If a molecule travels through a region of flow and encounters only a few collisions along the way then this region of flow is said to be “frozen”. Frozen flow can refer to internal energy transfer (thermally frozen) or chemical reactions (chemically frozen) or both. For a thermally frozen gas, vibrational and electronic energy is essentially trapped within a molecule because only minimal collisions are occurring. Once the collisions become more frequent the excess internal energy can be transferred into the surrounding molecules. At the opposite end of the scale a molecule may be bombarded by collisions before it has travelled very far across a region of flow. This region of flow is then said to be in equilibrium. If the situation is between these two extremes then the flow is classed as nonequilibrium. Thermal and chemical nonequilibrium states can occur independently of each other. An example of purely thermal nonequilibrium is given in validation case 5 where the hypersonic flow of Nitrogen over a sharp double cone is investigated. Here the test gas is pure Nitrogen, which does not dissociate until around 4000 K at atmospheric pressure. The vibrational energy mode becomes excited above 600 K. In this test case, the maximum temperature exceeds the temperature needed to dissociate Oxygen (2000 K at 1 atm) but does not quite reach the temperature needed to dissociate Nitrogen, hence there is no flow chemistry. If the test gas was air then chemistry would need to be considered. Nonequilibrium flow is the most general type of flow but also the hardest and most time consuming to calculate. Internal energy transfer and chemical reactions can be neglected for thermally and chemically frozen flow<sup>4</sup>, making them also straight forward to process. Equilibrium internal energy states and chemical equilibrium states are unique for a given pressure and temperature, hence they can be incorporated into an analysis relatively easily through the use of look-up tables or polynomial curve fits. Thermal and chemical nonequilibrium states are not as easy to predict because they require the incorporation of the vibrational and chemical rate equations which are based on empirical data. This data typically contains a fair amount of scatter. Vibrational relaxation rates are modelled in CFD-FASTRAN using a generalised Landau-Teller model. Chemical reaction rates are modelled in CFD-FASTRAN using the Arrhenius model with a preexponential temperature factor. These models are described in Appendix A.

## 2.5 Summary of High Temperature Effects

There are many aspects to consider when modelling gases at extreme temperatures. For air at atmospheric conditions and below 9000 K these effects are mostly limited to vibrational excitation, chemical reactions and nonequilibrium flow. Air at temperatures above 9,000 K may require consideration of electronic internal energy transfer, ionisation, radiation and magnetohydrodynamic effects. The latter relates to effects caused by the interaction

---

<sup>4</sup>Assuming that a frozen state is maintained throughout the entire flow field.

between strongly ionised flow and the electric and magnetic fields generated by that flow. Consideration of these effects is beyond the scope of this thesis. A valuable tool for assessing which effects are important in an analysis is provided by Anderson [7] in the form of a map. This map consists of the standard velocity-altitude map superimposed with regions of vibrational excitation, dissociation and ionisation. Figure 2.4 shows a reproduction of the chart from Anderson's text.

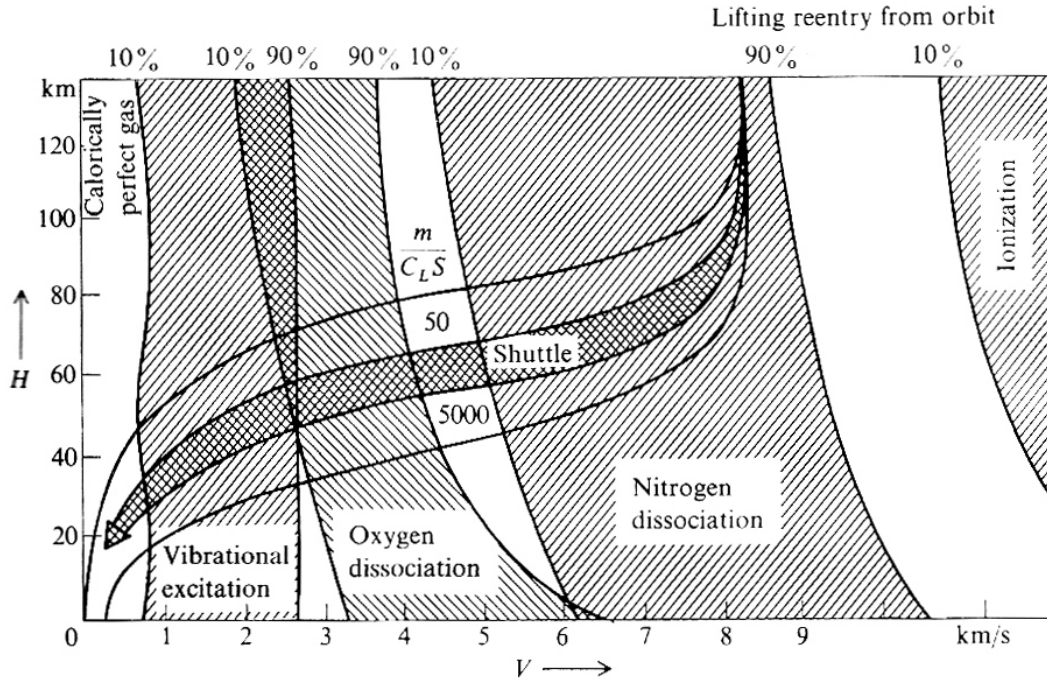


Figure 2.4: Velocity-altitude map with superimposed regions of vibrational excitation, dissociation and ionisation [7].

## 2.6 Continuity of Flow

One of the fundamental assumptions in classical fluid dynamics is that a fluid is a continuous substance. This assumption implies that a gas can be divided up infinitely many times and still be a continuous medium. We know from modern physics and chemistry that this is not the case and that gases are in fact composed of an extremely large number of interacting molecules. The average number of molecules ( $N$ ) occupying a given volume ( $V$ ) at a specific temperature ( $T$ ) and pressure ( $P$ ) is given by<sup>5</sup>:

$$N = \frac{PV}{kT}$$

Where  $k$  is Boltzmann's constant. In a system of such particles many collisions will occur. The average distance a particle will travel before encountering a collision is called

<sup>5</sup>See Anderson [7], Page 382 eqn 10.9.

the mean free path and is denoted by the symbol  $\lambda$ . The relationship of the mean free path to macroscopic properties such as temperature and pressure can be derived from kinetic theory. Combining equations 10.10 with equation 12.21 from Anderson [7] gives the relationship:

$$\lambda = \frac{kT}{\sqrt{2}\pi\sigma^2P}$$

Where  $\sigma$  is the collision diameter of a molecule. Table 2.3 shows the collision diameter for some common gases. For a cubic meter of air at sea level and at 25°C, there will be around  $2.46 \times 10^{25}$  particles of Oxygen and Nitrogen combined. The mean distance between collisions is 73 nanometers or just 206 times the effective diameter of the molecules. With this many particles in such a confined space the interactions between molecules are so frequent that the gas behaves as a continuous medium. In comparison, just ninety kilometers above the earth's surface there are only  $6.59 \times 10^{19}$  molecules in a cubic meter of air<sup>6</sup>. Under these conditions a molecule must travel 27 millimeters on average before colliding with another particle. Collisions between molecules are therefore infrequent given the collision diameter is a mere 0.35 nanometers. In this environment, the behaviour of the air deviates significantly from that of a continuous medium. One of the earliest observed effects of rarefied flow is the onset of velocity slip and thermal slip. Velocity slip occurs when the gas velocity at the wall no longer equals the velocity of that wall and similarly thermal slip occurs when gas temperature at the wall no longer equals the temperature of that wall. Some NS codes incorporate a slip wall boundary condition to extend the reach of problems which can be successfully modelled. Even with slip walls, NS solvers fail to predict truly rarified flow because the behaviour becomes fundamentally different to that of a continuous gas. The Knudsen number (Kn) is often used to judge the level of rarefaction in a flow. The Knudsen number is the ratio of the mean distance between collisions to the distance across the object of interest. This distance is the characteristic dimension of the object and is generally considered the largest dimension perpendicular to the flow. Anderson [7] defines a Knudsen number of 0.2 as the limit up to which the Navier-Stokes equations can be successfully applied with the condition that flows with a Knudsen number above 0.03 must consider the slip effects.

---

<sup>6</sup>Using pressure and temperature data from the US Standard Atmosphere [1].

Table 2.3: Collision diameters for some common gases [72].

Gas	$\sigma(m)$
Air	$3.542 \times 10^{-10}$
Ammonia (NH <sub>3</sub> )	$2.900 \times 10^{-10}$
Argon (Ar)	$3.542 \times 10^{-10}$
Carbon Monoxide (CO)	$3.690 \times 10^{-10}$
Carbon Dioxide (CO <sub>2</sub> )	$3.941 \times 10^{-10}$
Helium (He)	$2.551 \times 10^{-10}$
Hydrogen (H <sub>2</sub> )	$2.827 \times 10^{-10}$
Krypton (Kr)	$3.665 \times 10^{-10}$
Methane (CH <sub>4</sub> )	$3.758 \times 10^{-10}$
Nitrogen (N <sub>2</sub> )	$3.798 \times 10^{-10}$
Neon (Ne)	$2.820 \times 10^{-10}$
Oxygen (O <sub>2</sub> )	$3.467 \times 10^{-10}$
Xenon (Xe)	$4.047 \times 10^{-10}$



---

# Methodology of Modelling

---

This chapter provides an overview of the four stage modelling and analysis process within the CFD-FASTRAN system. The chapter contains practical guidance and advice for the newcomer to compressible CFD modelling. Whilst the focus is on modelling within the CFD-FASTRAN system, the concepts and techniques presented in this chapter should also apply to other codes of a similar nature such as those presented in Table 1.1.

## 3.1 Stages of Analysis

The CFD-FASTRAN package is a complete analysis system as it provides tools for constructing a grid, preparing a model, solving a model and viewing the results of an analysis. CFD-FASTRAN uses separate graphical interfaces for each of these four stages. The graphical interfaces are highlighted in `VERBATIM TEXT` for clarity. The stages of analysis are summarised in the next few paragraphs and a more detailed discussion on each stage of analysis is then provided in the remainder of the chapter.

### Stage I: Grid Generation

Stage I involves the construction of the grid on which the equations of flow are solved. `CFD-GEOM` is provided for this task. Geometry can be imported from a CAD package in several formats, including IGES or ACIS, as an aid for the construction of a grid. Alternatively the user can create the geometry and grid fully within the `CFD-GEOM` environment. Once the grid is completed, a Geometry and Grid Definition (GGD) file is saved which stores all grid and geometry related information. A Data Transfer Facility (DTF) file is also saved. The DTF file is read into `CFD-FASTRAN-GUI` for Stage II. The DTF file contains only grid information and cannot be read back into `CFD-GEOM` hence the need to keep a GGD file.

### Stage II: Model Preparation

`CFD-FASTRAN-GUI` is an application for preparing a model for analysis. A DTF file, typically exported from `CFD-GEOM`, is imported into the application and boundary conditions

and initial conditions are prescribed to the model. Gas properties are defined, models of flow are chosen and various solver options are selected. Once the model has been setup it can be submitted for analysis. This can be done directly from the `CFD-FASTRAN-GUI` environment or from a command shell. Multiple runs can be queued by creating a batch file and launching the solver from a shell.

### Stage III: Solver Routine

This stage is performed by the computer only and users do not need to be present once the solver has been initiated (assuming the solution is set up correctly and proceeds to convergence). Both a DTF file and a DAT file are needed to launch `CFD-FASTRAN-SOLVER`. The DTF file exported from `CFD-GEOM` is updated automatically by `CFD-FASTRAN-GUI` to include all the relevant model setup information. A DAT file is generated by `CFD-FASTRAN-GUI` which contains additional information such as initial conditions and solver parameters. The DAT file is written in ASCII format and can therefore be viewed or modified with any text editor. The DTF file is written in binary format and cannot be directly edited.

### Stage IV: Results Processing

If the solution has been successful, results will be produced. Depending on the output method requested, `CFD-FASTRAN-SOLVER` will either create new DTF files or overwrite the existing DTF file when results are recorded to disk. If output has been requested at every ten iterations for example, the files generated would be “Model.0010.DTF”, “Model.0020.DTF” etc. Alternatively, a minus symbol placed immediately before the requested output frequency instructs `CFD-FASTRAN-SOLVER` to overwrite the original DTF file at the specified iteration frequency. In this situation, the file “Model.DTF” would be updated with new results at every ten iterations. The overwrite option may be essential if hard disk space is minimal.

`CFD-VIEW` is used to open DTF files which contain results and process them for graphical display. `CFD-VIEW` offers a variety of tools for this task, many of which are discussed in Section 3.5. Once the results are displayed, images can be saved in common formats such as JPG or BMP files. If multiple result files were written, an animation of results over time can be output as an AVI or MPEG animation file. The layout of result tools within the `CFD-VIEW` environment is stored in a MDL file. Figure 3.1 illustrates the four stages of analysis. The solution stage is faded to highlight that user involvement is not required during this stage.

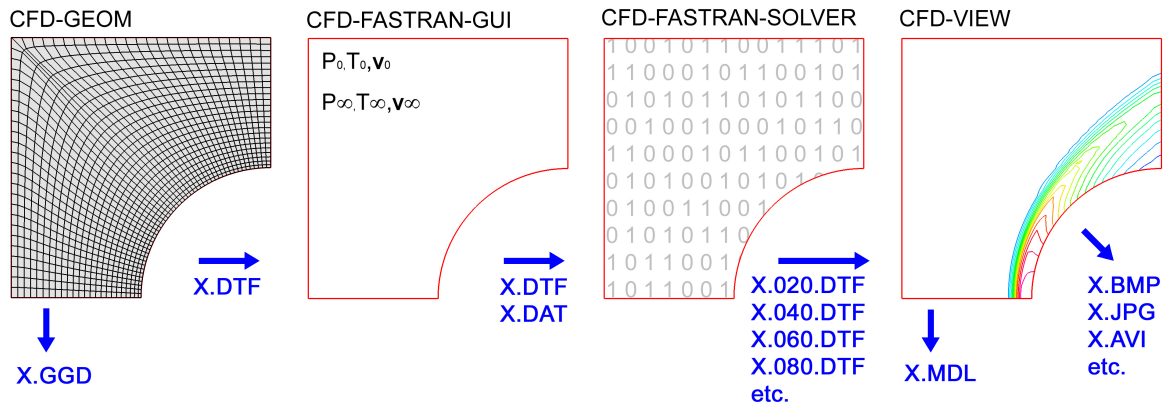


Figure 3.1: Stages of analysis within the CFD-FASTRAN system.

## 3.2 Grid Design Methodology

One of the most frequent questions asked by beginners in CFD (or indeed most numerical analysis) is “What grid should I be using and why?” This is not an unreasonable question for a newcomer faced with the multitude of different cell types, gridding schemes and solver options which modern CFD packages contain. Investigating all types of available cell shapes and grid schemes is a large undertaking and unfortunately beyond the scope of this thesis. This section does however introduce some common two dimensional gridding schemes and illustrates the application of these schemes on a typical aeroshell model.

CFD-GEOM is the tool provided within the CFD-FASTRAN system for the task of generating a grid. This program can be thought of as a tool for translation. The translation is from continuous geometric entities such as curves, surfaces and volumes to a discrete collection of cells known as a grid. Computers today are capable of processing models with many cells. As an indication of size, the largest analysis in this thesis used a grid which contained over two million cells and was run using a 2.8 GHz Pentium 4 processor for a period of one week. The model was two dimensional but a high resolution grid was required to adequately reconstruct a very thin boundary layer and its interaction with a shock wave. In the US, three dimensional flow models containing over one billion cells have been successfully run on the ASCI supercomputers. ASCI, the Accelerated Strategic Computing Initiative, is a US government project aimed at developing large scale computing capabilities. An overview of the ASCI project is available at [http://www.llnl.gov/asci/overview/asci\\_mission.html](http://www.llnl.gov/asci/overview/asci_mission.html) and an independent review of the ASCI project is given by Post and Votta [65].

### 3.2.1 Structured Grids

The term “structured grid” refers to a format whereby cells are spaced in an orderly fashion along a given coordinate system. The simplest of all structured grids is the cartesian

grid. As its name suggests, cartesian grids have cells which follow the X and Y axes for two dimensional grids and additionally the Z axis for three dimensional grids. Cartesian grids are fast to solve and their solution algorithms are the most straight forward. Support for cartesian grids is limited though, as their ability to handle curved wall boundaries is poor with only a stepped approximation available. Better definition of curved boundaries requires increasing the resolution but this leads to large increases in model size for small increases in definition. Figure 3.2 shows a cartesian grid applied to an axisymmetric model of an aeroshell (and attached sting) positioned in the test section of an expansion tube.

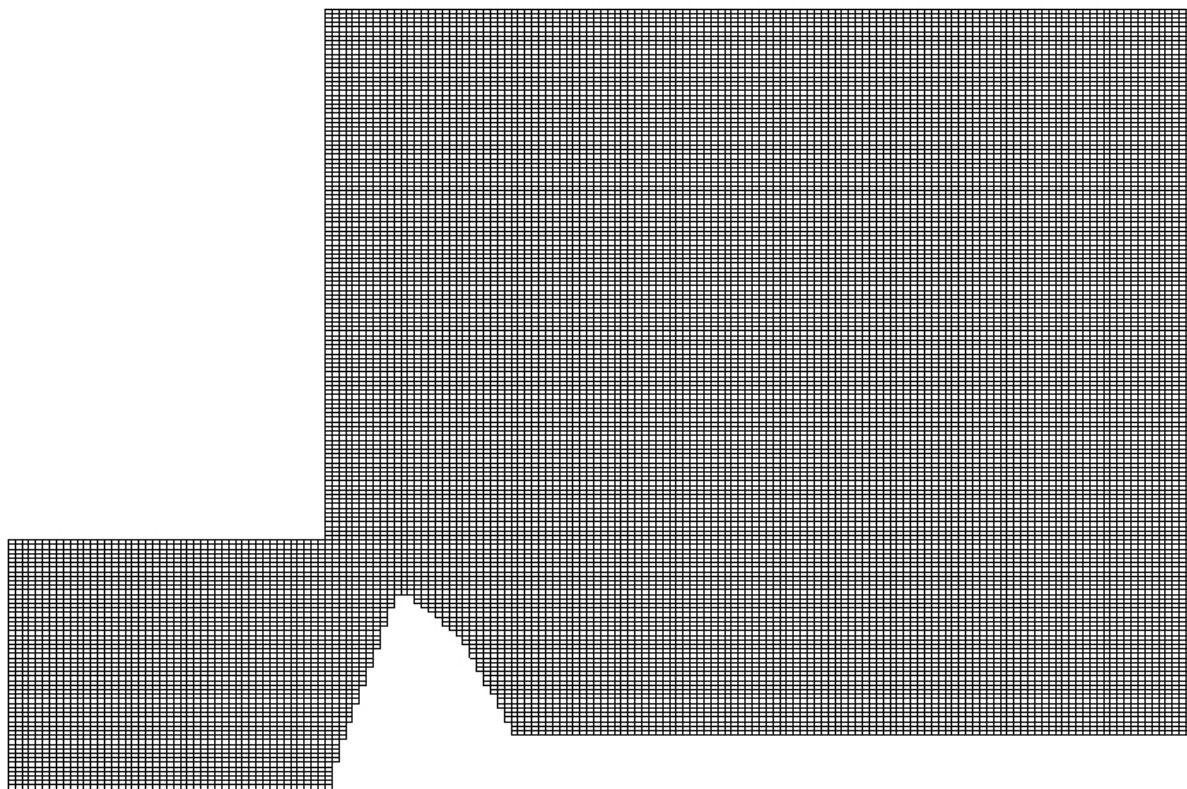


Figure 3.2: Axisymmetric cartesian grid of the pathfinder shape.

Most flow solvers allow a more general structured grid arrangement with cells that follow along any curvilinear coordinate system. This format of structured grid is referred to as “body fitted”. Body fitted grids are constructed in blocks. Each block is a region bounded by four curves in a two dimensional model or six surfaces in a three dimensional model. For each block a grid is commonly generated through a process known as Trans-Finite Interpolation (TFI), although other routines are available. For a two dimensional block these routines divide the block with curves that are interpolated between opposite edges. Interpolation may be lagrangian (linear) in the case of an evenly spaced grid, or nonlinear in the case of a biased grid (see Section 3.2.5). Figure 3.3 shows a single two dimensional block with nine curves interpolated between edge 1 and edge 3 and four curves between

edge 2 and edge 4, forming a grid of 50 cells. For three dimensional blocks, surfaces are interpolated between the three pairs of adjacent faces to form a grid of cells. Most solvers which accept body fitted grids also permit “multi-block” grids. Multi-block grids are composed of many blocks connected together thereby overcoming the limitation of four sided and six faced regions of flow. Blocks which are connected must have the same grid spacing at the shared interface.

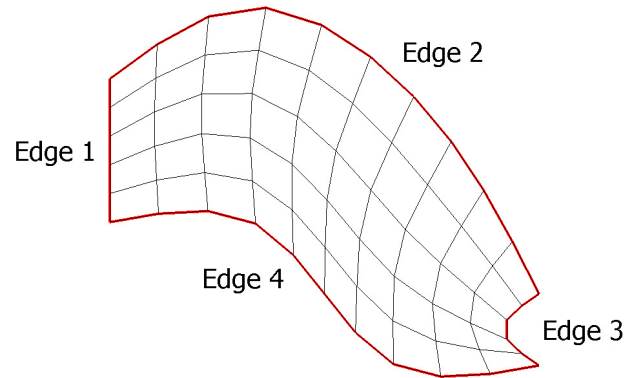


Figure 3.3: Single curvilinear block containing 50 cells.

### Practical Limitations of Block Sizes in CFD-FASTRAN

Although CFD-FASTRAN does not impose a restriction on the number of cells in a single block, large numbers of cells per block can generate a stack overflow causing the solver to terminate during initialisation. The limiting number of cells appears to be around 60,000 cells per block for a calorically perfect, single species gas simulation running under MS-Windows 2000 or XP. The limit is slightly larger for Linux but less when running more complex physics (such as mixing or turbulence). In a practical sense, this limit can be overcome by simply subdividing the single block into smaller blocks. Alternatively, the stack size limit imposed by the operating system can be increased but this can prove troublesome to implement when running under Windows.

### 3.2.2 Unstructured Grids

Unstructured grids are generated in a very different fashion than structured grids. Structured gridding routines interpolate between opposite edges of a four sided surface (or opposite surfaces of a six faced solid) to define cells. Unstructured grids are more general and can be generated using a number of approaches. CFD-GEOM uses an advancing-front Delaunay routine which builds cells inward from the bounding edges of a domain forming connections between the cells when they overlap. The routine continues to grow the cell front inwards until the entire area is covered with cells. The gridding of solid models

requires this routine to be performed on every face which bounds the solid. Solid cells are then built inwards from the bounding surfaces until the entire volume is gridded. Connectivity is established at the interfaces where three dimensional cells meet. A detailed guide to the advancing-front Delaunay method is given by Frey et al. [24].

Unstructured grids do not require the burden of splitting a domain into four sided areas or six sided volumes as multi-block structured grids do. Typically, domains can have any number of edges or faces including internal voids. Unstructured grids in two dimensions usually contain either triangular (tri) cells or quadrilateral (quad) cells or both. CFD-GEOM has both a tri-only gridding routine and a quad dominant gridding routine. The latter creates quad elements wherever possible but will split a quad cell into two tri cells if the quad cell becomes excessively distorted. Figure 3.5b shows a tri-only unstructured grid for the aeroshell model and Figure 3.5c shows a quad dominant unstructured grid.

### 3.2.3 Structured versus Unstructured - The Great Debate

So which gridding technique leads to a faster, more efficient overall solution? Structured and unstructured grids both have their own distinct advantages. Unstructured gridding certainly has the advantage over structured gridding when it comes to the speed and flexibility of generating a grid. This is particularly evident when dealing with complex three dimensional domains. Structured grids often require more time to produce but there are numerous advantages in both speed and overhead required for a solution. For example, multi-block structured grids tend to produce more consistent results in viscous near-wall regions because of their orderly structure. Solving on a structured grid is also more efficient because the connectivity of each cell to its neighbours is easy for the solver to establish as the cells are indexed along curvilinear coordinates. Unstructured grids require the solver to create and continually reference a link list. The link lists contains cell connectivity information such as “CELL 33:FACE 4 maps to CELL 89:FACE 1” and so forth. As would be expected, this additional burden on the solver tends to use extra CPU time and memory compared to solutions performed on structured grids. So as a general rule of thumb, unstructured grids save the user time and effort at the gridding stage but use up more time and resources at the solution stage. CFD-FASTRAN allows grid types to be combined to form a hybrid grid. Such a grid system is shown in Figure 3.5d where a structured grid is wrapped around the aeroshell surface and the remaining space is taken up with an unstructured quad dominant grid. With this approach results in the near wall region should be more consistent than that of a fully unstructured grid but the overall time required for gridding has been reduced. As a structured grid must be structured in all areas to be valid, hybrid grids must be solved with the polyhedral solver and as such do not share the benefit of a true structured grid.

A relatively new technique known as adaptive gridding has become a popular scheme in recent years. Adaptive gridding begins with an unstructured grid. A solution is obtained on this grid then a refined grid is generated based on the results from the initial grid. Refinement is usually based on a scalar variable such as pressure or the gradient of such a variable. Advanced adaptive gridding routines can even un-refine (coarsen) parts of the grid where the variables are not changing significantly. Figure 3.4 shows an example of adaptive gridding applied to supersonic flow over a ramp deflection. This figure has been obtained from Leyland [49]. At the time of writing, CFD-FASTRAN does not offer fully automated adaptive gridding.

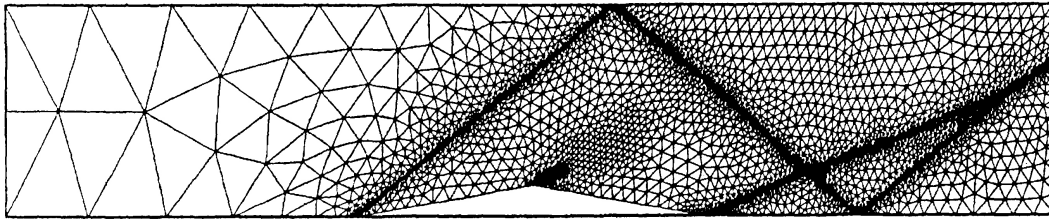


Figure 3.4: Adaptive gridding applied to a simulation of supersonic flow over a ramp deflection in a duct.

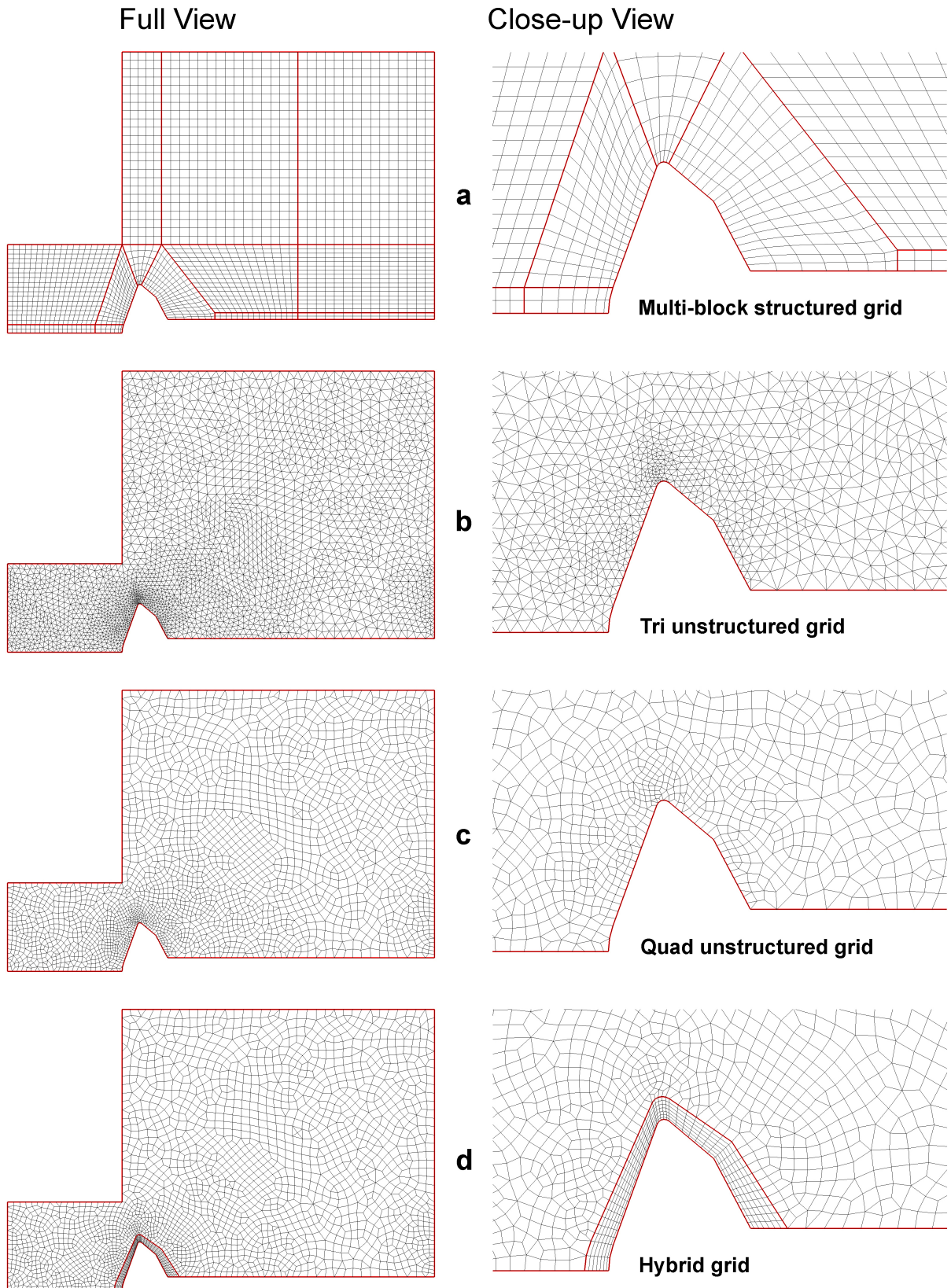


Figure 3.5: Structured and unstructured axisymmetric grids for the pathfinder shape inside the X3 expansion tube.

### 3.2.4 Grid Smoothing in Structured Grids

Structured grid smoothing algorithms attempt to minimise the distortion of cells within individual blocks of a multi-block grid. CFD-GEOM offers elliptic smoothing which works by solving a set of nonlinear partial differential equations on the grid which is being smoothed. The results are then used to distort the grid into a more optimal shape. The elliptic grid smoothing algorithm requires each corner of a block to be specified as either fixed or orthogonal. The fixed option maintains the defined grid spacing in a corner but will return a less than optimal solution. The orthogonal option will alter the grid spacing in a corner and return the best possible solution. By default a fixed condition is prescribed to all corners. As the solution to the set of equations is numerical, the user must define a maximum number of iterations for the solution. The default maximum is 25 but CFDRC recommend 250 iterations as a more suitable value. Figure 3.6 shows the result of applying both fully fixed and fully orthogonal grid smoothing on a single block. Figure 3.7 shows the improvement in cell quality gained by applying fully orthogonal smoothing to a multi-block grid created for planar flow over a double wedge.

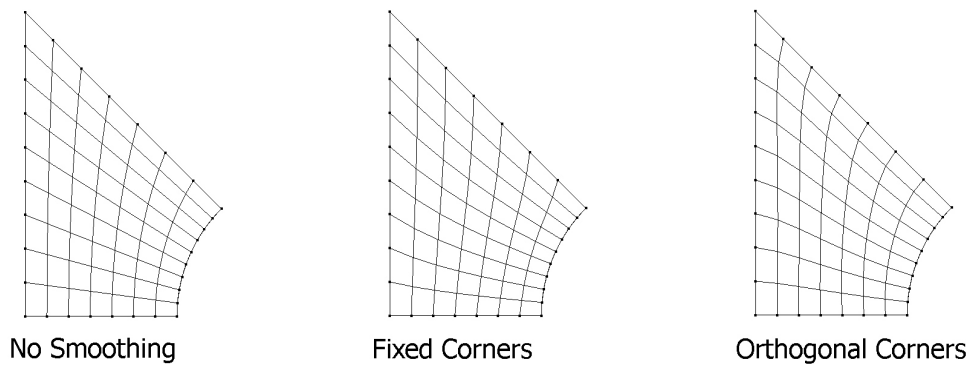


Figure 3.6: Examples of grid smoothing in structured grids.

### 3.2.5 Grid Biasing in Structured Grids

Grid biasing is a concept whereby the spacing of cells along an edge is nonlinear. In structured grids, biasing can be defined along any edge of a block in two or three dimensions. More often than not, pairs of opposite edges are chosen so that biasing occurs evenly in one or more parametric directions of a block. If an uneven amount of edges are biased, the resulting grid will be skewed. Figure 3.8 shows the difference between even and uneven biasing on a single two dimensional block. Biasing along an edge can be in a single direction (one-way biasing) or symmetric. In one-way biasing, cells are clustered more towards one end of an edge than the other. In symmetric biasing cells are either clustered towards each end of an edge or towards the center. Different options are available to define the nonlinear spacing, most of which give a power law type distribution.

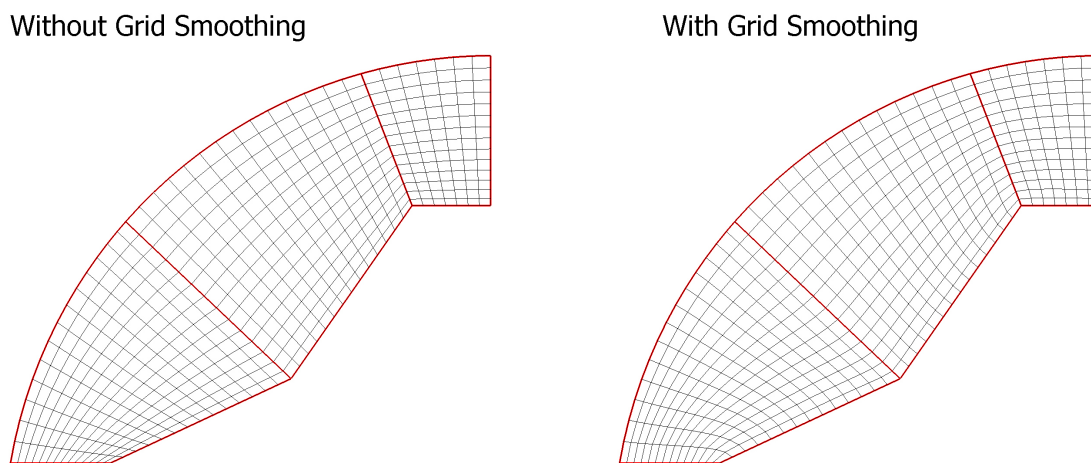


Figure 3.7: Orthogonal smoothing applied to a multi-block grid for flow over a double wedge.

Information on these options can be found in the *CFD-GEOM User Manual* [18]. Figure 3.9 shows an example of even one way biasing on a typical grid whilst Figure 3.10 illustrates even symmetrical biasing. A common problem with biasing is that cells can become too elongated. The elongation of a cell is measured by its aspect ratio which is defined as the the longest edge length divided by the shortest edge length. Aspect ratios of one are optimal but typically a grid will include ratios of around one to five. When the direction of flow is aligned to the longer edge of the cell, values of ten or more may be tolerated however cells with such high aspect ratios are susceptible to errors and may even prevent a model from converging.

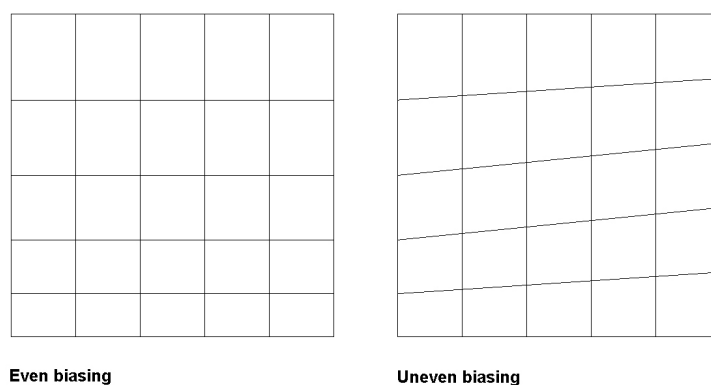


Figure 3.8: Even and uneven biasing.

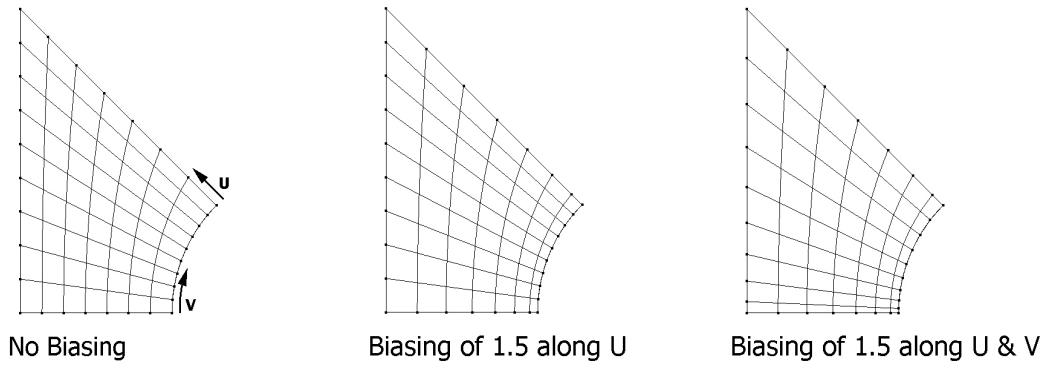


Figure 3.9: Examples of one-way grid biasing.

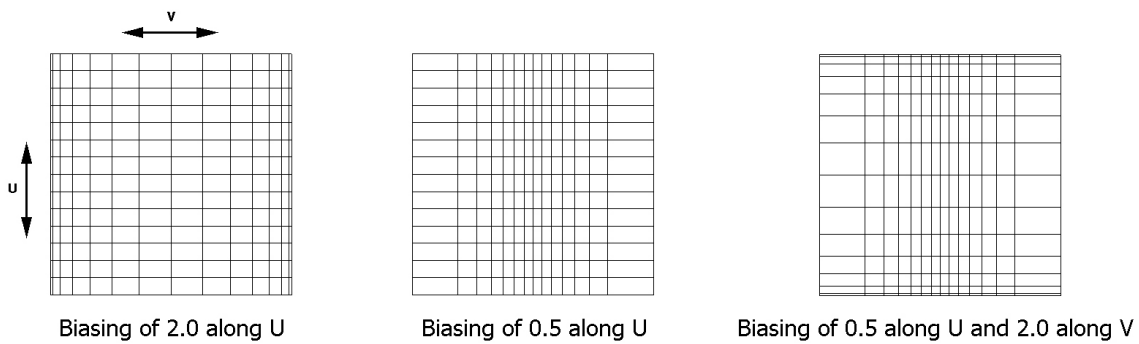


Figure 3.10: Examples of symmetric grid biasing.

### 3.2.6 Capturing Viscous Effects

All real gases have viscosity. Viscosity can be thought of as a measure of internal friction within a fluid<sup>1</sup>, or more precisely, a resistance to shearing deformation between adjacent elements of fluid. When analysing certain types of flow, viscous effects may be neglected without reducing the overall accuracy of the results. These flows are classed as inviscid. The assumption of an inviscid supersonic flow can work quite well in many applications, indeed Anderson [7] devotes four chapters of his book to inviscid methods for analysing supersonic flow. However, in many situations viscous effects do play an important role in determining the overall structure of the flow. Boundary layers are an important feature of viscous flow but accounting for viscous forces in a solution does not ensure that a boundary layer will be modelled. The ability to correctly predict the properties and behaviour of a boundary layer is dependent on the number of cells present in the boundary layer region. If the cell closest to the wall has a width larger than the boundary layer then the near wall velocity profile will ramp from zero to the freestream speed across a single cell. Such a velocity profile is a telltale sign that the grid must be refined in the boundary layer.

<sup>1</sup>Quoted from [23].

In this situation the solver is not reproducing a boundary layer, it is simply enforcing the no-slip boundary condition at the wall. No interaction with shockwaves or contact surfaces will be predicted and if separation occurs, it is likely to be in the wrong location. CFD-FASTRAN outputs a scalar “Y+” in laminar and turbulent models. The value of Y+ provides a useful indication of the resolution of the near wall grid relative to the scale of viscous effects. Y+ is defined as follows:

$$Y+ = Y \sqrt{\frac{\tau_w \rho}{\mu^2}}$$

The Y+ scalar is produced for each cell adjacent to the wall. The value of Y is taken as the distance from the cell center to the wall in a line normal to that wall.  $\tau_w$  is the wall shear stress (skin friction). It has been suggested by Liever et al. [50] that a Y+ of less than one is desirable for computing the heat transfer over blunt bodies in hypersonic flow. In the same environment a Y+ value of between one and five should prove adequate for resolving separated flow and viscous layer effects.

### 3.2.7 Shockwave - Boundary Layer Interaction

To illustrate this discussion on viscous effects, consider a sealed section of tube. The tube is 75 mm in length, 200 mm in diameter and is filled with gas. The tube is separated into two regions of different pressure by a membrane placed at  $x = 0$  mm. The region on the left is 10 kPa and extends 50 mm left of the origin whilst the region on the right is 1 kPa and extends 25 mm right of the origin. The initial temperature of both sections is 300 K. Assume that the membrane barrier can be instantaneously removed at time zero. This general class of problem is known as the Riemann initial value problem and is well studied (note the dimensions and ratio of pressure chosen for this exercise are arbitrary). When the membrane is removed a shockwave followed by a slower moving contact surface moves to the right travelling through the lower pressure gas. Simultaneously an expansion wave moves to the left into the high pressure region. The shockwave and contact surface reflect once they reach the end of the tube. This process can be summarised on an x-t diagram which plots distance on the horizontal axis and time on the vertical axis. Figure 3.11 shows the x-t diagram for the sealed tube problem.

The inviscid solution to this problem is one dimensional and relatively simple to compute but when viscosity is considered the problem becomes greatly complicated. The presence of viscosity causes a boundary layer to form behind the moving shockwave as it initially progresses through the undisturbed gas. When the shock wave reflects off the end of the tube it progresses through the gas in the opposite direction to the flow. A disturbance begins because the slower flow of the boundary layer is deflected away from the wall as it lacks the required momentum to cross through the shockwave head on.

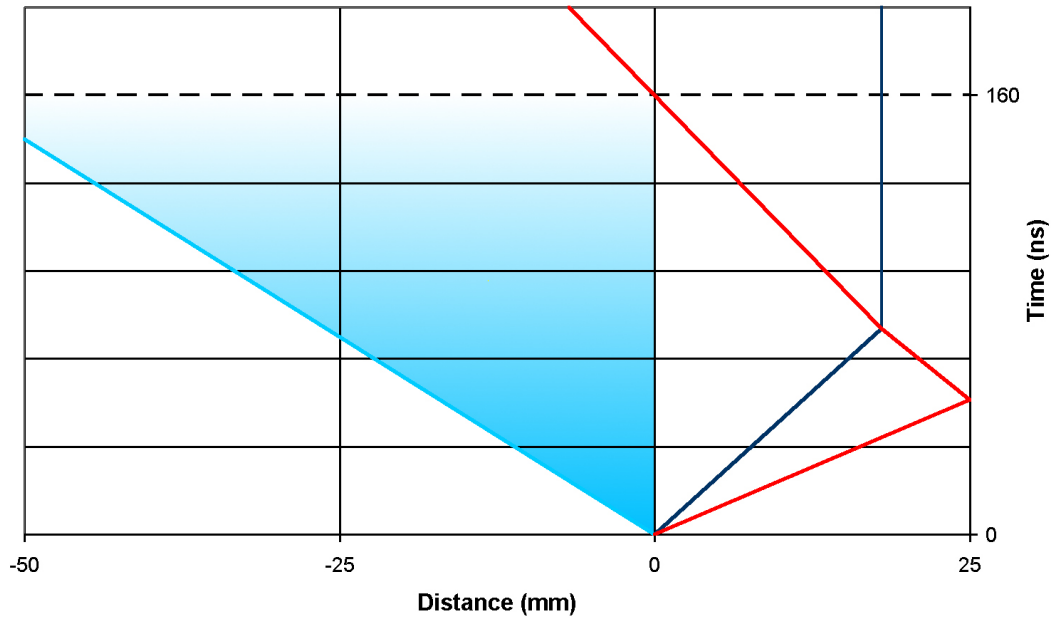


Figure 3.11: X-T diagram for the sealed tube.

The vented flow subsequently accelerates as it travels into the freestream and ultimately crosses through the shock obliquely. The freestream flow crossing normal to the shock has different properties to the boundary layer gas which has crossed through the shock obliquely. This generates a contact surface at the interface between the two streams of gas. This contact surface is unstable due to the different speeds of flow moving on either side. As this interaction continues, the instabilities on the contact surface form vortices behind the shockwave. This interaction produces a region of disturbed flow which grows larger and more complex with time. Figure 3.12 illustrates how a flow becomes perturbed as a shockwave is transmitted through a boundary layer. An axisymmetric model of the above problem was created and solved with CFD-FASTRAN. For this test, three grids

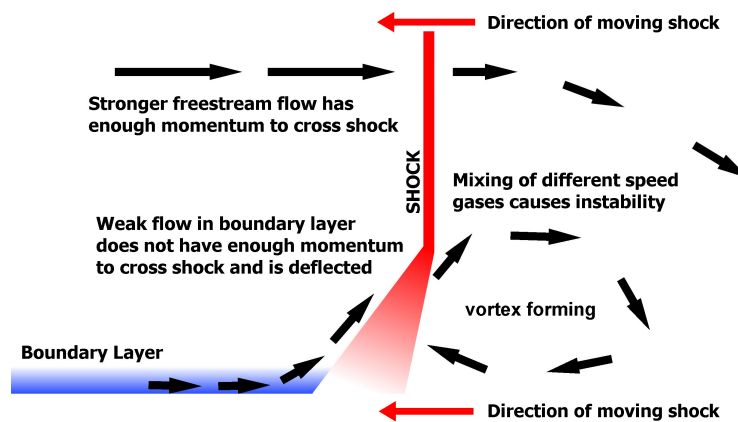


Figure 3.12: Schematic showing a typical form of shock boundary layer interaction.

were used. The first grid consisted of 150 cells in the radial direction and 113 along the length of sealed pipe. No grid biasing was used. The second model used the same grid but with a biasing of 1.4 towards the pipe surface. The third model used a grid which was halved in cell size for both directions resulting in a grid of 300 by 226 cells. A biasing of 1.4 was also used on this model. The near wall velocity profile is shown for all three models in Figure 3.13. This profile was taken at  $x = 0.01$  m at a time when the shockwave had passed but prior to the arrival of the contact surface. Note that the profile shows only the first 3 mm from the pipe wall so that the boundary layer is clearly discernable. The first grid shows no evidence of a boundary layer as the velocity is ramped down in only one cell. The second grid shows partial reconstruction but is lacking in resolution. The third grid shows the expected “text book” profile of the boundary layer. Figure 3.14 shows isopycnics (density contours) at a time when the shock wave has reflected from the end of the tube and travelled back to its original position. This time is marked in Figure 3.11 with a bold dotted line. From the contours it is apparent that the first grid predicts no shock boundary layer interaction. The second grid shows some interaction but it is poorly resolved. The third grid more clearly shows the formation of a vortex trailing behind the shockwave. This example demonstrates the importance of accurately resolving the boundary layers in viscous flows. In this example the effects of shock boundary layer interaction were minor but in other situations the effects can dramatically alter peak temperatures and pressure. Velocity profile checks and monitoring  $Y^+$  values should be undertaken whenever viscous interaction is suspected to effect the flow.

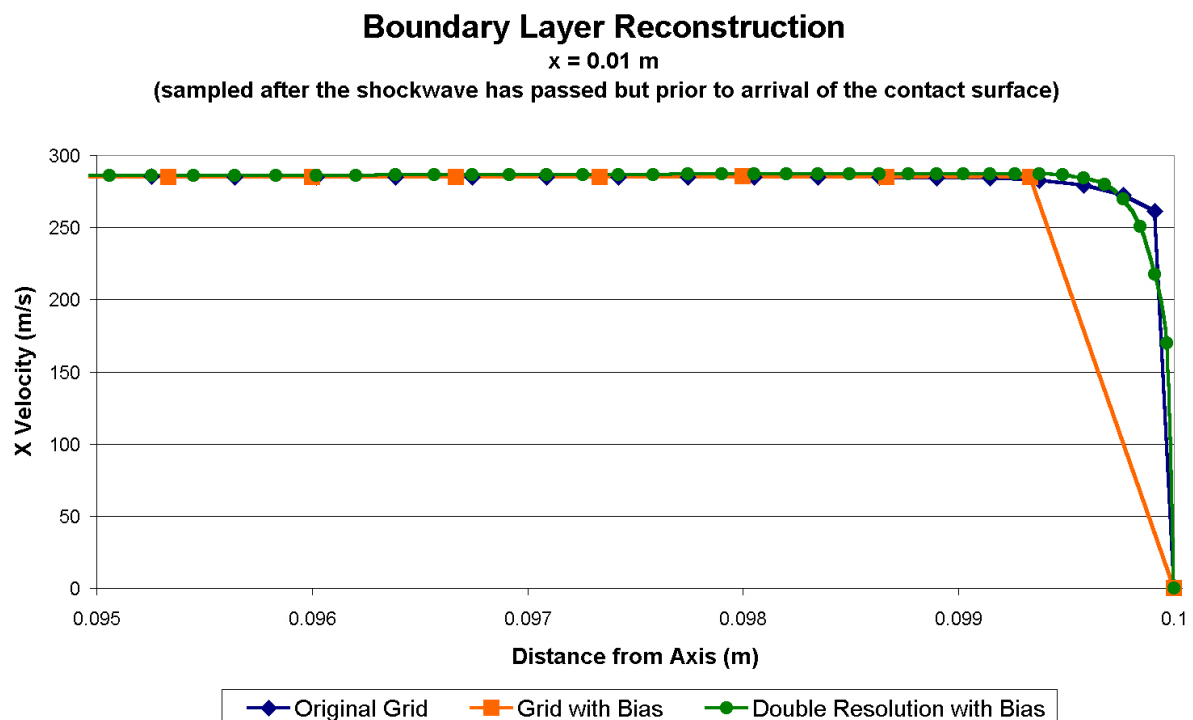


Figure 3.13: Near wall velocity profiles for the initial value problem.

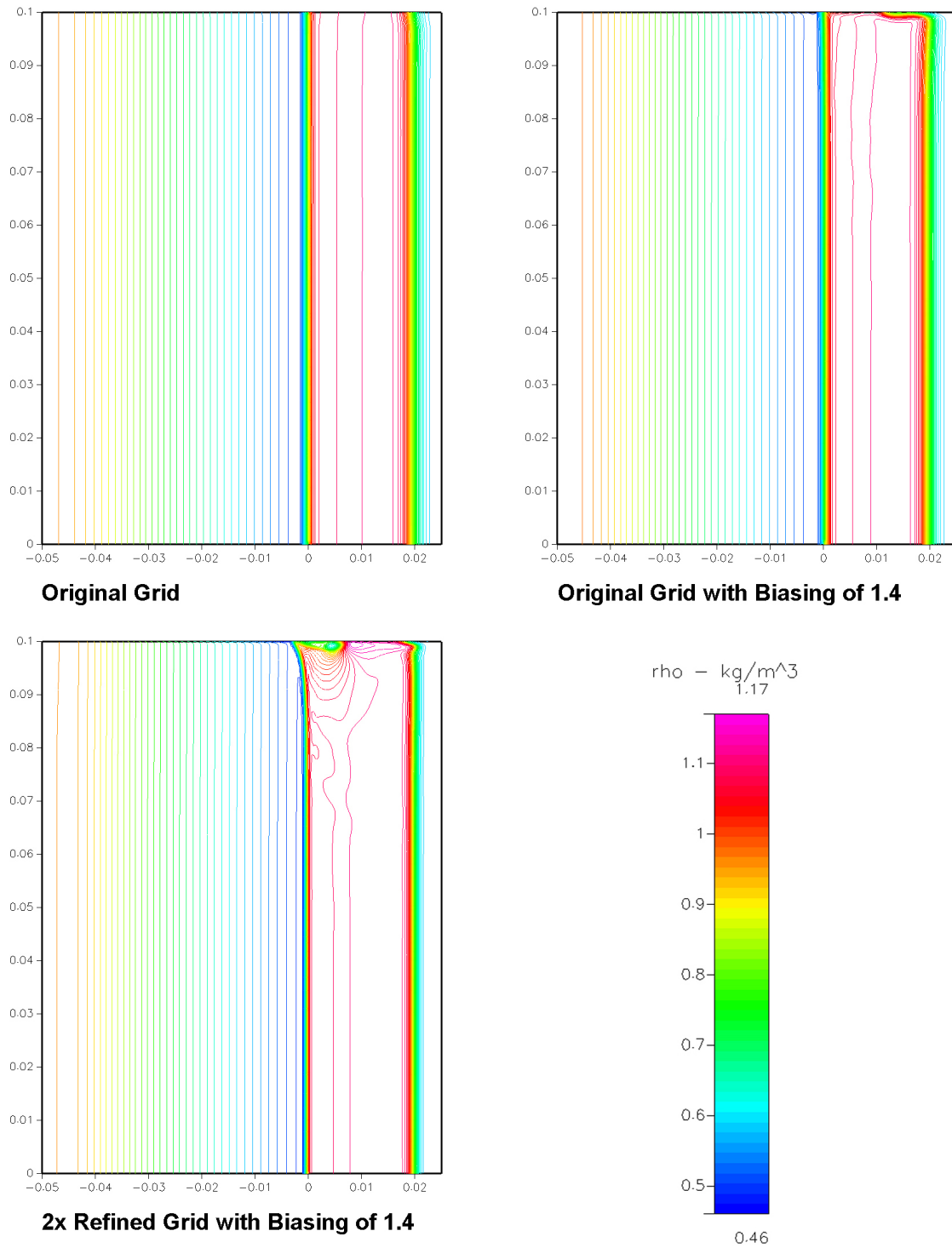


Figure 3.14: Shock boundary layer interaction in the initial value problem.

### 3.3 Model Setup and Solution

Once a grid has been constructed the model is ready to be configured for analysis. This section provides an introductory discussion of the setup process which involves specifying the physics to be included in the simulation as well as defining boundary conditions and the initial state of the gas. The selection of various solver options is also discussed in this section.

#### 3.3.1 Modelling Choices and Assumptions

Before any numerical simulation is attempted, CFD or otherwise, it is imperative to identify what physical effects dominate the process to be modelled. All numerical simulations contain some assumptions about the physics being modelled but only those models which limit the assumptions to second order effects will agree well with experiment. For example, Section 4.1 of this thesis discusses the simulation of a planar shock wave which is focused by a parabolic shaped channel. The flow was assumed not to vary normal to the cross section of the parabola and the effects of viscosity were neglected. The air through which the shockwave travelled was modelled as a single species calorically perfect gas. As Figure 4.3 shows, the simulation is in very good agreement with the experimental results despite the various limiting assumptions made. Cross flow, boundary layers and real gas effects would have been present in the experiment but their effects can be neglected because they were minor compared to effects such as the convective transfer of mass, momentum and energy, the compressibility of the gas and the shape of the reflector. In Sections 4.3 and 4.4 the effects of viscosity are noticeable but assumption of an ideal gas is still acceptable. In Section 4.6 the effects of thermal and chemical nonequilibrium are important to the flow because of the high enthalpy of the oncoming flow. In this study the assumption of an ideal gas leads to a significant margin of error as is shown in Figure 4.50. When planning the setup of a model, the following points should be noted:

1. Know where to apply the appropriate assumptions
2. Know the limitations of the assumptions being used
3. Understand the implication of the assumptions on coupled processes
4. Start with a simple model and add complexity in stages

#### 3.3.2 Model Setup

Using the CFD-FASTRAN system, setup of a model is performed in the program `CFD-FASTRAN-GUI`. In this program, the model is transformed from a blank grid into a mathematical description of flow. Typically, `CFD-FASTRAN-GUI` is used to specify the:

- format of the grid geometry - planar vs axisymmetric (two dimensional models only)
- stability of the flow - steady vs transient
- physics to be included in the simulation - viscosity, chemistry etc.
- properties of the gas / gases to be modelled
- treatment of the solution at each boundary to the model (boundary conditions)
- initial state of the model (initial conditions)
- numerical integration schemes to be used by the solver
- results output format and frequency

When the model setup is completed an analysis can be requested from the `CFD-FASTRAN-GUI` interface. Once requested, the program will search for a valid license and if successful, launch the executable `CFD-FASTRAN-SOLVER`. The solver executable has no interface and requires only a DTF file and a corresponding DAT file to run, though there are plans to eliminate the need for the DAT file in future versions. The solver process can alternatively be executed directly from a command shell, allowing for multiple simulations to be launched sequentially via a batch file. Once a simulation is running, `CFD-FASTRAN-GUI` can be used to monitor the convergence of the solution as it progresses.

### 3.3.3 Boundary Conditions

In a numerical analysis such as CFD, the treatment of the solution at the boundaries must be specified in order to achieve a result. Boundary conditions can have a large influence on the solution so the choice of boundary conditions and their positioning should be considered carefully. `CFD-FASTRAN` offers a range of standard boundary conditions, some of which offer multiple subtypes. In `CFD-FASTRAN-GUI` the available options specific to each boundary condition will depend on what modules have been activated. For example, if a  $k\epsilon$  model of turbulence has been enabled then the option to specify the kinetic energy and turbulent dissipation at each inlet will become available. If the turbulence module is disabled, these options are hidden.

#### Wall Boundaries

`CFD-FASTRAN` supports four types of wall boundaries. For each boundary the pressure at the wall is set to the pressure of the cell center adjacent to the wall. The normal velocity is set to zero at the wall to maintain impermeability but the tangential velocity is dependent on the model of flow chosen. The inviscid flow model uses extrapolation to determine the tangential velocity of the gas at the wall whilst the laminar model

maintains the no-slip boundary condition by enforcing a tangential velocity equal to that of the wall. The treatment of the energy equation at the wall is dependent on the type of wall boundary chosen. Table 3.1 shows the thermal boundary conditions for each wall boundary condition subtype. For chemically reacting flows the user must also specify the conditions at the wall as fully-catalytic, non-catalytic or define a set of surface reactions. A wall roughness height can be assigned for turbulent flows.

Table 3.1: Thermal boundary conditions for different subtypes of wall.

BC subtype	temperature
adiabatic	$T_w = T_c$
isothermal	$T_w = T_{user}$
heat flux	$T_w = T_c - \frac{\delta \cdot q_{user}}{\kappa}$
radiative	$\frac{\kappa(T_c - T_w)}{\delta} = \varepsilon_{user} \sigma T_w^4$

A fifth type of wall boundary known as ‘‘Aeroelastic (MDICE)’’ is also available. This boundary condition is for coupling to a finite element solver for modelling fluid-solid interaction and conjugate heat transfer. This boundary condition is highly specialised and requires extensive programming with the MDICE interface to setup.

### Inlet Boundaries

CFD-FASTRAN provides two types of inlet. The first is a fixed mass flow rate inlet. The user must provide the static pressure, static temperature and velocity at the inlet. For supersonic inflows all quantities are held constant. For subsonic inflow only the density and velocity are held constant to ensure a fixed mass flux. The remaining variables are extrapolated from the values at the cell centers adjacent to the inlet. The second type is a fixed total pressure inlet. The user must again provide the static pressure, static temperature and velocity at the inlet. From this information CFD-FASTRAN calculates the total pressure and total temperature which is enforced as constant through the solution. The velocity magnitude, static pressure and static temperature can vary across the inlet and throughout the solution provided the total pressure and total temperature remain constant. The velocity direction is also kept constant. The static conditions and the flow speed are calculated from the adjacent cell centers using an isentropic relationship. For both inlet types, the species mass fractions at the inlet must be specified in mixing or reacting models. These mass fractions are held constant throughout the solution.

### Outlet Boundaries

Two outlet conditions are provided by CFD-FASTRAN. A fixed pressure condition is available which requires the static pressure to be defined at the outlet. This pressure is

then used to evaluate the Mach number of the exiting flow. If the flow is supersonic then all variables, including the pressure, are extrapolated from the cell centers adjacent to the outlet. If the flow is subsonic then the user specified pressure is kept whilst all other variables are extrapolated from the adjacent cell centers. The second type of outlet is extrapolated. The extrapolated outlet assumes all flow exiting the domain is supersonic and extrapolates all the variables from the adjacent cell centers irrespective of the local Mach number.

### **Inflow / Outflow Boundaries**

The inflow / outflow boundary condition is the most general boundary condition and also the most complex. `CFD-FASTRAN-SOLVER` identifies the mass flux at each cell edge of the boundary as supersonic inflow, supersonic outflow, subsonic inflow or subsonic outflow. For incoming flow, the boundary acts as a total pressure inlet when the inflow is subsonic whilst supersonic inflow uses the pressure, temperature and velocity set by the user. For outgoing flow, the boundary acts like a fixed pressure outlet, checking the Mach number to determine if the pressure should be extrapolated or held at the value set by the user.

### **Symmetry Boundaries**

The symmetry boundary condition maintains a zero gradient of quantities normal to the boundary. The symmetry condition is commonly applied along the centerline of a symmetric planar model or axisymmetric model. For examples on the application of symmetry see Figure 1.5.

### **Interface Boundaries**

Interfaces are the internal boundaries between individual blocks or domains. These boundary conditions are set automatically by `CFD-FASTRAN` and should not normally require any adjustment. It is possible to change one or more internal boundaries from interfaces to walls. This will have the effect of creating an infinitely thin barrier.

### **Other Boundaries**

Two other boundary conditions are available, the “Time Profile” boundary condition which allows for transients in the inflow, and the “Overset” boundary condition which is used in conjunction with chimera grids. Information on these boundary conditions are available in the `CFD-FASTRAN` User Manual [16].

### **Boundary Conditions for Shock Diffraction Studies**

Shock diffraction problems such as those discussed in Section 4.1 - 4.4 of this thesis require a single shockwave moving at a finite speed. To produce a single shock moving at

a constant speed the inlet boundary condition must be assigned the post-shock conditions necessary to push the shock wave through the initially stagnant gas. To calculate these conditions consider a stationary normal shock with a pre-shock speed, temperature and pressure of  $U_1, T_1$  and  $P_1$  respectively and post-shock conditions of  $U_2, T_2$  and  $P_2$ . The ratio of flow quantities across a normal shock are shown in the equations below. The derivation of these equations is provided in Fox and McDonald [23] or any other introductory fluid dynamics text.

$$\begin{aligned}\frac{U_2}{U_1} &= \frac{M_2}{M_1} \sqrt{\frac{1 + (\frac{\gamma-1}{2})M_1^2}{1 + (\frac{\gamma-1}{2})M_2^2}} \\ \frac{T_2}{T_1} &= \frac{1 + (\frac{\gamma-1}{2})M_1^2}{1 + (\frac{\gamma-1}{2})M_2^2} \\ \frac{P_2}{P_1} &= \frac{1 + \gamma M_1^2}{1 + \gamma M_2^2}\end{aligned}$$

Where

$$M_2^2 = \frac{M_1^2 + \frac{2}{\gamma-1}}{(\frac{2\gamma}{\gamma-1})M_1^2 - 1}$$

If the normal shock is travelling through gas at constant speed it can be considered as a stationary shock with a constant speed flow passing through. When the moving shock is considered in this “shock stationary” frame of reference, the ratio of quantities across the moving shock can be obtained by simply subtracting the speed of the shock from the pre-shock and post-shock speeds. The speed of the moving shock is usually expressed as a Mach number ( $M_{Shock}$ ) so the pre-shock and post-shock speeds become  $U_1 - (M_{Shock}a_1)$  and  $U_2 - (M_{Shock}a_1)$  respectively. In terms of a CFD solution,  $U_1, T_1$  and  $P_1$  should be set as the initial conditions and  $U_2, T_2$  and  $P_2$  become the boundary conditions for the inlet to the flow. The solutions for  $U_{Inlet}, T_{Inlet}$  and  $P_{Inlet}$  can be found algebraically in terms of  $M_{Shock}, R, \gamma, P_{Initial}$  and  $T_{Initial}$ . These solutions are shown below.

$$\begin{aligned}U_{Inlet} &= \frac{2\sqrt{\gamma RT_{Initial}}(M_{Shock}^2 - 1)}{(\gamma + 1)M_{Shock}} \\ P_{Inlet} &= \frac{2\gamma M_{Shock}^2 - (\gamma + 1)}{(\gamma + 1)P_{Initial}} \\ T_{Inlet} &= \frac{T_{Initial}(2 + (\gamma - 1)M_{Shock}^2)(2\gamma M_{Shock}^2 - (\gamma - 1))}{(\gamma + 1)^2 M_{Shock}^2}\end{aligned}$$

### 3.3.4 Initial Conditions

All CFD solvers require a valid initial state to begin from. The meaning of this initial condition depends on whether the analysis is steady or transient. In a steady analysis, the initial condition is just a starting guess which is used to begin the iteration cycle. The initial conditions will have no bearing on the final result for an infinitely converged solution but may have an effect on the rate of convergence or even whether or not convergence is ever achieved. In a transient simulation the initial conditions are the solution at time zero and as such should be physically realistic. An initial value for each variable to be iterated must be provided. Pressure, velocity and temperature will always be required. Additionally, variables such as turbulent kinetic energy and dissipation rate, internal temperature<sup>2</sup> and species mass fractions may be required depending on the physics to be included in the solution. CFD-FASTRAN requires that the pressure and temperature are given in absolute terms (Pa(a) and K). Different initial conditions can be setup for different zones. The results from a previous analysis can also be used as the initial condition, provided the grid remains unchanged.

---

<sup>2</sup>See Section 2.2.

## 3.4 Overview of the Solution Process

This section aims to provide a brief summary of the solution process. A more detailed description of the numerical techniques used by the CFD-FASTRAN solver is provided in the CFD-FASTRAN Theory Manual [15]. The numerical techniques used in the solver are based on the methods discussed in Hirsch's two volume textbook *Numerical Computation of Internal and External Flow* [29], [30]. Those not familiar with numerical solution techniques for fluids might also consider *Computational Fluid Dynamics: The Basics with Applications* [8] and *Numerical Heat Transfer and Fluid Flow* [63] which provide a more elementary discussion of the concepts behind CFD solution techniques. A more compact overview of the essentials of flux calculators, flux limiting and spatial reconstruction is given in Johnston's PhD dissertation [44].

### 3.4.1 Solver Approach

The solver inside CFD-FASTRAN uses a cell-centered finite volume approach for solving either the Navier-Stokes equations or the reduced Euler equations for inviscid flow models. With each iteration, the algorithm marches in time to progress the solution from an initial condition which is defined by the user. Transient flows are progressed in time evenly across each cell in the model. Steady flows are progressed differently in each cell depending on the size of the cell and the flow conditions. At every iteration the solver performs sub iterations to solve the linearised equations describing the flux of mass, momentum and energy at each interface between two cells. From this solution, updated conditions at the cell centers are estimated and the procedure is repeated. Two levels of iteration are therefore used in the solution procedure. The global iteration is an advancement in time whereas the sub iterations solve the equations at each time step. Evaluation of the flow field spatially is performed through the use of a flux calculator. The solver offers a choice of two flux calculators:

1. Roe's Flux Difference Splitting (FDS)
2. Van Leer's Flux Vector Splitting (FVS).

These schemes are discussed in the following section. The solver also offers a choice of four schemes for integration in time:

1. multi-stage Runge Kutta
2. point implicit (Block Diagonal Iterative)
3. fully implicit (Jacobi Point Iterative)
4. LU-SGS

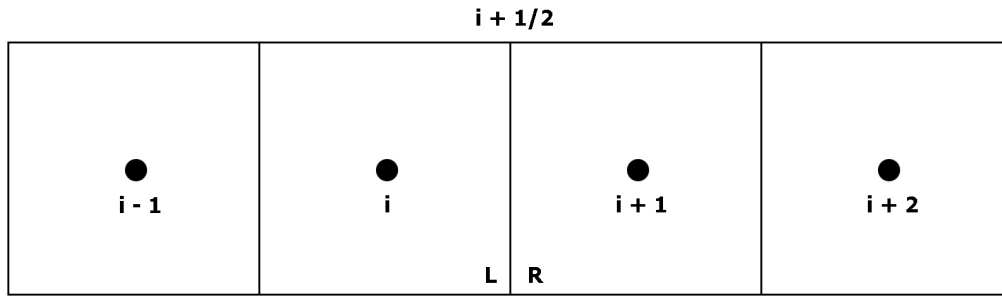


Figure 3.15: Left and right states for the evaluation of flux.

The multi-stage Runge Kutta method is an explicit scheme. Explicit integration schemes are generally much faster than implicit schemes per time step but require smaller time steps to be taken, resulting in more overall steps for a given solution. Explicit schemes tend to be less dissipative for time accurate solutions, as noted in the CFD-FASTRAN Theory Manual [15]. The solver also supports three implicit schemes as listed above. Unlike explicit schemes, implicit schemes are not conditionally stable. The point implicit method considers only the nearest neighbours to each cell during the solution whereas the fully implicit method considers all cells. The LU-SGS scheme is an approximate-factorisation matrix-free solution method and is only available for use with the polyhedral grid solver. Details of the above integration schemes are available in the CFD-FASTRAN Theory Manual [15] and in Hirsch [30]. Lastly, as discussed in Section 3.2.1, the solver can work with both structured and unstructured polyhedral grids. It should be noted that at the time of writing, the mixing and chemistry functionality is not supported on polyhedral grids. Axisymmetric models and the Van Leer flux calculator are also not supported when using polyhedral grids.

### 3.4.2 Flux Calculators

At the core of the solution process is the flux calculator. This routine estimates the flux of mass, momentum and energy from one cell into another through their shared interface. A flux calculator interpolates between cell centers to estimate the vector of flow variables, denoted as  $q$ , at the interface between cells. This interpolation can be linear in the case of a first-order scheme or a polynomial in the case of a higher order scheme. Interpolation is performed on either side of an interface resulting in a left (L) and right (R) value. Figure 3.15 shows a 1D example grid. For a first order upwind scheme the new vector of flow variables at each interface is taken to be the value of the old vector at the cell center upwind of that interface:

$$\begin{aligned} q_{i+\frac{1}{2}}^L &= q_i \\ q_{i+\frac{1}{2}}^R &= q_{i+1} \end{aligned}$$

For a higher order scheme, the new vector of flow variables at each interface is predicted by extrapolating that value from the cell center to the interface. A flux limiter  $\Psi$  is used in this case to prevent instability:

$$\begin{aligned} q_{i+\frac{1}{2}}^L &= q_i + \Psi^L(q_i - q_{i-1}) \\ q_{i+\frac{1}{2}}^R &= q_{i+1} - \Psi^R(q_{i+2} - q_{i+1}) \end{aligned}$$

A choice of two flux calculators is available in CFD-FASTRAN. The user must specify to apply either the Roe's Flux Difference Splitting (FDS) scheme or the Van Leer Flux Vector Splitting (FVS) scheme. Roe's FDS scheme was developed by Philip Roe around 1980 [70], [69]. Roe's scheme is classed as an approximate Riemann solver which is a linearised form of the Godunov scheme. Godunov [27] proposed that a flow domain could be divided into a number of cells with each cell containing a constant flow condition. At each interface between two cells the equations of flow could be posed as an initial value problem such as that discussed in Section 3.2.7 but without boundaries. The one dimensional wave dynamics which result from an initial state problem are well understood so Godunov proposed that the solution, after some time  $\Delta t$ , could be imposed at each interface and the whole process repeated. The problem with this scheme is that the solution to the initial value problem is non-linear and so the resulting formulation of equations is time consuming to solve. In 1981 Roe proposed an approximate linearised scheme thereby greatly reducing the computational overhead required to achieve a solution. Roe's scheme is quite good at capturing detail in a flow but unfortunately is not particularly stable and can be shown to exhibit failures under certain conditions. A discussion of such failures is given in Section 3.4.5. The failures of Roe's scheme can be mostly avoided with the use of an entropy correction such as that provided in CFD-FASTRAN but this results in increased dissipation. The alternative flux calculator provided by CFD-FASTRAN is Van Leer's FVS scheme. At the time of writing, Van Leer's scheme is only available for use on structured grids and can only be used for modelling a single species, calorically perfect gas. Van Leer's FVS scheme was developed by Bram Van Leer in 1982 [76]. Van Leer's scheme is quite different from Roe's scheme and does not suffer from the same failures. More formally, Van Leer's scheme is classed as "monotonic" whereas Roe's scheme is considered non-monotonic. Hirsch defines a monotonic scheme in Page 413 of his text [30]:

*a monotonic scheme has the property of not allowing the creation of new extrema and does not allow unphysical discontinuities.*

The "price" paid for this constraint on the solution is much higher levels of dissipation in comparison to Roe's FDS scheme. A scheme which combines the best of both flux calculators is a newer "low cost" scheme developed by Liou et al. [52], [53] in 1991 and is known as the Advection Upwind Splitting Method (AUSM). AUSM tends to have

the stability of FVS scheme with the low dissipation of a FDS scheme. Since its conception many improvements have been suggested. MB-CNS [38], [39] currently implements a AUSMDV scheme [79] together with the Equilibrium Flux Method (EFM) [66], [54]. At this stage there are no reported plans to incorporate AUSM into CFD-FASTRAN.

### 3.4.3 Flux Limiters

Supersonic flows pose a challenge for interpolation schemes because of the strong discontinuities that develop within the flow. Linear interpolation is usually avoided because it tends to smear out these discontinuities whereas higher order interpolation schemes suffer from a different problem. A shockwave or contact surface creates an instantaneous jump in flow conditions. When attempting to fit higher order polynomials near such a feature, over and undershoots occur. In a two or three dimensional simulation this effect is seen as ripples emanating out from a shockwave or contact surface. A simulation suffering excessively from this effect is shown in Figure 3.16. In this figure the bow shockwave has generated spurious waves as it expanded out from the cylinder.

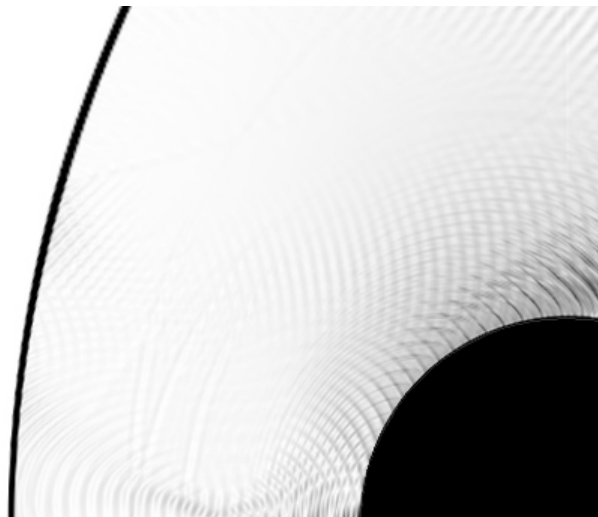


Figure 3.16: Numerical Schlieren image showing spurious waves.

Flux limiters are one solution to the problem of discontinuities in higher order schemes. First suggested by Boris and Book in 1973 [11], flux limiters reduce the effect of higher order interpolation around the location of a discontinuity but have a minimal effect in other areas of the flow. Flux limiters have an effect which is proportional to the ratio of gradients ( $r$ ) between adjacent cells. For the grid of evenly spaced cells shown in Figure 3.15:

$$r_{1+\frac{1}{2}} = \frac{q_{i+2} - q_{i+1}}{q_{i+1} - q_i}$$

In the presence of a strong discontinuity this ratio will be high and the flux limiter will curtail the use of higher order interpolation. In a region of nearly constant flow conditions, the ratio of quantities is very close to one and the flux limiter will have no effect. For many years, researchers have sort after the perfect formulation for a limiter and there has been much debate on the topic. CFD-FASTRAN offers a choice of four flux limiters for use with structured grids and a choice of two for use with polyhedral grids. Table 3.2 shows the formulation for the four structured limiters available in CFD-FASTRAN as well as two other popular flux limiters. Figure 3.18 shows these limiters plotted against the ratio of gradients. Negative values of  $r$  correspond to opposing gradients. Note the Van Leer limiter is undefined for  $r = -1$ .

Figure 3.17 is taken from Page 549 of Volume 2 of Hirsch's text [30]. This figure shows the effect of using a first and second order upwind scheme to capture the convection of a moving square wave. The effect of several limiters is also shown. The first order scheme is stable but there is excessive dispersion of the wave. The unlimited second order scheme suffers from spurious oscillations but the limited second order upwind schemes are stable and capture the gradient of the square wave with reasonable clarity. In the validation exercises presented in Chapter 4, the use of flux limiters was essential in achieving an acceptable result but the choice of limiters did not appear to have a great effect on the overall solution. The Min-Mod limiter appeared to be slightly more dissipative than the Osher-C limiter but the Osher-C limiter tended to be less stable.

Table 3.2: Formulations for some common flux limiters.

flux limiter	formulation
Minimum Modulus (Min-Mod)	$\max[0, \min(1, r)]$
Van Leer	$\frac{r+ r }{1+r}$
Osher-Chakravarthy with $\kappa = \frac{1}{3}$	$\frac{1}{3} \max(0, \min(\frac{5}{2}, r)) + \frac{2}{3} \max(0, \min(1, \frac{5r}{2}))$
MUSCL	$\max(0, \min(2r, \frac{r+1}{2}, 2))$
Van Albada	$\frac{r^2+r}{r^2+1}$
Roe's Superbee	$\max[0, \min(2r, 1), \min(r, 2)]$

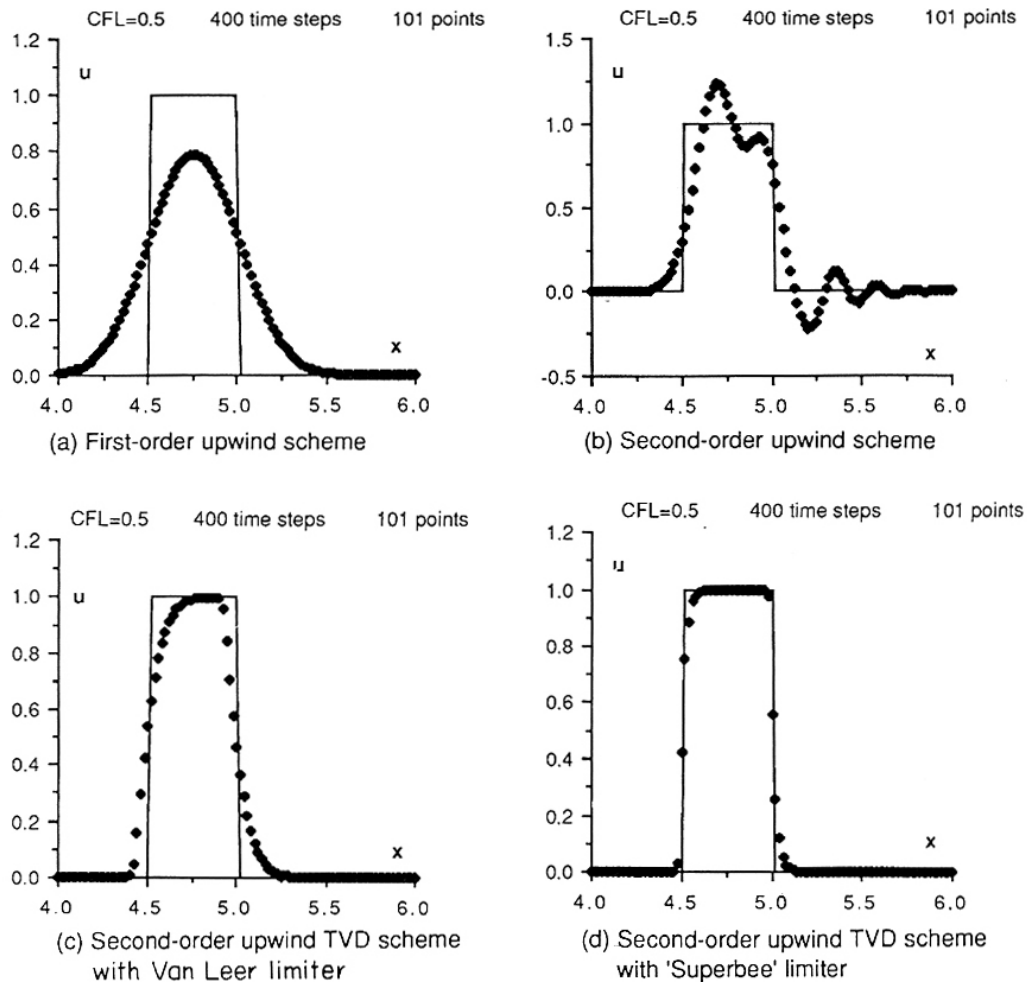


Figure 3.17: Effects of limiters on the linear convection of a square wave [30].

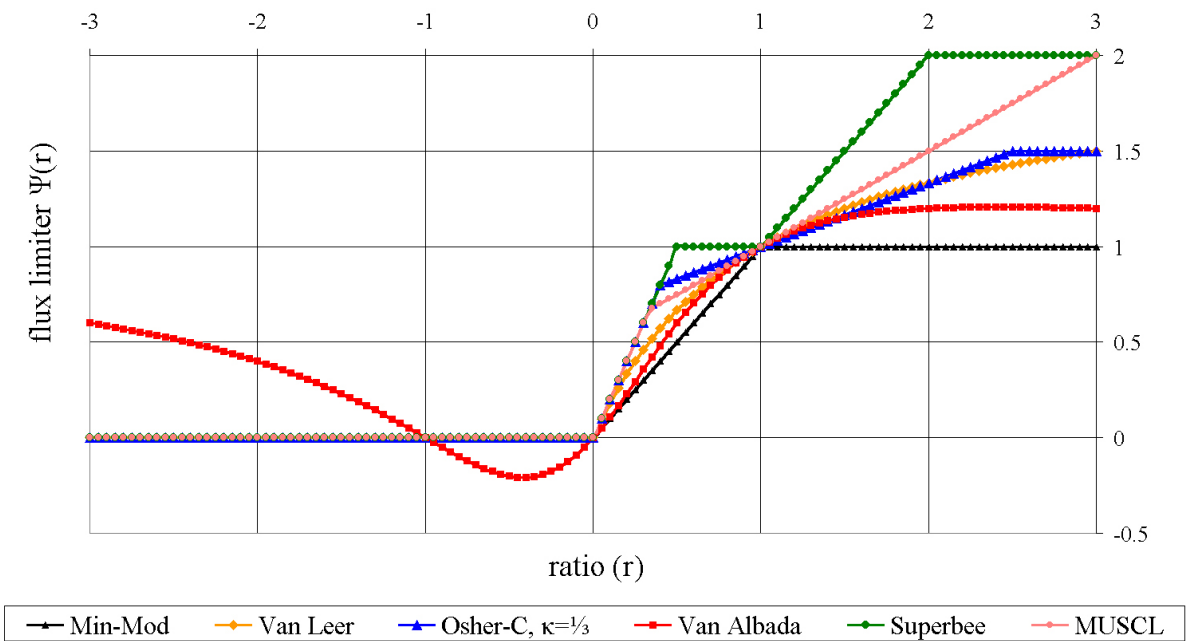


Figure 3.18: Comparison of some common flux limiters.

### 3.4.4 Integration in Time

Timesteps in CFD-FASTRAN are not constant by default, instead the user is required to define a CFL number which is then used by the solver to generate a timestep at each iteration. The CFL number, named after Courant, Friedrichs and Lewy [20], is a measure of how fast information propagates throughout a solution. The definition of the CFL number for a cell is as follows:

$$\text{cell local CFL number} = \min \left[ \left( \frac{\Delta_i}{|u_i| + c} \right), \left( \frac{\Delta_j}{|u_j| + c} \right), \left( \frac{\Delta_k}{|u_k| + c} \right) \right]$$

Where:

$\Delta_i, \Delta_j, \Delta_k$  = cell length in the i, j and k directions

$u_i, u_j, u_k$  = i, j and k components of the flow velocity in the cell

$c$  = cell local speed of sound

The difference between a steady and transient solution in CFD-FASTRAN is the issue of time accuracy. Transient solutions in CFD-FASTRAN are time accurate. A time accurate solution is one where every cell marches in time by the same amount,  $\Delta t_{min}$ , at each iteration.  $\Delta t_{min}$  is the minimum timestep required to ensure the CFL in any given cell is not higher than the number specified by the user.

$$\Delta t_{min} = \min_{All\ cells} \left[ \min_{Each\ cell} \left[ \left( \frac{CFL \cdot \Delta_i}{|u_i| + c} \right), \left( \frac{CFL \cdot \Delta_j}{|u_j| + c} \right), \left( \frac{CFL \cdot \Delta_k}{|u_k| + c} \right) \right] \right]$$

Where ‘‘CFL’’ is the desired CFL number as specified by the user

When running a steady flow model only the final solution is of interest so the solver can take advantage of the fact that larger cells and those with little or no flow can be marched forward in time by a greater amount compared to smaller cells and cells with higher speed flow. In essence, the flow evolves at different rates depending on the local grid size and flow speed. This procedure is called local time stepping and can appreciably reduce the number of iterations needed to achieve a solution. Clearly, the intermediate results generated with this technique are not physically realistic as time is progressing at different rates in each cell.

If required, CFD-FASTRAN can be forced to use a constant timestep by typing the desired value into both the initial and final CFL boxes and appending the value with a negative sign. For example, typing  $-1E-6$  into both the initial and final CFL number will force constant timesteps of one microsecond.

### Guidelines for the choice of CFL number

Higher CFL numbers decrease the iterations needed to achieve the final solution but the trade off is stability. The higher the CFL number, the less the stability and the higher the probability of divergence. For explicit schemes, the stability is conditional on  $CFL \leq 0.5$ . For the implicit schemes larger CFL numbers can be used. CFD-FASTRAN also offers the option of CFL ramping to aid in the numerical stability of a solution. CFD-FASTRAN will ramp the CFL from the initial CFL to the final CFL values specified in the number of iterations requested. Ramping is linear for transient solutions and quadratic for steady solutions.

### 3.4.5 When solutions become unstable

As mentioned in Section 3.4.2, Roe's scheme in conjunction with higher order interpolation can produce artificial waves near strong discontinuities in the flow field. The use of the entropy fix and flux limiters can help to avoid these effects but cannot eliminate the effects entirely. The instabilities generated in Roe's scheme can sometimes lead to the catastrophic failure of a solution. Examples of failures resulting from the use of Roe's scheme are shown in Figures 3.19 - 3.21.

Figure 3.19 shows two solutions based on validation case 3 (Section 4.3). On the top is shown a Van Leer FVS solution and on the bottom is a Roe's FDS solution. The solutions are fundamentally similar but the solution which used Roe's FDS scheme shows significantly more detail including tiny shockwaves and vortices not present in the Van Leer FVS solution. On first inspection, the Roe's FDS solution seems to be valid but a comparison with experimental data suggests that the solution which used the Van Leer FVS scheme is more correct. It is arguable that the exposure time of 50 ns may have blurred some of the detail present in the experimental Schlieren images (Figures 4.16 and 4.17) but an animation produced from the numerical solution revealed that most of this detailed flow was generated or corrupted by artificial waves. Note that the solution which used Roe's FDS scheme was run on a grid which was slightly higher in cell count than the solution which used the Van Leer FVS scheme due to a small change in the overall grid structure. It is expected that differences between the results would not change if the two simulations were run on the identical grids.

Figure 3.20 is from validation case 1 (Section 4.1) where a planar shock wave is reflected off a parabolic surface. The figure shows two points in time for both an affected simulation (top) and unaffected simulation (bottom). A short while after the planar shock begins to move through the gas it starts to disintegrate. Quirk [67] calls this type of failure "odd-even decoupling". By the time the shock has reflected off the parabolic wall

the spurious waves have engulfed the solution. Whilst the solution appears to be mainly noise, the physically real shockwaves and contact surface are still reconstructed correctly by the solver. This can be seen from a comparison with the unaffected solution.

Figure 3.21 shows one example of an effect termed the “carbuncle phenomenon”. This effect appears as a bubble or bubbles which form along the bow shock close to the centerline. This carbuncle effect is also discussed in Quirk’s paper [67]. Quirk notes that this disturbance is more likely to form in higher Mach number flows and becomes more pronounced when the grid is in close alignment to the discontinuity. Case 6 of the validation studies met both of the above criteria and the carbuncle effect was noted when using Roe’s scheme in conjunction with a min-mod flux limiter. Figure 3.21 shows the effected result at one point during the solution. A more stable solution was obtained with the first order upwind scheme, though this resulted in a poor estimate of heat transfer.

Unfortunately, there are no easily definable set of rules to determine whether or not the shortcomings of Roe’s scheme will pollute a solution beyond all repair. The situations that seem to enhance the shortcomings of Roe’s scheme include aligning the grid closely with a flow discontinuity and using limiters which have a high cut-off value. For example, the Osher-C limiter is more susceptible than the Min-Mod or Van-Leer limiters. Increasing the constants used in the entropy fix from 0.2 to 0.3 or 0.4 will also help suppress unwanted waves but will increase the artificial dissipation in the solution.

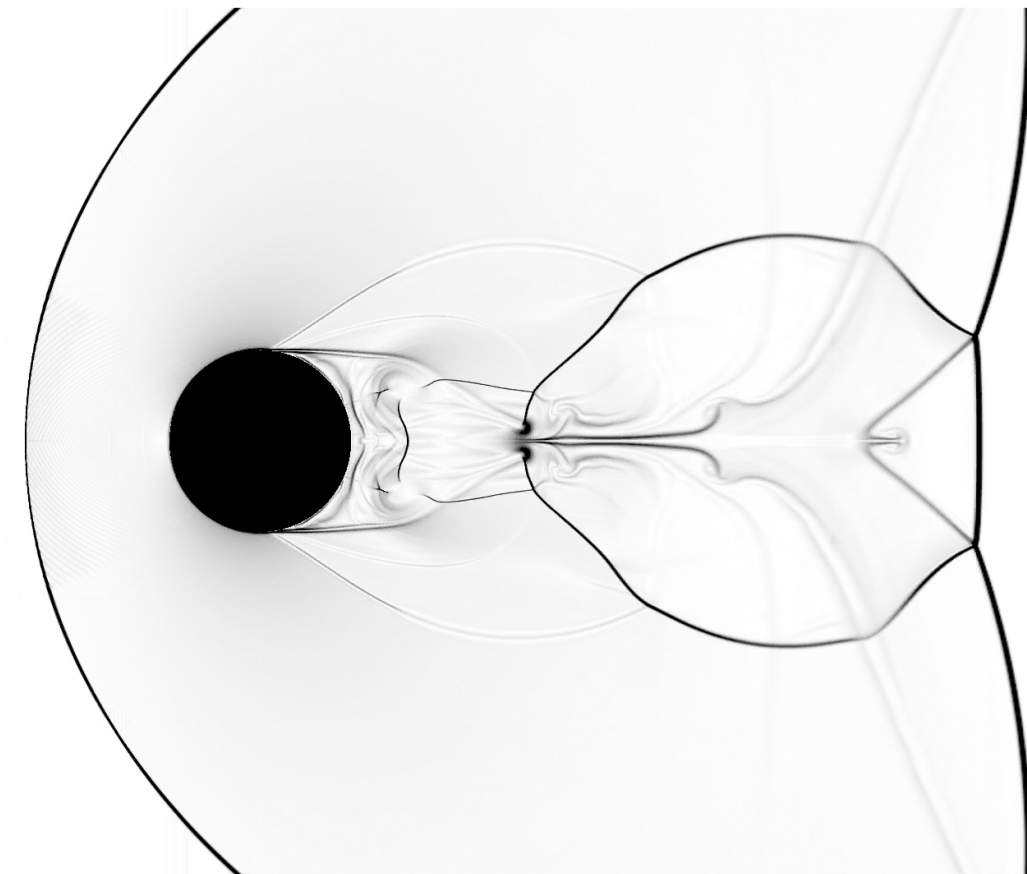
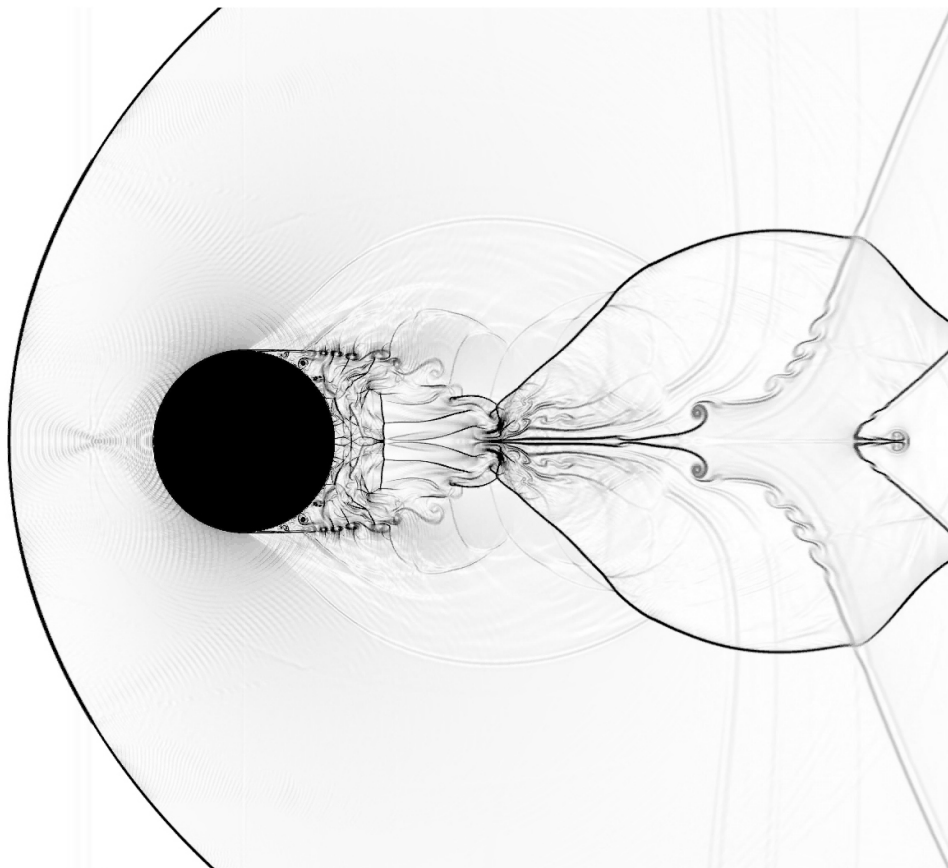
**Van Leer FVS****Roe FDS**

Figure 3.19: Example of the effects of using different flux calculators.

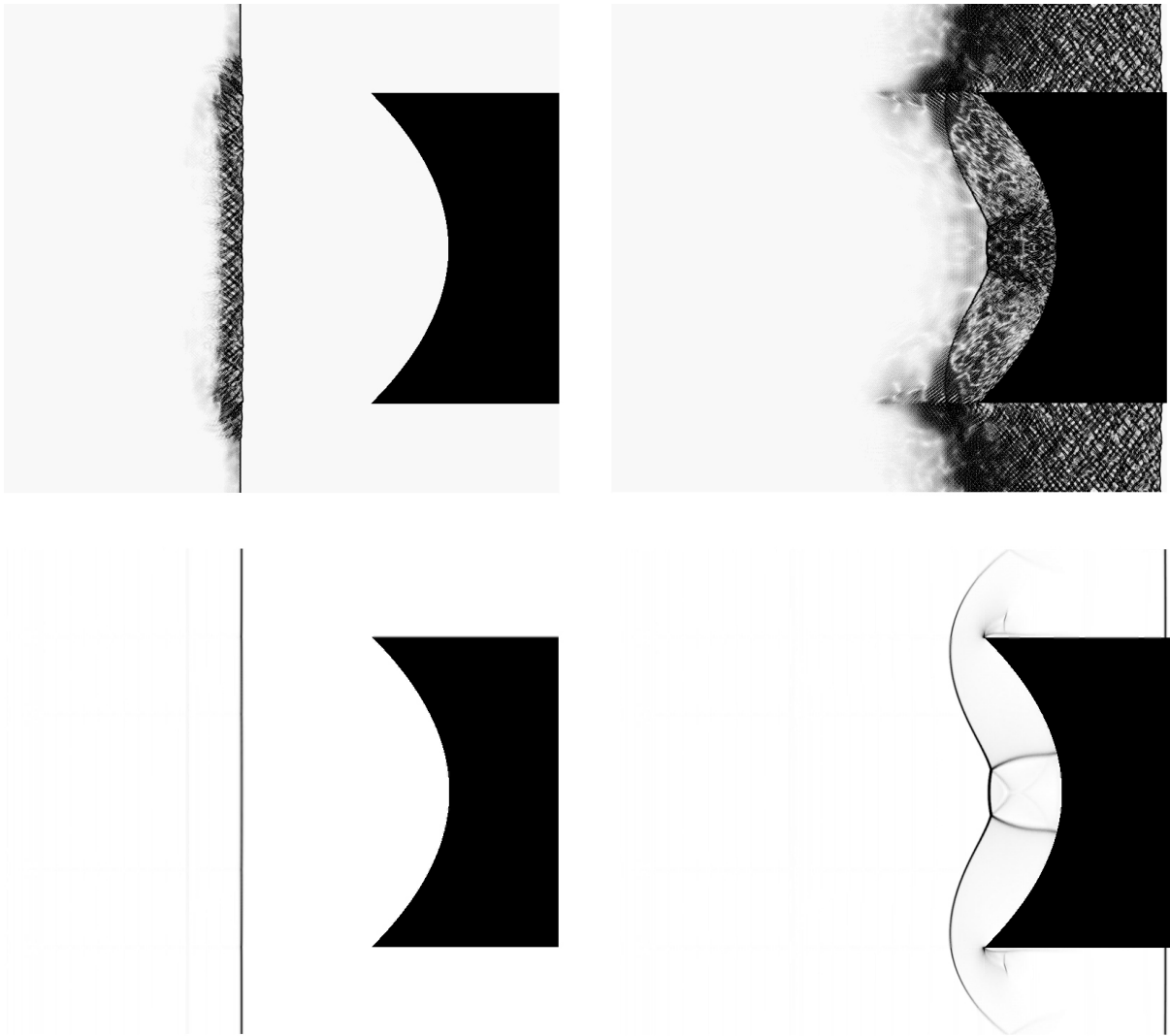


Figure 3.20: Failure in the reconstruction of a planar shockwave through odd-even decoupling.

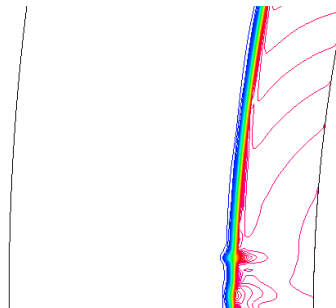


Figure 3.21: Failure in the reconstruction of a bow shockwave through the carbuncle phenomenon.

### 3.4.6 Convergence and Residuals

Because of the inherent non-linearity in fluid dynamics, CFD solvers require an iterative approach to solving the equations of flow. An iterative approach begins with an initial value for each flow variable (the initial conditions) and from this computes updated values. The difference between the value of a flow variable from one iteration to the next is termed the residual. The iteration process is repeated until either a selected number of iterations is reached or the residuals for all flow variables fall below a user defined limit. Residuals are calculated for each flow variable for all cells at every iteration. For a steady flow, convergence in a general sense is achieved when a solution does not change considerably from one iteration to the next. In this situation the residuals will approach zero. If the simulation becomes highly unstable, as can occur when the CFL number is set too large, the residuals will increase from iteration to iteration and the solution will diverge. The solution process will terminate if the residuals become greater than the predefined allowable maximums. For transient simulations where the flow is unsteady, convergence will occur only for the sub-iterations which are performed at each time step. The higher level iterations, which march through time, are not expected to decrease significantly as an unsteady solution will change as time progresses.

A residual plot is the most common way of tracking the overall convergence of a solution. A residual plot presents a weighted average of the residuals over all cells for each flow variable and plots this information versus the number of iterations. The weighted average residual value is known as the “2-norm” or “L2 norm value”. A downfall of using the residual plot to determine convergence is that a mere handful of elements which are not converging can prevent the L2 norm average from decreasing below the specified convergence level. These cells may not even be located in a place which is deemed important to the solution. Fortunately, the convergence of a solution can be evaluated in more than one way to get a more balanced indication. Monitor points are provided in CFD-FASTRAN as a tool for recording flow variables throughout the history of a solution. Convergence at the location of these monitor points is achieved when the recorded values do not change significantly with increasing iterations. CFD-FASTRAN also provides a tool known as “Aero. Force Summary”. This is a tool which integrates the pressure and skin friction along a boundary to provide a total force. When plotted against the number of iterations, the variation in force from iteration to iteration gives another indication of overall convergence of the solution.

Figure 3.22 illustrates the convergence of supersonic aerofoil model. This figure includes flooded contours of pressure at various stages of convergence on the left, a residual plot on the top right and the output from the Aero. Force Summary file in the middle right. The flooded contours show little change from 2,000 iterations to 4,000 iterations. This is

in agreement with the force plot which shows that the lift and drag forces and the pitching moment stabilise after 1,500 iterations or so. The residual plot, which is shown in the default log scale, also begins to show convergence after 1,500 iterations. The highest rate of convergence is seen between 2,000 - 2,500 iterations followed by a steady uniform decrease in residuals.

### 3.4.7 Grid Dependence

In all forms of numerical analysis, the governing equations are solved at discrete points throughout a given domain. In the case of flow analysis this domain can be defined in physical space and, if transient, defined in time as well. The results from a numerical solution depend on the locations in space and time at which the equations are evaluated. The solution is therefore a function of the grid size and structure and of the timestep size as well. The user generally has control over the placement of points in space and time. In CFD-FASTRAN, the user has control over the placement of cells through the choice of grid scheme combined with the selected size and spacing of cells. The user also has control over the choice of timestep either indirectly through the choice of CFL number or directly by enforcing a constant time step. To assess the ability of a grid in resolving a solution with the desired amount of precision, the grid must be refined and changes in the solution noted. If the solution deviates by a smaller amount each time a refinement in the grid is made then the solution is deemed to be “grid independent”. Transient solutions also require the dependence of the solution on the timesteps to be investigated in the same way.

#### Supersonic Flow Over a Wedge

For a case study of grid dependence, the inviscid flow of air over a  $15^\circ$  wedge was investigated using several different grids. The freestream pressure and temperature were 101,300 Pa and 300 K respectively and the freestream Mach number was 3.0. The theoretical solution for this case can be obtained relatively easily. Firstly, the theoretical shock angle  $\beta$  can be obtained from equation 2.16, Page 36 of Anderson [7]:

$$\tan \theta = 2 \cot \beta \frac{M_1^2 \sin^2 \beta - 1}{M_1^2 (\gamma + \cos 2\beta) + 2}$$

Given the wedge angle  $\theta$ , of  $15^\circ$  and the freestream Mach number the shock angle can be found through iteration. The corresponding shock angle for a wedge of  $15^\circ$  at Mach 3.0 is  $32.24^\circ$ . Knowing this shock angle, equation 2.1, Page 33 of Anderson can be used to determine the exact pressure ratio across the oblique shock:

$$\frac{P_2}{P_1} = 1 + \frac{2\gamma}{\gamma+1} (M_1^2 \sin^2 \beta - 1)$$

The theoretical pressure is therefore 285,825 Pa. CFD-FASTRAN was used to run the model using five different grids. The first solution was obtained with a grid of only 200 cells. The grid was then doubled in both directions to give a grid of 800 cells. This process was repeated three more times giving grids of 3200, 12800 and 51200 cells. Flooded pressure contours for each solution are shown at the top of Figure 3.23. This gives a qualitative idea of convergence as the solution is seen to remain constant with refinement of the grid, with the exception of the shock thickness. Quantitatively, an estimate of the true value of any computed quantity,  $q_{TRUE}$ , may be obtained from plotting the pressure against the cell size,  $\Delta X$ , and fitting a curve through the set of points. As cell sizes vary throughout a given grid an indication of cell size can be expressed as  $\Delta X \approx \frac{1}{\sqrt{N}}$  for a 2D grid or  $\Delta X \approx \frac{1}{\sqrt[3]{N}}$  for a 3D grid where N is the total number of cells in the grid. Curve fits are usually expressed in the form:

$$q(\Delta X) = q_{TRUE} + C\Delta X^m$$

The exponent m is typically in the range of 1.5 - 3. For a given value of m, the value of C and  $P_{TRUE}$  can be found. The plot in the lower half of Figure 3.23 shows the pressure from the example simulations plotted against  $\frac{1}{\sqrt{N}}$  for each of the five simulations. Several curve fits were obtained using a least squares method:

$$P(\Delta X) = 285742 - 956197\Delta X^2 \quad (m = 2)$$

$$P(\Delta X) = 285521 - 13023900\Delta X^3 \quad (m = 3)$$

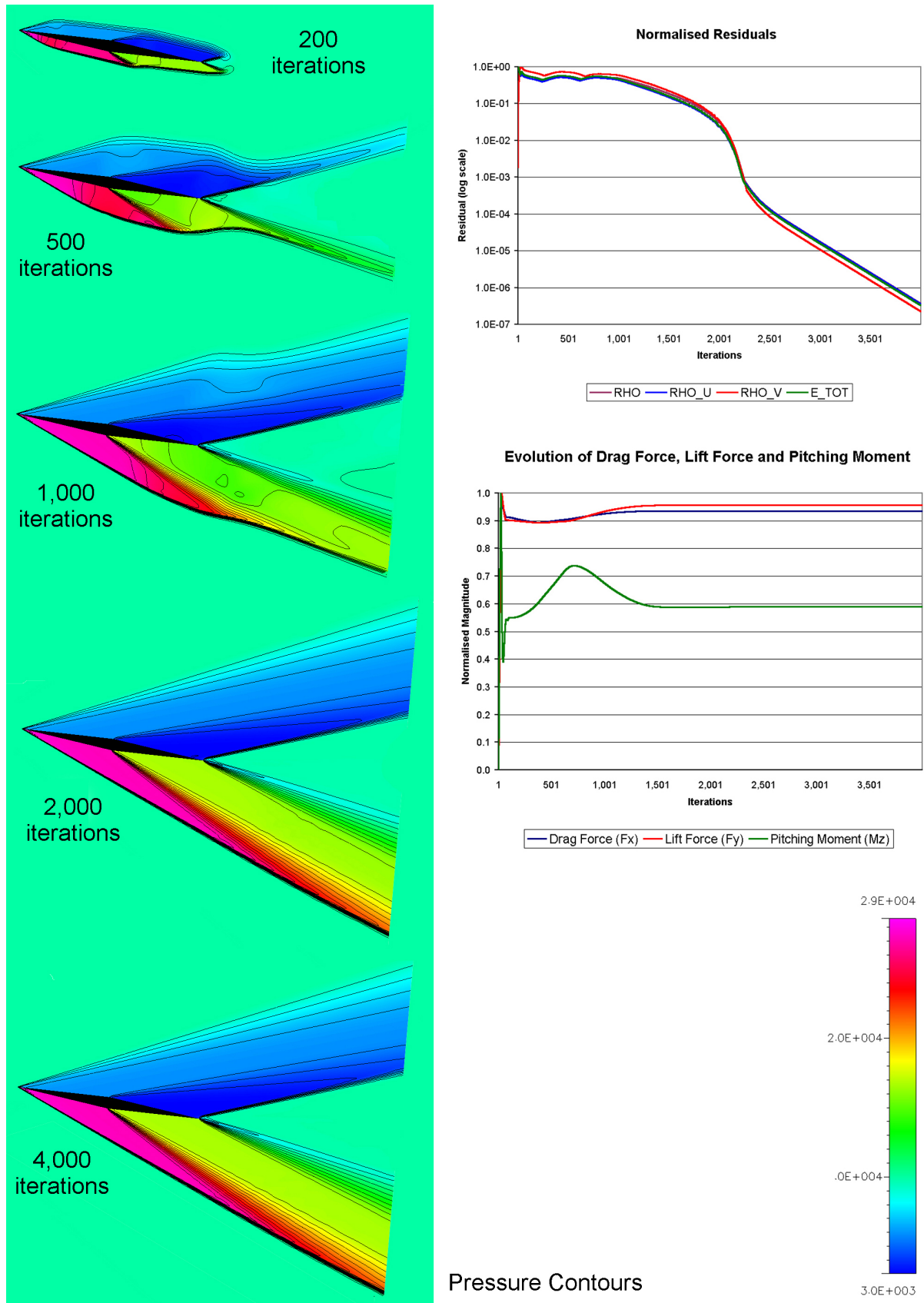


Figure 3.22: Convergence for a supersonic aerfoil at 1 km/s.

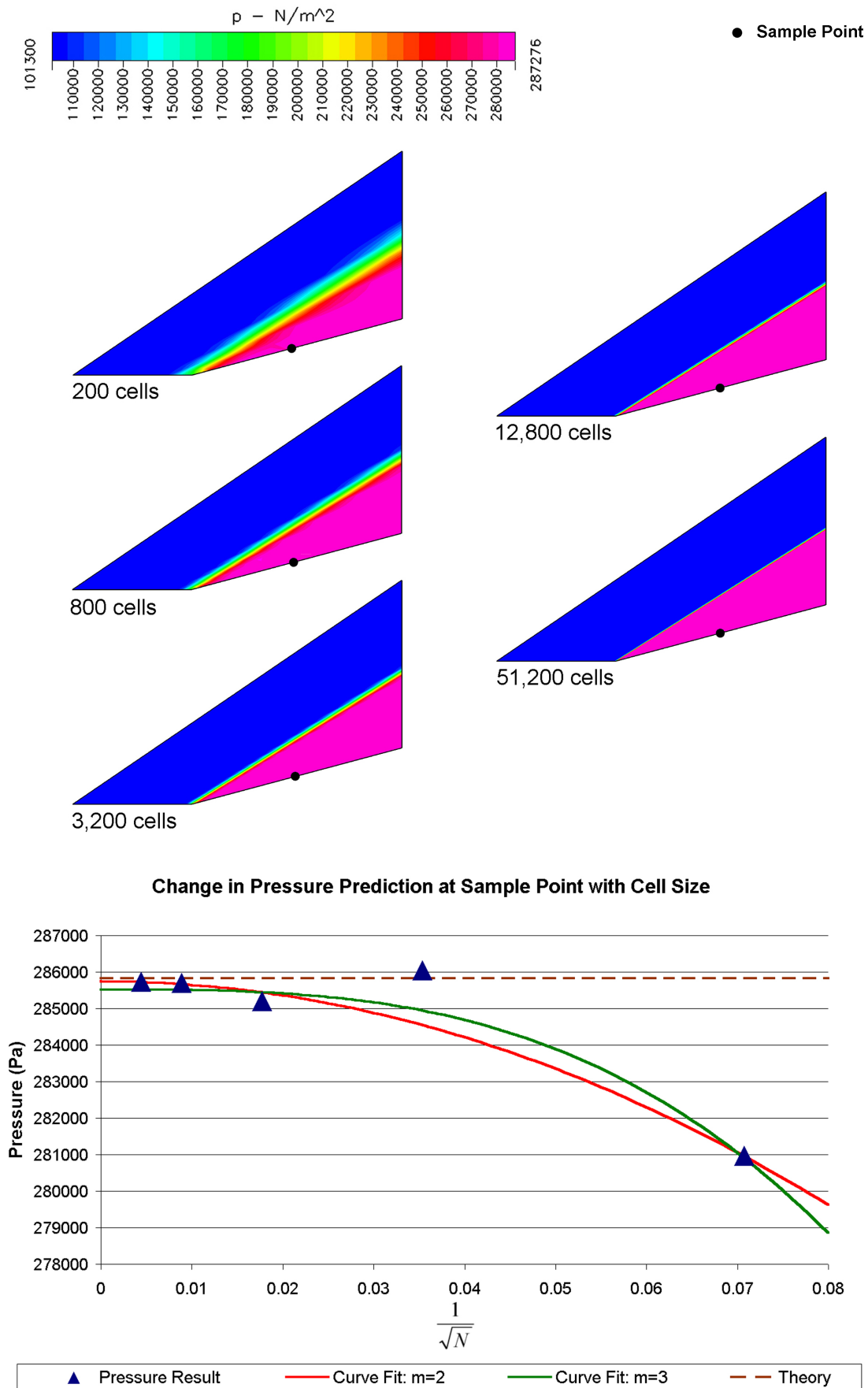


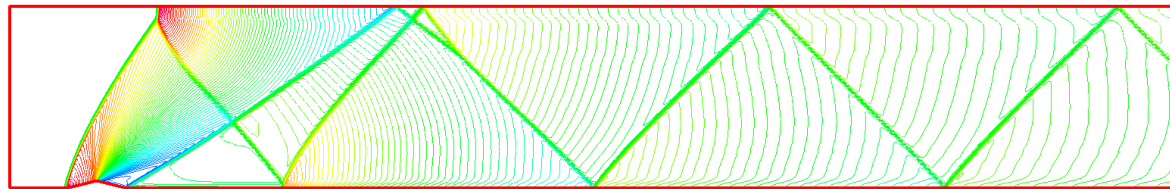
Figure 3.23: Change in pressure with grid refinement.

### 3.5 Processing Results Data

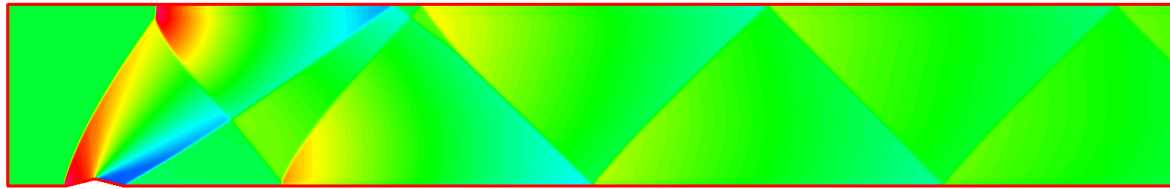
A typical CFD analysis running on a modern personal computer can accrue some gigabytes worth of results data in a matter of hours. As the power and storage capacity of computers increase, so will the size of CFD models and the output they produce. Several decades ago the output from analysis codes was of a much lesser scale and could be read as numbers directly from an output file. This method became increasingly unsuitable as computers grew faster and larger models were analyzed. It was around this time that computer graphics techniques began to be developed for the processing of results data. These techniques allowed the analyst to “see” the features of the flow as if a virtual experiment was being conducted rather than just reading flow quantities at particular locations. With time, these techniques have matured to a point where results applications today can be powerful tools for processing information and scientific visualisation is now a field of study in its own right. Results processing is often overlooked as an important stage of analysis but this stage is crucial for many reasons. Some of these reasons include:

- understanding and correctly interpreting results data
- communicating results from a complex analysis to a general audience
- matching experimental data in a particular format (i.e. interferograms, data from gauges)

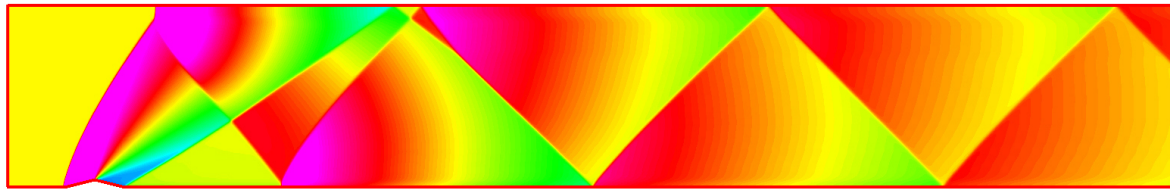
The way in which data is presented is usually up to the analyst to choose but this choice will have an impact on how the results are interpreted by others. As an example of the impact that visualisation can have, consider Figure 3.24. In this figure, the density field from a CFD-FASTRAN simulation has been used to create seven different images. The simulation is of Mach 1.5 flow over an obstacle in a duct using atmospheric freestream conditions and assuming planar inviscid flow. The top four images and the bottom image show the density field whereas the Schlieren images depict the magnitude of the gradient of the density field. Each image has been generated either directly or indirectly from the density field output from CFD-FASTRAN but the images do not all highlight the same features. In this way, visualisations can tend to promote particular features of a flow and hide others.



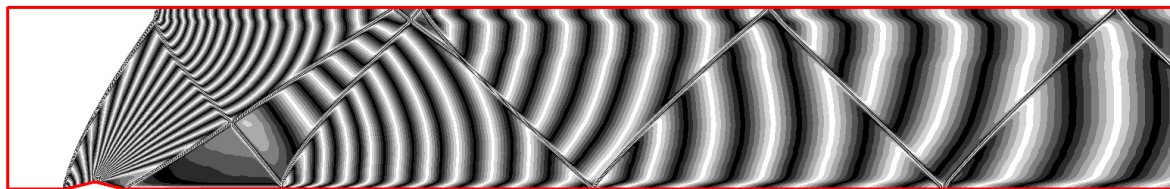
contour plot, true scale



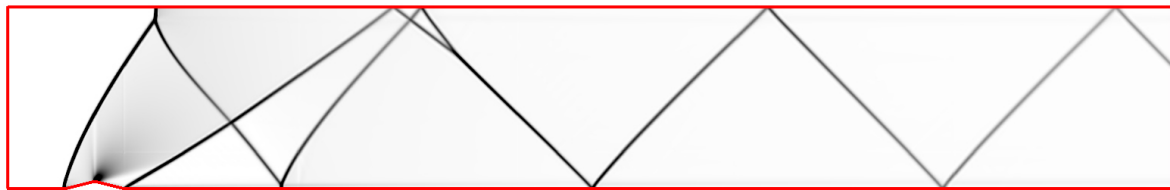
flooded contour plot, true scale



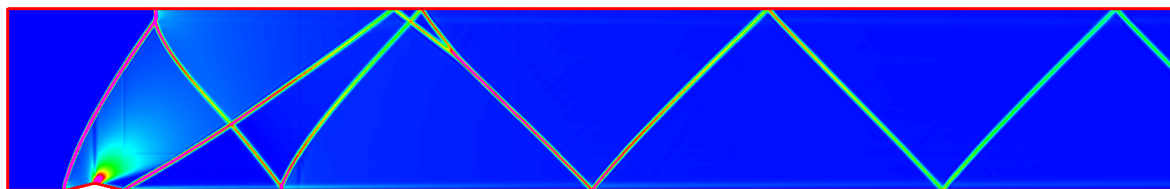
flooded contour plot, truncated scale



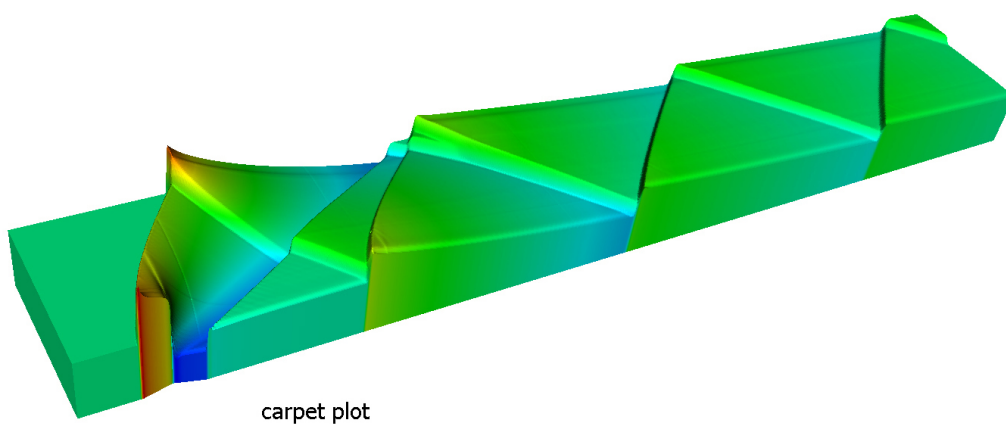
interferogram



greyscale schlieren image



colour schlieren image



carpet plot

Figure 3.24: Supersonic flow over a ramp deflection: different ways of visualising the density field.

### 3.5.1 General Visualisation Tools

Many visualisation tools have been developed for use with CFD data. This section describes visualisation tools which are available in the package `CFD-VIEW`, however, most packages offer some if not all of the tools discussed here. Figure 3.25 shows the result of using a selection of tools discussed here on a three dimensional supersonic flow field generated by `CFD-FASTRAN`. A three dimensional example was chosen so that as many tools as possible could be presented.

#### Point Probes

A point probe is simply a point defined in space which extracts data from the flow field at that location. For structured multi-block grids, a point probe can be defined using  $i, j$  and  $k$  coordinates together with a block number or by using  $x, y$  and  $z$  coordinates. For an unstructured grid, a point probe can be defined by using  $x, y$  and  $z$  coordinates only. When using  $x, y$  and  $z$  coordinates the data is reconstructed through interpolation of the neighbouring nodes.

#### Line Plots

The line plot tool requires a one dimensional entity (a line or curve) that is contained fully within the flow domain. The line plot tool generates a graph of any scalar variable versus distance along that line or curve. Data from the line plot tool can be exported as a text file for use in spreadsheet applications.

#### Contour Plots

A contour plot is a tool which requires a surface defined within the flow domain or a bounding surface to the flow domain. This surface can be arbitrarily shaped and need not be planar. A contour plot produces a series of contour curves which follow along paths of constant value across the surface. Different contours follow different values and hence trace out different paths. `CFD-VIEW` allows a minimum of 2 curves and a maximum of 99 curves to be displayed in any one contour plot. The contours are displayed by the colour in the spectrum which represents their value. Values for each curve are usually chosen to be spread evenly across the range of the variable being plotted. Regions on the surface where contour curves are bunched close together indicate a steep change in a variable, whereas regions where contours are sparse indicate little change. Contour plots are also used in everyday applications such as weather maps and topographical maps. In the field of fluid dynamics, special names have been allocated to commonly used contours. These include pressure contours (isobars), density contours (isopycnics) and temperature contours (isotherms).

### **Flooded Contour Plots (Fringe Plots)**

Flooded contour plots are similar in concept to standard contour plots. The difference is that for flooded contour plots, the spaces between adjacent contour lines are filled with solid colour and the contour lines are hidden. The result is a multi-coloured surface where each colour represents a discrete range of values. When many levels are displayed, the range for each colour becomes very small and the colours blend together seamlessly resulting in a continuous spectrum of colour across a surface. Flooded contour plots can also be displayed with contour lines overlaid. When contour lines are overlaid they are displayed as a single colour so they are visible over the flooded contour plot. The default contour colour is black.

### **Volume Cuts (X,Y and Z Cuts)**

A volume cut creates a two dimensional slice through a three dimensional model. Results from the cells intersected by this slice surface are recorded onto that surface and can be used to plot contours, fringes, vectors and grid lines. The volume cut can be located normal to the x, y or z axis or alternatively orientated more generally using x, y and z coordinates and two angles. For multi-block structured grids, volume cuts can be produced where the slicing surface is constant in the i, j or k value for a single block. The resulting surfaces can then be non-planar depending upon the shape of the block.

### **Isosurfaces and Isocurves**

An isosurface is similar to the idea of a contour but extended to three dimensional space. Just as contours are curves of constant value plotted across a given surface, isosurfaces are surfaces of constant value plotted in a given volume. Isosurfaces can be produced from any valid scalar field and the number of surfaces can be controlled by the user. Standard and flooded contours, vectors and grid lines can all be plotted on an isosurface once it has been created. If the volume cut or isosurface tool is used on a surface object instead of a volume the result is a curve. This “isocurve” is a valid one dimensional object and can be used to produce a line plot.

### **Vector Plots**

Vector plots produce an arrow at each cell center showing the direction and magnitude of a particular vector field at that cell. Vector plots can be produced from any vector quantity defined in a two or three dimensional domain, though vector plots in three dimensional space can become difficult to interpret on a computer monitor or print out. In CFD simulations, vector plots are most commonly used for visualising the velocity field. By default the size of each arrow is proportional to the magnitude of the vector field at each location but equal size vectors can be displayed if only the direction of the field is of

interest. Vectors drawn on a volume cut have the option of being shown projected onto that surface.

### Carpet Plots

A carpet plot requires scalar data on a planar surface. From this data a second surface is generated. In *CFD-VIEW* this surface is shown in a separate window. The second surface is created with an elevation which is determined by the value of a chosen scalar on the original surface. The result is like a relief map where the height represents the magnitude of the variable. The carpet plot can be coloured by the same variable, which will result in a colour versus height pattern, or with a separate scalar variable. Using a different scalar to define the colour allows two variables to be visualised simultaneously but this option should be used with caution as the resulting plots can become confusing for a general audience to interpret.

### Particle Traces

A particle trace is the trajectory of a massless particle acted upon by a vector field. As with the vector plot, it is most common for this tool to be used on the velocity field, in which case the trajectories represent streamlines. The particle trace tool requires the user to define a specific location inside a flow domain, termed the injection point. When a massless particle is released from this point, the location of the particle after some finite amount of time can be computed, assuming it keeps its initial velocity. This assumption is quite valid if the particle moves only a small distance. At the new location, the new velocity can be used to create a further point in the flow and so on. This process continues until the particle either exits the domain through an outlet or a maximum number of timesteps is reached. Once all of the points are calculated they can be joined together with lines to form a single trajectory curve. The user has control over the maximum amount of steps and the size of the time step. A smaller timestep will result in a smoother trajectory but will require more steps to be taken and will therefore take longer to compute. By default the trajectory is displayed as a curve without thickness but the user can choose to instead plot ribbons or tubes. Ribbons show not only a trajectory but also the curl of the vector field throughout that trajectory. The local curl is shown by the amount of twist in the ribbon. The tube option renders particle traces with a circular cross section to enhance the display. Particle traces shown as curves, ribbons or tubes can all be coloured by any available scalar variable.

The particle trace tool is most effective in visualising flows when an array of injection points is used. An array of injection points in one, two or three dimensions can be defined by specifying the desired number of points and their spacing for each direction. For each trace, a number of markers can be evenly spaced along the length and the user is able

to control both the amount of markers and their offset from the start point. The offset parameter can be animated resulting in the apparent movement of markers along each trace. The trace itself can then be hidden so that only the individual markers are visible. If this technique is used with a two dimensional array and the markers are rendered as spheres, the result is a sheet of of spherical particles. This sheet will become stretched and twisted as it passes through the flow. Viewing a sheet of particles sweeping through a flow can be quite a natural way for a person to comprehend CFD results. This tool is therefore very effective for presentations where the audience may not be well versed in CFD. If animation is not an option, a single image can be produced with the particle sheets shown at various stages throughout the flow. Such a system is shown in Figure 3.25.

### Strip Charts

A strip chart requires a series of result files recorded from a single simulation. A strip chart produces a plot of a variable at one location in the flow as it changes through the series of result files. In the case of a transient solution, this is a plot of a variable versus time. For a steady solution this tool can be used to explore the convergence history at one location in the flow.

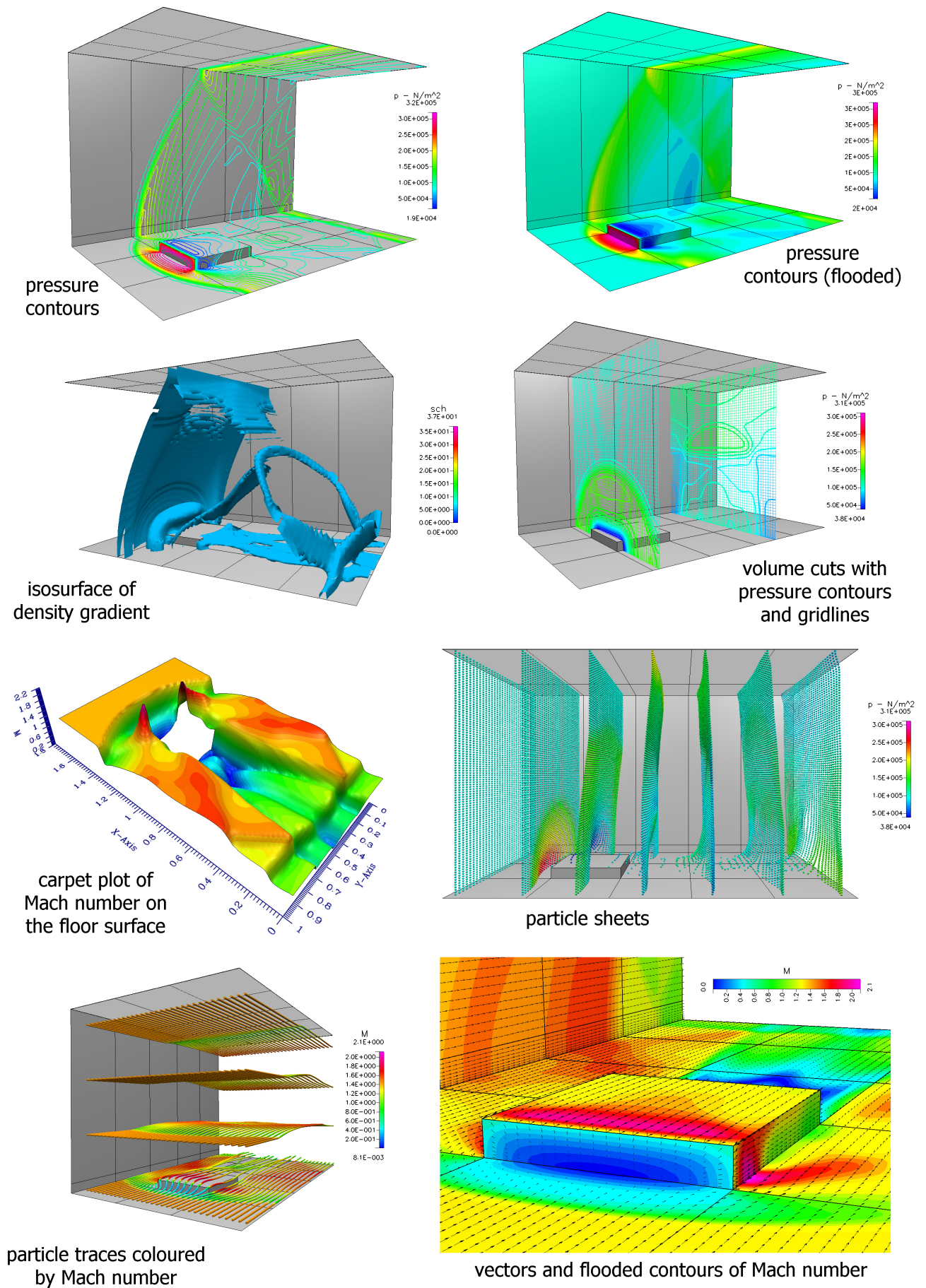


Figure 3.25: Visualisation techniques in CFD-VIEW.

### 3.5.2 Special Visualisation Techniques for Supersonic Flow

It is often desirable to compare experimental images obtained with optical techniques, such as interferograms or Schlieren images, directly to the results of a CFD simulation. This section discusses the application of visualisation tools in ways which can approximately construct such images from CFD data.

#### Numerical Interferograms

Interferograms are a technique for capturing spatial changes in the density field for experiments involving fluid flow. Using **CFD-VIEW**, interferograms can be constructed for two dimensional planar flows but cannot be reproduced for axisymmetric or three dimensional flow. For planar flow, an interferogram simply requires that the density field be viewed with a spectrum which alternates from black to white a number of times throughout the spectrum. The number of times the spectrum colour is alternated equals the total number of fringes in the interferogram. Interferograms constructed with **CFD-VIEW** are limited to infinite fringe interferograms. Finite fringe interferograms would require an artificial density gradient running crosswise to the freestream to be superimposed onto the results. The creation of a black-white alternating spectrum in **CFD-VIEW** is quite a tedious affair but it is possible to record a script which can automate the process. One technique for constructing a numerical interferogram in **CFD-VIEW** is to:

1. create a flooded contour plot
2. choose density as the variable and set the spectrum range from 0 to 1
3. create a number of tabs in the spectrum so that the total is equal to the number of desired fringes<sup>3</sup>
4. space the tabs at equal intervals (a spacing of  $1/n$  where  $n$  is the number of tabs)
5. change the colour of the tabs to alternate from black to white
6. perform the “maximise” or “maximise all” operation to scale the spectrum to the upper and lower limits in the model

Note that the maximise button scales the spectrum to the upper and lower limits of the variable on the item which is currently selected. The maximise all button scales the spectrum to the upper and lower limits present in the entire model for that variable. For 3D and axisymmetric flows, volume rendering techniques or a program which traces rays of light through a 3D density field are required. **CFD-VIEW** is a general visualisation package

---

<sup>3</sup>New tabs can be created by dragging the uppermost or lowermost tabs into the middle of the spectrum.

and as such does not support these advanced techniques. Advice on how to compose computer code for performing these calculations is given by Wen [80] in Section 3.2 of his PhD thesis. Wen’s advice is applied to axisymmetric interferograms. Additionally, Olejniczak [59] has produced numerical interferograms for 3D flows in his PhD dissertation.

### Numerical Schlieren Images

As with interferograms, Schlieren photography is another experimental technique for recording spatial changes in the density field. Breazeale [12] gives a topical review of the history of Schlieren optics up to and including colour Schlieren photography for those readers not familiar with this experimental technique.

Schlieren images are traditionally greyscale with the white end of the spectrum indicating no gradient and the black end indicating a maximum gradient. As with numerical interferograms, the creation of numerical Schlieren images for axisymmetric and 3D flows require special tools whereas the creation of Schlieren images for planar flow is relatively straightforward. In a planar flow the intensity of light ( $I$ ) striking the camera which records the Schlieren image is proportional to the magnitude of the gradient of density:

$$I \propto |\nabla\rho(x, y)|$$

CFD-VIEW provides a gradient function within its calculator facility. The syntax “Schlieren=gra2dm(rho)” will return the magnitude of the density field gradient in 2D as the scalar field “Schlieren”. With this scalar field, a flooded contour plot using a greyscale spectrum will provide the required Schlieren image. The range of this scalar will depend on the type of problem and the resolution of the grid. Generally, larger gradients will be produced for finer grids. The maximum value of the gradient usually needs to be reduced several orders of magnitude in order to display all relevant features of the Schlieren. To replicate a standard Schlieren image, a greyscale spectrum should be chosen with white as the zero value and black as the reduced maximum gradient. Any regions in the model where the density gradient is beyond this maximum value will be rendered black. Some experiments make use of a colour Schlieren facility. This type of result can be replicated simply by choosing or creating a colour spectrum which matches the experimental spectrum and, as with the greyscale Schlieren, setting the maximum gradient to an appropriate value.

Figure 3.26 shows two greyscale numerical Schlieren images prepared from the same result. The image on the left was prepared with a lower maximum gradient than the image on the right. Fainter features such as a weak contact surface are visible in the left image. The incident shockwave is also displayed as being much thicker in the left image due to the lower maximum value of gradient.

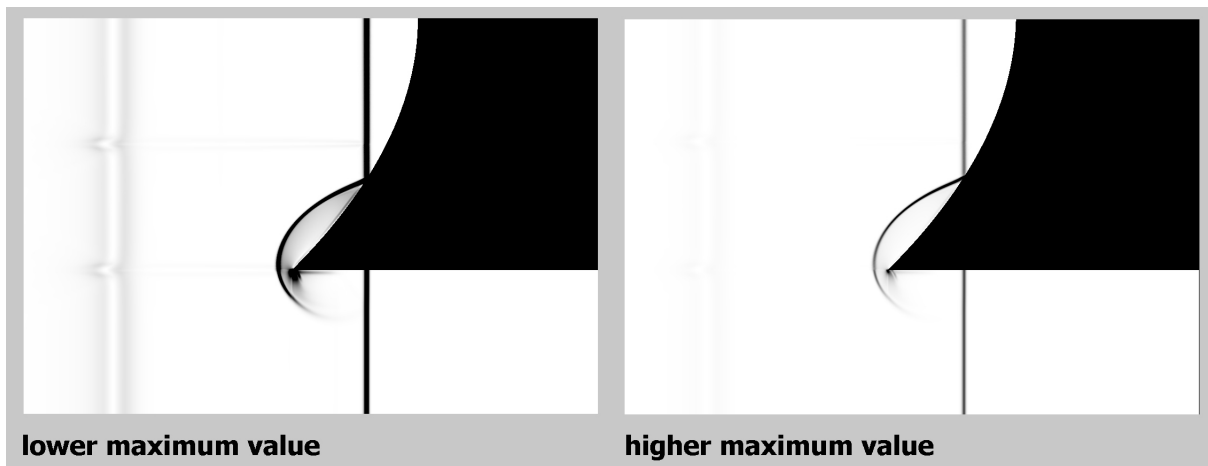


Figure 3.26: Effect of the maximum gradient in Schlieren images.



## Validation Studies

---

This chapter discusses the application of CFD-FASTRAN to some compressible flows for which published experimental results are available. The aim of this section is to benchmark CFD-FASTRAN against both experimental data as well as results from other CFD codes. Six test cases were chosen in total. It is intended that these test cases will be beneficial to future students in the UQ hypersonics group who are involved in simulation. The cases were chosen based on the quality and quantity of experimental results provided as well as the range of flow features present. Within the six test cases, features of the flow included:

- shock wave diffraction
- shock wave focusing
- steady and unsteady shock-shock interaction
- steady and unsteady shock-vortex interaction
- complex Mach reflection
- boundary layer separation and reattachment
- attached and detached shock waves
- nonequilibrium exchange of vibrational energy (thermal nonequilibrium)
- finite rate chemistry
- high enthalpy flow
- hypervelocity flow

All of the test cases undertaken are assumed to be either planar or axisymmetric compressible flows. The problems chosen contain flow speeds in the low supersonic range to mid hypersonic range. Correctness of the numerical solution is gauged by comparison to experimental Schlieren images or interferograms as well as wall heat flux and pressure

distributions, where possible. For selected cases, the effects of viscosity in the flow have been emphasized by running a model both with and without viscosity. Table 4.1 shows a list of the validation cases presented in this thesis. Table 4.2 provides general information about the flow characteristics of each case.

Table 4.1: Description of validation cases.

case	description
<b>1</b>	inviscid planar shock focusing with a parabolic reflector in air
<b>2A</b>	laminar axisymmetric shock diffraction over a 43° cone in Nitrogen (N <sub>2</sub> )
<b>2B</b>	laminar axisymmetric shock diffraction over a 43° cone in Argon (Ar)
<b>3A</b>	inviscid planar shock diffraction over a cylinder in air
<b>3B</b>	laminar planar shock diffraction over a cylinder in air
<b>4A</b>	inviscid planar shock diffraction over a half diamond in air
<b>4B</b>	laminar planar shock diffraction over a half diamond in air
<b>5A</b>	inviscid axisymmetric N <sub>2</sub> flow over a 25° - 55° sharp double cone
<b>5B</b>	laminar axisymmetric N <sub>2</sub> flow over a 25° - 55° sharp double cone
<b>6A</b>	laminar axisymmetric ideal air flow over a sphere
<b>6B</b>	laminar axisymmetric chemically reacting nonequilibrium air flow over a sphere

Table 4.2: Setup of validation cases.

case	gas	$Re_\infty^a$	$Kn_\infty^b$	$M_\infty^c$	$M_S^d$	$k \left( \frac{MJ}{kg} \right)^e$	type	viscosity	gas model <sup>f</sup>	comparison <sup>g</sup>	format	references
1	air	-	$9.75 \times 10^{-7}$	0.96	2.00	0.093	unsteady	inviscid	CPG	exp, CFD	planar	[37]
2A	N <sub>2</sub>	29,766 <sup>h</sup>	$4.95 \times 10^{-5}$	1.15	2.38	0.162	unsteady	laminar	TPG-VE	CFD	axisym.	[40], [22], [74]
2B	Ar	18,378	$6.94 \times 10^{-5}$	0.91	2.38	0.110	unsteady	laminar	TPG-VE	CFD	axisym.	[40], [22], [74]
3A	air	-	$2.32 \times 10^{-6}$	1.31	2.82	0.254	unsteady	inviscid	CPG	exp, CFD	planar	[13]
3B	air	766,891 <sup>j</sup>	$2.32 \times 10^{-6}$	1.31	2.82	0.254	unsteady	laminar	CPG	exp, CFD	planar	[13]
4A	air	-	$2.10 \times 10^{-5}$	1.32	2.85	0.258	unsteady	inviscid	CPG	exp, CFD	planar	[26], [67]
4B	air	85,036	$2.10 \times 10^{-5}$	1.32	2.85	0.258	unsteady	laminar	CPG	exp, CFD	planar	[26], [67]
5A	N <sub>2</sub>	-	$1.57 \times 10^{-3}$	15.56	-	2.142	steady	inviscid	TPG-VNE	exp, CFD	axisym.	[28], [35], [36], [34]
5B	N <sub>2</sub>	30,931	$1.57 \times 10^{-3}$	15.56	-	2.142	steady	laminar	TPG-VNE	exp, CFD	axisym.	[28], [35], [36], [34]
6A	air	145,000	$4.27 \times 10^{-5}$	5.33	-	11.810	steady	laminar	CPG	exp	axisym.	[81], [80]
6B	air	145,000	$4.27 \times 10^{-5}$	5.33	-	11.810	steady	laminar	CRG-CVN	exp	axisym.	[81], [80]

$$^a Re_\infty = \frac{\rho_\infty U_\infty D}{\mu_\infty}$$

$$^b Kn_\infty = \frac{\mu_\infty k \cdot T}{\sigma_d^2 \pi \sqrt{2} \cdot P \cdot D}$$

$$^c M_\infty = \frac{U_\infty}{a_\infty}$$

$$^d M_S = \frac{U_{ShockWave}}{a_\infty}$$

$$^e k = \frac{U_\infty^2}{2}$$

<sup>f</sup>gas thermodynamic model:

CPG = calorically perfect gas

TPG-VE = thermally perfect gas in vibrational equilibrium

TPG-VNE = thermally perfect gas in vibrational non equilibrium

CRG-CVE = chemically reacting gas in chemical and vibrational equilibrium

CRG-CVN = chemically reacting gas in chemical and vibrational nonequilibrium

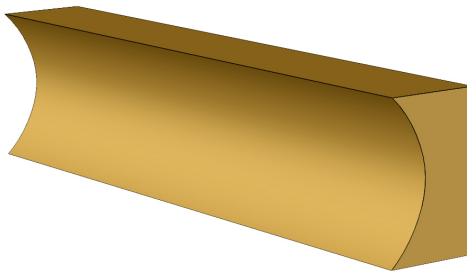
<sup>g</sup>exp = experiment

<sup>h</sup>evaluated with a characteristic length (L) of 20mm

<sup>i</sup>The experimental value is  $2.11 \times 10^{-5}$ . The difference is discussed in Section 4.3.4

<sup>j</sup>The experimental value is 77,900. The difference is discussed in Section 4.3.4

## 4.1 Shock Focusing in a Parabolic Reflector



### 4.1.1 Problem Overview

The focusing of a planar shock wave with a parabolic reflector has been modelled numerically using CFD-FASTRAN. The simulation has been set up to closely match experiments performed at Kyushu University by Izumi et al. in 1992 [37]. Izumi used a conventional shock tube measuring 6.4 m in length and 44 mm square in the test section. Air was used as the driver and driven gases. In these experiments, five Schlieren images were obtained revealing detail about the shock structure at different stages throughout the flow period. To capture these images, a conventional Schlieren approach was used with a 50 ns flash light duration. The experimental setup contained a single parabolic reflector, 28 mm in height and with a profile described by the equation  $X = CY^2$ , where  $X$  and  $Y$  are the coordinates normalised to the reflector height<sup>1</sup> and  $C$  is a scaling constant. This setup is shown in Figure 4.1 which has been adapted from a figure shown in Izumi's paper. Many combinations of shock wave Mach numbers ( $M_S$ ) and scaling constants were investigated both experimentally and numerically by Izumi. For this CFD study only the combination of  $C = 0.5$  and  $M_S = 2.00$  was investigated numerically.

### 4.1.2 Key Features

The key features of the validation study are as follows:

- shock wave Mach number of 2.00
- unsteady shock-shock interaction
- unsteady complex Mach reflection with a changing wall angle
- comparison with experimental Schlieren images
- comparison to an inviscid numerical solution from Izumi et al. [37]

---

<sup>1</sup> $Y$  ranges from -1 to 1 across the height of the parabolic reflector.

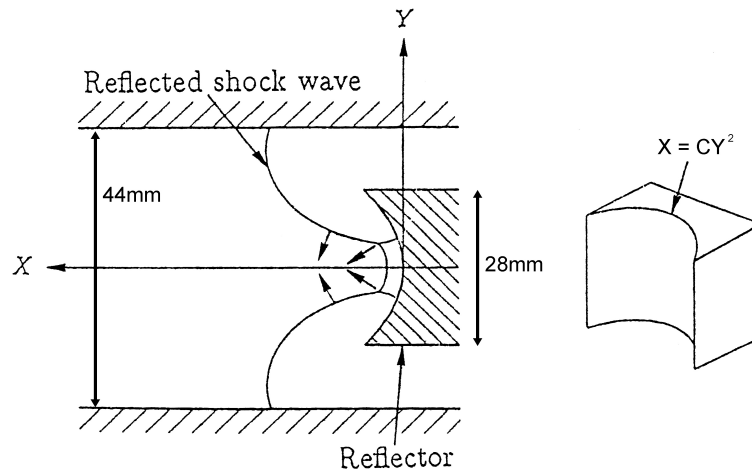


Figure 4.1: Experimental setup of Izumi et al.

### 4.1.3 Assumptions

The following assumptions have been made:

- planar flow
- inviscid compressible flow
- calorically perfect gas
- air is a single species
- adiabatic walls

### 4.1.4 Grid Setup, Boundary Conditions and Initial Conditions

The layout of the multi-block grid is shown in Figure 4.2. The boundaries patches are numbered and Table 4.3 shows the boundary conditions for each patch. Table 4.4 shows the initial conditions which were applied globally to the model. The model contained 420,000 cells and 423,857 nodes in 7 blocks. There were 300 cells spaced across (half) of the parabolic reflector surface (boundary patches 6 - 7). 450 cells were placed along the inlet (boundary patches 10 - 12).

### 4.1.5 Solution Setup

A Roe's Flux Difference Splitting (FDS) scheme was used together with a Minimum Modulus (Min-Mod) second order flux limiter for spatial integration. The default values for the entropy fix were used (0.2 for both linear and nonlinear waves). A Jacobi Point Iterative implicit scheme was used together with a time accurate Backward-Euler scheme for integration in time. A constant CFL number of 0.5 was used throughout the time integration.

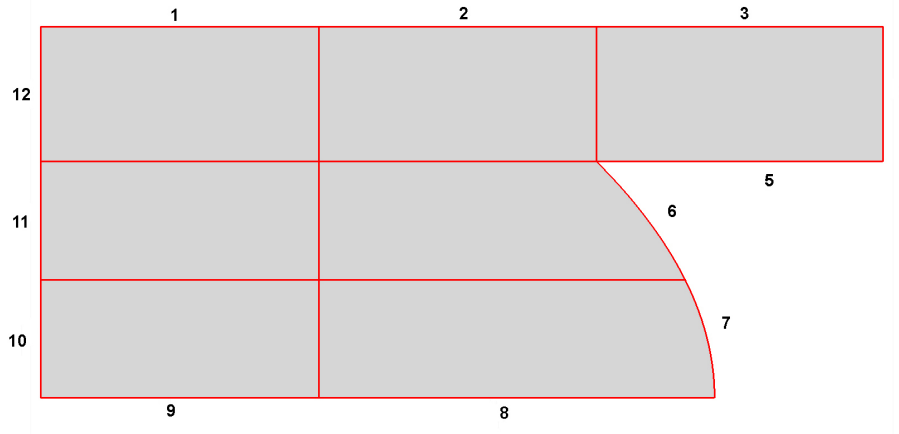


Figure 4.2: Multi-block grid for Case 1.

Table 4.3: Boundary conditions for Case 1.

patch	BC type	BC sub type	$\mathbf{v}$ (m/s)	P(Pa)	T(K)
1 - 3	wall	adiabatic	calculated	calculated	calculated
4	outlet	extrapolated	calculated	calculated	calculated
5 - 7	wall	adiabatic	calculated	calculated	calculated
8 - 9	symmetry	-	calculated	calculated	calculated
10 - 12	inlet	flow rate	(431.81,0)	454,500	501.19

Table 4.4: Initial conditions for Case 1.

quantity	value
velocity (u,v) (m/s)	(0,0)
pressure (Pa)	101,000
temperature (K)	297

### 4.1.6 Results and Comparisons

The results of this study are compared to results from both the physical experiment as well as accompanying numerical results presented in Izumi's paper. Izumi used a planar inviscid code which incorporated a Piecewise-Linear-Method (PLM) scheme for spatial integration. Izumi's simulations were run on a cartesian grid of 130 x 102 points where the wall boundary was approximated with steps. The CFD-FASTRAN simulation used a body fitted grid and so did not contain the same discontinuities. An inviscid solution was computed with CFD-FASTRAN to provide a direct comparison with the results obtained by Izumi.

Figure 4.3 shows a split-view comparison with Izumi’s experimental Schlieren images shown on the top half and numerical Schlieren images from CFD-FASTRAN shown on the bottom half. Figure 4.4 shows another split-view comparison with isopycnics from Izumi on the top half and corresponding isopycnics from CFD-FASTRAN on the bottom half. For the five frames displayed in Figure 4.3 and 4.4 it was estimated, from a comparison of the CFD-FASTRAN simulation and the physical experiment, that the frames were shot at approximately the times shown in Table 4.5. The times are referenced to the initial impact of the shock on the parabolic surface.

Table 4.5: Estimation of flow time for each experimental image.

frame	time
1	6 $\mu s$
2	14 $\mu s$
3	18 $\mu s$
4	23 $\mu s$
5	28 $\mu s$

In frame one, a reflected shock has formed which connects to the initial incident shock and an expansion is present, centered about the cusps of the parabolic section. In the second frame, the expansion at the cusps has grown stronger and the two reflections have merged with a further shock and contact surface formed near the centerline. These are the result of a type of reflection known as a “complex Mach reflection” which was formed when the union of the incident and reflected shocks travelled along the parabolic surface. Both pairs of shocks and contact surfaces meet the reflected shock at points known as the triple points. In frame three, the triple points meet each other and cross over. The Mach reflection shocks follow closely behind. The point at which the triple points meet is known as the gasdynamic focus.

In frame four, the Mach reflection shocks have completely crossed over and proceed in opposite directions, driven by the expansion of the gasdynamic focus. This focal point has expanded into a region of high pressure bounded by the reflected shock and the two Mach reflection shocks. An X shape is formed within this region by the two contact surfaces. In the final frame, the shock structure is similar to the previous frame but with the expansion of the high pressure region causing it to grow even larger. The simulation was continued past this point and the results suggested that the high pressure region eventually engulfs the flow as it expands. The reflected shocks merge to become one normal shock spanning the complete test section. This shock travels upstream as it forms, developing a choked flow.

### Comparison with Experiment

The CFD-FASTRAN solution shows good agreement with both the experimental and numerical results from Izumi, however some differences are noted. One example is the apparent absence of the contact surface from the CFD-FASTRAN results. Also, the regions of expansion centered about the cusps of the parabolic section appear much smaller in the CFD-FASTRAN simulation than in the experimental Schlieren images.

Both of these discrepancies relate to the sensitivity of the Schlieren images to gradients in the density field. As discussed in Section 3.5.2, the appearance of a numerical Schlieren image is affected by the choice of the maximum gradient. Lowering this value has the effect of highlighting smaller changes in density, which may otherwise have been faint. The disadvantage is that regions surrounding strong density gradients, such as a reflected shock, become dark and this tends to reduce the overall definition of the feature. The maximum gradient chosen when creating the Schlieren images presented in Figure 4.3 was a trade-off between clarity and definition. Because of this, the contact surface appears very faint and is almost non-existent by the fifth frame. The region of expansion is also shown smaller than is rendered in the experimental image. Confirmation that the contact surface exists can be seen in Figure 4.4, as the isopycnics form a kink in the location of the contact surface.

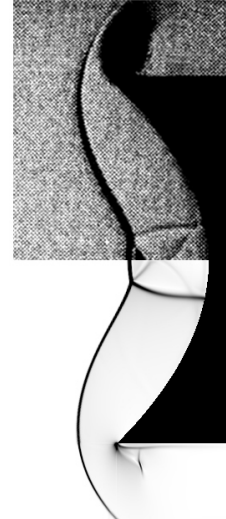
### Comparison with PLM Code

Whilst the agreement between the isopycnics generated by Izumi's PLM code versus those from CFD-FASTRAN are generally good, the contours shown by Izumi contain some disturbances. These disturbances are most pronounced in the second frame. It is likely that the disturbances are non physical as no corresponding features appear in the experimental results. It is also likely that the disturbances are a product of the routine used by Izumi's PLM code for flux calculation and spatial reconstruction. Disturbances of a similar nature are explored in Section 3.4.5. It is possible that disturbances may also be introduced into the flow from the stepped approximation of the parabolic shaped wall.

**6  $\mu\text{s}$  after  
impact**



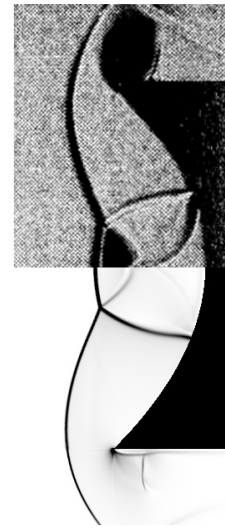
**23  $\mu\text{s}$  after  
impact**



**14  $\mu\text{s}$  after  
impact**



**28  $\mu\text{s}$  after  
impact**



**18  $\mu\text{s}$  after  
impact**



Figure 4.3: Focusing of a planar shock: Izumi et al. experimental Schlieren (top half), CFD-FASTRAN numerical Schlieren (bottom half).

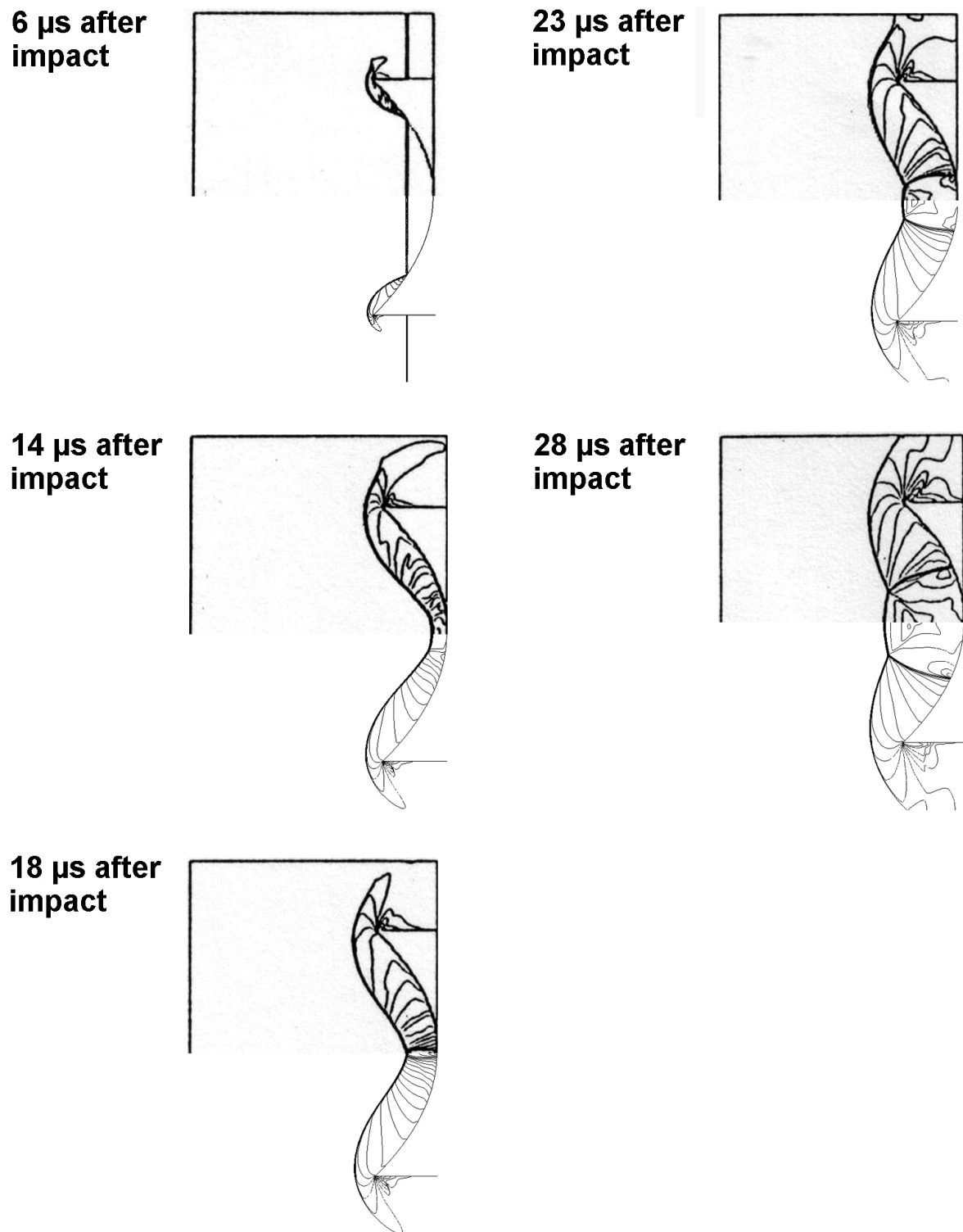
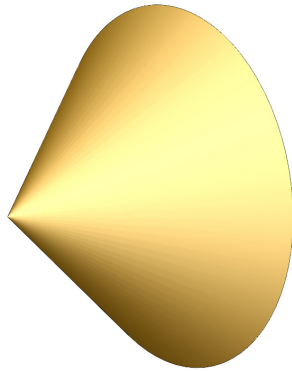


Figure 4.4: Focusing of a planar shock: Izumi et al. numerical isopycnics (top half), CFD-FASTRAN numerical isopycnics (bottom half).

## 4.2 Shock Diffraction Over a 43° Cone



### 4.2.1 Problem Overview

The diffraction of a planar shock wave across the sloping surface of a 43° cone has been simulated using CFD-FASTRAN. The cone was considered perfectly smooth with a half angle of 43°. Both Argon (Ar) and Nitrogen (N<sub>2</sub>) were considered in this study using a shock Mach number of 2.38 for both test gases. The study was completed in response to a call for papers announced in the journal *Shock Waves* during the first half of 2003 [74]. As requested by the organisers of this benchmark, results have been recorded when the incident shock is at 5 mm, 10 mm, 15 mm and 20 mm from the cone tip along the horizontal axis. These results include isopycnics as well as pressure, heat transfer and skin friction along the cone surface.

### 4.2.2 Key Features

The key features of this study are:

- shock wave Mach number of 2.38
- unsteady shock-shock interaction
- unsteady complex Mach reflection
- comparison of pure Nitrogen (N<sub>2</sub>) and pure Argon (Ar) flow
- comparison to solution from MB-CNS code

### 4.2.3 Assumptions

The following assumptions have been made:

- axisymmetric flow
- laminar compressible flow
- thermally perfect gas
- isothermal walls
- no-slip walls

#### 4.2.4 Grid Setup, Boundary Conditions and Initial Conditions

The layout of the multi block grid is shown in Figure 4.5 with the boundaries patches numbered. Table 4.6 shows the boundary conditions for each patch for the Nitrogen flow model and similarly Table 4.7 shows the conditions for the Argon flow model. Table 4.8 shows the initial conditions which were applied globally to both models. Both models contained 20 blocks, 716,900 cells and 725,760 nodes. 750 cells were spaced along the cone from  $x = 0$  mm to  $x = 20$  mm (boundary patches 11 - 12). The inlet (boundary patches 14 - 18) contained 535 cells.

#### 4.2.5 Solution Setup

When gathering the data necessary to perform this simulation, a reliable source of Sutherland's viscosity constants for Argon could not be found. Whilst several references were located, it was found that these values did not produce the same viscosity for a given temperature to within a reasonable tolerance. Given this difficulty, it was decided to invoke Wilke's law of mixing to calculate the viscosity. This was done by activating the mixing module in CFD-FASTRAN-GUI. When Wilke's law is used for a single gas the viscosity reduces to a function of temperature, molecular weight, collision diameter and the collision integral for that gas. In CFD-FASTRAN, Wilke's method requires no input from the user, other than the chemical composition, as all of the required information is referenced from a file which is supplied with the program. Details on the source of data for this file and Wilke's law of mixing is given in Section 3 of Appendix A. The disadvantage of this method is that when the mixing module is enabled, CFD-FASTRAN does not permit constant specific heats. Instead, CFD-FASTRAN uses the chemical composition to reference either a polynomial curve fit or spectroscopic data to determine the specific heats. The time and computer resources required to perform the simulation are therefore greatly increased. This was unfortunately necessary as there is no way to directly invoke Wilke's law for a single calorically perfect gas given the current setup of CFD-FASTRAN.

The Nitrogen simulation was also run in this manner for reasons of consistency. It is expected that there would have been very little deviation from the results presented here

had reliable values of Sutherland's constants for Argon been found.

Spatial integration was performed with Roe's FDS scheme in conjunction with a Min-Mod flux limiter. The default values were used for the entropy fix (0.2 for both linear and nonlinear waves). A Jacobi Point Iterative implicit scheme was used together with a time accurate Backward-Euler scheme for integration in time. The CFL was set to a constant value of 0.5 throughout the time integration.

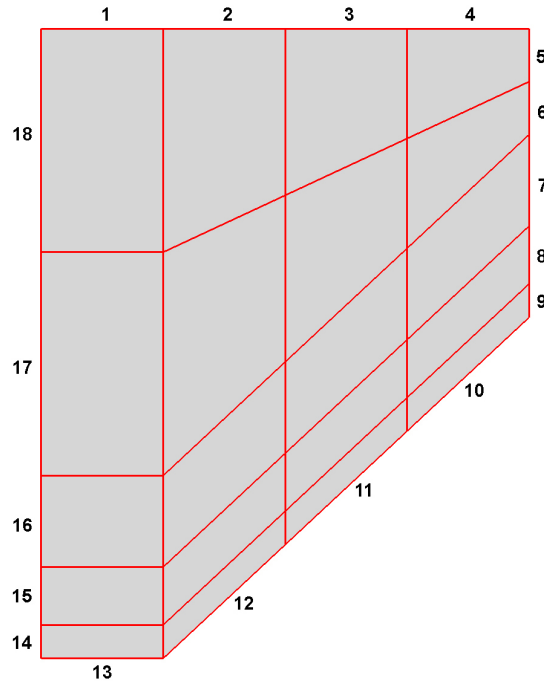


Figure 4.5: Multi-block grid for Case 2.

Table 4.6: Boundary conditions for Case 2A.

patch	BC type	BC sub type	$\mathbf{v}$ (m/s)	P(Pa)	T(K)
1 - 4	symmetry	-	calculated	calculated	calculated
5 - 9	outlet	extrapolated	calculated	calculated	calculated
10 - 12	wall	isothermal	(0,0)	calculated	293
13	symmetry	-	calculated	calculated	calculated
14 - 18	inlet	flow rate	(569.86,0)	12,884	592.25

## 4.2.6 Results and Comparisons

This validation case is unique to this thesis in that there is no experimental data to compare the numerical results to. The original call for papers invited both experimental as well as numerical results but at the time of writing, only purely numerical submissions

Table 4.7: Boundary conditions for Case 2B.

patch	BC type	BC sub type	$\mathbf{v}$ (m/s)	P(Pa)	T(K)
1 - 4	symmetry	-	calculated	calculated	calculated
5 - 9	outlet	extrapolated	calculated	calculated	calculated
10 - 12	wall	isothermal	(0,0)	calculated	293
13	symmetry	-	calculated	calculated	calculated
14 - 18	inlet	flow rate	(468.59,0)	13,661	765.32

Table 4.8: Initial conditions for Case 2A and 2B.

quantity	value
velocity (u,v) (m/s)	0
pressure (Pa)	2,000
temperature (K)	293

have been received. Due to the lack of experimental submissions, the organisers of this benchmark exercise have not yet released a paper and may not do so in the future. The correctness of the CFD-FASTRAN numerical solution is therefore judged solely on the comparison to numerical results produced by Dr Peter Jacobs using the code MB-CNS [38], [39]. It is important to note that the two models were created completely independently with no relevant communication prior to the generation of results. As this case study relies on the comparison between two simulations it is noted that there may be some physical processes which are not accounted for by either code. Although this seems unlikely, it is a possibility which only experimental results can dismiss.

The solution produced by MB-CNS used second-order interpolation in conjunction with a geometric-mean limiter for spatial integration. An adaptive flux calculator was used which switches between the equilibrium flux method and an AUSMDV flux method depending on the proximity of a given cell to the nearest shock wave. A predictor-corrector explicit time-stepping scheme was used to integrate in time. The MB-CNS solution used a perfect gas model and the viscosity was evaluated using Sutherland's law<sup>2</sup>. More comprehensive thermodynamic models were available but were not necessary for this simulation. Four solutions each for both Argon and Nitrogen were computed by Jacobs to verify grid convergence. The comparison presented in this section uses the results from the largest MB-CNS solution which contained 255,150 cells in 7 blocks. Grid convergence is also verified for the CFD-FASTRAN model but only for the case of Nitrogen and using only three different grid sizes. In the CFD-FASTRAN simulation,  $Y^+$  values were calculated

<sup>2</sup>Dr P. Jacobs had found more consistent data on the Sutherland's constant for Argon.

across the cone surface for both Nitrogen and Argon. A maximum value of around 1.7 and 1.3 is noted for the Nitrogen and Argon models respectively. Such values indicate that a good estimate of skin friction and a reasonable estimate of heat transfer should be obtained, although a maximum  $Y^+$  of 1.0 or less is desirable for heat transfer calculations.

Figures 4.6 - 4.9 show isopycnics plotted in a split-view fashion with the results of MB-CNS on the top half together with the results from CFD-FASTRAN on the bottom half. A shaded cone has been added to aid in the visualisation of these results. Note that the values output from MB-CNS are actual density values ranging from one tenth of the initial density and limited to  $0.15 \text{ kg/m}^3$ . The CFD-FASTRAN data has been normalised to the initial density with the full range of density values displayed. The colour spectrums also differ between the two results. In light of these differences, the results show good similarity. Pressure, heat flux and skin friction results along the cone surface for both MB-CNS and CFD-FASTRAN are plotted together in Figures 4.10 - 4.12 respectively. The similarity of the output is very encouraging given the “blind” nature of the validation study in combination with the use of different grids and numerical integration schemes.

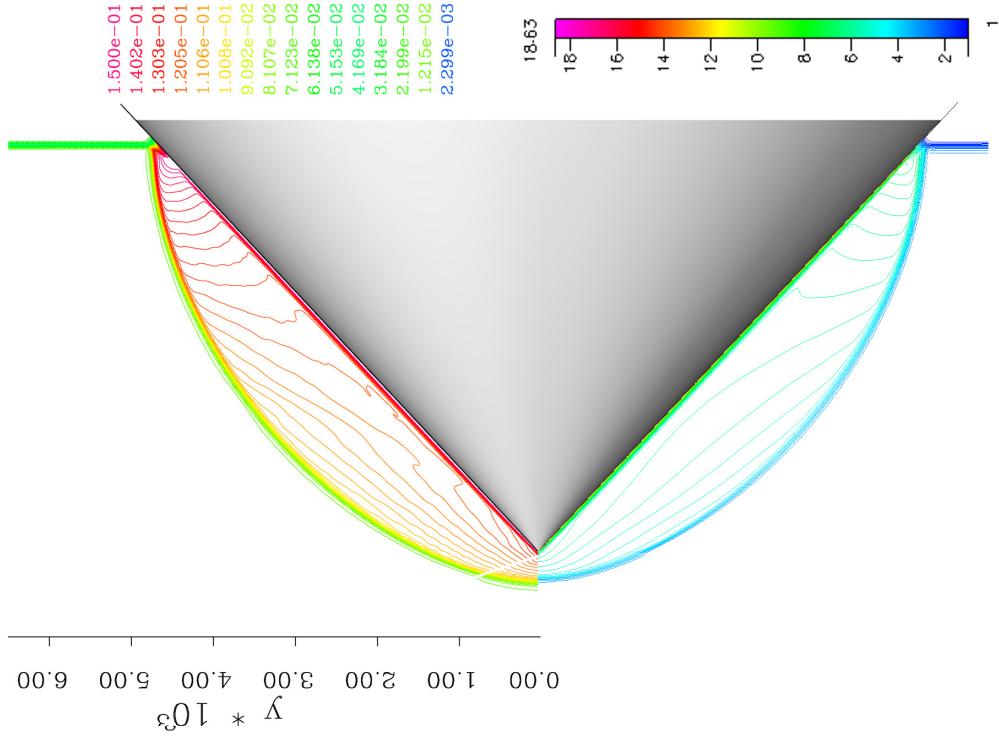
Some minor discrepancies are noted, for example, in the heat flux and skin friction plots. Figure 4.13 shows isopycnics of the flow field together with a plot of the skin friction distribution along the cone. The incident shock has progressed 20 mm past the apex of the cone in these results. The skin friction plot shows a sharp rise generated by the incident shock and a smaller secondary peak behind this rise. The secondary peak is marked “D” on the plot. There is a small difference in magnitude between the CFD-FASTRAN and MB-CNS predictions of this peak. The peaks are also slightly misaligned. Misalignment is also apparent in the the sharp rise caused by the incident shock suggesting that the two results were recorded at slightly different simulation times.

In Figure 4.13, a red line is drawn from the secondary peak on the plot to the corresponding location on the cone. It can be seen from this that the secondary peak is located at the point where the contact surface (labelled C) meets the cone. The contact surface forms at the interface between gas which is processed by the incident shock (A) and gas which is processed by the Mach stem (B). The two streams of post shock gas travel at different speeds forming shear within the contact surface. The estimation of this shear is sensitive to the numerical dissipation inherent in the grid and to the spatial integration schemes implemented in the solver. The observed discrepancy between the predicted magnitude of shear is therefore likely to be attributable to differences in grid sizing and numerical schemes between the two models. Note that confirmation that this feature is in fact a contact surface and not a shockwave is given in Figure 4.14 where there is an absence of strong pressure gradients behind the Mach stem.

```

cone43_n2.xs05mm rho TITLE = ;Mach 2.38 flow over a 43 degree cone;
x1 x2 dx -1.00e-03 5.50e-03 1.00e-03 y1 y2 dy 0.00e+00 5.50e-03 1.00e-03
v1 v2 dv 2.30e-03 1.50e-01 2.30e-03

```

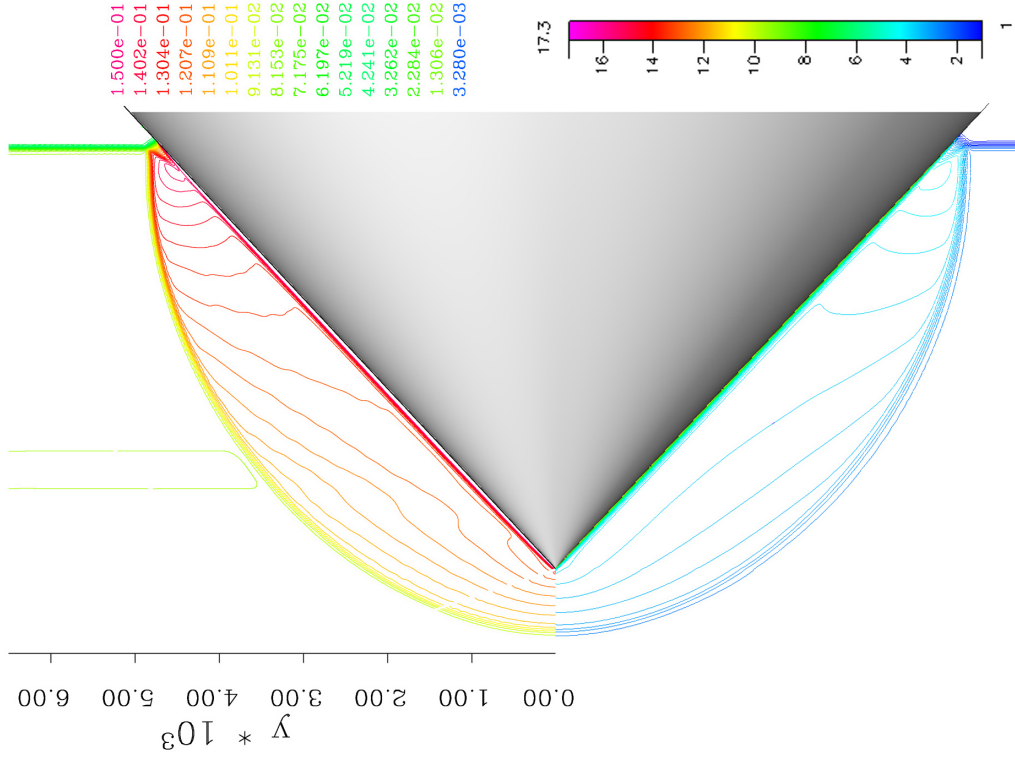


Nitrogen, Xs=5mm

```

cone43_ar.xs05mm rho TITLE = ;Mach 2.38 flow over a 43 degree cone; ;
x1 x2 dx -1.00e-03 5.50e-03 1.00e-03 y1 y2 dy 0.00e+00 5.50e-03 1.00e-03
v1 v2 dv 3.28e-03 1.50e-01 3.28e-03

```

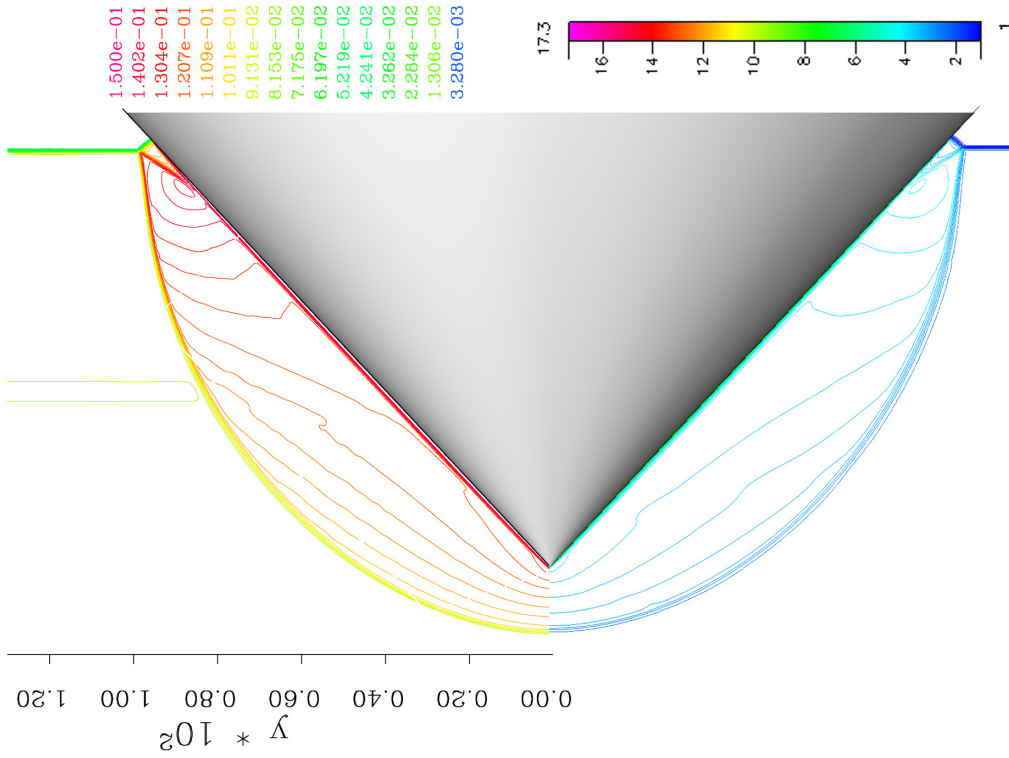


Argon, Xs=5mm

Figure 4.6: Comparison between MB-CNS laminar simulation (top half) and CFD-FASTRAN laminar simulation (bottom half), Xs = 5 mm.

```

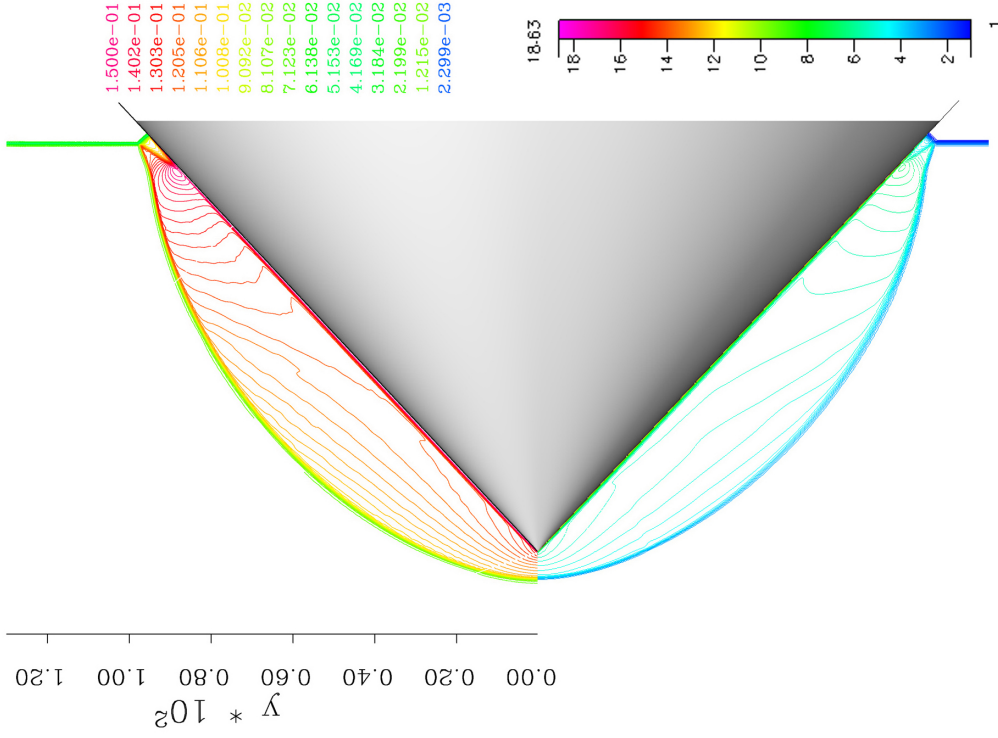
cone43_ar.xs10mm rho TITLE = ;Mach 2.38 flow over a 43 degree cone;
x1 x2 dx -2.00e-03 1.10e-02 2.00e-03 y1 y2 dy 0.00e+00 1.10e-02 2.00e-03
v1 v2 dv 3.28e-03 1.50e-01 3.28e-03
    
```



Argon, Xs=10mm

```

cone43_n2.xs10mm rho TITLE = ;Mach 2.38 flow over a 43 degree cone;
x1 x2 dx -2.00e-03 1.10e-02 2.00e-03 y1 y2 dy 0.00e+00 1.10e-02 2.00e-03
v1 v2 dv 2.30e-03 1.50e-01 2.30e-03
    
```

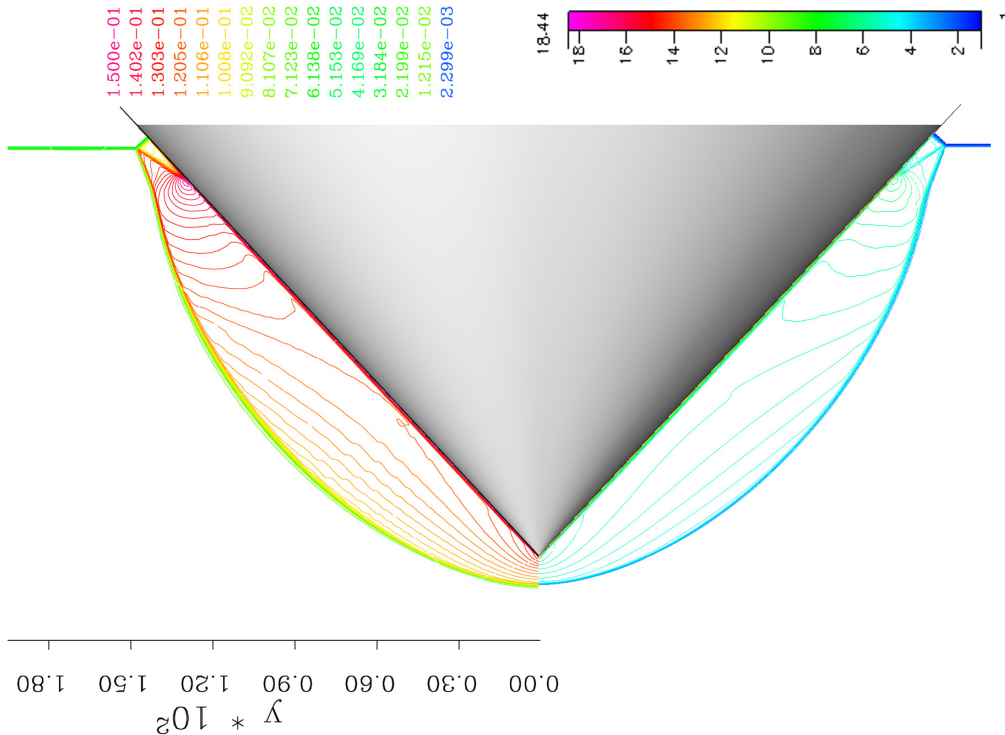


Nitrogen, Xs=10mm

Figure 4.7: Comparison between MB-CNS laminar simulation (top half) and CFD-FASTRAN laminar simulation (bottom half), Xs = 10 mm.

```

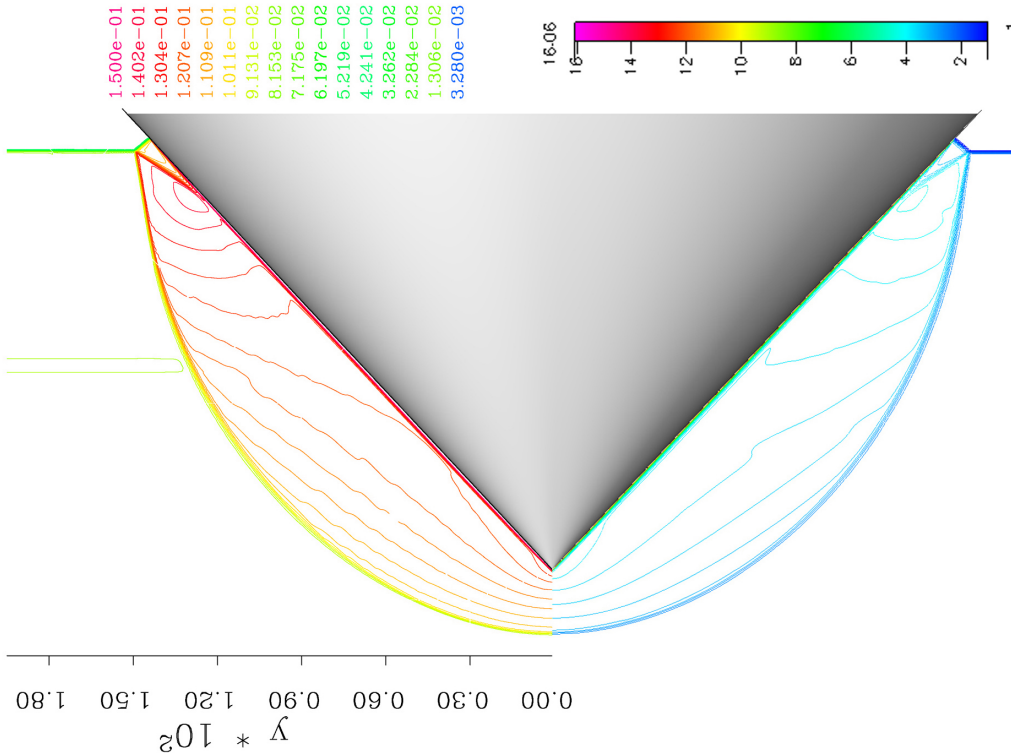
cone43_n2.xs15mm rho TITLE = ;Mach 2.38 flow over a 43 degree cone;
x1 x2 dx -3.00e-03 1.65e-02 3.00e-03 y1 y2 dy 0.00e+00 1.65e-02 3.00e-03
v1 v2 dv 2.30e-03 1.50e-01 2.30e-03
    
```



Nitrogen, Xs=15mm

```

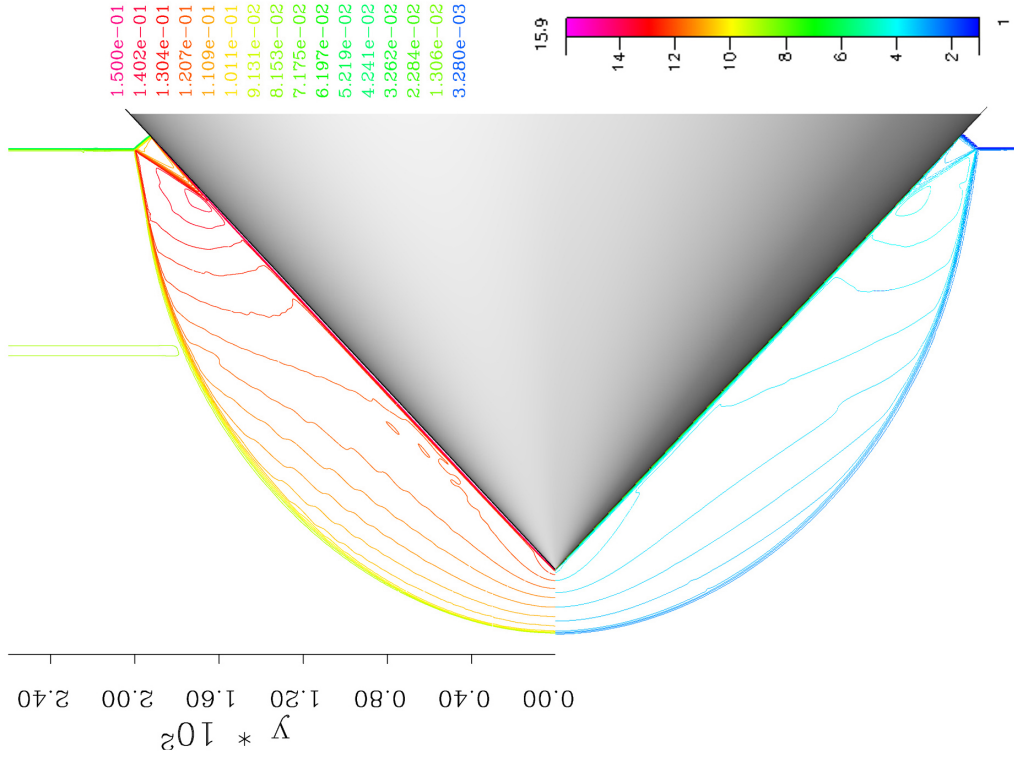
cone43_ar.xs15mm rho TITLE = ;Mach 2.38 flow over a 43 degree cone; ;
x1 x2 dx -3.00e-03 1.65e-02 3.00e-03 y1 y2 dy 0.00e+00 1.65e-02 3.00e-03
v1 v2 dv 3.28e-03 1.50e-01 3.28e-03
    
```



Argon, Xs=15mm

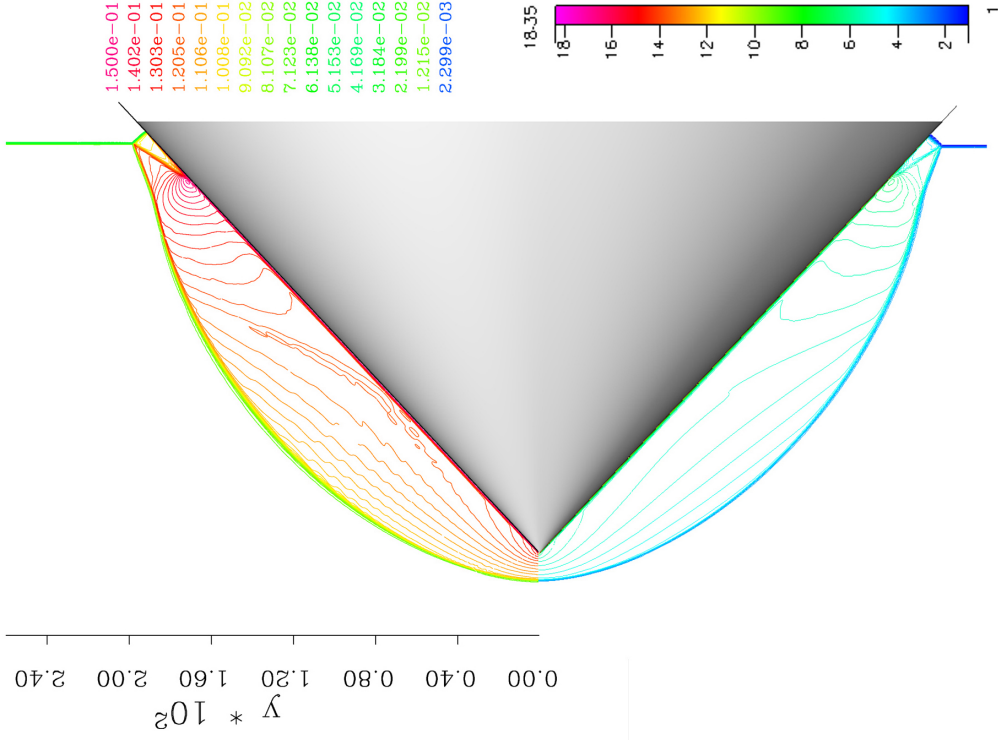
Figure 4.8: Comparison between MB-CNS laminar simulation (top half) and CFD-FASTRAN laminar simulation (bottom half), Xs = 15 mm.

```
cone43_ar.xs20mm rho TITLE = ;Mach 2.38 flow over a 43 degree cone;
x1 x2 dx -4.00e-03 2.20e-02 4.00e-03 y1 y2 dy 0.00e+00 2.20e-02 4.00e-03
v1 v2 dv 3.28e-03 1.50e-01 3.28e-03
```



Argon, Xs=20mm

```
cone43_n2.xs20mm rho TITLE = ;Mach 2.38 flow over a 43 degree coi
x1 x2 dx -4.00e-03 2.20e-02 4.00e-03 y1 y2 dy 0.00e+00 2.20e-02 4.00e-03
v1 v2 dv 2.30e-03 1.50e-01 2.30e-03
```



Nitrogen, Xs=20mm

Figure 4.9: Comparison between MB-CNS laminar simulation (top half) and CFD-FASTRAN laminar simulation (bottom half), Xs = 20 mm.

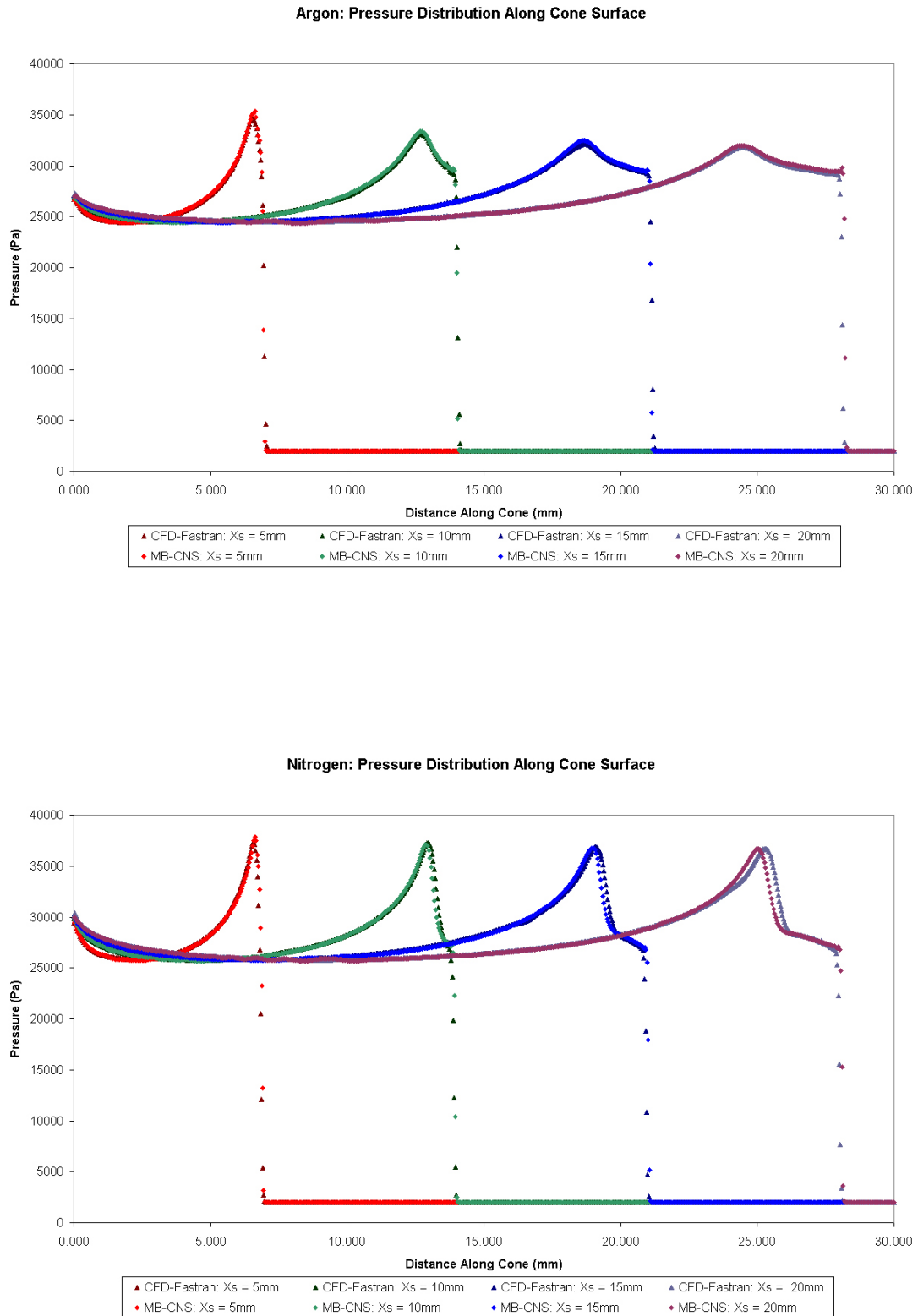


Figure 4.10: Comparison of MB-CNS and CFD-FASTRAN: pressure along the cone.



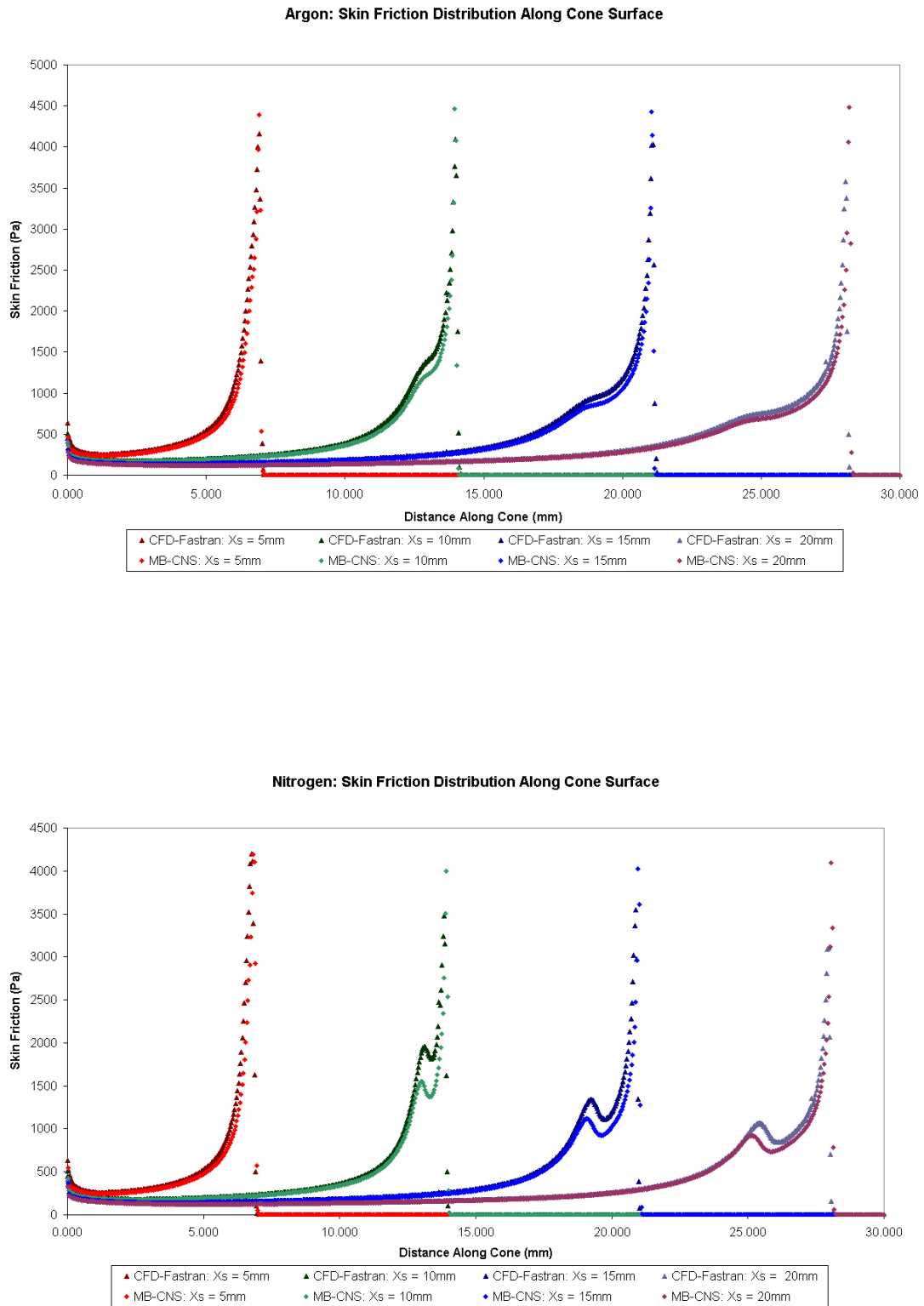


Figure 4.12: Comparison of MB-CNS and CFD-FASTRAN: skin friction along the cone.

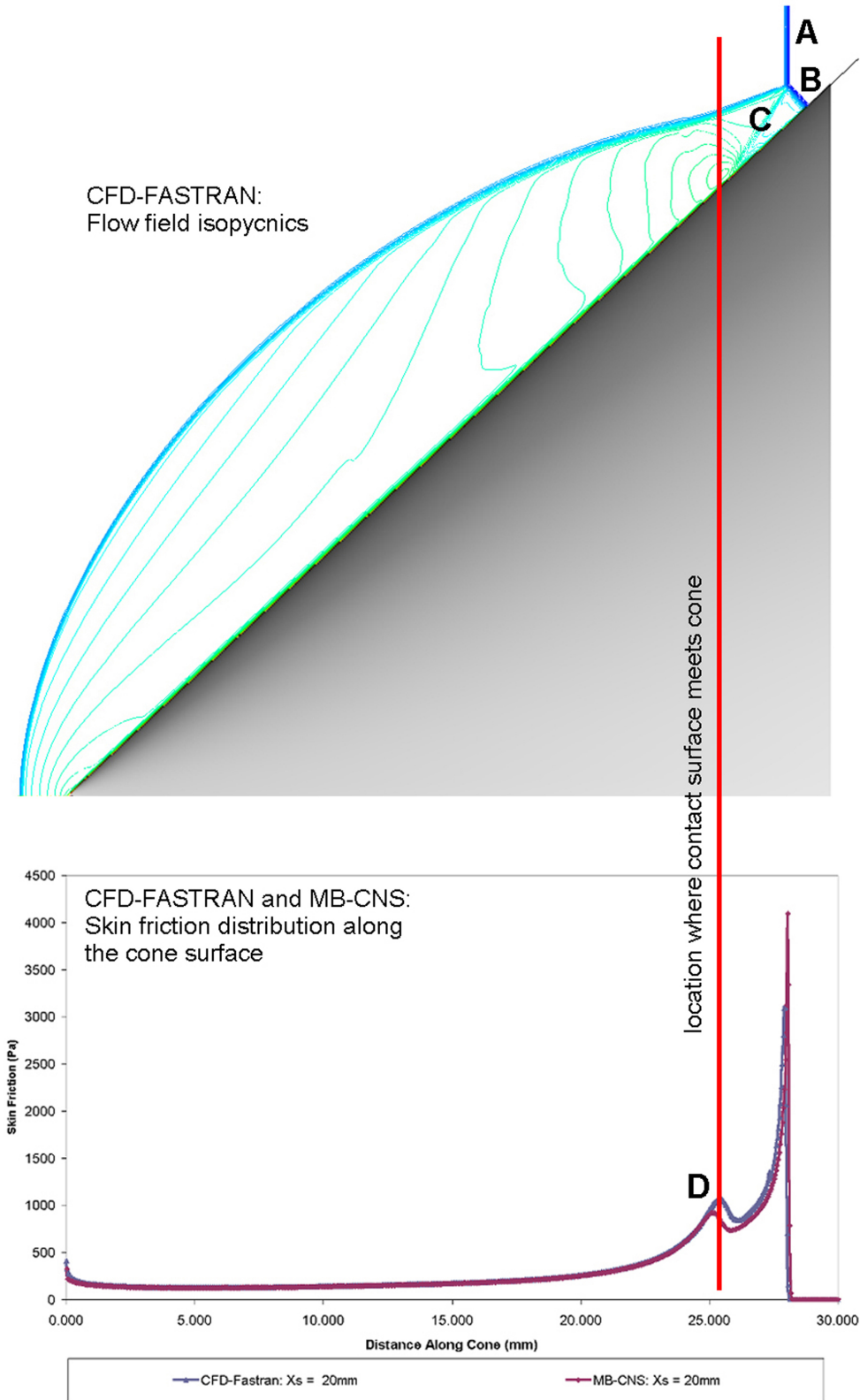


Figure 4.13: Origins of secondary peak in skin friction.

### 4.2.7 Grid Convergence

A grid convergence study has been performed on the cone model. The number of cells in each direction of every block was approximately halved and the model was run again with the same parameters as the original model. This process was repeated. The results are shown in Figure 4.14. The results suggest that there is less difference overall between the full model and half model than between the half model and quarter model. The model should then continue to converge with further refinement of the grid, although the relative change should be small.

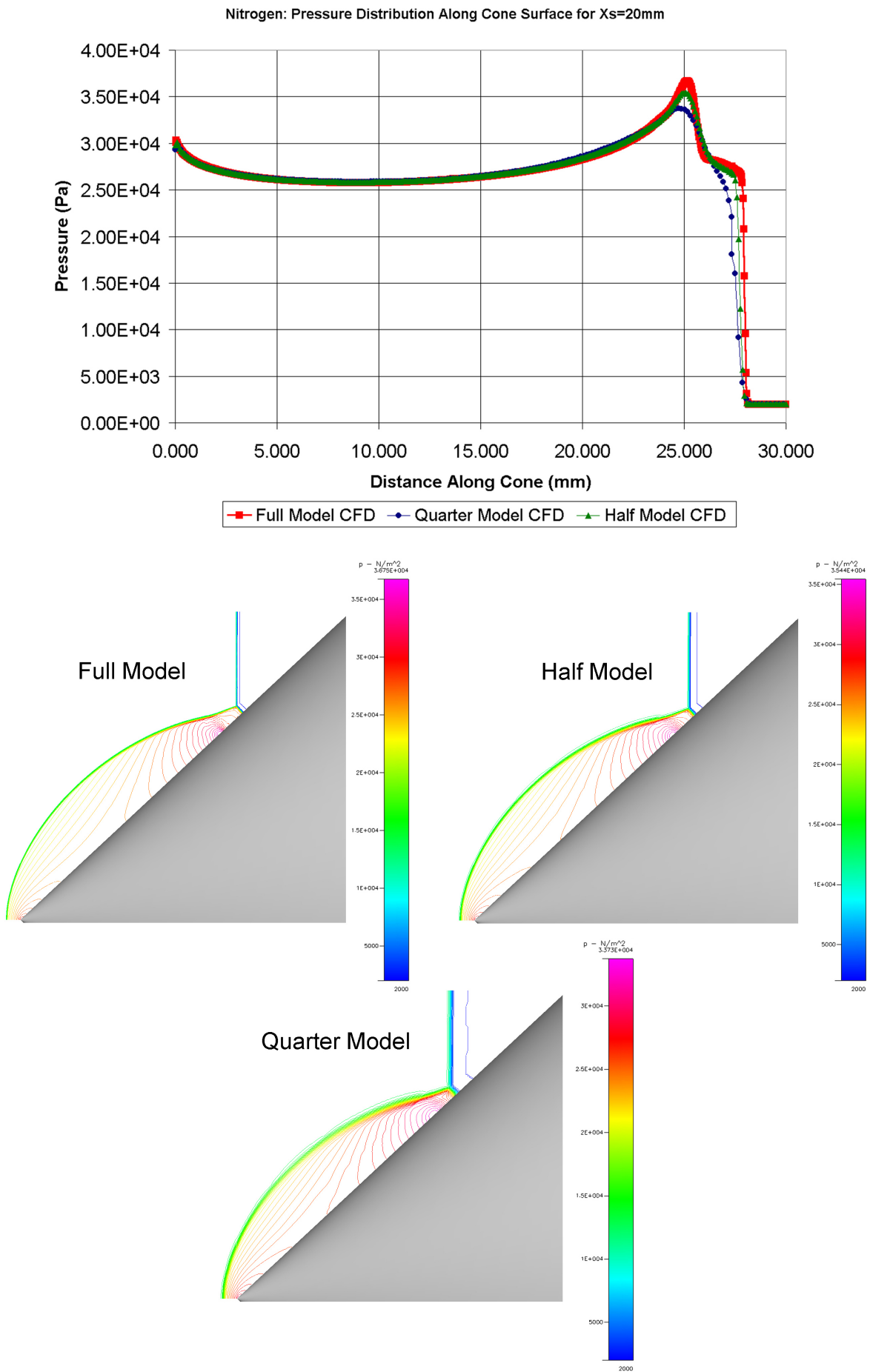
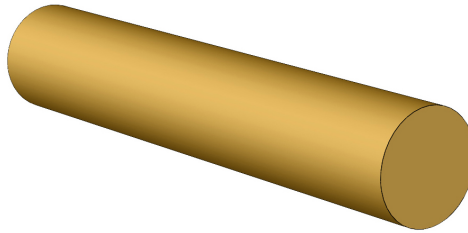


Figure 4.14: Pressure results for the full, half and quarter models.

## 4.3 Shock Diffraction Over a Cylinder



### 4.3.1 Problem Overview

The diffraction of a planar shock wave over a cylinder has been simulated numerically using CFD-FASTRAN. The cylinder diameter was 0.0127 m ( $\frac{1}{2}$ " ) and the Mach number of the incident shock was 2.82 based on the properties of the undisturbed gas. The simulation was setup to represent physical experiments performed by Bryson et al. [13] in the Harvard University 4"  $\times$  12" forty-foot shock tunnel. Bryson obtained three Schlieren images over three different experiments with approximately the same conditions. Each Schlieren image corresponds to a different point in time. The numerical results from CFD-FASTRAN were processed to obtain Schlieren like images and these were compared to the experimental images as a means of validation. The simulation was run for slightly longer than the last experimental image, which showed the shock structure in the wake as it had progressed to around seven diameters behind the cylinder. The optical system which captured the Schlieren images had a spark duration of around 200ns.

### 4.3.2 Key Features

- shock wave Mach number of 2.82
- unsteady shock-shock interaction
- unsteady shock-vortex interaction
- unsteady shock boundary layer interaction
- laminar separation
- unsteady complex Mach reflection with changing wall angle
- comparison of laminar and inviscid flow
- comparison with experimental Schlieren images
- comparison to MB-CNS code

### 4.3.3 Assumptions

The following assumptions have been made:

- planar flow
- inviscid compressible flow (Case 3A), laminar compressible flow (Case 3B)
- calorically perfect gas
- air is a single species
- adiabatic walls
- no-slip walls (Case 3B)

### 4.3.4 Grid Setup, Boundary Conditions and Initial Conditions

The layout of the multi-block grid is shown in Figure 4.15. The boundaries patches are numbered and Table 4.9 shows the boundary conditions for each patch. Table 4.10 shows the initial conditions which were applied globally to the model. Centerline symmetry was used so the domain of the simulation was limited to the upper half of the flow. The model contained 1,264,196 cells and 1,280,000 nodes in 46 blocks. The (half) cylinder was described by 1,296 cells across the upper half of the circumference with 598 on the windward side (boundary patches 23 - 24) and the remainder across the leeward side (boundary patches 21 - 22). 1,025 cells were spaced across the inlet (boundary patches 28 - 32).

Some issues have arisen in this test case in regards to the application of boundary and initial conditions. Firstly, in Bryson's experiments, two ambient pressures were reported with each pressure corresponding to a different series of shots. It was not clear from the literature which pressure was used in the experiment for which the Schlieren images were obtained for the paper. However, Bryson notes that the vortex is not clearly seen in the Series 2 experiment but is visible in the Schlieren images presented. On this basis it was chosen to use the 68.5 kPa pressure as used in the Series 1 experiment. Secondly, due to misinterpretation of the literature, this pressure was taken to be the ambient pressure when in fact it should have been the post-shock pressure to be applied to the inlet of the CFD model. The inlet conditions were instead calculated from the normal shock relations in a shock-stationary frame of reference giving a post-shock pressure of around 625 kPa. It follows that the Reynolds number (based on the cylinder diameter), which should have been around 77,900 according to the literature, was in fact 766,891. A Reynolds number of this magnitude indicates that the flow should have been fully turbulent and presumably quite different in structure. Interestingly the differences did not noticeably impact the

solution as the simulation results closely matched the experimental results regardless of the difference in pressure. Once the error was detected, a modified solution using the correct conditions was run for most of the original simulation time. No major differences were observed so the solution, which would have required a full week to complete, was terminated early<sup>3</sup>. A possible explanation for the similarity between the two simulations is that the flow was not sensitive to changes in the Reynolds number because there was no turbulence model included in the calculations. As the updated model did not deviate significantly from the original it was decided not to pursue a complete revision of this section.

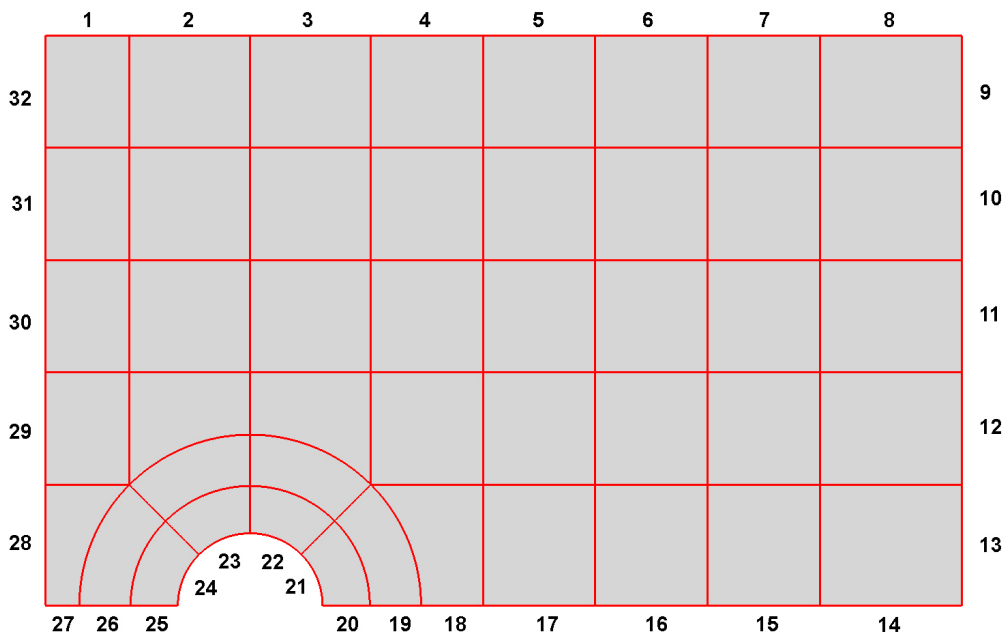


Figure 4.15: Multi-block grid for Case 3.

Table 4.9: Boundary conditions for Case 3A and 3B.

patch	BC type	BC sub type	$\mathbf{v}$ (m/s)	P(Pa)	T(K)
1 - 8	symmetry	-	calculated	calculated	calculated
9 - 13	outlet	extrapolated	calculated	calculated	calculated
14 - 20	symmetry	-	calculated	calculated	calculated
21 - 24	wall	adiabatic	†	calculated	calculated
25 - 27	symmetry	-	calculated	calculated	calculated
28 - 32	inlet	flow rate	(713.30,0)	624,586	741.98

† The flow velocity at the wall, relative to the wall, is equal to 0 in the normal direction. The tangential component is 0 for viscous flow and extrapolated for inviscid flow.

<sup>3</sup>A computer with an Intel 2.8 GHz Pentium 4 processor was used to perform the simulation.

Table 4.10: Initial conditions for Case 3A and 3B.

quantity	value
velocity (u,v) (m/s)	0
pressure (Pa)	68,552
temperature (K)	300

### 4.3.5 Solution Setup

Simulations were run for both a laminar and inviscid model. These simulations were run using the Van Leer's FVS scheme in combination with the Osher-Chakravarthy flux limiter. Van Leer's FVS scheme was chosen because preliminary runs had shown that Roe's FDS scheme in combination with the same flux limiter did not perform as well (as discussed in Section 3.4.5). Roe's FDS scheme produced a more detailed result but suffered from the formation of spurious waves emanating from discontinuities in the flow. Whilst these disturbances started small there was a tendency for them to pollute the solution with the overall solution growing worse as it progressed in time. The more dissipative nature of Van Leer's FVS scheme was an advantage to this solution. A Runge-Kutta explicit scheme with a Backwards-Euler time accuracy was used for integration in time. The explicit scheme was chosen for its speed advantage over the implicit scheme. A constant CFL of 0.5 was chosen to maintain the stability of the solution.

### 4.3.6 Results and Comparisons

Three experimental frames are provided in Bryson's paper and it was estimated, from a comparison of computation and experiment, that the frames were taken at approximately the times shown in Table 4.11. The times are referenced to the initial impact of the shock on the cylinder.

Table 4.11: Estimation of flow time for each experimental image.

frame	time
1	17.4 $\mu$ s
2	31.0 $\mu$ s
3	65.7 $\mu$ s

When reviewing the results, it should be noted that the CFD-FASTRAN solution was setup to produce an incident shock which travelled from left to right, however, the results were reflected horizontally during post-processing to match the setup of the physical experiment where the shock is shown travelling in the opposite direction. For consistency,

all results in this section are shown with the shock travelling from right to left.

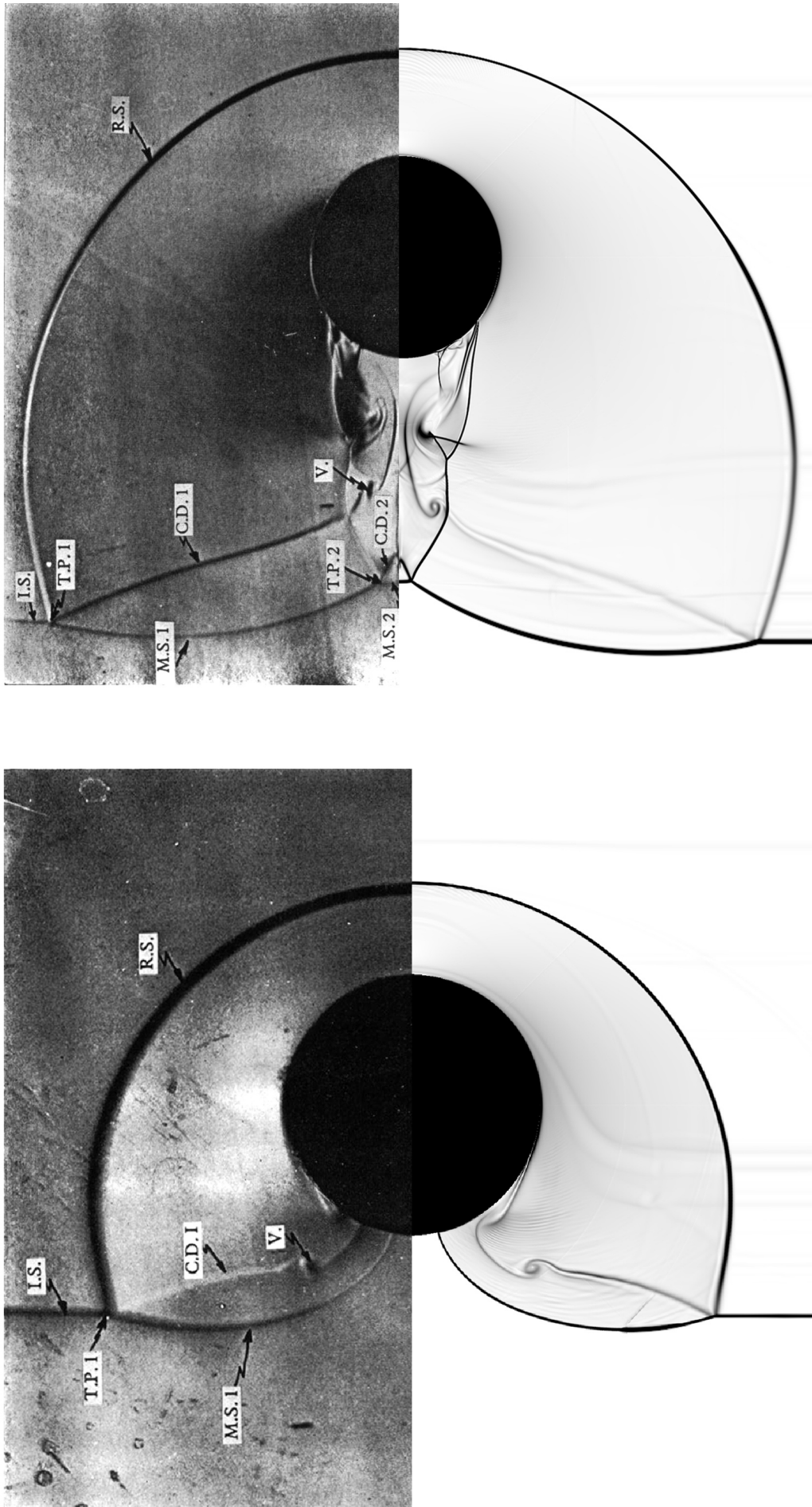
The shock diffraction begins with an incident planar shock wave (I.S.) moving towards the cylinder at Mach 2.82 as a result of the upstream conditions. When this I.S. first impacts the cylinder it begins to form a reflection. This reflected shock (R.S), or bow shock as it is also referred to, remains connected to the I.S. and quickly becomes curved as it expands out from the cylinder. As the I.S. moves further across the cylinder, the effective wall angle seen by the I.S. changes from being normal to the flow to being parallel when the shock is inline with the center of the cylinder. There is a limiting wall angle where the local flow must be turned by an angle exceeding that possible with a normal reflection. At this point, the normal reflection transforms into a Mach reflection which is characterized by a lambda shock formation.

The two forks of the lambda shock are the R.S and the newly formed Mach Shock (M.S. 1). The I.S., R.S. and M.S. 1 all meet at a triple point (T.P. 1). Between the two forks of the lambda shock is a contact discontinuity (C.D. 1) which forms at the boundary of two co-flowing gases at different densities. An instability forms in this shear discontinuity which results in the formation of a vortex (V.) that is carried downstream into the wake region. As the the upper and lower M.S.1 shocks collide at the centerline in the wake region, two normally reflected shocks are formed that define part of the bounding shock structure in the wake flow. As these shocks expand and are carried further downstream, the reflection at the centerline transforms from a normal reflection into a Mach reflection. During this process a second Mach shock (M.S. 2) is created. The I.S., R.S. and M.S. 2 all meet at a second triple point (T.P. 2). Instability is present in the T.P. 2 region resulting in the formation of a second vortex. This formation is not labelled in the experimental images from Bryson et al. .

### Comparison with Experiment

Figures 4.16 and 4.17 show numerical Schlieren images produced from the laminar CFD-FASTRAN results together with the corresponding experimental Schlieren images. These figures are shown in split-view format with the experimental images obtained from Bryson's paper [13] on the top half together with the corresponding CFD-FASTRAN images on the bottom half. The degree of similarity between the experimental and numerical images is quite good. Dominant features of the flow such as the bow shock shape and standoff distance were predicted accurately. Viscous effects such as the boundary layer separation angle were also predicted accurately despite a maximum  $Y^+$  value of 7.22. Secondary features such as vortices, triple points and contact discontinuities resulting from shock-shock interaction appear to be formed correctly and tracked accurately throughout the unsteady simulation.

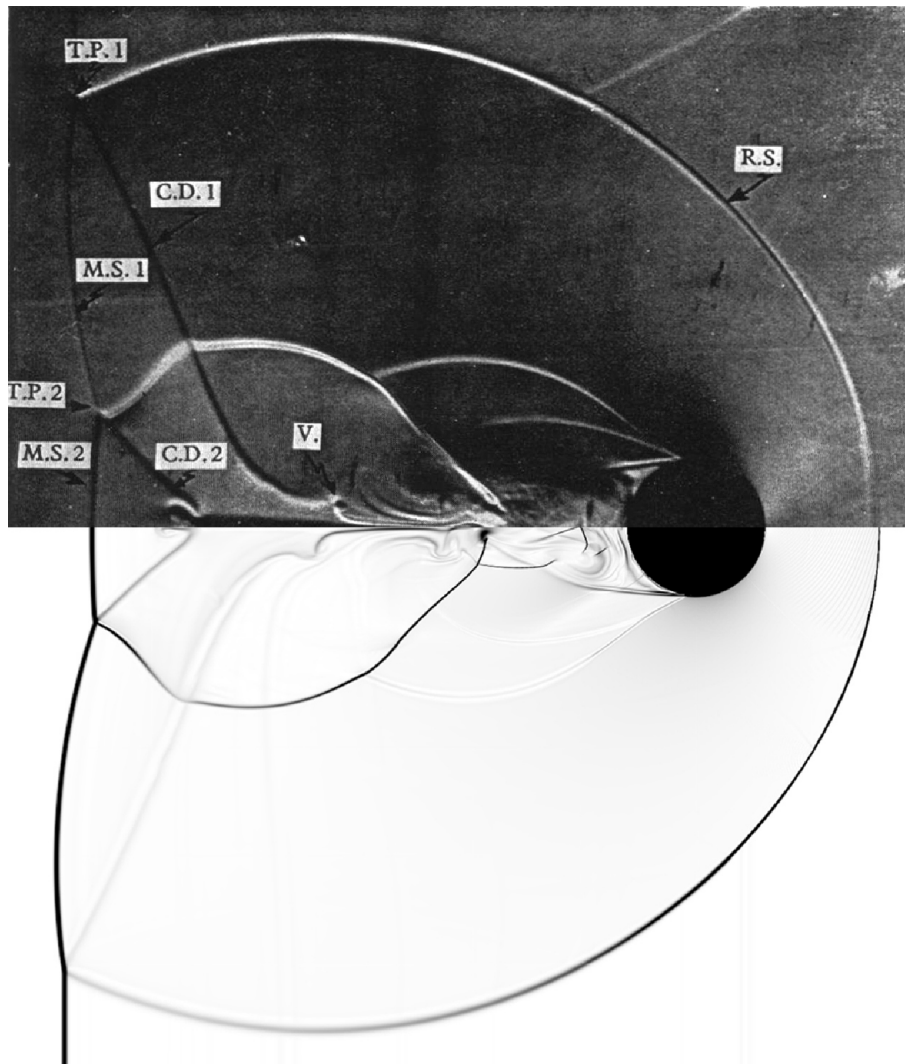
The strongest correlation occurs in frame 1 with slight differences appearing in frame 2 and by frame 3 these differences have grown larger. In frame 3 the experimental results are asymmetric suggesting that there may be some non-ideal behaviour in the experimental setup. This behaviour may include inconsistencies in the freestream flow resulting from uneven rupture of the shock tunnel diaphragm or possibly complications stemming from the connection of the cylinder ends to the test section walls.



Frame 1

Frame 2

Figure 4.16: Comparison between experiment (top half) and CFD-FASTRAN laminar simulation (bottom half), frame 1 and frame 2.



**Frame 3**

Figure 4.17: Comparison between experiment (top half) and CFD-FASTRAN laminar simulation (bottom half), frame 3.

### Comparison with MB-CNS Code

MB-CNS is a numerical code developed primarily by Dr Peter Jacobs [38], [39] for the solution of planar and axisymmetric compressible flows on a multiblock grid. A laminar simulation was undertaken in MB-CNS by Goozee [41] matching the experimental conditions of Bryson. A split-view comparison is shown in Figure 4.18 with Schlieren images generated from the MB-CNS simulation on the top half together with Schlieren images generated from the CFD-FASTRAN simulation on the bottom half. Good agreement is observed between the two results but there a number of minor discrepancies in the wake region of both frames. A third frame was not provided by Goozee as his simulation did not run for long enough to obtain that result. Note the simulation domain of the MB-CNS model was smaller than the CFD-FASTRAN model and the grid resolution was not as fine.

In Frame 1 of Goozee's solution, separation of the flow is marked with a discontinuity emanating out from the cylinder. This bears more similarity to the inviscid CFD-FASTRAN result shown in the bottom half of Frame 1 in Figure 4.21, than the laminar CFD-FASTRAN result to which MB-CNS is compared. By Frame 2, the separation detail is more closely aligned to the laminar CFD-FASTRAN result, as would be expected. This discrepancy might be due to less definition of the boundary layer in Goozee's model which would effect the results during the formation of separated flow but give a more accurate result once the separated flow is established.

Some discrepancies are present which may be attributable to the difference in maximum gradients chosen for the MB-CNS Schlieren images compared to the CFD-FASTRAN Schlieren images. The value chosen for the maximum gradient has an impact on which flow discontinuities are discernable, as discussed in Section 3.5.2. In Frame 2, expansion of flow across the top of the cylinder is visible in the CFD-FASTRAN Schlieren as light grey shading in that area. This is much fainter in the MB-CNS model. Also, the contact discontinuity C.D. 1 and the vortex V. are more easily discernable in the CFD-FASTRAN Schlieren. Finally, there is a triangle of three discontinuities present half way through the wake in the CFD-FASTRAN Schlieren. In the MB-CNS Schlieren, only two of these discontinuities appear to be visible. Upon careful inspection of the MB-CNS Schlieren the third appears to be present, though the resolution of the image makes this difficult to confirm. It appears that the third discontinuity has moved further away from the cylinder and no longer overlaps with the other discontinuities to form a triangle. This indicates that the MB-CNS Schlieren was taken a small while after the CFD-FASTRAN Schlieren as the formation of the triangle shape is only temporary, occurring as the discontinuities pass through each other. This is confirmed by an animation of the CFD-FASTRAN solution, provided on compact disc in Appendix B.

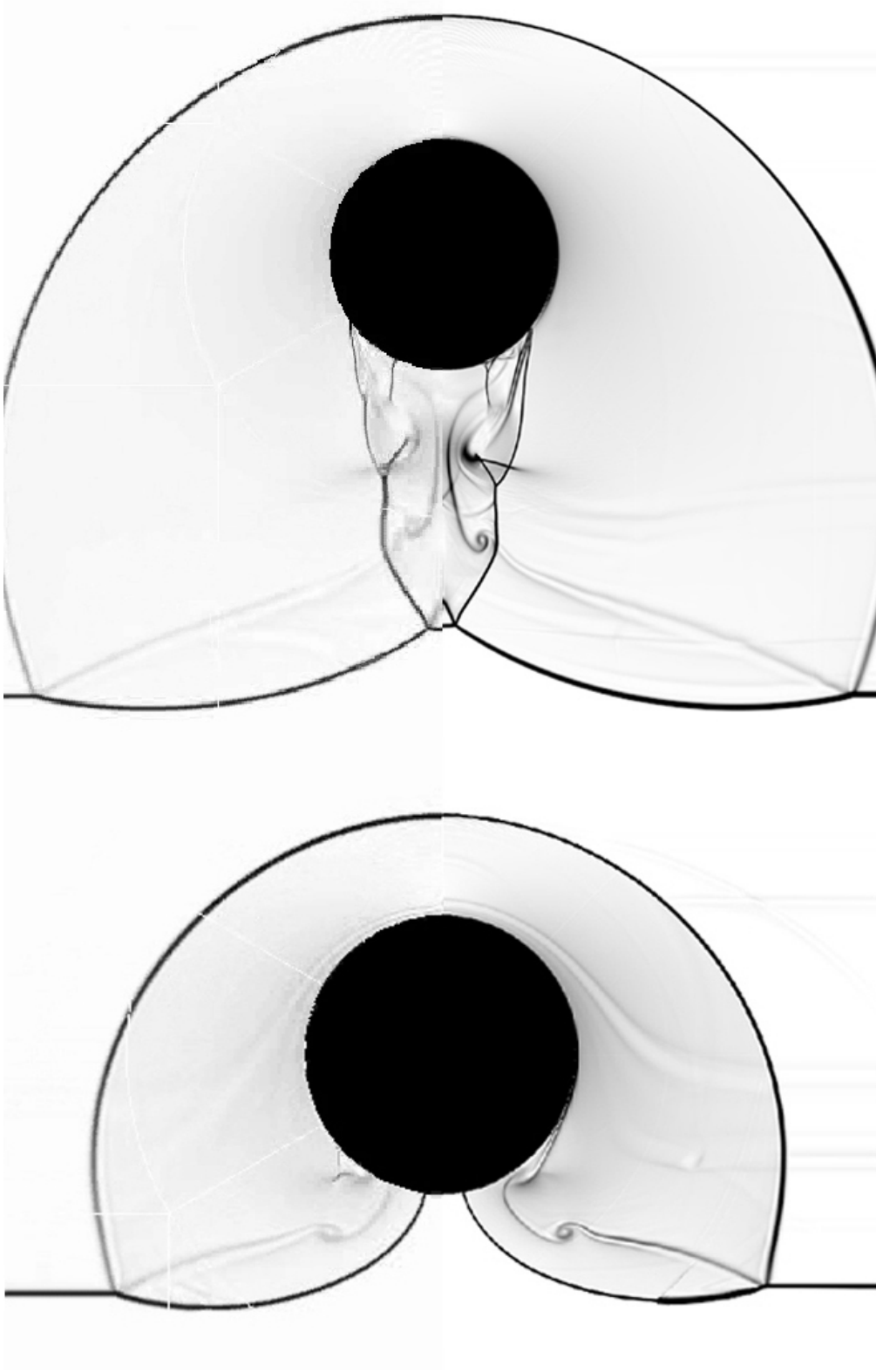
**Frame 2****Frame 1**

Figure 4.18: Comparison between MB-CNS laminar simulation (top half) and CFD-FASTRAN laminar simulation (bottom half), frames 1 and 2.

### Comparison of Laminar and Inviscid Models

In addition to the laminar CFD-FASTRAN simulation, a model which ignored viscous effects was also solved on the same grid. A comparison between the two solutions is discussed in this section. Figure 4.19 shows the flow field coloured by the local flow speed together with the streamlines of flow. The image is split-view with the laminar solution in the top half and the inviscid solution in the bottom half. Perhaps the most striking difference between the laminar and inviscid simulations is the separation angle. In the inviscid case the separation occurs much further back than is predicted by both the laminar simulation and the experiment. Note that separation in this context refers to the point along the cylinder wall at which the flow reverses direction and the freestream separates.

Figure 4.21 shows a split-view comparison of numerical Schlieren images. Results from the laminar CFD-FASTRAN simulation are shown on top with the inviscid CFD-FASTRAN results shown on the bottom. Frame 2 reveals a difference in the behaviour of the Mach shock at the cylinder wall as the angle between the shock and the cylinder wall differs between the two simulations. In Frame 3 the separation points have stabilised and the differences between the two solutions are more pronounced. It is interesting to note that a vortex formation is present in both the laminar and the inviscid model indicating that the vortex is not the result of shock boundary layer interaction, as suggested by Bryson, but instead the result of a Kelvin-Helmholtz type instability in the contact discontinuity.

Figure 4.20 shows a plot of flow speed along radial lines. The lines are projected from the center of the cylinder, with the line beginning at the cylinder wall and ending a distance of 1.5 mm into the flow. Flow speeds from both the inviscid and the laminar models are shown in the plot, extracted from lines at  $45^\circ$  and  $90^\circ$  to the freestream flow. A distinct difference is noticeable between the speed profiles of the laminar model versus those of the inviscid model. The inviscid model predicts a maximum flow speed at the wall whereas the laminar model has a zero velocity enforced at the wall (the no-slip boundary condition). Close to the wall, the two predictions branch away from each other due to the boundary layer which occurs only in the laminar model. Many points can be seen along the boundary layer region of the curve giving it a smooth profile but it should be noted that the actual resolution of the grid in this region was higher than is shown in the plot. The points in the plot are spaced evenly across the lines at approximately  $21\mu$  intervals. This was the spacing at which the data from the CFD models were sampled at. Close to the cylinder wall however, the cell edge length was as small as  $2.34\mu$  suggesting that the boundary layer has been resolved with more than adequate resolution.

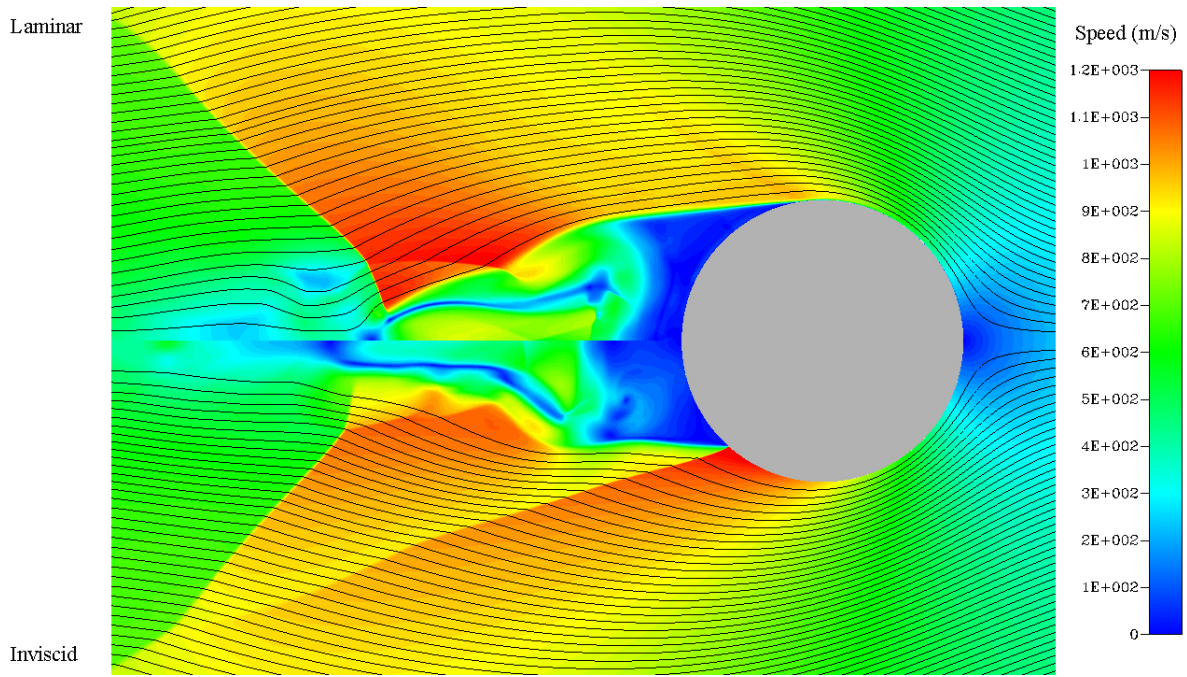


Figure 4.19: Streamlines and flooded contours of speed for laminar and inviscid solution at  $80 \mu s$  ( $68 \mu s$  after initial impact of shock on cylinder).

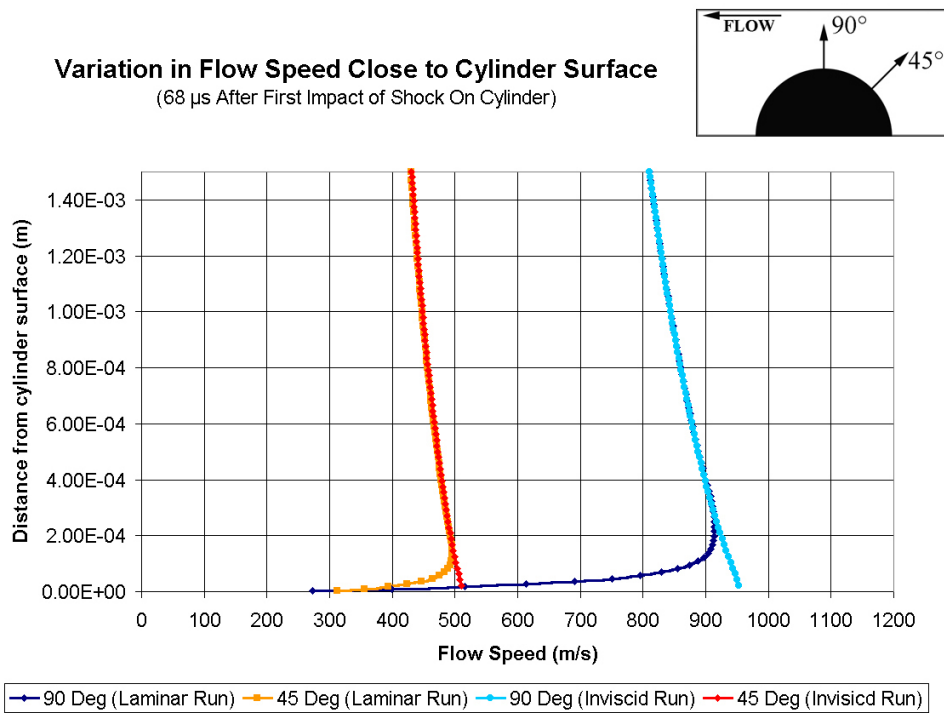


Figure 4.20: Plots of flow speed on radial lines at  $80 \mu s$  ( $68 \mu s$  after initial impact of shock on cylinder).

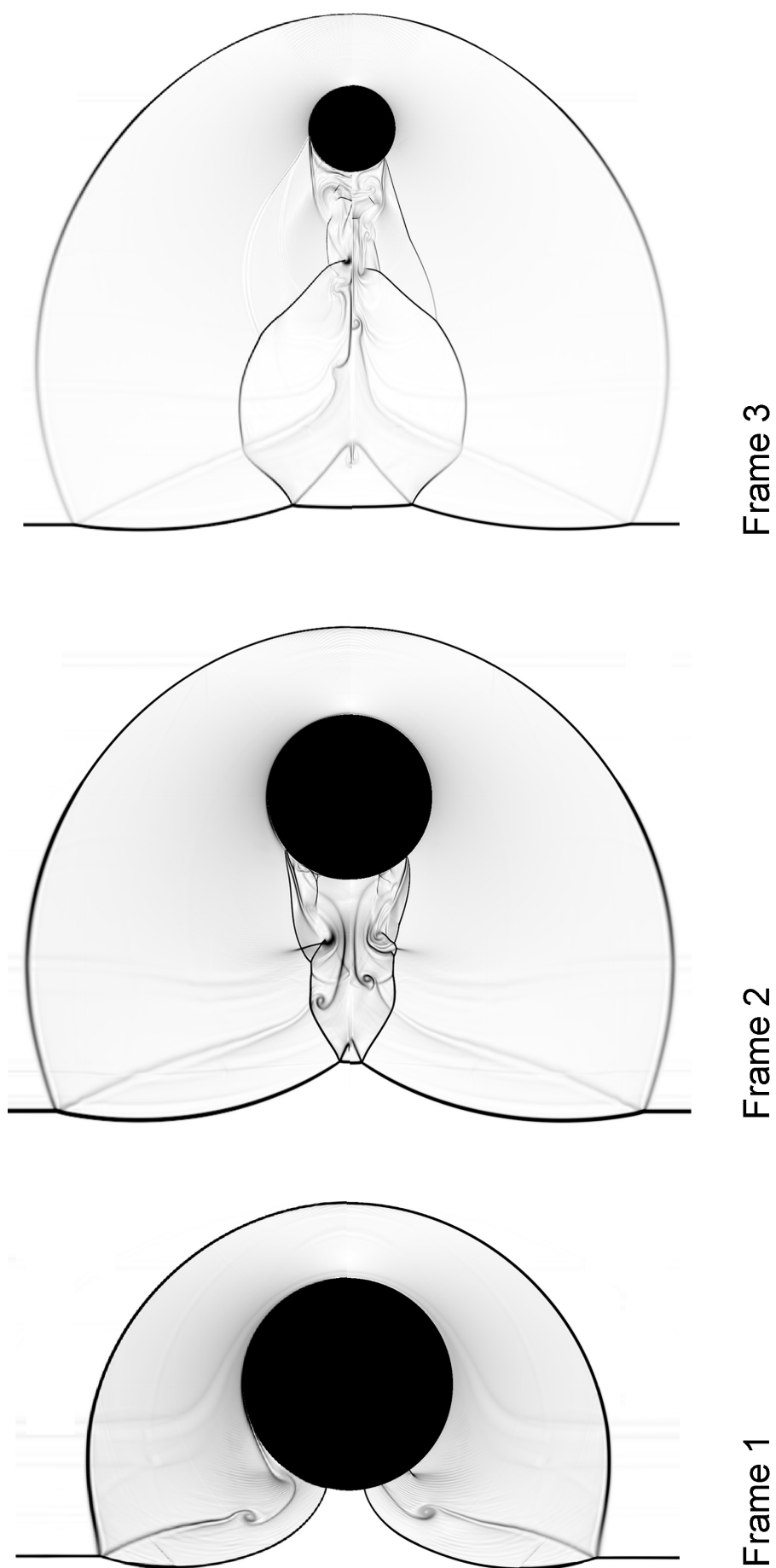
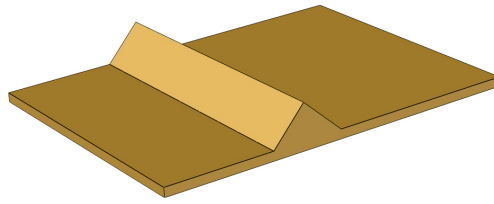


Figure 4.21: Laminar CFD-FASTRAN simulation (top half) and inviscid CFD-FASTRAN simulation (bottom half), frames 1, 2 and 3.

## 4.4 Shock Diffraction Over a Half Diamond



### 4.4.1 Problem Overview

In this study, the diffraction of a planar shock wave across a half diamond shape has been simulated using CFD-FASTRAN. The Mach number of the incident shock was 2.85 based on the properties of the undisturbed gas. Both a laminar and inviscid solution have been obtained. The model was setup to match the experimental work of Glass et al. [26] as closely as possible. The results are compared to experimental and numerical work from Glass as well as a numerical simulation from Quirk [67]. The experimental work was performed in a hypervelocity shock tube located at the University of Toronto Institute for Aerospace Studies (UTIAS). This facility has a 100 mm x 180 mm test section. Infinite-fringe interferograms have been recorded during the experiment and are the main source for validating the numerical results presented here.

### 4.4.2 Key Features

- shock wave Mach number of 2.85
- unsteady shock-shock interaction
- unsteady shock-vortex interaction
- unsteady shock boundary layer interaction
- laminar separation
- complex Mach reflection
- comparison with experimental interferograms
- comparison of laminar and inviscid flow
- comparison to an inviscid numerical solution from Quirk

### 4.4.3 Assumptions

The following assumptions have been made:

- planar flow
- inviscid compressible flow (Case 4A), laminar compressible flow (Case 4B)
- calorically perfect gas
- air is a single species
- isothermal walls
- no-slip walls (Case 4B)

### 4.4.4 Grid Setup, Boundary Conditions and Initial Conditions

Unfortunately, many of the required details of the experimental setup are not documented by either Glass or Quirk so some estimations had to be made for the initial conditions and model sizing. In the paper by Glass et al. the top left interferogram in Figure 1 contains some text describing the initial conditions. This is the only interferogram presented in the paper which contains such information but the information relates to an experiment on the diffraction of a shock wave over a semi-cylinder. As the experiments were similar in nature and performed in the same facility it has been assumed that the initial conditions were the same. As with Cases 1 - 3, the inlet conditions have been calculated from the initial conditions and the Mach number of the incident shockwave. The model size was chosen to have the same characteristic dimension as the cylinder in Case 3<sup>4</sup> because the two shock tube facilities have similar vertical dimensions (100 mm high for the UTIAS facility versus 4" high for the Harvard facility).

The layout of the multi block grid is shown in Figure 4.22. The boundary patches are numbered and Table 4.12 shows the boundary conditions for each patch. Table 4.13 shows the initial conditions which were applied globally to the model. This study contained the largest grid run in this thesis with 2,464,000 cells and 2,488,239 nodes in 59 blocks. The half diamond (boundary patches 21 - 26) was divided up into 1,500 cells with an even amount on both the windward and leeward faces. The cells were clustered towards the apex for the purposes of capturing more flow detail in that region.

---

<sup>4</sup>Due to an error in scaling the half diamond in the simulation was slightly more than half an inch in height.

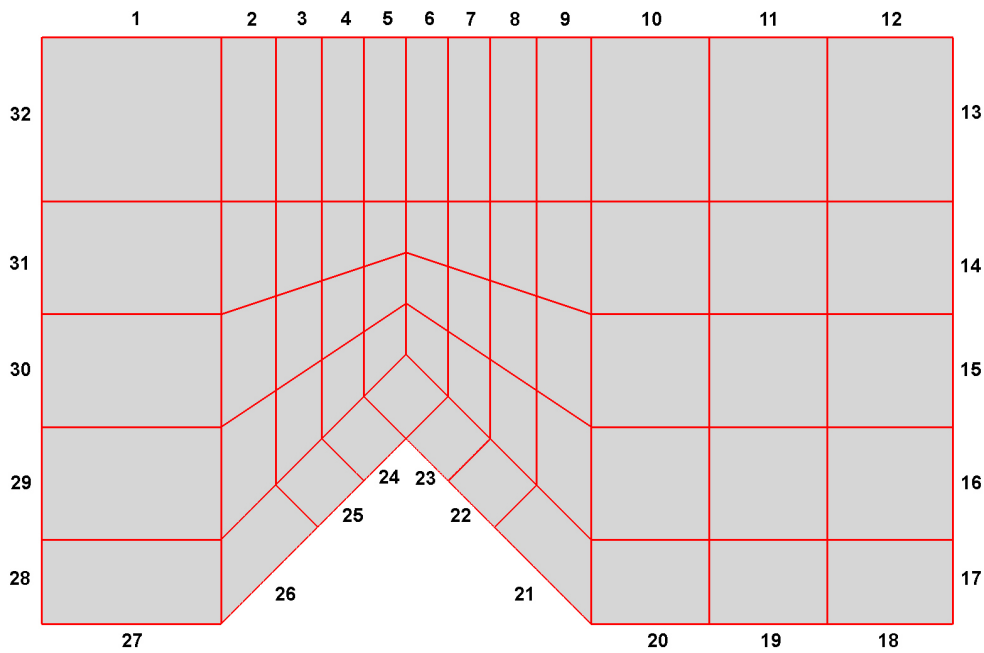


Figure 4.22: Multi-block grid for Case 4.

Table 4.12: Boundary conditions for Case 4A and 4B.

patch	BC type	BC sub type	$\mathbf{v}$ (m/s)	P(Pa)	T(K)
1 - 12	symmetry	-	calculated	calculated	calculated
13 - 17	outlet	extrapolated	calculated	calculated	calculated
18 - 27	wall	isothermal	†	calculated	295.7
28 - 32	inlet	flow rate	(717.86,0)	68,705	741.24

† The flow velocity at the wall, relative to the wall, is equal to 0 in the normal direction. The tangential component is 0 for viscous flow and extrapolated for inviscid flow.

Table 4.13: Initial conditions for Case 4A and 4B.

quantity	value
velocity (u,v) (m/s)	0
pressure (Pa)	7,380
temperature (K)	295.7

#### 4.4.5 Solution Setup

A Van Leer's FVS scheme was used together with an Osher-Chakravarty flux limiter for spatial integration whilst a Jacobi Point Iterative implicit scheme with a Backwards-Euler time accuracy was used for integration in time. As with Case 3, Van Leer's scheme was chosen for stability. A constant CFL of 0.5 was used throughout the solution.

### 4.4.6 Results and Comparisons

Results from Glass's experiment, CFD-FASTRAN and other numerical results are shown in Figures 4.23 - 4.28.

Figure 4.23 shows isopycnics plotted at various stages of the shock wave diffraction. The diffraction process begins with the incident shock moving from left to right through the gas inducing motion of the gas behind it. This moving gas forms a boundary layer on the floor of the test section.

At 4,000 iterations the incident shock has impacted upon the half-diamond obstacle and formed a complex reflection pattern. This pattern includes a fork in the incident shock and a reflected shock (bow shock) which joins the incident shock at the point where it branches into a fork. The left branch of the fork is a contact discontinuity whilst the right branch is a shock which for reference purposes will be called the Mach shock. The reflected shock is kinked at the top and bottom. This pattern of reflection is similar in some respects to the results from the  $43^\circ$  cone presented in Section 4.2 (see the isopycnics for the Nitrogen model in Figure 4.9). The half diamond model differs from the cone as there is a kink in the reflected shock where it meets the test section floor.

At 6,000 iterations the similarity with the cone ends as the incident shock has now progressed over half way across the obstacle and a complex expansion centered about the apex has begun. A prominent feature of this expansion is a normal shock located mid-stream in the wake region. This feature can be positively identified as a shock as it also appears in the isobar plots of Figure 4.29. The shock is due to the gas which has accelerated as it expanded over the apex meeting the slower flow behind the incident shock. The formation is sometimes referred to as an "upstream facing shock".

At 8,000 iterations, the Mach shock begins to lag behind the incident shock as it travels down the leeward side of the obstacle. A triangular region with three triple points can clearly be seen in the oncoming flow. This region is bounded by part of the reflected shock, the connecting shock and the contact discontinuity. At the bottom triple point an additional contact discontinuity which has formed in the wake is also connected. This second contact discontinuity is perturbed by the upward motion of the triangular region. The Mach reflection continues to move down the leeward side of the obstacle until reflecting against the floor at around 13,000 iterations. At this point the triangular region has moved upwards and the perturbed second contact surface has begun to roll up into a sheet of vortices. The shock boundary layer interaction on the windward side of the model has grown progressively larger and more complex.

At 14,000 iterations, the maximum  $Y^+$  value recorded was 10.7. The region of flow containing the maximum value was located on the test section floor, upstream of the incident shock. An increase in  $Y^+$  values in this region was due to a boundary layer forming. This boundary layer had not yet reached its fully developed thickness and therefore could not be resolved to the same degree as one situated in a region of established flow.

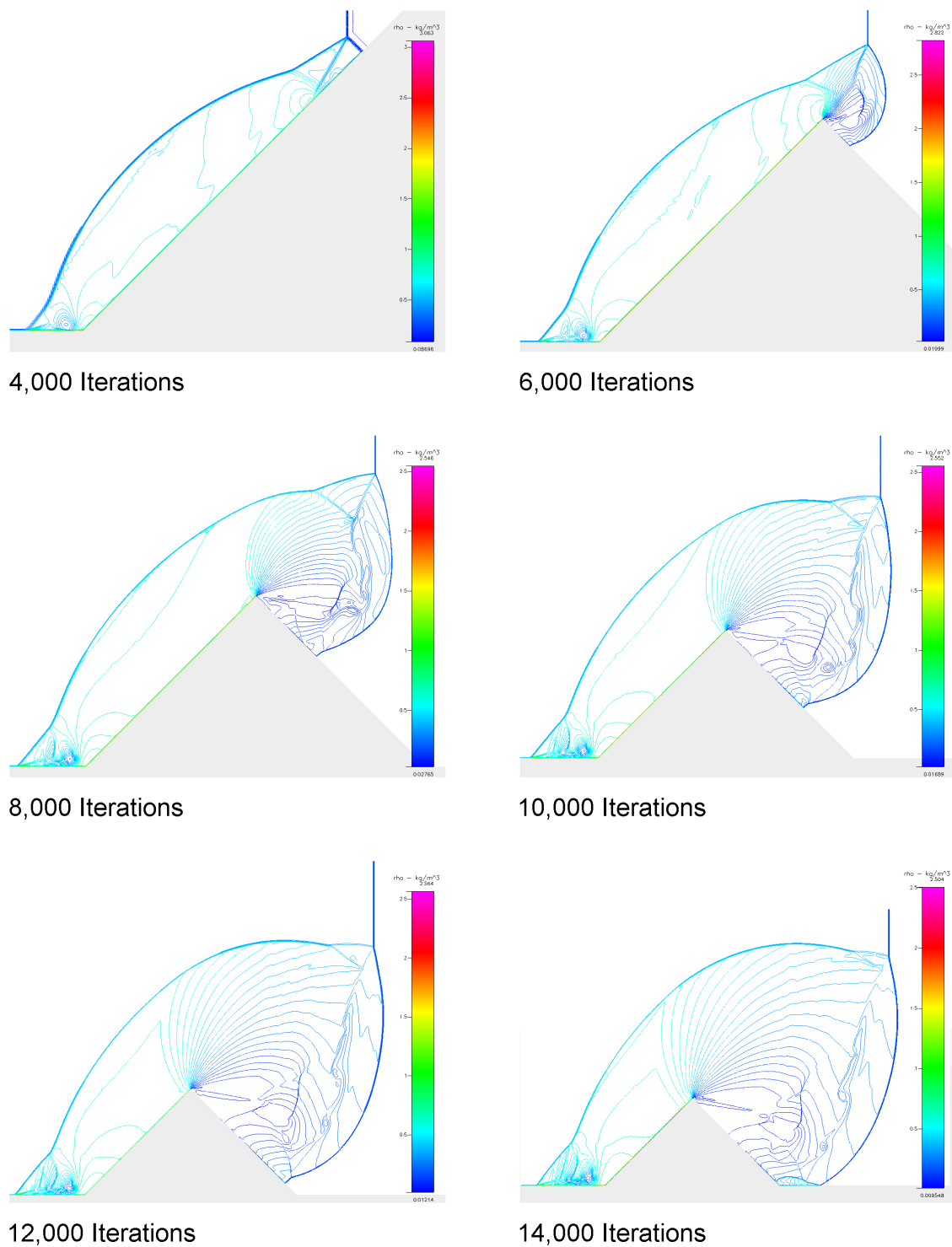


Figure 4.23: Shock diffraction over a half diamond: isopycnics computed at different stages of diffraction.

### Comparison with Experiment

Figure 4.24 shows an experimental interferogram from Glass in the top half of the figure together with an interferogram generated from the CFD-FASTRAN laminar simulation on the bottom half. The main features of the diffracted shock structure seen in the experimental interferogram can also be seen in the CFD-FASTRAN result. Viscous effects, such as the interaction between the reflected shock and the boundary layer formed on the test section floor, are also reproduced with reasonable accuracy. Validation of the finer scale detail in the wake is limited though, given the quality of the experimental image.

### Comparison to Other Codes

Both Glass et al. [26] and Quirk [67] have presented results from numerical simulations of the half diamond shock diffraction experiment. Glass et al. have presented numerical results alongside their experimental results whilst Quirk performed the simulation as a case study for his Adaptive Riemann Solver. Both of the simulations solved the Euler equations and so viscous effects were not modelled. Figure 4.25 shows a split-view style comparison of the results from both Glass and Quirk on the top half compared to the equivalent results from the inviscid CFD-FASTRAN simulation on the bottom half. The results are in good agreement although the results from Glass are relatively coarse as they were published in 1989. Quirk's results were published in 1992 and appear to be much better resolved than those of Glass.

### Comparison of Laminar and Inviscid Models

In comparison to the inviscid CFD-FASTRAN results, the laminar results show a fundamental difference in the formation of the reflected shock. At first it was thought that this result might be attributable to a numerical error but as Figure 4.24 shows, the same kink is present in the experimental interferogram. A comparison of laminar and inviscid results is given in Figures 4.26 and 4.27. The absence of distortion in the lower portion of the reflected shock wave for the inviscid model reinforces the notion that the kink is indeed a viscous effect and is not of a purely numerical origin. Glass also notes the absence of the kink when comparing his simulation to the experiment: "Both figures illustrate that agreement between experiment and computation is excellent, except where viscous effects dominate the former (i.e., boundary layer lambda shock configurations)". Figure 4.28 shows a detailed view from one timestep in the shock diffraction process. The image comprises of a Schlieren image with superimposed velocity vectors shown in red. One vector for every cell vertically and one vector for every fifth cell horizontally is shown. The vectors in the bottom left corner of the figure confirm the presence of a boundary layer whilst the remaining portion of the figure shows the effect of that boundary layer interacting with the reflected shock.

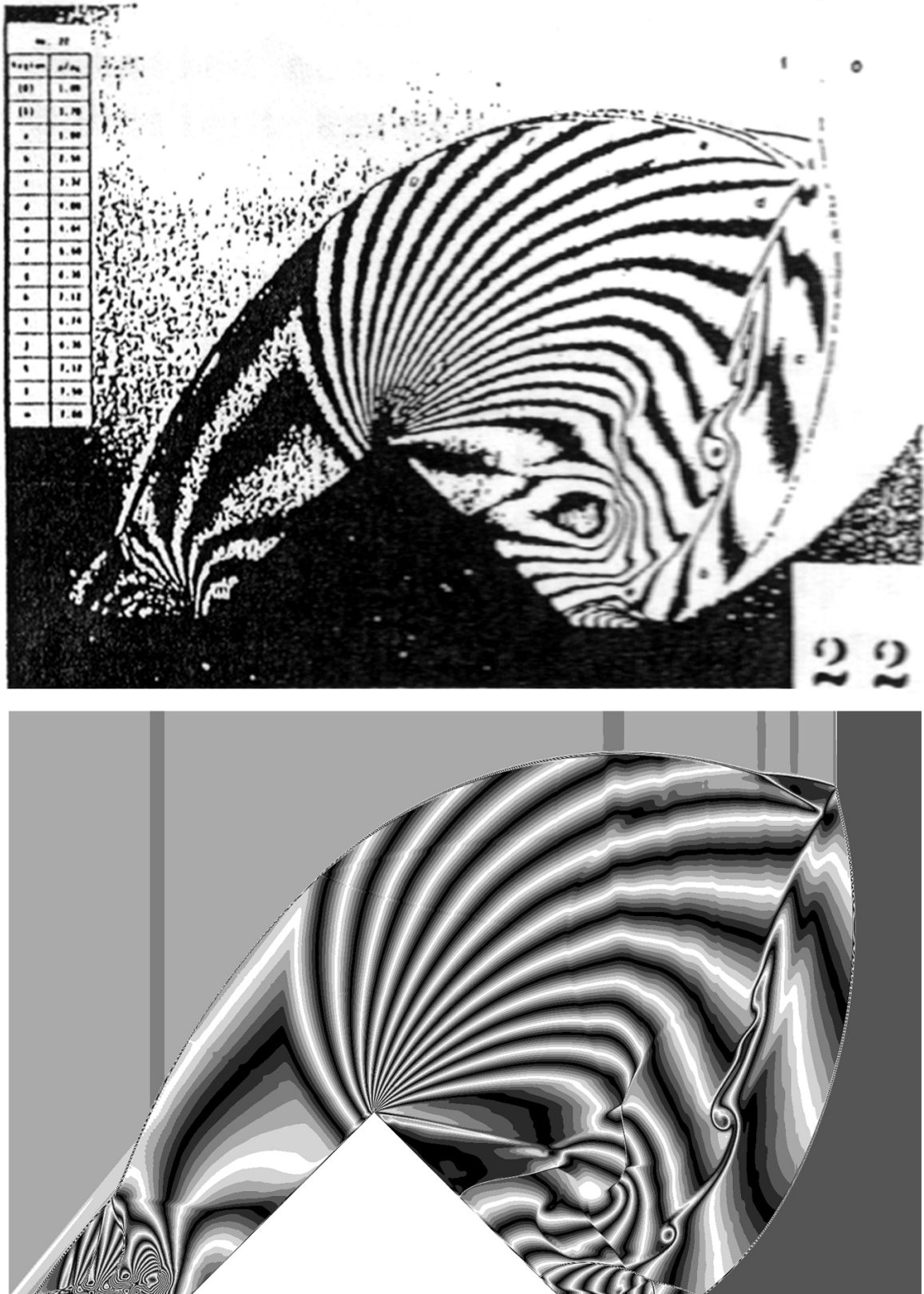


Figure 4.24: Comparison between experimental interferogram (top) and CFD-FASTRAN numerical interferogram (bottom).

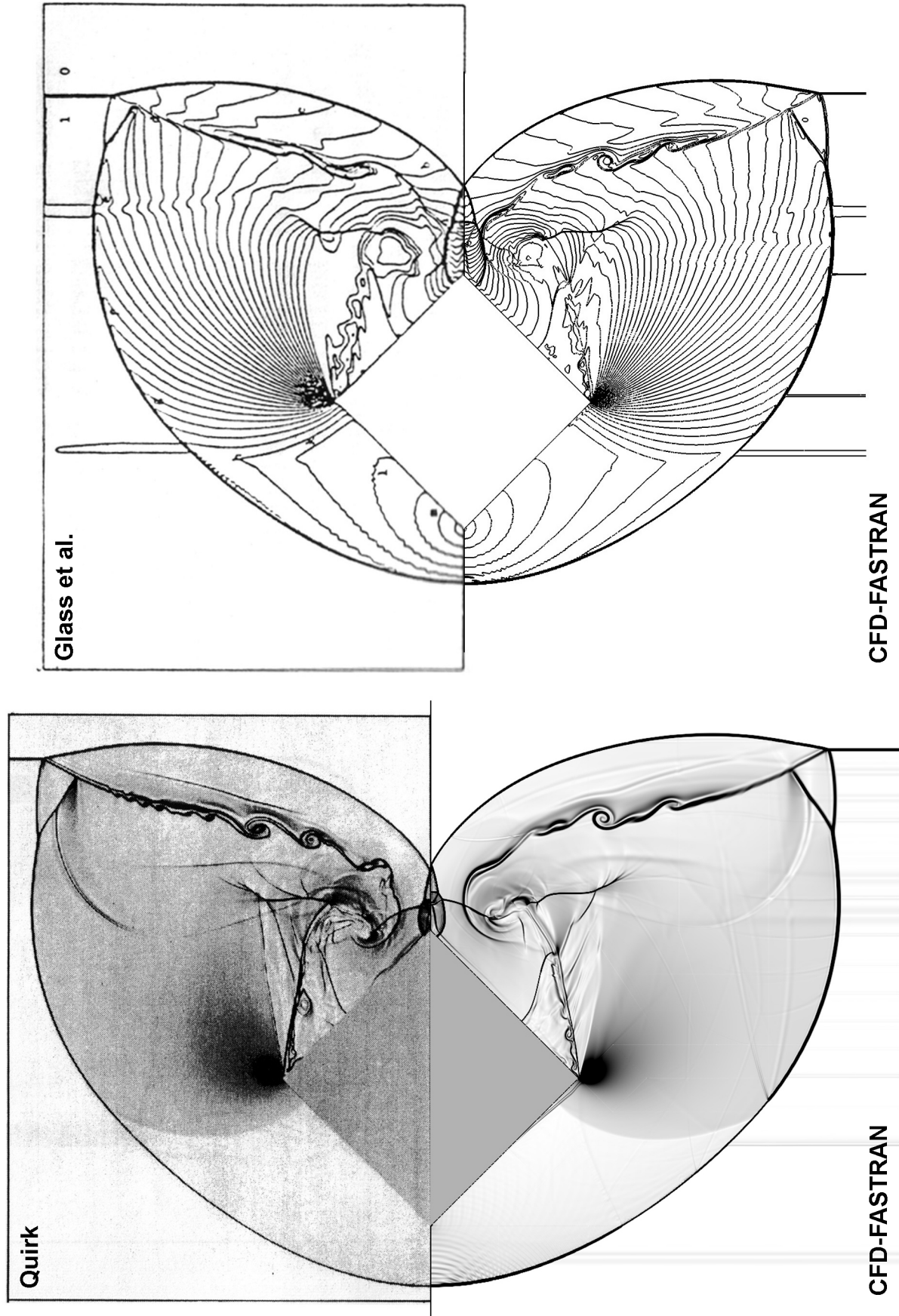


Figure 4.25: Comparison of CFD-FASTRAN results to CFD results from Quirk (left) and Glass et al. (right)

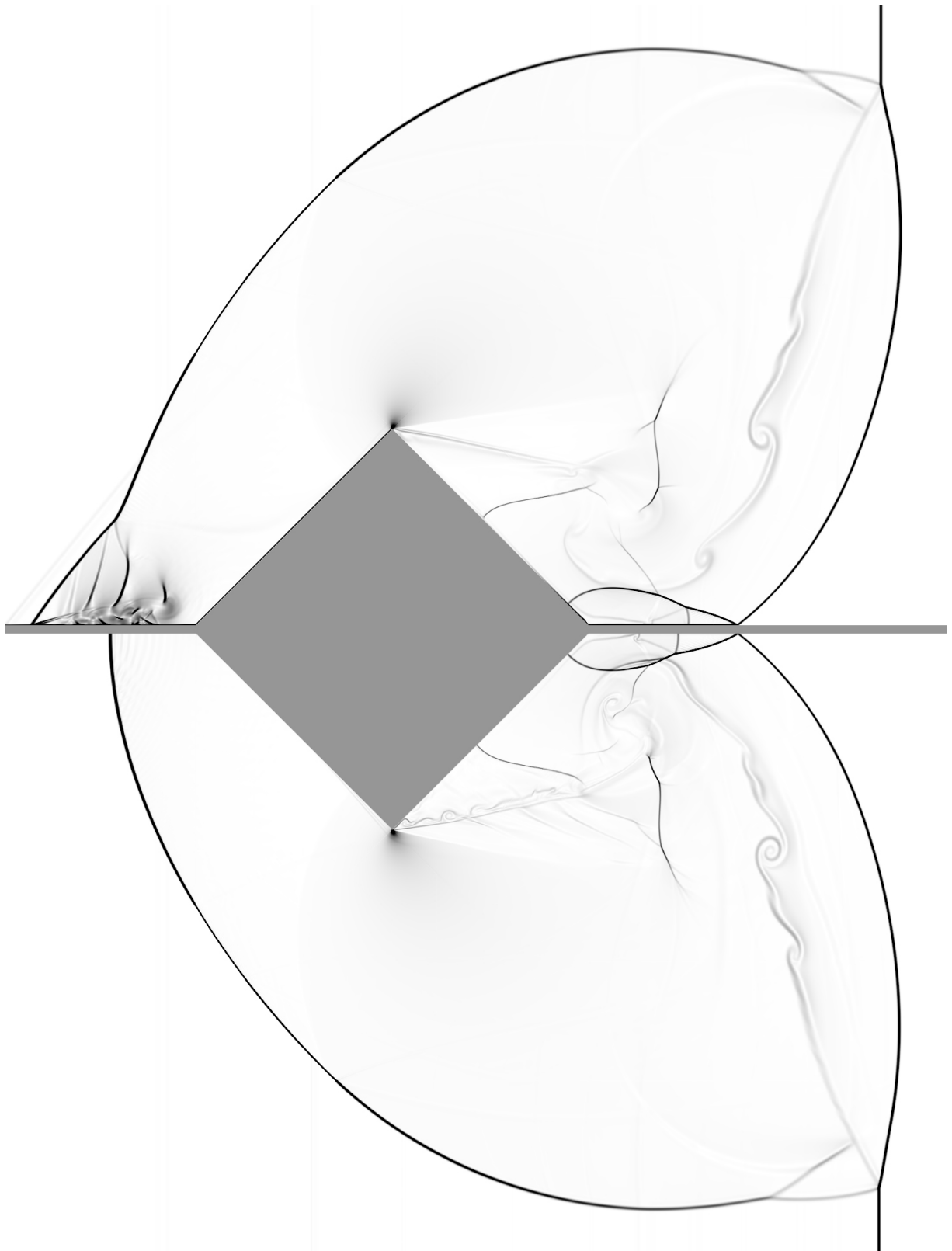


Figure 4.26: Comparison between numerical Schlieren images from CFD-FASTRAN results: laminar simulation (top half), inviscid simulation (bottom half).

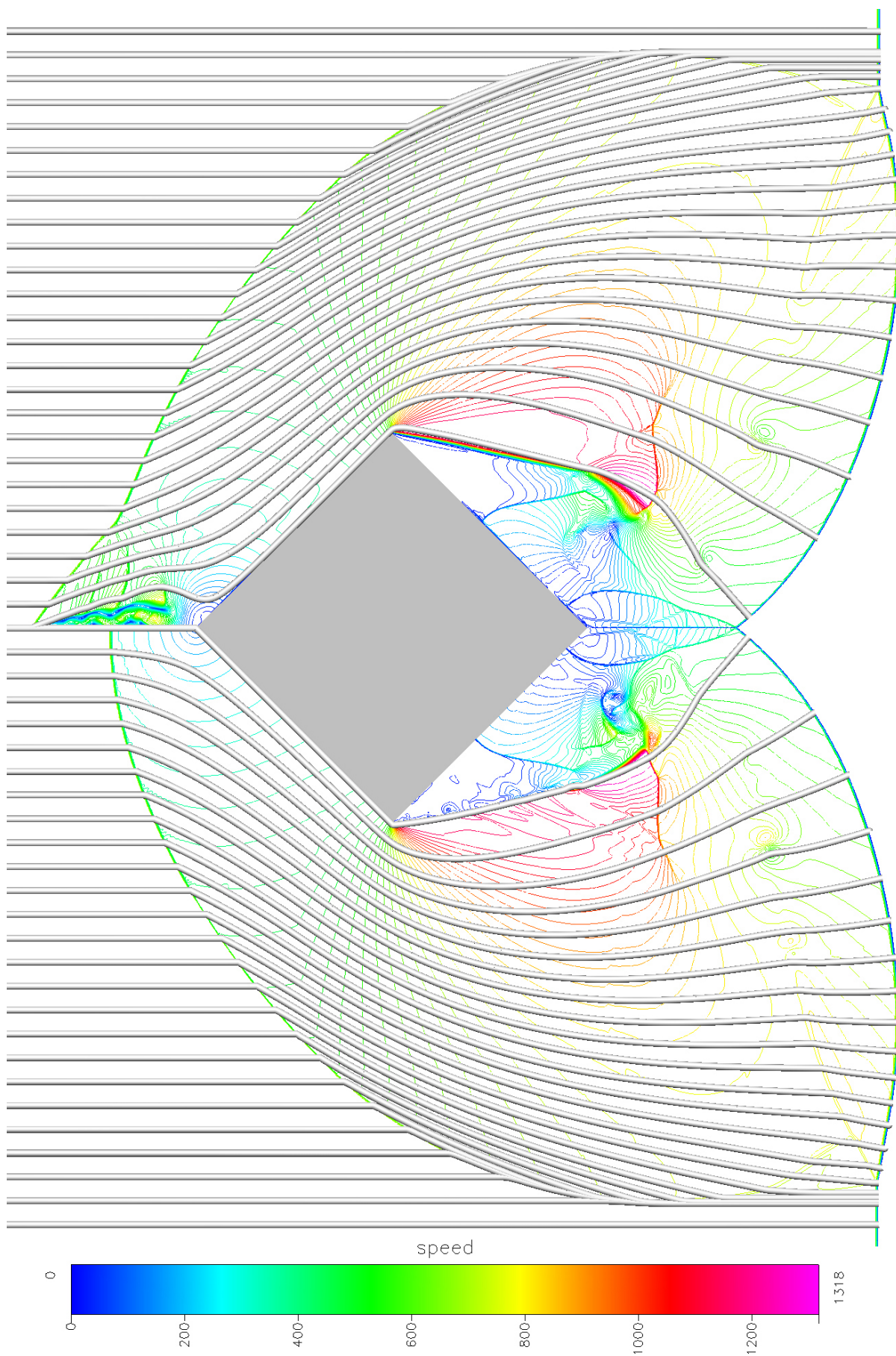


Figure 4.27: Streamlines and contours of speed for the CFD-FASTRAN laminar solution (top half) and inviscid solution (bottom half).

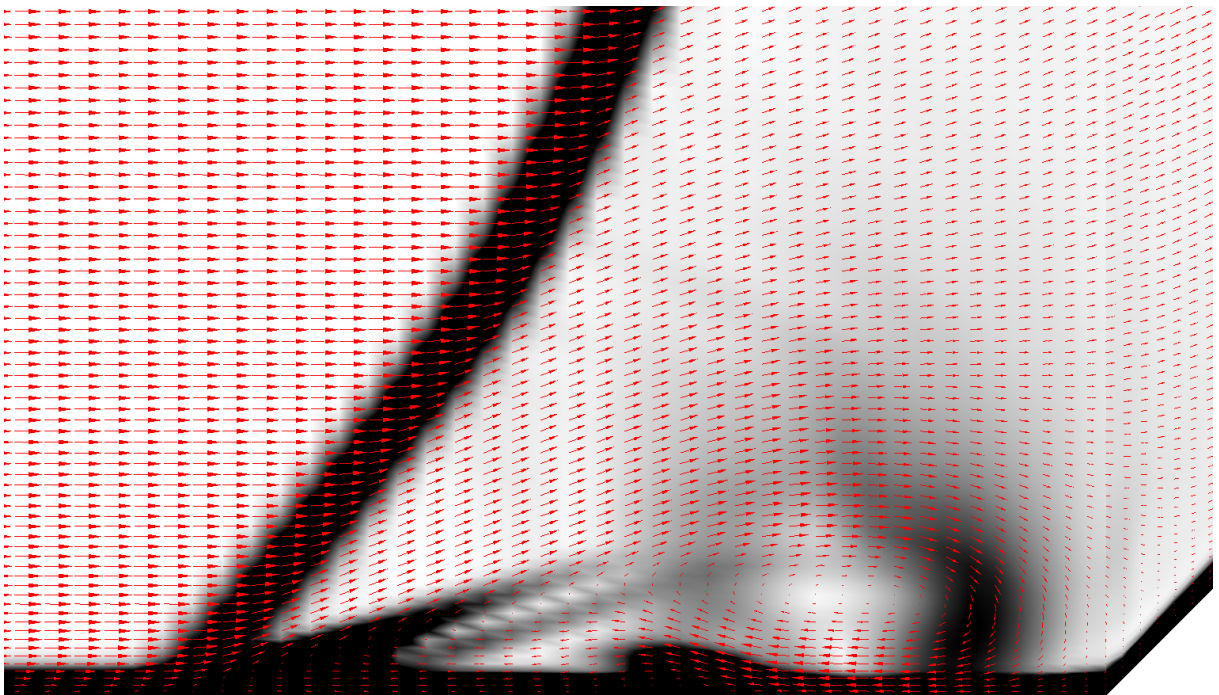


Figure 4.28: Close up view of the shock boundary layer interaction region of the CFD-FASTRAN solution: Schlieren image with superimposed velocity vectors (red).

#### 4.4.7 Grid Convergence

A grid convergence study has been performed on the half-diamond model. The number of cells in each direction of every block was approximately halved and the model was run again with the same parameters as the original model. This process was repeated. The results are shown in Figure 4.29. The results appear to approach a specific set of values except in the shock boundary layer interaction region where further refinement is needed to test the convergence.

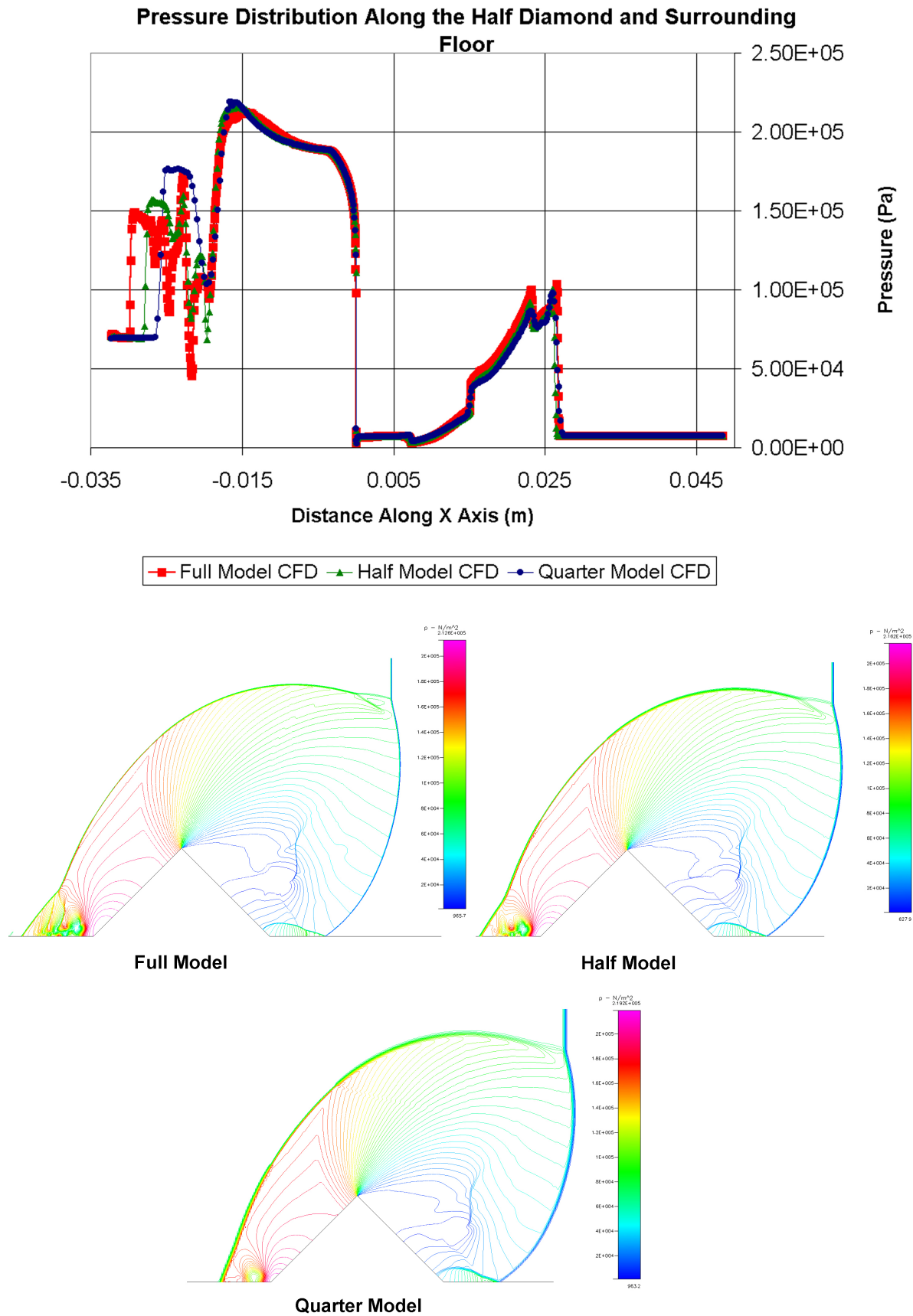
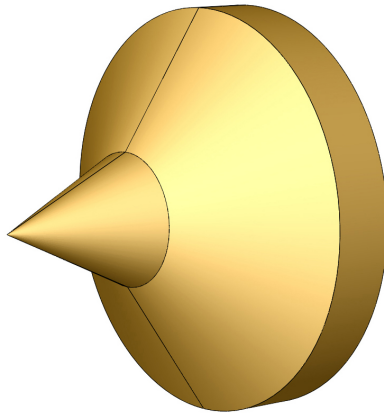


Figure 4.29: Pressure results for the full, half and quarter models.

## 4.5 Hypersonic Flow Over a Sharp Double Cone



### 4.5.1 Problem Overview

In this section, the steady hypervelocity flow of Nitrogen ( $N_2$ ) over a sharp double cone is considered. The double cone configuration, or “biconic” as it is also known, contains a forward cone followed by a steeper aft cone with a cylinder on the end. Flow over various double cone type models has been the focus of much attention recently with a number of articles written on experiment and simulation of hypervelocity flow past this shape. The double cone makes for an extremely rigorous test of a CFD code as the boundary layer separation and reattachment points are notoriously difficult to predict. Accurate prediction of the flow field is difficult because the locations of separation and reattachment points are sensitive to real gas effects such as the transfer of vibrational energy and the presence of chemical reactions in the flow. In the study considered here, the model has a forward cone half angle of  $25^\circ$  and an aft cone half angle of  $55^\circ$ . The freestream Mach number and velocity are 15.56 and 2,070 m/s respectively and real gas effects are limited to the transfer of vibrational energy as the temperature generated by the impact of oncoming flow is not sufficient to dissociate any significant amounts of Nitrogen. The simulation has been setup to match the experimental work performed by Holden et al. [32] using the Large Energy National Shock (LENS) facilities. The LENS facilities are located at the CALSPAN-UB research center (CUBRC) in Buffalo, NY and comprehensive information about these facilities can be found in Holden’s paper. Holden performed many experiments on the double cone configuration but in this test case only run number 7, one of the low density runs, is simulated. The conditions for this run are given in a paper by Harvey [28] and are also reported here. The results from CFD-FASTRAN are compared to the experimental results from Holden et al. [32] as well as computational results from researchers using both the Navier-Stokes (NS) method

as well as the Direct Simulation Monte Carlo (DSMC) method. The results from CFD-FASTTRAN are assessed primarily by comparing pressure and heat transfer data along the surface of the double cone. Less emphasis has been placed on optical techniques in this study due to a lack of clarity in the experimental images imposed by a very low density in the freestream flow. Figure 4.30 gives the exact dimensions for the experimental model used at CUBRC as well as some photographs of the experimental setup which have been reproduced from Holden's paper.

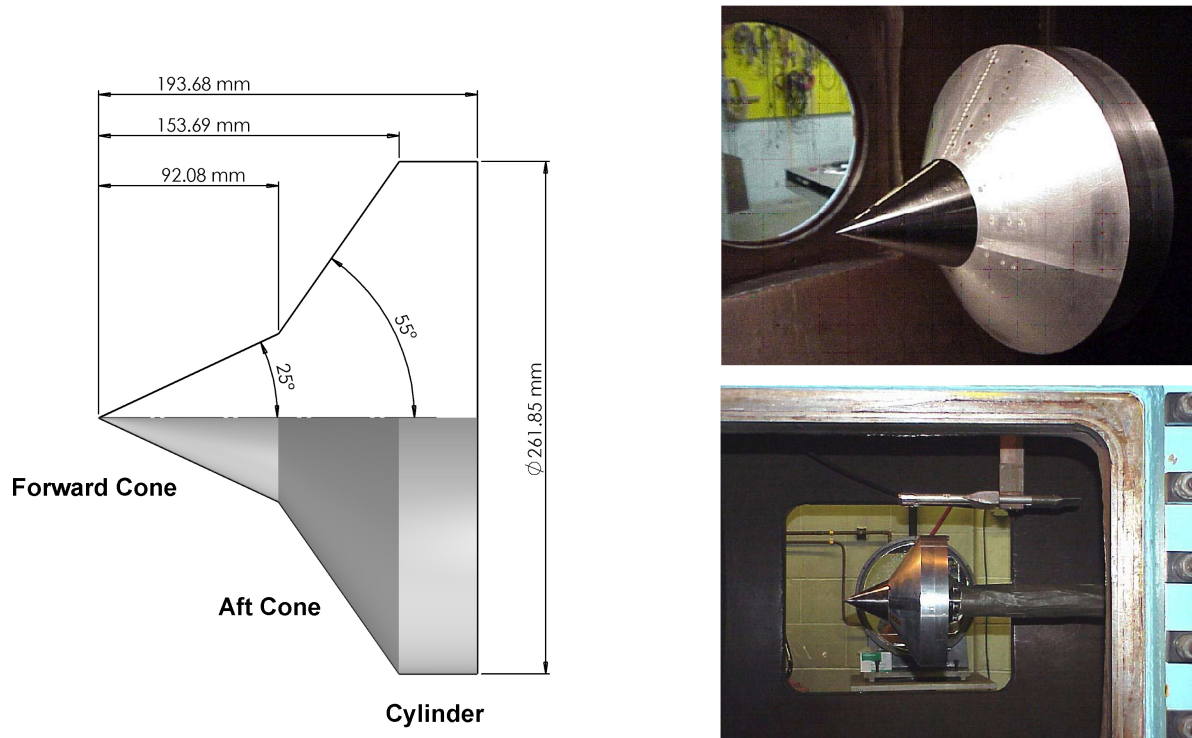


Figure 4.30: Sharp double cone model used by Holden et al.

## 4.5.2 Key Features

The key features of the validation include:

- low enthalpy “cold” hypersonic flow ( $T_\infty = 43$  K)
- low density flow ( $\rho_\infty = 1.761 \times 10^{-3}$  kg/m<sup>3</sup>,  $Kn = 1.57 \times 10^{-3}$ )
- freestream Mach number of 15.56, freestream flow speed of 2.07 km/s
- nonequilibrium exchange of vibrational energy (thermal nonequilibrium)
- attached and detached shocks
- laminar separation and reattachment

- steady shock-shock and shock-boundary layer interaction
- comparison with pressure and temperature data sampled with high spatial resolution
- comparison to Navier-Stokes (NS) codes and Direction Simulation Monte Carlo (DSMC) codes
- comparison of laminar and inviscid solutions

### 4.5.3 Assumptions

The following assumptions have been made:

- axisymmetric flow
- inviscid compressible flow (Case 5A), laminar compressible flow (Case 5B)
- continuum flow
- Nitrogen is chemically frozen
- vibrational internal energy states are excited in the Nitrogen
- exchange of vibrational energy is governed by the vibrational relaxation equation defined in Section 4 of Appendix A
- isothermal walls
- no-slip walls (Case 5B)

### 4.5.4 Grid Setup, Boundary Conditions and Initial Conditions

The sharp double cone model contained 85,520 cells and 86,814 nodes in 5 blocks. The forward cone surface was defined by 400 cells whilst the aft cone surface contained 200. The layout of the multi block grid is shown in Figure 4.31. The boundaries patches are numbered and Tables 4.14 shows the boundary conditions for each patch. Table 4.15 shows the initial conditions which were applied globally to the model. The task of obtaining freestream conditions for this model was complicated by the fact there were two rounds of experiments performed on the same sharp double cone model. The first round of experiments were performed as part of a blind code validation study. The results of this study were not revealed until the 39<sup>th</sup> AIAA Aerospace Sciences Meeting and Exhibit at Reno, NV in 2001. A second round of experiments were performed in 2002 because the DSMC codes were shown to perform poorly in the 2001 blind code validation study. It was suggested by Roy et al. [71] that if the experiments could be repeated using one third of the original freestream density, the DSMC results may be more successful. The model chosen in this study, CUBRC Run 7, was part of the second group of experiments.

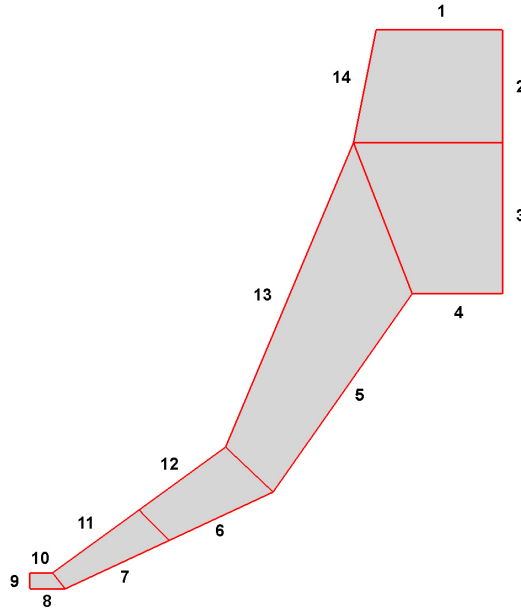


Figure 4.31: Multi-block grid for Case 5.

Table 4.14: Boundary conditions for Case 5A and 5B.

Patch	BC Type	BC Sub Type	$\mathbf{v}$ (m/s)	P(Pa)	T(K)	$T_{\text{VIB}}$ (K)
1	symmetry	-	calculated	calculated	calculated	calculated
2 -3	outlet	extrapolated	calculated	calculated	calculated	calculated
4 - 7	wall	isothermal	(0,0)	†	297	calculated
8,10	symmetry	-	calculated	calculated	calculated	calculated
9,11 - 14	inlet	flow rate	(2070,0)	2.227	42.6	1986

† The flow velocity at the wall, relative to the wall, is equal to 0 in the normal direction. The tangential component is 0 for viscous flow and extrapolated for inviscid flow.

Table 4.15: Initial conditions for Case 5A and 5B.

quantity	value
velocity (u,v) (m/s)	(0,0)
pressure (Pa)	2.227
temperature (K)	42.6
vibrational temperature (K)	297

### 4.5.5 Solution Setup

The double cone simulations were run using Roe's FDS scheme in combination with a Min-Mod flux limiter for spatial integration. The default values were used for the entropy fix parameters (0.2 for both linear and nonlinear waves). A Jacobi Point Iterative implicit scheme was used together with a time accurate Backward-Euler scheme for integration in time. The gas was modelled using the two-temperature thermal nonequilibrium option in conjunction with the default low temperature (curve-fit) thermodynamic database.

The CFL number was adjusted several times throughout the solution in an attempt to accelerate the convergence as much as possible. Values ranged from 0.5 to 2.0. The solution was terminated and restarted with a more aggressive (higher) CFL number when it appeared that the solution was stabilising. After each restart, the solution was monitored to check for divergence. Divergence occurred several times when the increase in CFL was too aggressive or was imposed too suddenly. When the solution diverged, the solver was simply restarted from an earlier result file with a more conservative CFL number.

### 4.5.6 Results and Comparisons

Results from CFD-FASTRAN are shown in Figures 4.32 - 4.35. The results indicate separation of the boundary layer on the forward cone with subsequent reattachment on the aft cone. This separation can be seen in Figure 4.32 as a blank region and more clearly in closeup view of Figure 4.33. The effects of separation are also seen in the pressure plot of Figure 4.34 and 4.37 with an oblique shock forming at the point of separation and twin high pressure zones where reattachment occurs. During the CFD-FASTRAN solution, monitoring of the results revealed that the separation and reattachment points were highly unstable, shifting across more than a quarter of the model even after two orders of magnitude convergence had been reached. The solution was continued until over four orders of magnitude convergence had been reached at which point no subsequent movement of the attachment and reattachment points was observed. Whilst it is tempting to conclude that the experimentally obtained data was not truly steady, this seems unlikely with such a close match in data between the two different test facilities (see Figure 4.36).

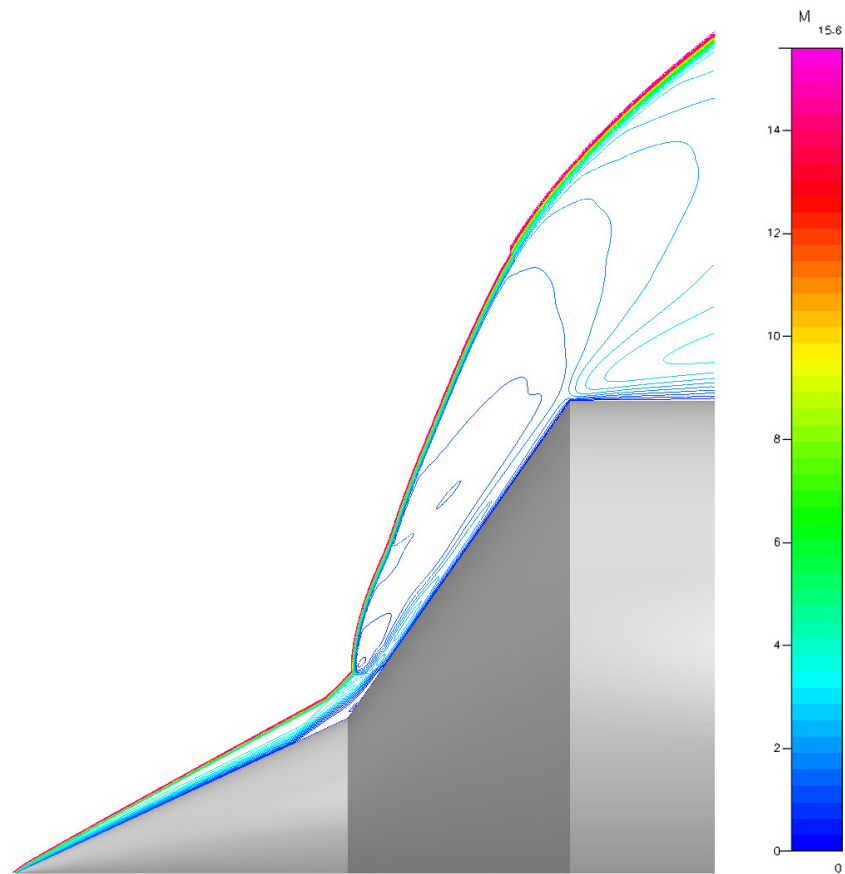


Figure 4.32: CFD-FASTRAN: Mach contours for the sharp double cone model.

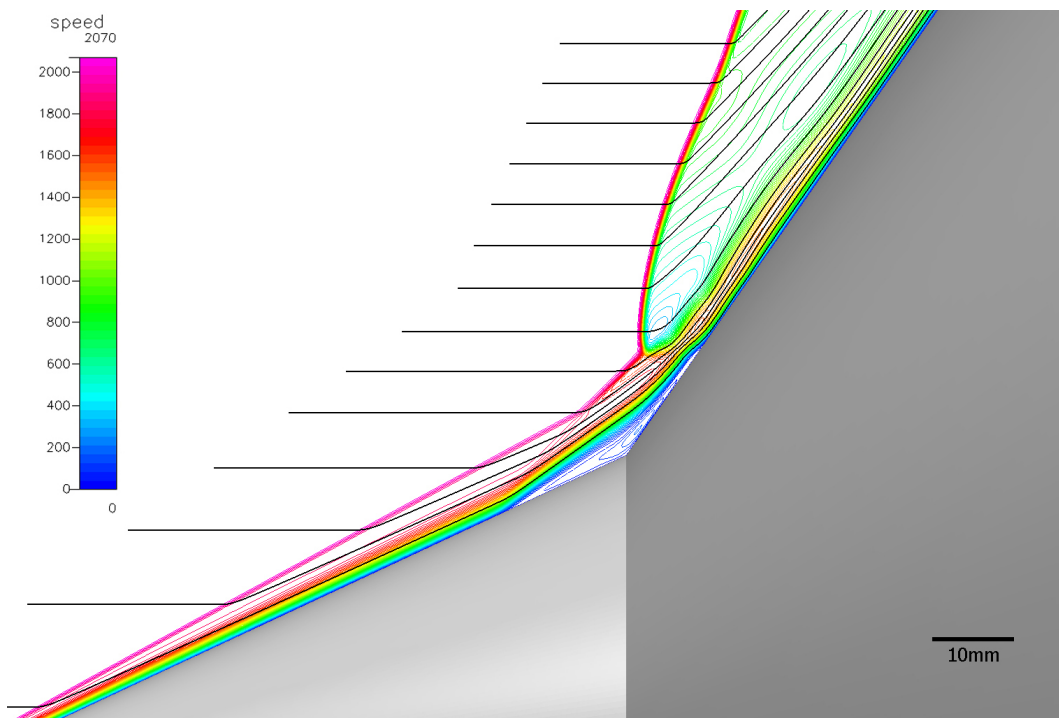


Figure 4.33: Streamlines and contours of flow speed for the sharp double cone model (closeup view).

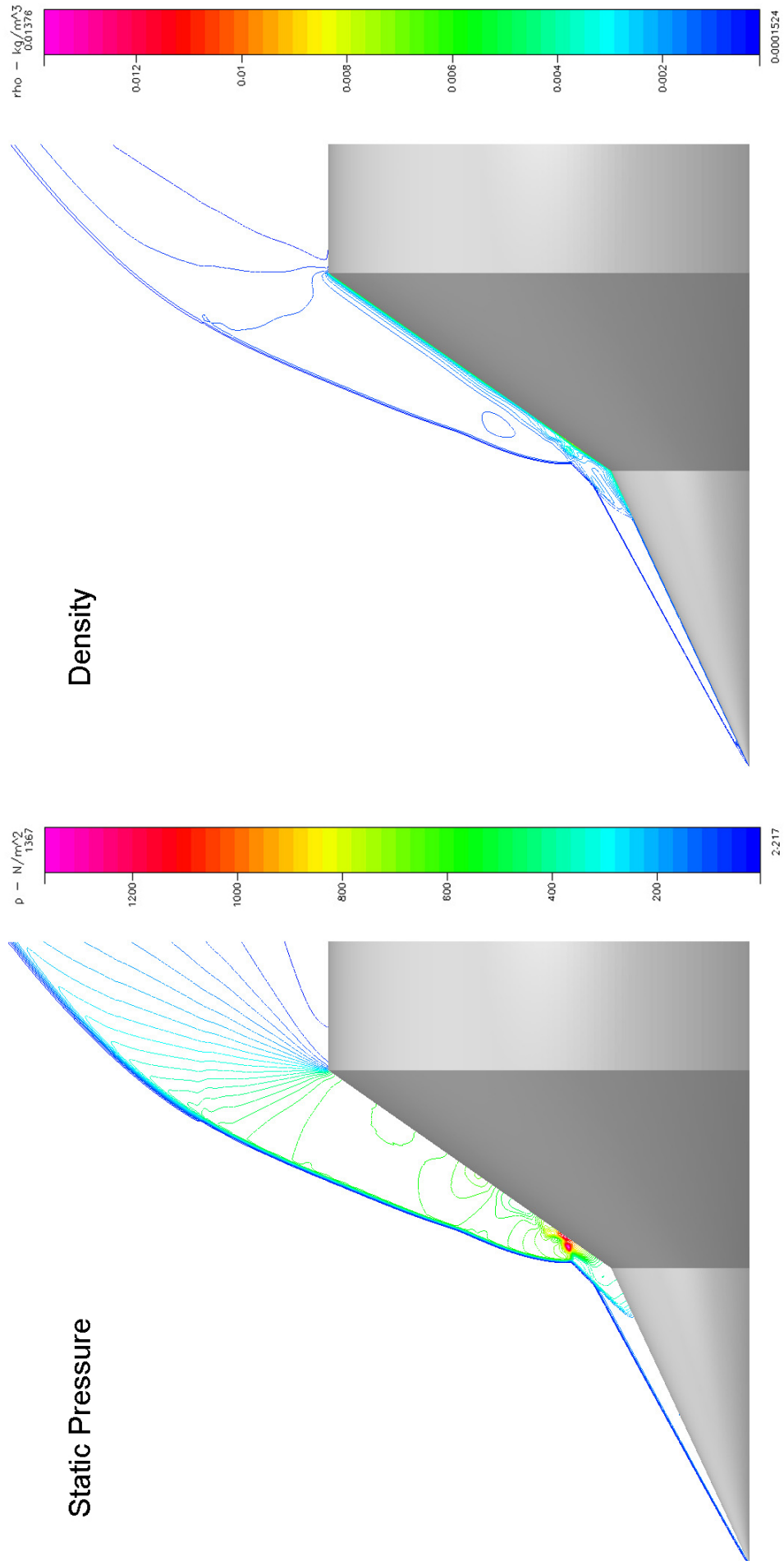


Figure 4.34: CFD-FASTRAN: Isobars and isopycnics for the sharp double cone model.

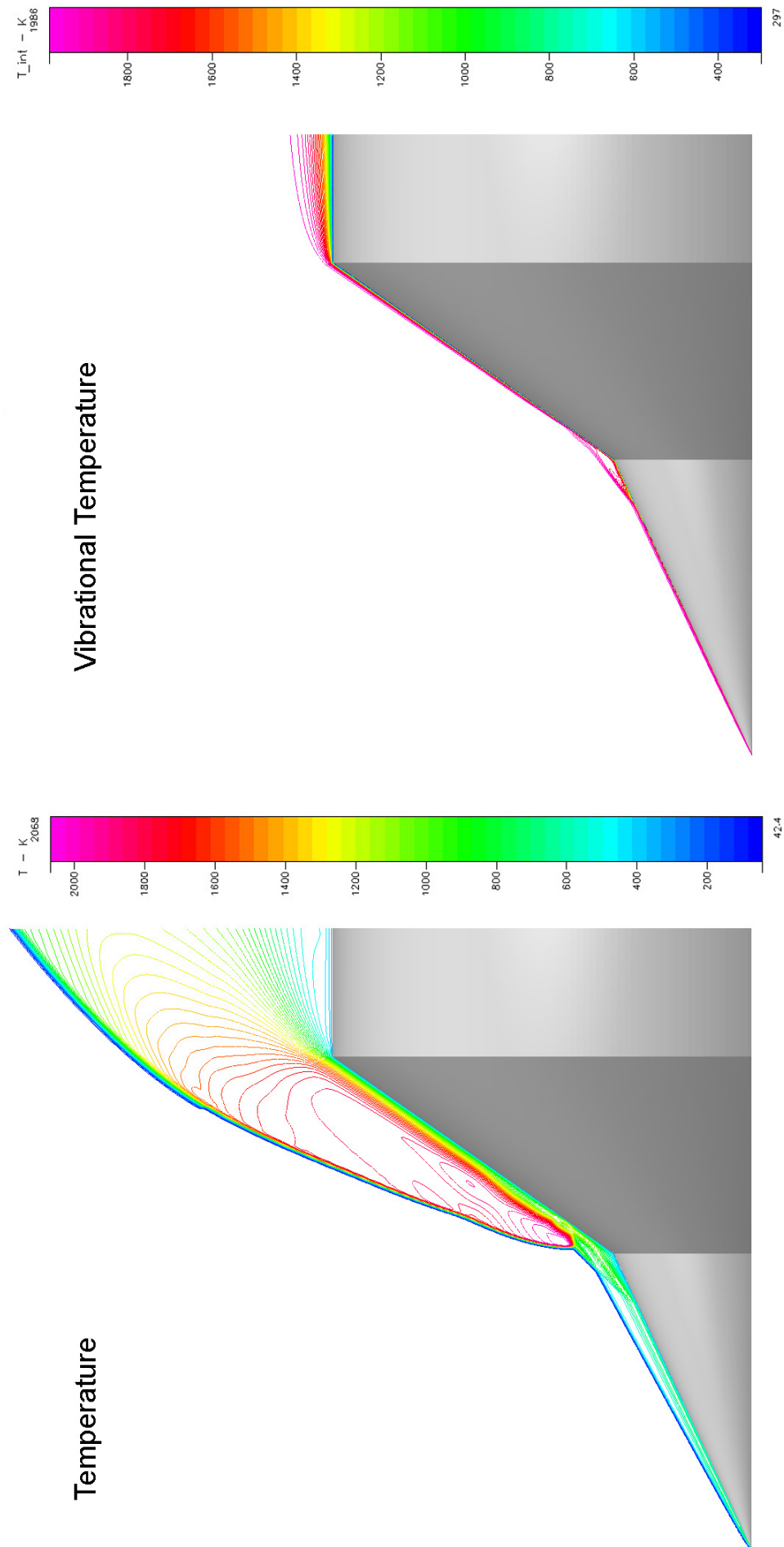


Figure 4.35: CFD-FASTTRAN: Temperature and vibrational temperature contours for the sharp double cone model.

### Comparison with Experiment

The experimental data provided by Holden for the second round of experiments [32] has been cross-checked by running the model in both the 48" shock tunnel as well as the LENS-I shock tunnel. The two sets of experimental data are shown plotted against each other in Figure 4.36 and as can be seen there is good agreement between them. Note the legend in this figure has been redrawn for clarity reasons.

The axisymmetric nature of the flow was confirmed using fast-response temperature sensitive paint. Flush mounted piezoelectric pressure gauges were used to obtain pressure measurements in both tunnels whilst thin film calorimeters were used for measuring heat transfer data in one tunnel and coaxial thermocouple gauges in the other. The overall accuracy of the measurement equipment was estimated to be around  $\pm 4\%$  for the pressure gauges and  $\pm 6\%$  for the heat transfer gauges, assuming the conditions given in Holden's experimental review [32]. Figure 4.38 shows plots of pressure and heat transfer along the double cone with numerical results from CFD-FASTRAN shown together with experimental data from Holden, as published in Harvey's paper.

The comparison of pressure distributions suggests that CFD-FASTRAN has captured the general profile shown in the experimental result but failed to accurately model the location of peak pressure, which occurs at the point where the flow is reattached to the cone. In the CFD-FASTRAN simulation, reattachment is predicted to occur approximately 5 mm upstream of the experimentally recorded peak value. This error in position represents 8.1% of the aft cone axis. The secondary peak in pressure, located downstream of the primary peak, is also predicted to be upstream of the position shown in the experimental result.

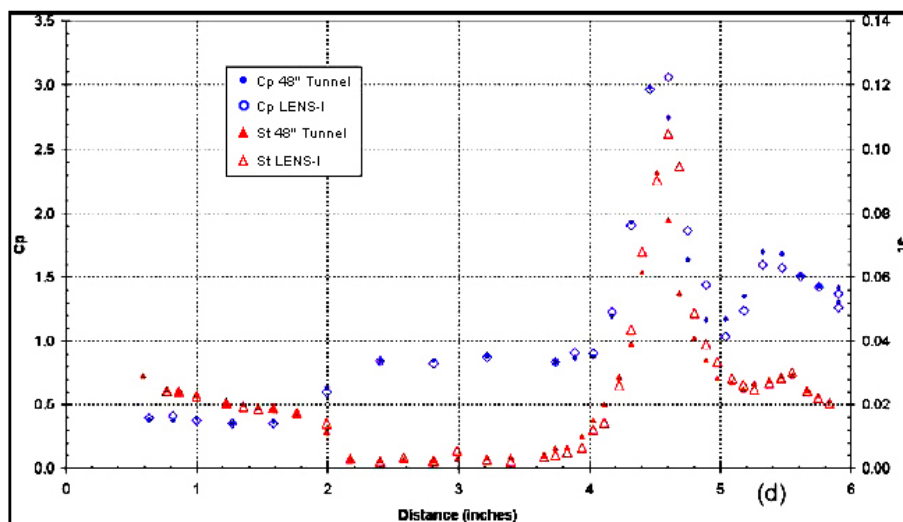


Figure 4.36: Experimental results from Holden et al. for CUBRC run 7.

The comparison of heat transfer also indicates that the CFD-FASTRAN solution reproduced the general profile of the graph but was again unable to predict the location of reattachment accurately. Furthermore, the location of separation is also in disagreement with the experimental result. The points of separation and reattachment were predicted to be approximately 5 mm and 4 mm upstream of the experimental measurement respectively. This error in position corresponds to 5.5% of the forward cone axis and 6.5% of the aft cone axis respectively. The comparison also shows that CFD-FASTRAN tended to underestimate the magnitude of heat transfer along the forward and aft cone. Whilst an acceptable explanation for the deviations discussed here has not been found, the instability of the separation and reattachment points during the solution procedure may provide a clue as to the origins of the problem. Note that a maximum  $Y^+$  value of 3.1 was observed in the results.

It is worth noting that the accuracy with which the location of the peak pressure and heat transfer is measured is dependant upon the spatial resolution at which these quantities are sampled. In the experiment discussed here, this resolution is quite high with pressure sensors located 3.7 mm either side of the peak pressure measurement and a heat transfer sensor located 1.8 mm upstream and 2.9 mm downstream of the peak heat transfer measurement. Nevertheless, the location of the actual peak values may not necessarily coincide exactly with the location of the peak measurements but rather will be located somewhere between the upstream and downstream sensors.

A split-view style comparison with an experimental Schlieren image on the top half and numerical isopycnics from CFD-FASTRAN on the bottom half is presented in Figure 4.43. The quality of the experimental Schlieren is extremely poor because of the low densities involved in the experiment.

### Comparisons with Other Numerical Codes

At least four groups have submitted numerical results for the case of the sharp double cone with the conditions reported for CUBRC run 7. These results have been collected together and discussed in a paper by Harvey [28]. The groups include Moss using a DSMC code known as “DS2V”, Markelov et al. using the DSMC code “SMILE”, Boyd using a DSMC code and Candler using a NS code. All simulations were modelled as axisymmetric and it is worth noting that the results from Candler are shown for simulations both with and without surface slip modelled. The presence of surface slip in Candler’s model appears to have had little effect on the pressure distribution aside from at the cone tip. The estimate of heat transfer was however improved on the forward cone but less accurate on the aft cone downstream of the reattachment point. The peak heat transfer is also

predicted to be higher in the model which includes surface slip. The CFD-FASTRAN simulation did not include surface slip as this option was not available.

Pressure and heat transfer results along the surface of the double cone are shown in Figure 4.39 for Moss, Figure 4.40 for Markelov et al. , Figure 4.41 for Boyd and Figure 4.42 for Candler<sup>5</sup>. The results tend to show more accurate prediction of the separation and reattachment locations than CFD-FASTRAN but, as with the CFD-FASTRAN simulation, all fail to accurately predict the location of the secondary peak in pressure and heat transfer. This error is unlikely to be numerical in nature as it shows up in both the NS results as well as the DSMC results. Curiously, all of the codes seem to predict the location of the secondary peak in pressure to be upstream by a similar amount and underestimate the magnitude. A similar observation can be made with the heat transfer however the secondary peak is less pronounced in the experimental results.

A portion of the pressure field surrounding the sharp double cone, as predicted by Moss et al., is provided in Figure 17 of Harvey's paper [28]. This figure has been reprinted in the bottom half of Figure 4.37 of this section together with pressure contours from CFD-FASTRAN on the top half. The pressure range predicted in the solution from Moss is slightly less than that predicted by CFD-FASTRAN. The peak pressure predicted by Moss was 1,295 Pa whilst CFD-FASTRAN predicted 1,367 Pa. In Figure 4.37, the CFD-FASTRAN pressure scale has been truncated to the same range as Moss so that each colour corresponds to a unique and consistent value of pressure in both solutions. Despite the difference in the range, the simulations agree quite well. Features such as the twin pressure peaks and the gradual rise in pressure across the aft cone appear to be in good agreement. Note that in this figure, the points marked "S" and "R" are the separation and reattachment points respectively.

### Comparison of Laminar and Inviscid Models

In addition to the laminar CFD-FASTRAN simulation, an inviscid model which also included the effects of vibrational nonequilibrium, was run using the same grid. Results from the inviscid flow model contained very different flow features due to the absence of separated flow. The removal of viscous effects in the solution appeared to cause undamped instability between two adjacent streams of gas in the shock layer. This instability prevented a steady result from ever being reached. Figure 4.44 shows a split-view style image with CFD-FASTRAN isobars for the laminar case on the top half together with the inviscid case on the bottom half. The inviscid case was not converged but instead was trapped in a cyclic pattern of unsteady flow. The contours shown in Figure 4.44 are from one point in that cycle.

---

<sup>5</sup>These figures have been reproduced from [28] and [33].

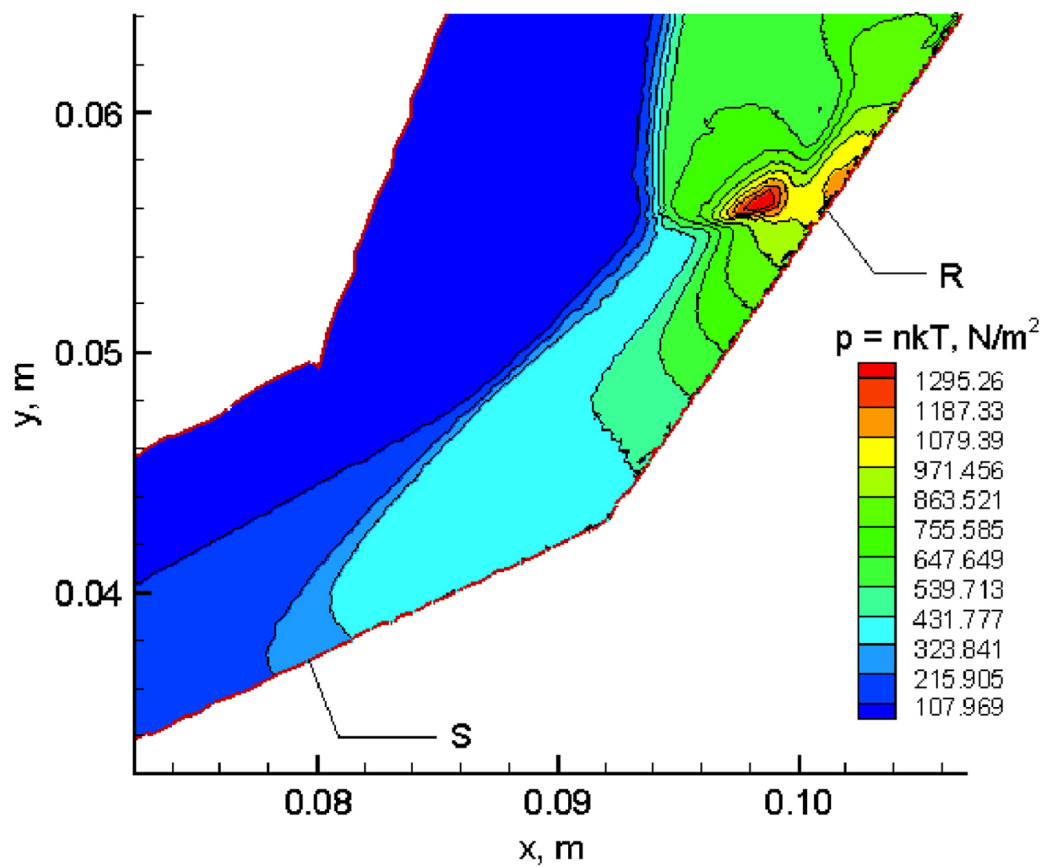
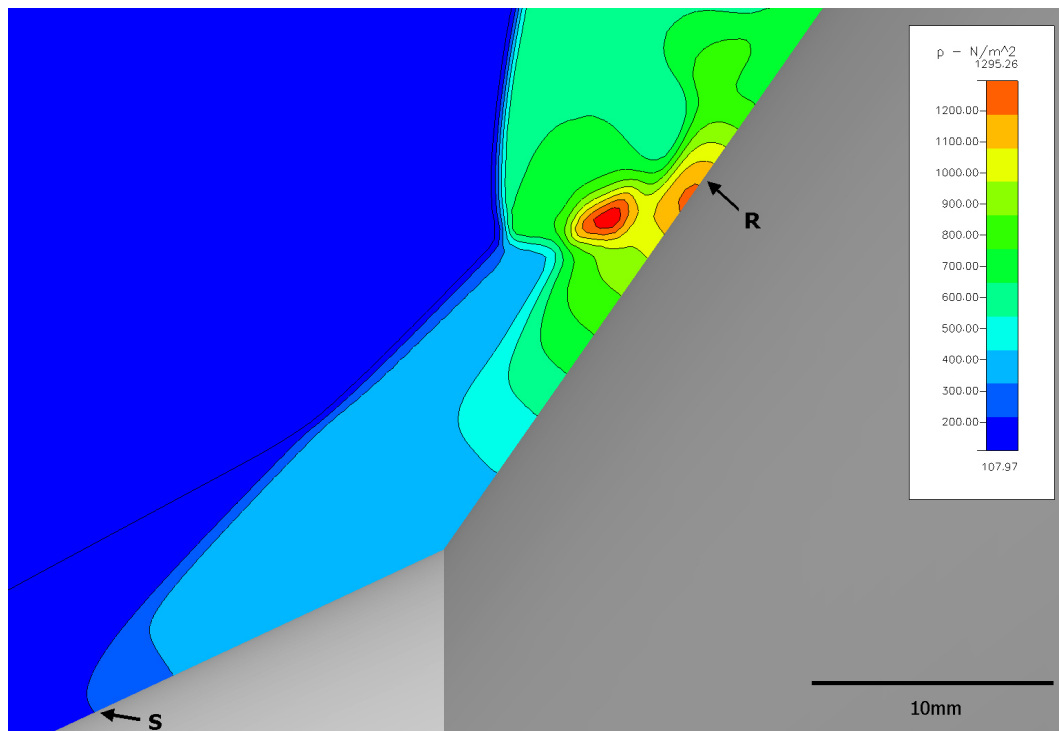


Figure 4.37: Pressure contours in the separated flow region: CFD-FASTRAN NS simulation (top) and Moss DSMC simulation (bottom). The CFD-FASTRAN contour range has been truncated to the same scale as Moss's results.

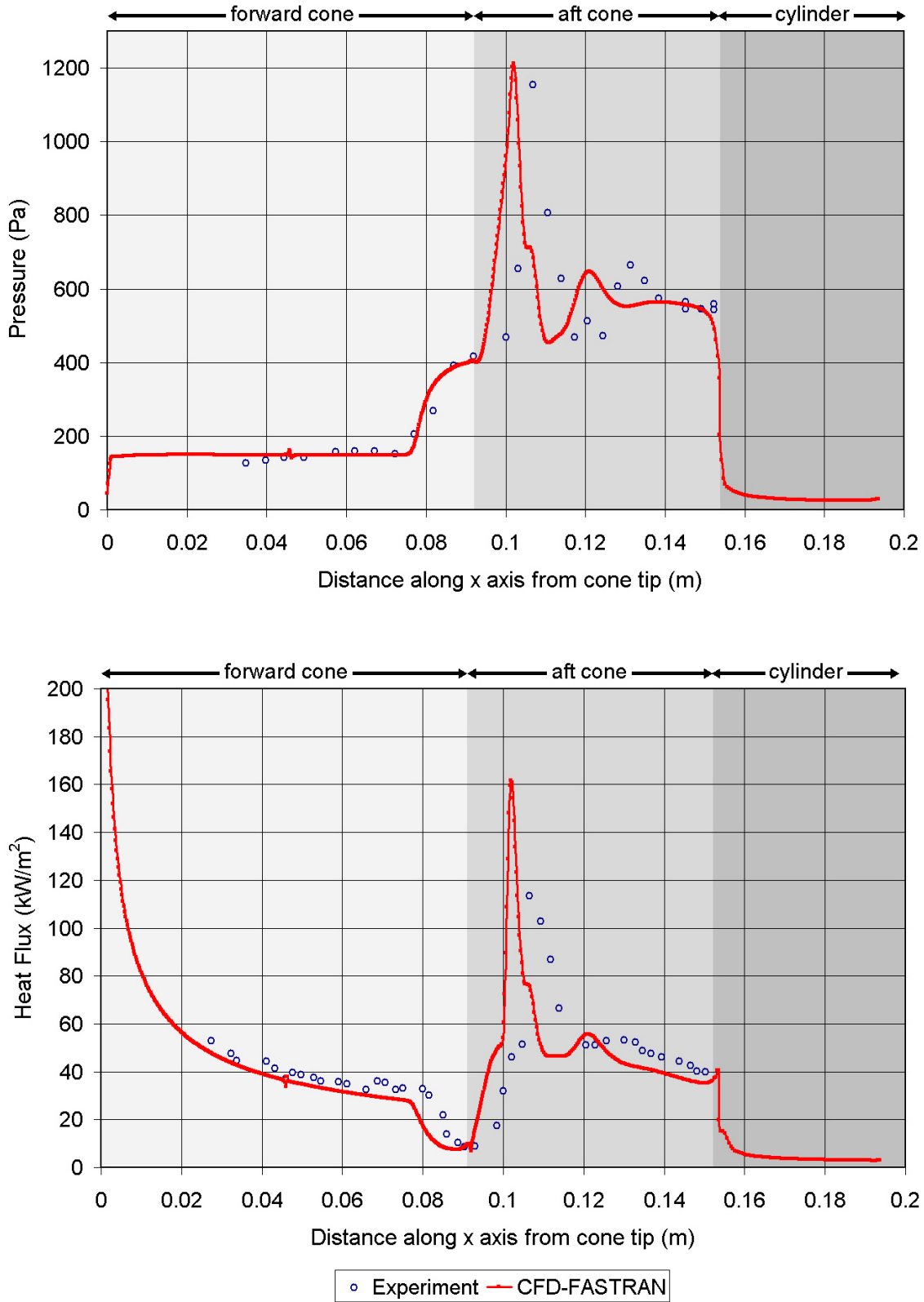


Figure 4.38: Comparison between CFD-FASTRAN simulation and experimental data from Holden et al.

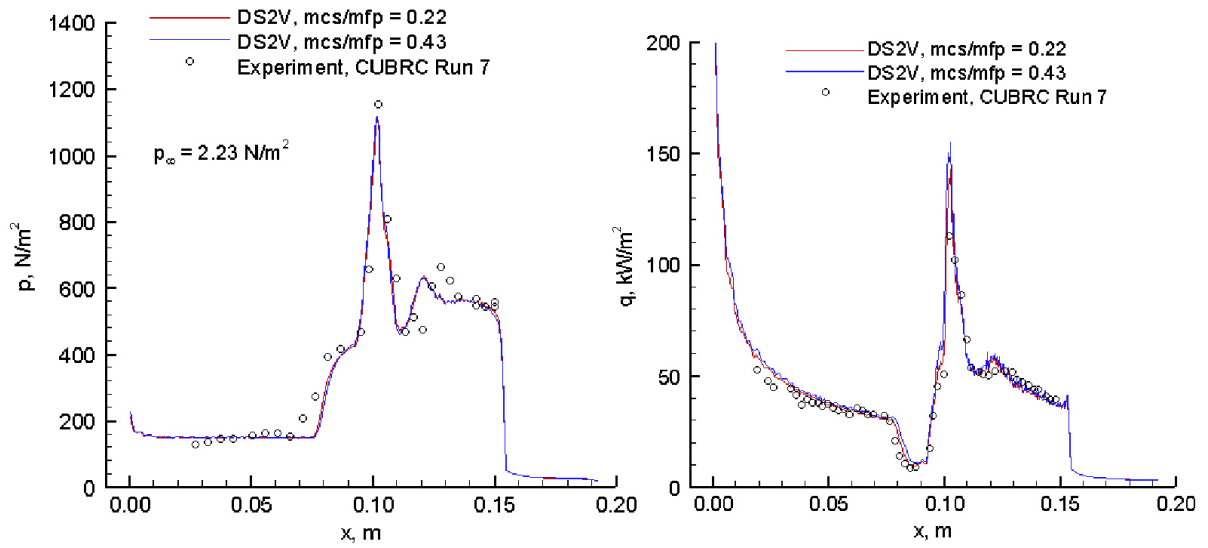


Figure 4.39: DSMC results from Moss using the DSMC code “DS2V” [28].

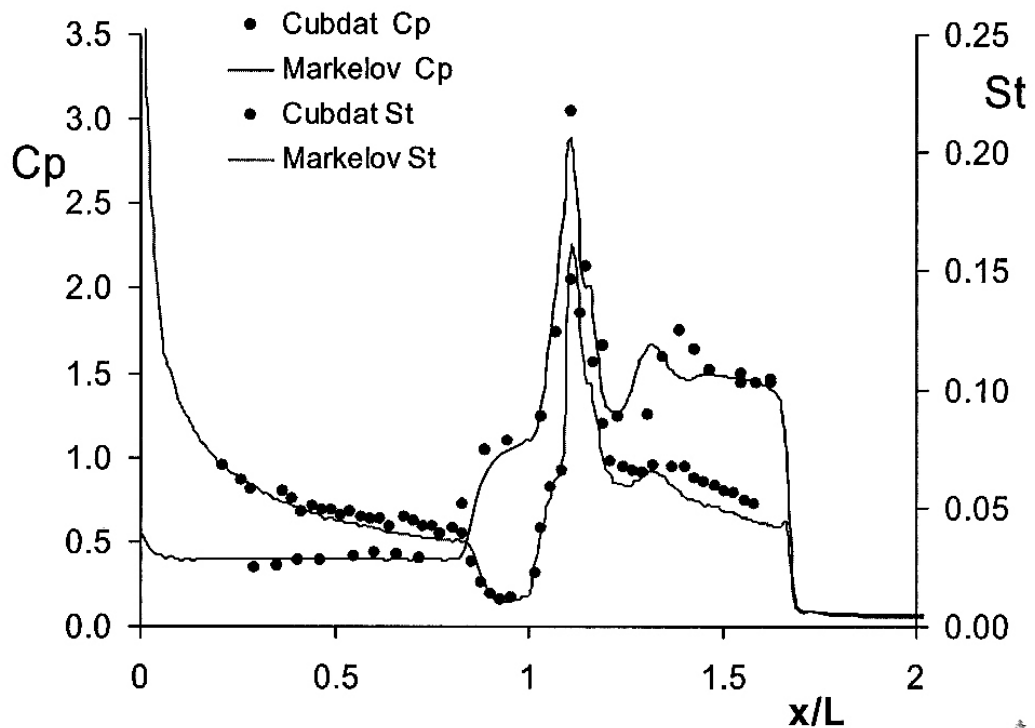


Figure 4.40: DSMC results from Markelov et al. using the DSMC code “SMILE”.

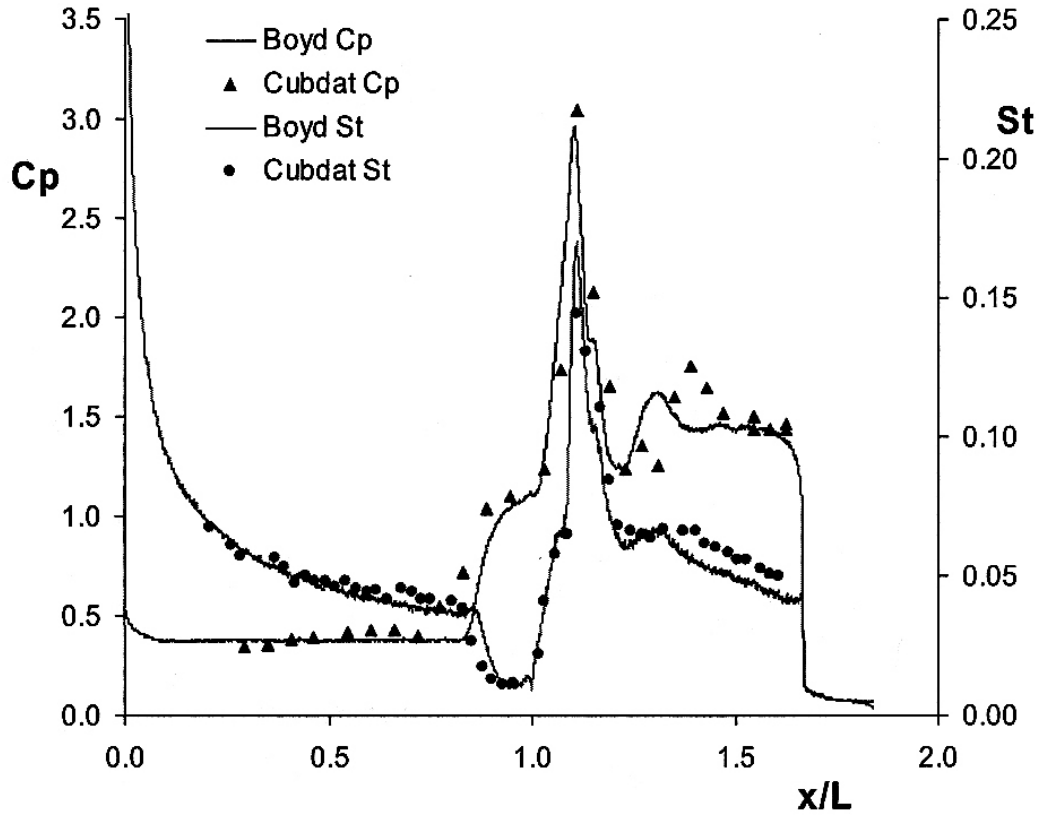


Figure 4.41: DSMC results from Boyd.

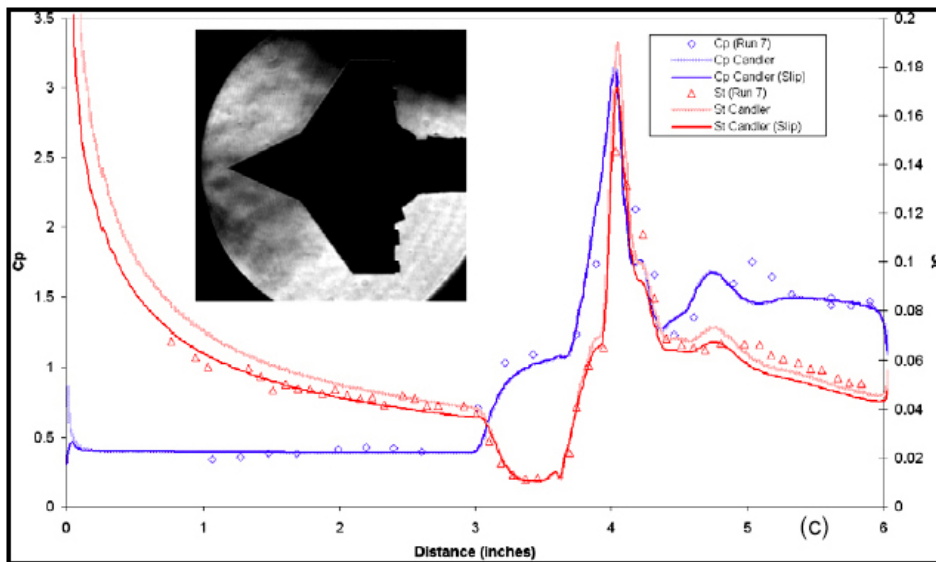


Figure 4.42: NS results from Candler.

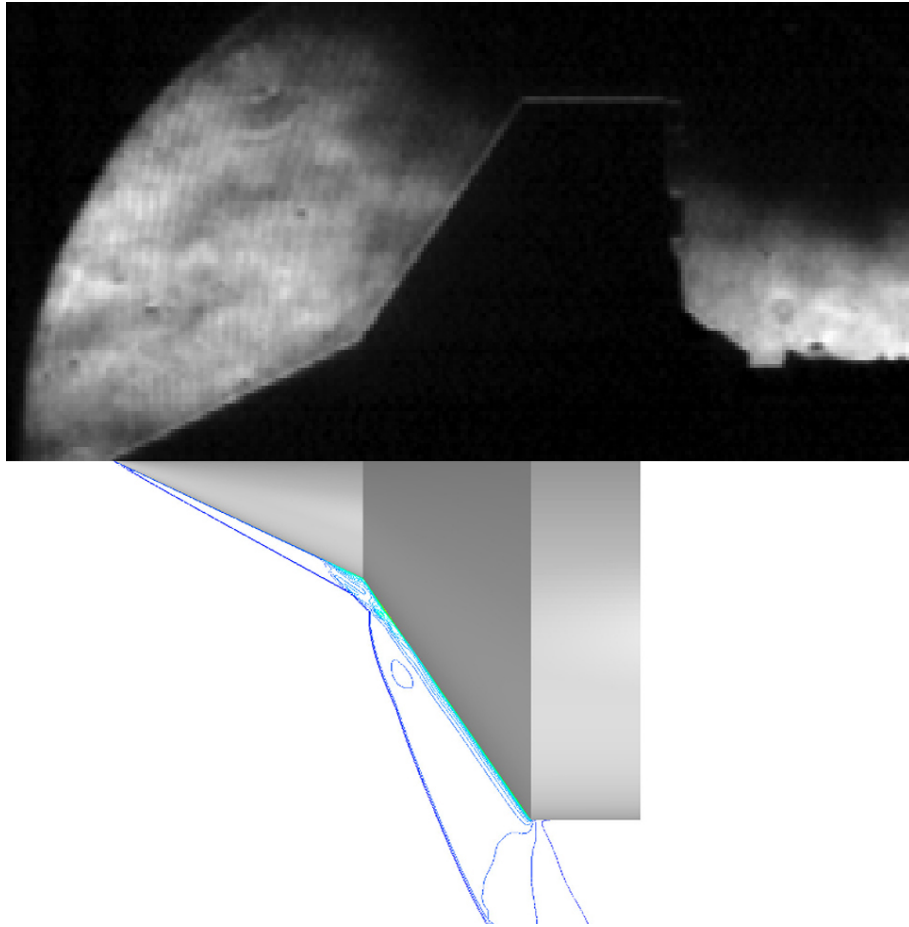


Figure 4.43: Comparison between experimental Schlieren image and numerical isopycnics.

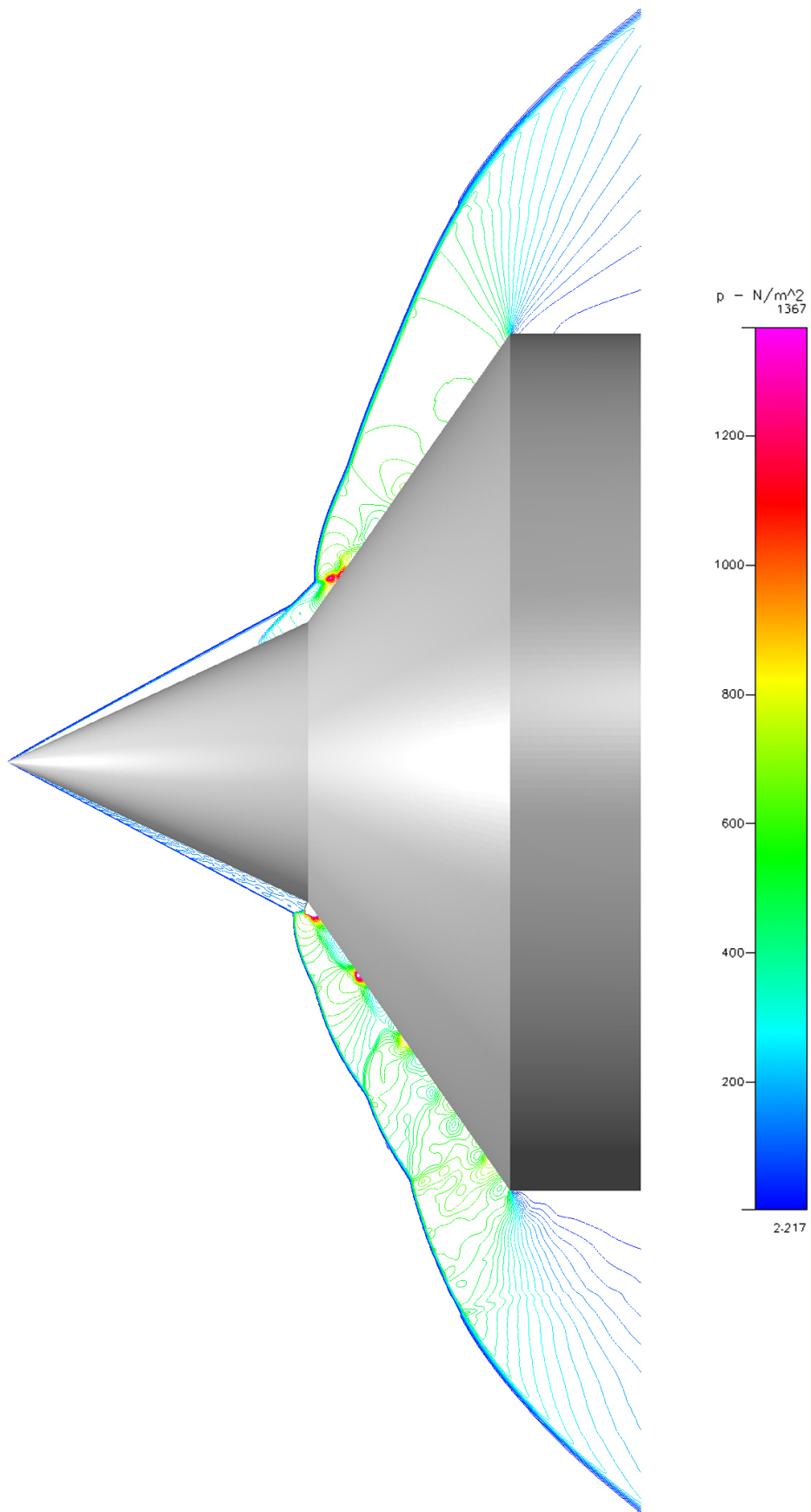


Figure 4.44: Comparison of pressure contours for the CFD-FASTRAN laminar simulation (top half) and inviscid simulation (bottom half).

### 4.5.7 Grid Convergence

A grid convergence study has been performed on the sharp double cone model. The number of cells in each direction of every block was approximately halved and the model was run again with the same parameters as the original model. This process was repeated. The results are shown in Figure 4.45. The results suggest that major flow features, including the separation and reattachment points, stabilize with global refinement of the grid.

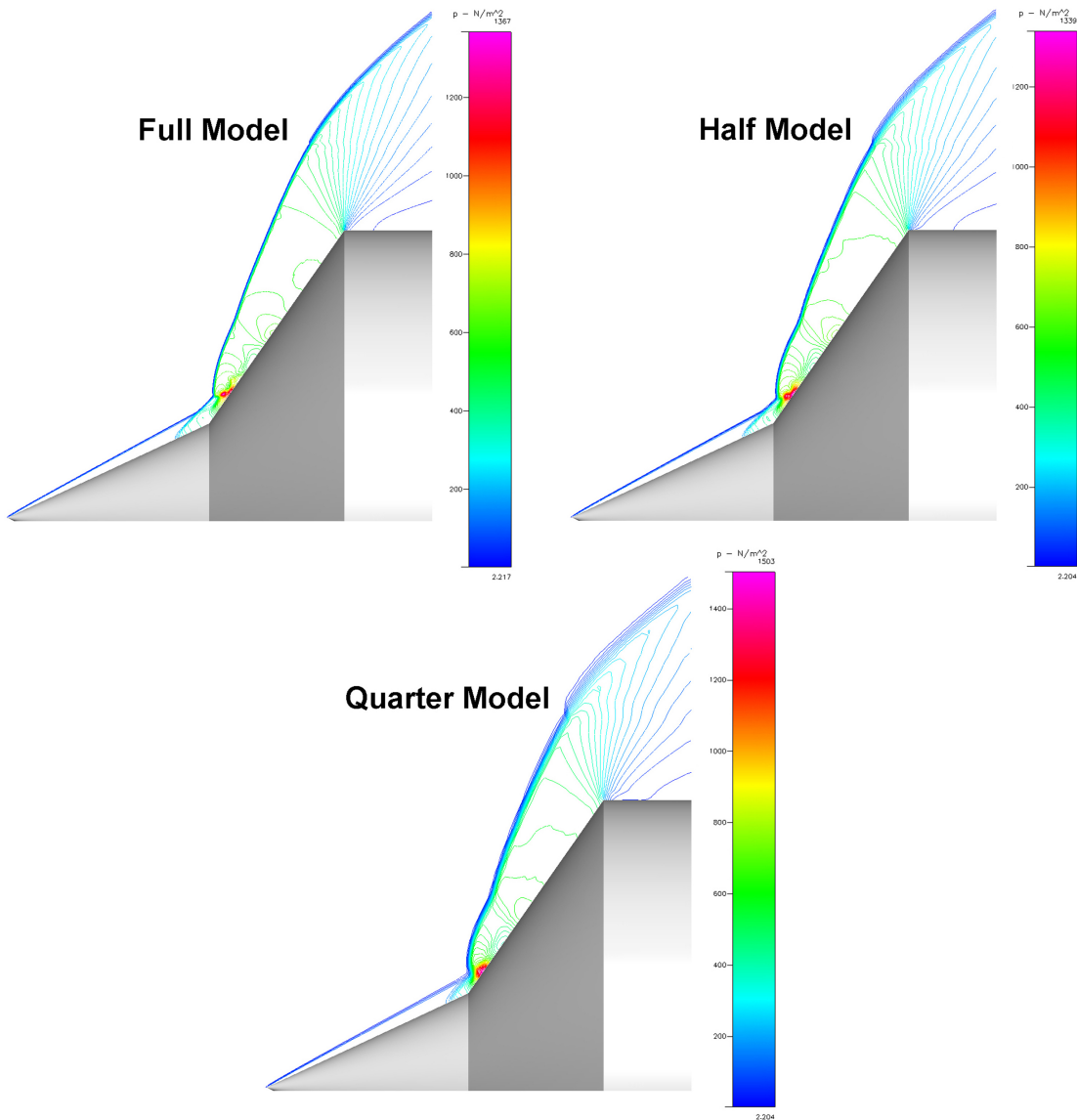
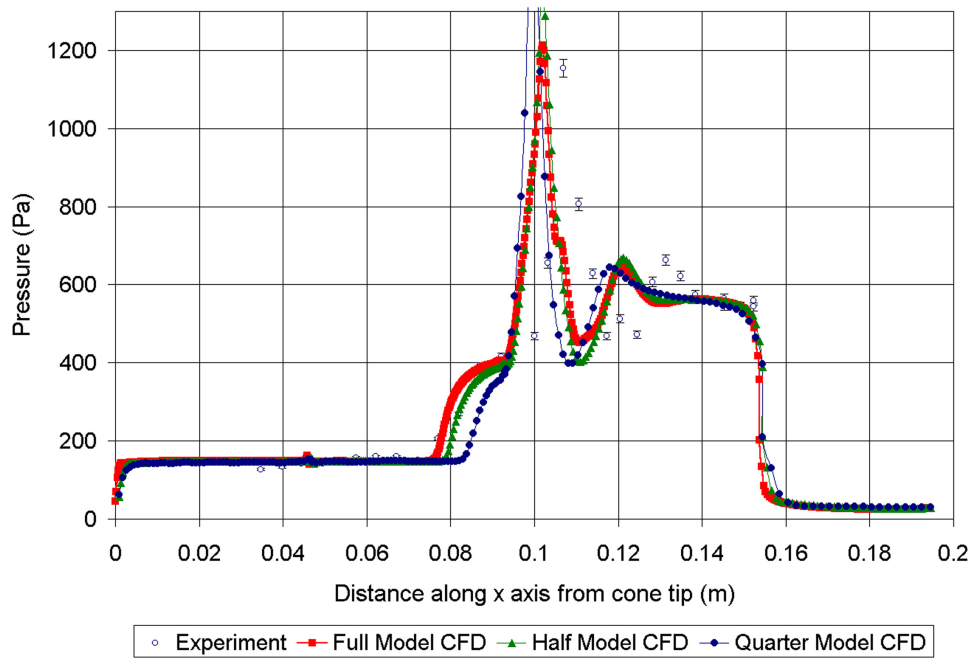
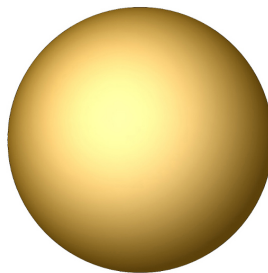


Figure 4.45: Pressure results for the full, half and quarter models.

## 4.6 Hypersonic Flow over a Sphere



### 4.6.1 Problem Overview

In this section, the steady hypervelocity flow of air over the forebody of a sphere has been studied numerically using CFD-FASTRAN. The freestream Mach number and velocity are 5.33 and 4,860 m/s respectively and the sphere is 101.6 mm (4") in diameter. The setup of this simulation has been chosen to match "Shot 491" as performed by Dr Chihyung Wen in the T5 free-piston shock tunnel at the Graduate Aeronautical Laboratories, California Institute of Technology (GALCIT). The setup of this and other experiments involving hypervelocity flow over spheres is documented in his PhD dissertation [80]. The success of this validation is judged on how well the bow shock stand-off distance and heat transfer to the sphere agree with experiment. Two simulations were undertaken. The first simulation (Case 6A) assumed a perfect gas model whilst the second (Case 6B) used a more complex two temperature model for thermal nonequilibrium and a set of reactions to account for chemical nonequilibrium. The flow was modelled as laminar in both simulations.

### 4.6.2 Key Features

- high enthalpy "hot" hypersonic flow ( $h_0 = 16.01$  MJ/kg,  $T_\infty = 2,070$  K)
- freestream Mach number of 5.33, freestream flow speed of 4.86 km/s
- detached bow shock where the shock stand off distance is sensitive to flow chemistry
- thermal nonequilibrium
- finite rate nonequilibrium chemistry
- comparison of a calorically perfect gas model to a reacting gas model
- comparison with an experimental interferogram
- comparison with experimental heat transfer measurements

### 4.6.3 Assumptions

The following assumptions have been made:

- axisymmetric flow
- laminar compressible flow
- isothermal walls
- no-slip walls
- non catalytic walls<sup>6</sup>
- reactions rates obey the Arrhenius model with the rates described in Table 4.19
- reaction rates are a function of temperature only (no vibration-dissociation coupling)

### 4.6.4 Grid Setup, Boundary Conditions and Initial Conditions

The grid used in this section was optimised by trimming the region of the grid prior to the bow shock where no information can be transmitted. Case 6A was initially run on a relatively coarse grid to determine the approximate bow shock shape and stand-off distance. Once this model converged below four orders of magnitude, isobars were plotted inside the `CFD-VIEW` interface and a handful of point probes were manually positioned outside the bow shock at roughly constant distances. The location of each probe was then noted and the coordinates were entered into `CFD-GEOM` as points alongside the original grid. The series of points were connected together with a spline curve and the initial grid was modified to use the spline as the new inlet boundary. The grid was also modified to sweep back a further  $10^\circ$  and the outlet was bent to reduce the grid distortion evident in the sharp corners of the original grid. Figure 4.46 shows the original grid superimposed with the optimised grid. The layout of the optimised multi-block grid is shown in Figure 4.47. This model contained 48,000 cells and 48,642 nodes in 2 blocks. The sphere forebody was described by 400 cells across a  $100^\circ$  span of the circumference.

In Figure 4.47 the boundary patches are numbered and Table 4.16 shows the boundary conditions for each patch. Table 4.17 shows the initial conditions which were applied globally to the model. It should be noted that the freestream pressure was not reported by Wen for any of his experiments but this value is required by `CFD-FASTRAN` when defining an inlet. The freestream pressure was estimated initially using an ideal gas assumption and then adjusted iteratively until the freestream density reported by Wen for Shot 491 was achieved in the CFD solution. Additionally, the freestream temperature of the air is very high so chemical reactions are already taking place even before the gas is

---

<sup>6</sup>This implies that the component of mass fraction gradient normal to the wall for each species is zero.

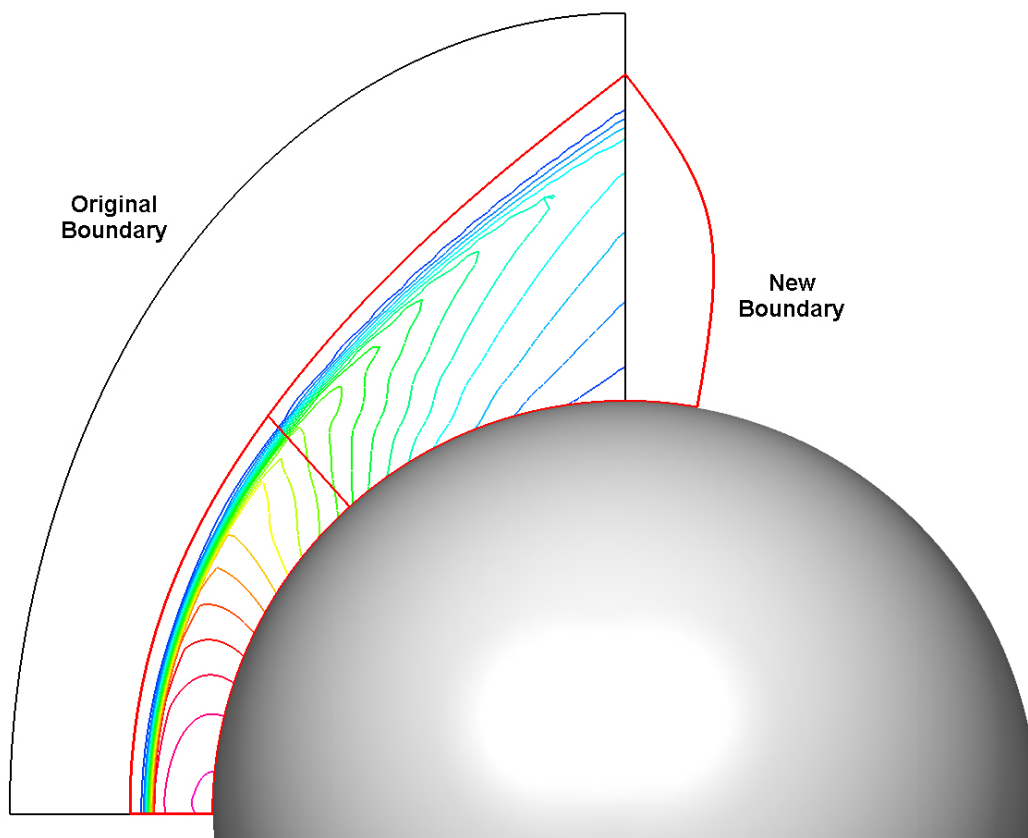


Figure 4.46: Original and reduced grids with isobars from the original grid.

slowed down by the bow shock. It is therefore necessary to define the freestream species concentrations at the inlet. This information was recorded by Wen during his experiment but the reported concentrations did not sum to one. This is presumably a typing error so each concentration has been appropriately scaled such that the fractions sum to one. The freestream value of monatomic Nitrogen was also truncated to zero. Table 4.18 shows both the reported and adjusted concentrations. The adjusted concentrations were used for the inlet boundary condition and the initial condition for all regions of the model.

There is a further issue with regards to the boundary and initial conditions. In Wen's thesis there is no mention of the freestream vibrational temperature for any of his experiments. A model which considers thermal nonequilibrium effects requires the vibrational temperature to be specified at the inlet as well as an initial condition. Whilst the initial vibrational temperature should have no bearing on the final steady result, the inlet vibrational temperature will. Assessment of the freestream vibrational temperature is difficult as parts of the experimental facility must be considered in order to assess how the vibrational temperature changes before reaching the inlet to the flow domain. To account for this unknown freestream vibrational temperature, the sensitivity of the model to this value was briefly explored. The results of this study are discussed in the following section.

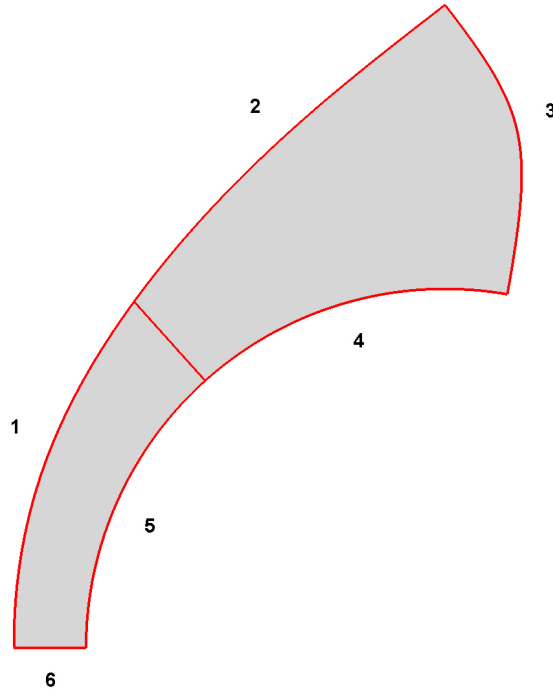


Figure 4.47: Multi-block grid for Case 6.

Table 4.16: Boundary conditions for Case 6A and 6B.

patch	BC type	BC sub type	$\mathbf{v}$ (m/s)	P(Pa)	T(K)	$T_{\text{VIB}}$ (K)
1 - 2	inlet	flow rate	(4860,0)	13,039	2070	2,500 K <sup>‡</sup>
3	outlet	extrapolated	calculated	calculated	calculated	calculated
4 - 5	wall	isothermal	(0,0)	calculated	297	calculated
6	symmetry	-	calculated	calculated	calculated	calculated

<sup>‡</sup> Refer to Section 4.6.5.

Table 4.17: Initial conditions for Case 6A and 6B.

quantity	value
velocity (u,v) (m/s)	(4860,0)
pressure (Pa)	13,039
temperature (K)	2070
vibrational temperature (K)	2,500 K <sup>‡</sup>

<sup>‡</sup> Refer to Section 4.6.5.

Table 4.18: Freestream species concentrations for Case 6B.

species	reported mass fraction for Shot 491	adjusted mass fraction
N <sub>2</sub>	0.733	0.7430
O <sub>2</sub>	0.0982	0.0995
NO	0.0474	0.0480
N	$2.49 \times 10^{-6}$	0.000
O	0.108	0.1095

### 4.6.5 Solution Setup

The model was run with a Jacobi Point Iterative implicit time integration scheme using a CFL of 2.5 together with Roe’s FDS scheme for spatial integration. Backwards-Euler time accuracy was used for integration in time. The default values were used for the entropy fix parameters (0.2 for both linear and nonlinear waves). A flux limiter was not used for this model because of problems resulting from the proximity of the optimised grid to the bow shock. Optimisation of the grid shape allowed for a more efficient solution but it was found that this caused problems within the solution itself due to close alignment of the inlet boundary to the bow shock. It was found that slight misalignment between the inlet boundary and the bow shock introduced disturbances in the form of artificial waves emanating from points at which the bow shock crossed over grid lines. In addition to this effect a perturbation in the bow shock would often form along the symmetry line. This effect is known as the “carbuncle phenomenon” [51], [64], [53] and as noted by Quirk [67] appears to be more pronounced when the grid is closely aligned to the bow shock. These disturbances were greatly exacerbated by the use of higher order flux limiters which amplified and sustained the disturbances throughout the simulation and prevented convergence of the model past 2 - 3 orders of magnitude. The dissipative nature of the first order scheme tended to dampen and even suppress the disturbances. The higher order flux limiters were therefore removed in the final solution thereby increasing the stability and filtering out the disturbances but at the same time increasing the dissipation and decreasing the overall accuracy of the solution.

### Chemical Reaction Scheme

For Case 6B, air was treated as a mixture of reacting gases. The forward rate at which chemical reactions proceeded was calculated using a modified Arrhenius relation whilst the backwards rate was modelled by assuming equilibrium:

$$K_f = C_1 T^\eta e^{\left[\frac{-\epsilon_0}{kT}\right]}$$

$$K_b = \frac{K_f}{K_{eq}}$$

$C_1, \eta$  and  $\frac{-\epsilon_0}{k}$  are experimentally derived constants which differ for each reaction. The reaction scheme also contained a third body (M) for each of the dissociation reactions and a corresponding third body efficiency ( $\text{eff}_M$ ). The third body represents any species which is not directly involved in the reaction but does effect the reaction rate through its presence. The third body efficiency is a multiplying factor on the reaction rate such that numbers less than one imply a retardation of the reaction whilst numbers greater than one imply an accelerated reaction. The reaction scheme used in this study is PARK-I [60]. PARK-I is one of the most common schemes used for modelling the chemistry of air without the consideration of ionisation. The PARK-I reaction scheme involves five species ( $\text{N}_2$ ,  $\text{O}_2$ ,  $\text{N}$ ,  $\text{O}$  and  $\text{NO}$ ) and seventeen reactions. These reactions and their corresponding rate data are listed in Table 4.19.

Table 4.19: Park-1 reaction scheme for air

type	reaction	M	$C_1$	$\text{eff}_M$	$\eta$	$\frac{-\epsilon_0}{k}$
dissociation	$\text{O}_2 + \text{M} \leftrightarrow \text{O} + \text{O} + \text{M}$	N	$8.25 \times 10^{16}$	3.0	-1.00	59,500
		$\text{N}_2$	$2.75 \times 10^{16}$	1.0	-1.00	59,500
		O	$8.25 \times 10^{16}$	3.0	-1.00	59,500
		$\text{O}_2$	$2.75 \times 10^{16}$	1.0	-1.00	59,500
		NO	$2.75 \times 10^{16}$	1.0	-1.00	59,500
dissociation	$\text{N}_2 + \text{M} \leftrightarrow \text{N} + \text{N} + \text{M}$	N	$1.11 \times 10^{19}$	3.0	-1.60	113,200
		$\text{N}_2$	$3.70 \times 10^{18}$	1.0	-1.60	113,200
		O	$1.11 \times 10^{19}$	3.0	-1.60	113,200
		$\text{O}_2$	$3.70 \times 10^{18}$	1.0	-1.60	113,200
		NO	$3.70 \times 10^{18}$	1.0	-1.60	113,200
dissociation	$\text{NO} + \text{M} \leftrightarrow \text{N} + \text{O} + \text{M}$	N	$4.60 \times 10^{14}$	2.0	-0.50	77,500
		$\text{N}_2$	$2.30 \times 10^{14}$	1.0	-0.50	77,500
		O	$4.60 \times 10^{14}$	2.0	-0.50	77,500
		$\text{O}_2$	$2.30 \times 10^{14}$	1.0	-0.50	77,500
		NO	$2.30 \times 10^{14}$	1.0	-0.50	77,500
neutral exchange	$\text{NO} + \text{O} \leftrightarrow \text{N} + \text{O}_2$	-	$2.16 \times 10^5$	-	1.29	19,220
neutral exchange	$\text{O} + \text{N}_2 \leftrightarrow \text{N} + \text{NO}$	-	$3.18 \times 10^{10}$	-	0.10	37,700

### Nonequilibrium Considerations

The flow moving through the nozzle of the T5 shock tunnel expands rapidly and so the molecules of air become more sparse and are less likely to collide the further they move down the nozzle. It is therefore inappropriate to assume that equilibrium conditions will occur at the inlet to the CFD model. If the flow at the inlet is not in equilibrium then the vibrational temperature needs to be known in order to perform a simulation. Unfortunately, this information has not been made available in Wen's thesis. Case 6B was run twice with different inlet vibrational temperatures to explore the sensitivity of the

solution to the freestream vibrational temperature. The first model assumed equilibrium ( $T_{VIB\infty} = T_{\infty} = 2,070$ ) whilst the second model used a vibrational temperature of around 20% higher (this temperature was rounded up to 2,500 K). Results for the maximum pressure, density, temperature and vibrational temperature are reported for both models in Table 4.20. The relative difference is also reported. Fortunately, the simulation does not appear to be greatly sensitive to the freestream vibrational temperature. The change in freestream vibrational temperature also had little impact on the structure of the flow as shown in Figure 4.48 which shows a split-view style plot of temperature contours with the top half showing contours for  $T_{VIB\infty}$  at equilibrium and the bottom half showing  $T_{VIB\infty}$  at 2,500 K. The value of vibrational temperature used for the final simulation was 2,500 K. This value was also used as the initial vibrational temperature.

### 4.6.6 Results and Comparisons

Results from the CFD-FASTRAN simulation of the hypervelocity flow over a 4" sphere are shown in Figure 4.49 - 4.52. Figure 4.49 shows a split-view style image with an experimental finite fringe interferogram taken during Shot 491 on the top half together with isopycnics from the chemically reacting CFD-FASTRAN simulation on the bottom. The experimental interferogram is not directly compared to a numerical interferogram because the axisymmetric structure of the flow makes the numerical interferogram quite complex to reproduce and beyond the abilities of the available software (see Section 3.5.2). The comparison between the two images is good in terms of both the bow shock stand off distance, which is sensitive to the flow chemistry, and the boundary layer thickness. Figure 4.50 shows a split-view style comparison of pressure, density, temperature and speed with the calorically perfect gas model on the top half and the real gas model on the bottom half. The range has been kept constant between the two models for each quantity. The main differences between the two models include the reduction in shock stand-off distance and peak temperature seen in the reacting gas model. The peak temperature is smaller in the reacting gas model because thermal energy is absorbed by the chemical reactions. Figure 4.51 shows the distribution of vibrational temperature and species mass fractions for the chemically reacting CFD-FASTRAN model. The mass fractions are also plotted across the stagnation streamline (centerline) in Figure 4.52 so that the change in species concentration across the shock can be seen more clearly.

Table 4.20: Sensitivity of the solution to freestream vibrational temperature.

quantity	$T_{VIB\infty} = 2,070$ (equilibrium)	$T_{VIB\infty} = 2,500$ (frozen)	difference
$P_{max}$ (Pa)	450,342	450,507	0.04%
$\rho_{max}$ , (kg/m <sup>3</sup> )	4.725	4.707	0.38%
$T_{max}$ (K)	9,203	9,286	0.90%
$T_{VIB_{max}}$ (K)	8,232	8,392	1.94%

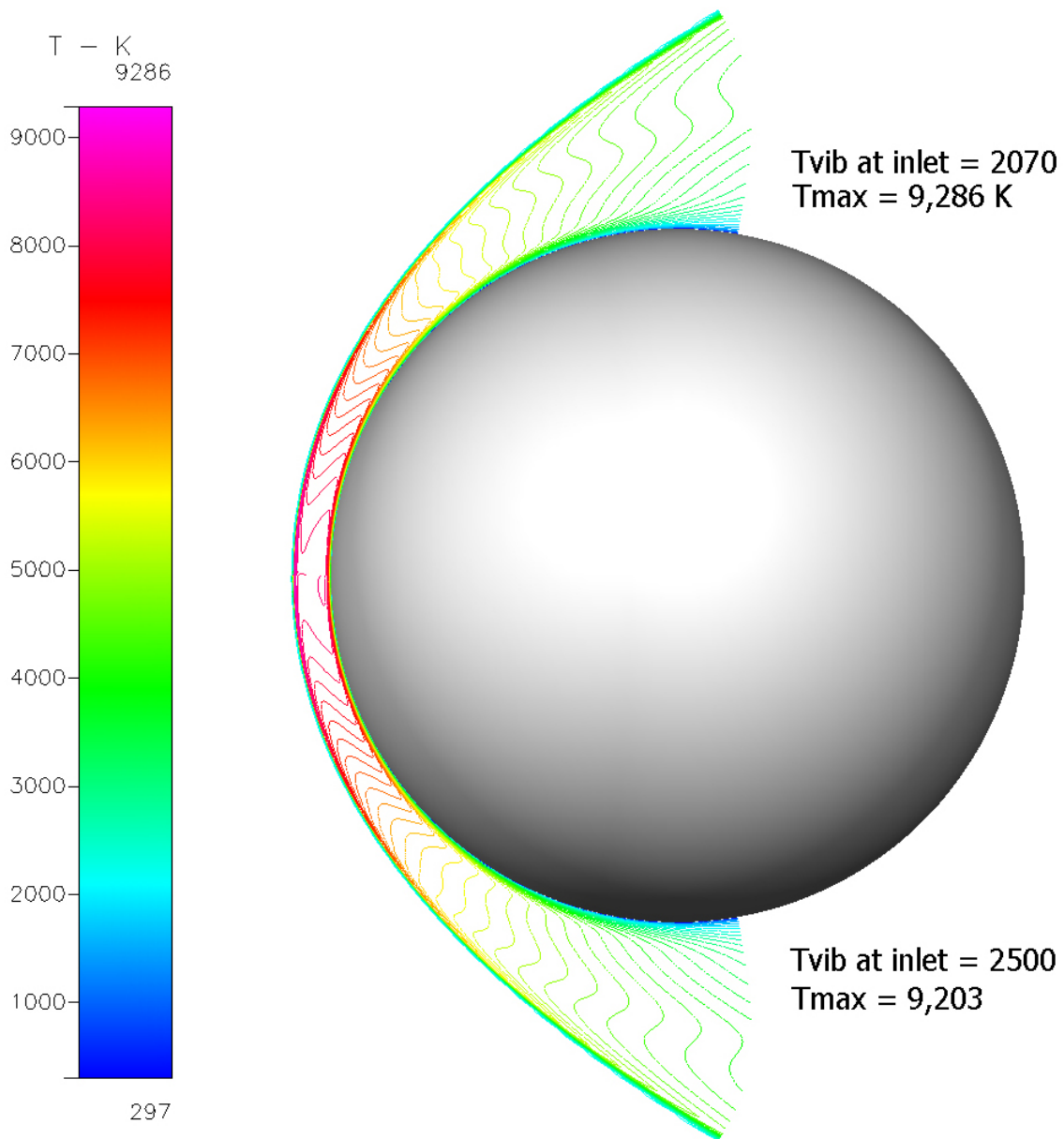


Figure 4.48: Contours of temperature for different freestream vibrational temperatures.

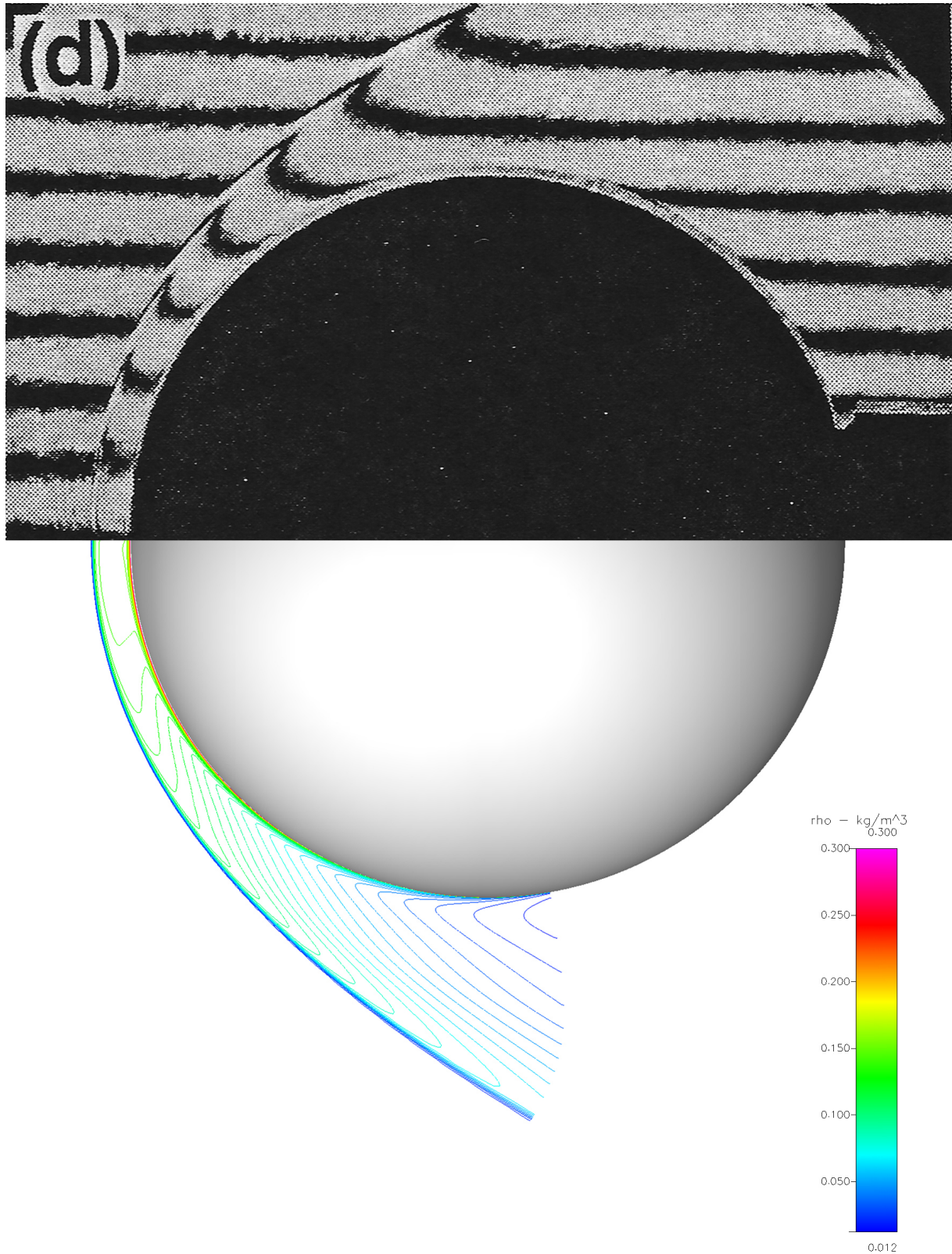


Figure 4.49: Comparison of an interferogram from Shot 491 (top half) with isopycnics from the chemically reacting CFD-FASTRAN simulation (bottom half).

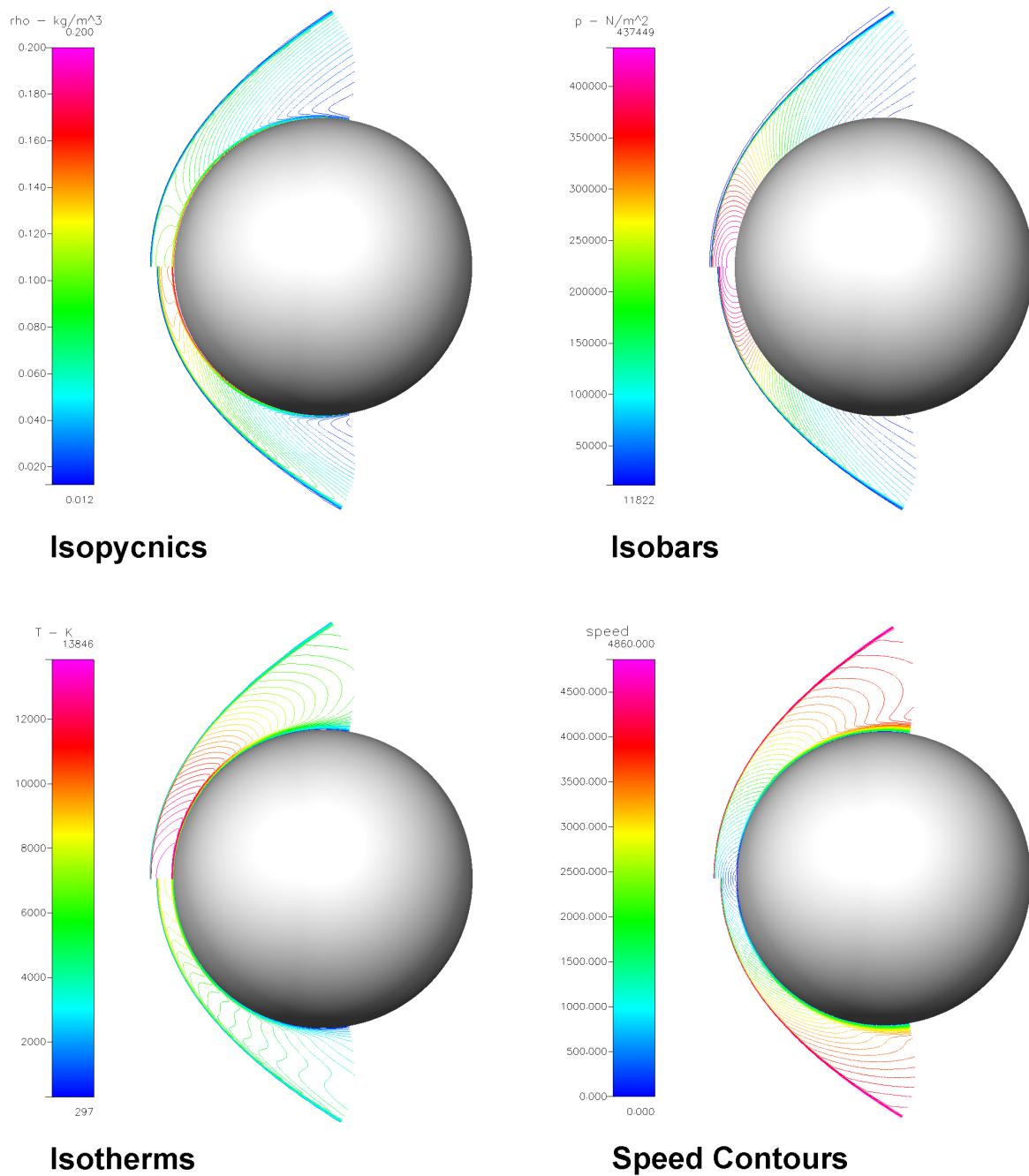


Figure 4.50: Comparison of results for the CFD-FASTRAN perfect gas simulation (top half) and chemically reacting simulation (bottom half).

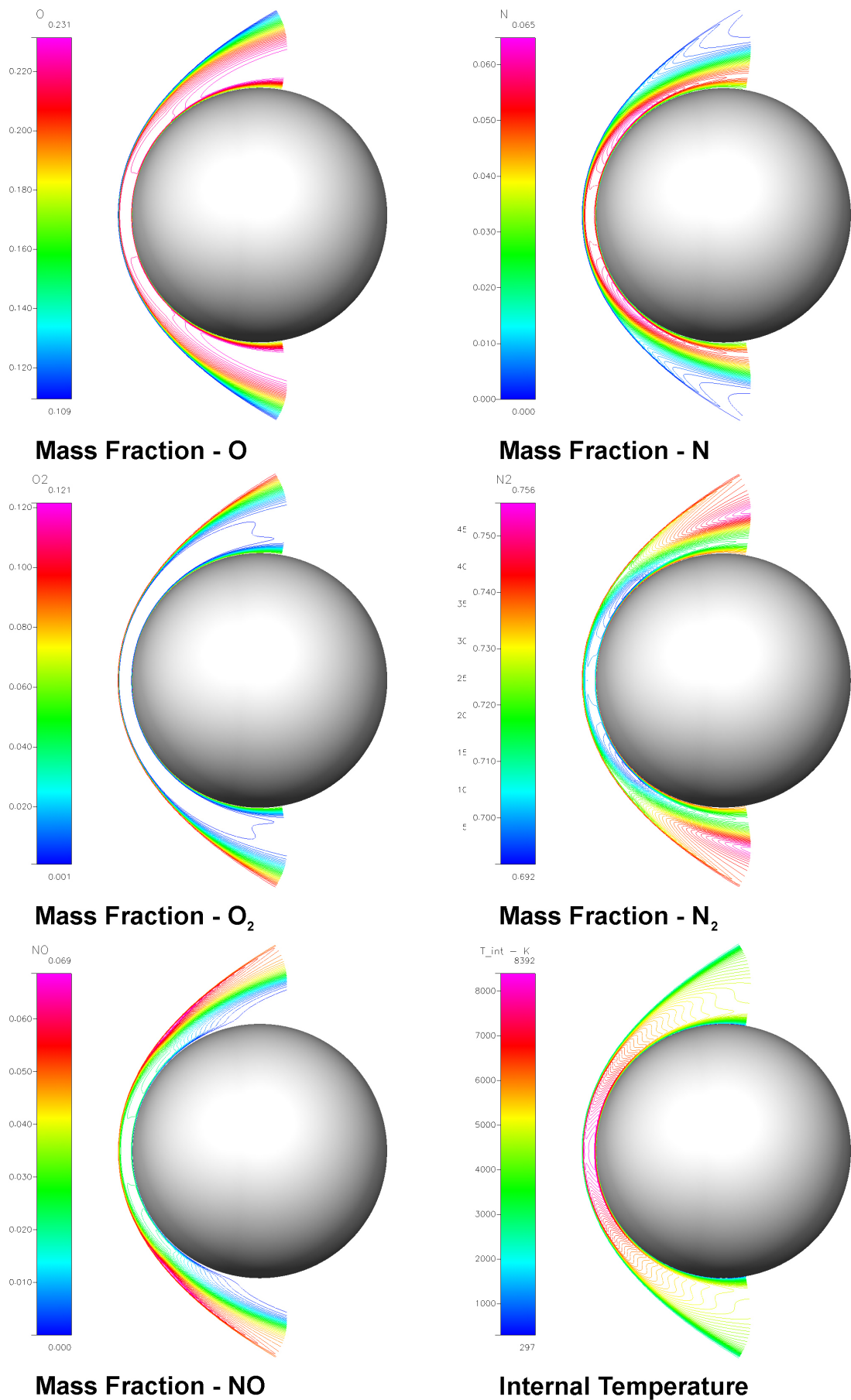


Figure 4.51: Contours of species mass fraction and vibrational temperature for the chemically reacting CFD-FASTRAN simulation.

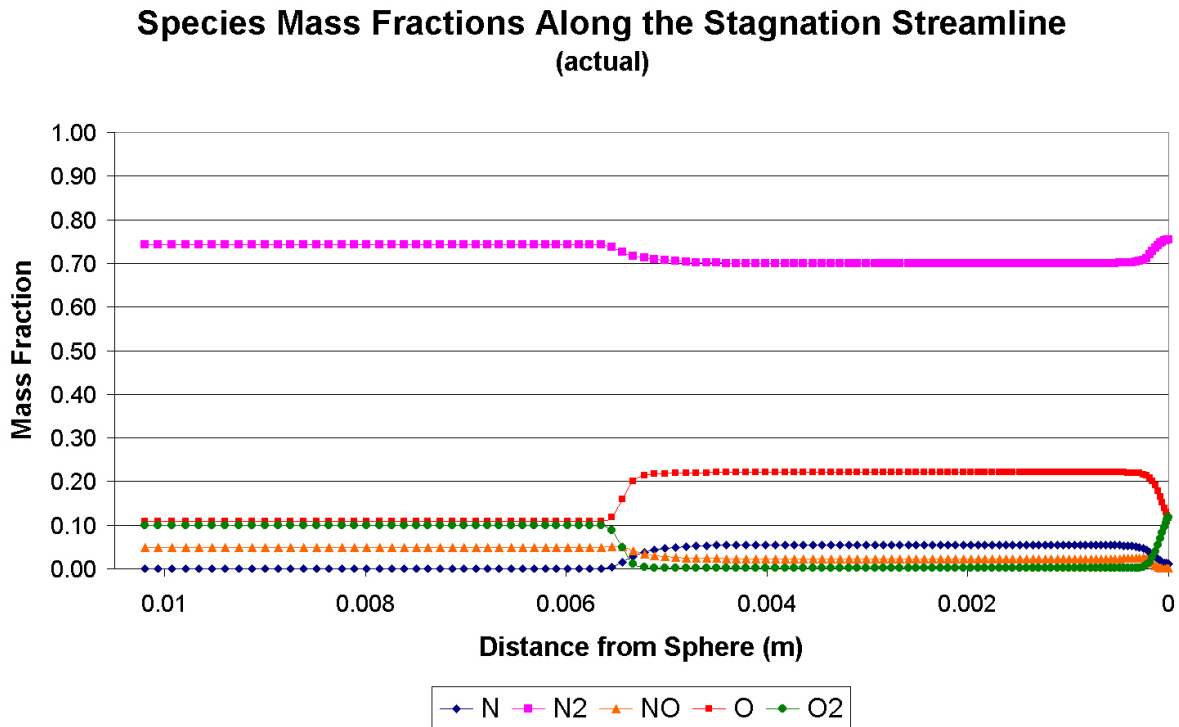


Figure 4.52: Species mass fractions along the stagnation streamline (centerline).

### Stagnation Point Heat Flux

For the purposes of resolving the boundary layer and predicting heat flux, the model contained cells which were clustered towards the sphere as much as possible by biasing the grid in the radial direction. This biasing produces thin cells with high aspect ratios so there is a limit to how strong a bias can be used. The problem can be alleviated by increasing the number of cells along the circumferential direction but the model can easily become large and solution times become long. The maximum  $Y+$  value output from the solution was 5.26 for the ideal gas model and 5.78 for the real gas model. A maximum  $Y+$  of 1.0 or less is optimum for predicting heat fluxes on blunt bodies so it is not surprising that the heat flux is out by a substantial amount in this test case. It is likely that the use of a first order scheme has added to this inaccuracy.

In Wen's thesis, a note is made on the relationship between the Stanton Number at the stagnation point ( $St_s$ ) and the freestream Reynolds number ( $Re_\infty$ ).

$$St_s = \frac{\dot{q}_s}{\rho_\infty U_\infty (h_0 - h_w)} = \frac{k}{\sqrt{Re_\infty}}$$

Where:

$q_s$  = Stagnation point heat transfer

$\rho_\infty$  = Freestream density

$u_\infty$  = Freestream velocity

$h_0$  = Stagnation (reservoir) enthalpy

$h_w$  = Enthalpy at wall at stagnation point

$k$  = Heat transfer coefficient<sup>7</sup>

Wen notes that the enthalpy at the wall is not significant compared to the stagnation enthalpy so the stagnation heat flux can be estimated as follows:

$$q_s \approx \frac{\rho_\infty U_\infty h_0 k}{\sqrt{Re_\infty}}$$

Wen reports the following data for Shot 491 (converted to SI units):

$$\rho_\infty = 0.0199 \text{ kg/m}^3$$

$$u_\infty = 4,860 \text{ m/s}$$

$$h_0 = 16.01 \times 10^6 \text{ J/kg}$$

$$Re_\infty = 145,000$$

For all shots using air as a test gas, Wen calculated a mean and standard deviation for the heat transfer constant using Lee's theory, Fay and Riddell's theory, experimental data and CFD. These values are listed in Table 4.21.

Table 4.21: Estimation of the heat transfer constant for a 4" sphere.

	$\bar{k}$	$\sigma/\bar{k}$
Lee's Theory	4.41	2.2%
Fay and Riddell's Theory	4.76	2.0%
Wen's Experimental Data	4.77	5.5%
Wen's CFD Data	5.07	5.6%

Using data from experiment, theory and simulation, Wen has shown that a strong correlation between the stagnation Stanton number and the freestream Reynolds number exists. This relation is shown in Figure 4.53 which is a reproduction of Figure 4.7 from Wen's

<sup>7</sup>Note that this is different to thermal conductivity.

thesis. The actual measured stagnation point heat flux for Shot 491 is not reported by Wen but it can be estimated using the above relationship. If the variation in the heat flux constant reported by Wen (excluding the CFD) is to be considered then the upper and lower bounds of the stagnation point heat flux for Shot 491 are 20.46 MW/m<sup>2</sup> and 17.54 MW/m<sup>2</sup> respectively. The stagnation heat transfer rate predicted by CFD-FASTRAN for the real gas model (Case 6B) was around 50 MW/m<sup>2</sup>. This large error may be attributable to several factors. Firstly, a Y+ value of 1.0 suggests that there is insufficient resolution in the boundary layer for resolving heat transfer. Secondly, a first order scheme was used to maintain stability around the bow shock but this scheme is more dissipative and less accurate than a higher order scheme. Unfortunately it was not possible to investigate these ideas due to time constraints. Future investigation could involve changes to the model such as the addition of more cells in the boundary layer as well as splitting the grid close to the boundary layer to define separate blocks. The inner blocks could then be setup to use a higher order scheme whilst the outer blocks retain the first order scheme.

### Heat Flux Spatial Distribution

Lee's theory also describes the heat flux distribution across a blunt nose body. Lee's theory states the following equation for the heat transfer distribution normalised by the stagnation point heat flux:

$$\frac{\dot{q}(\theta)}{\dot{q}_s} = \frac{2\theta \sin \theta \{(1 - a) \cos^2 \theta + a\}}{\sqrt{(1 - a) \left(\theta^2 - \frac{\theta \sin 4\theta}{2} + \frac{1 - \cos 4\theta}{8}\right) + 4a \left(\theta^2 - \theta \sin 2\theta + \frac{1 - \cos 2\theta}{2}\right)}}$$

Where

$$a = \frac{1}{\gamma_\infty M_\infty^2}$$

The freestream ratio of specific heats ( $\gamma_\infty$ ) is difficult to estimate because the freestream is partly dissociated. Fortunately, the above relation is only a weak function of  $\gamma_\infty$  as can be seen in Figure 4.55 which shows Lee's theory plotted for a  $\gamma_\infty$  of 1.2 and 1.4 with a freestream Mach number of 5.33. Figure 4.55 also shows the normalised heat flux distribution from CFD-FASTRAN. The normalised distribution of heat flux output from CFD-FASTRAN differs somewhat from Lee's theory but this variation is also seen with CFD data from Wen. Figure 4.54 is a reproduction of Figure 4.29 from Wen's thesis. This figure shows the heat flux distribution from experiment, CFD and Lee's theory for Shot 474 (such data was not made available for Shot 491). Shot 474 uses air for a test gas but the sphere is only 3" in diameter. The stagnation enthalpy was 18.97 MJ/kg and the freestream velocity and density were 0.0172 kg/m<sup>3</sup> and 5,250 m/s respectively. The Reynolds number was 94,000. The same trend in Figure 4.55 is noted with the CFD and experimental results shown in Figure 4.54 as both plots predicting a slightly steeper slope than Lee's theory.

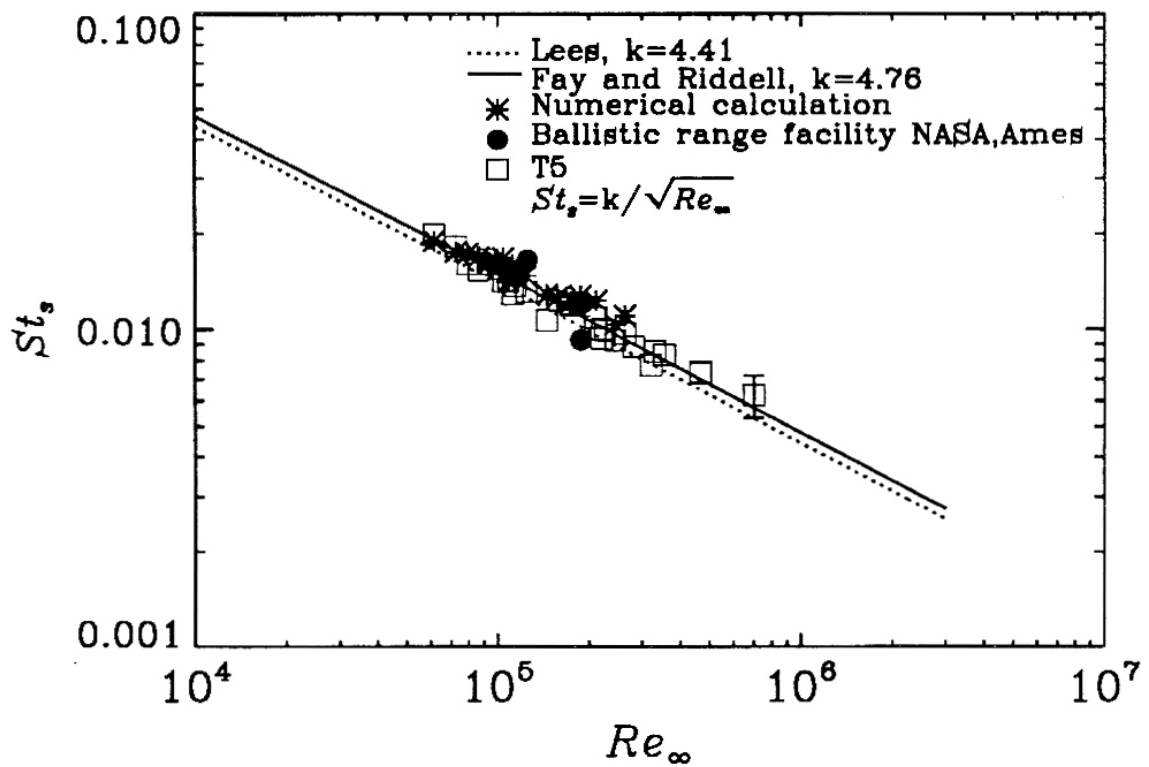


Figure 4.53: Correlation of stagnation Stanton number ( $St_s$ ) and the freestream Reynolds number  $Re_\infty$  for experiment, CFD and theory (reproduction of fig. 4.7 from Wen).

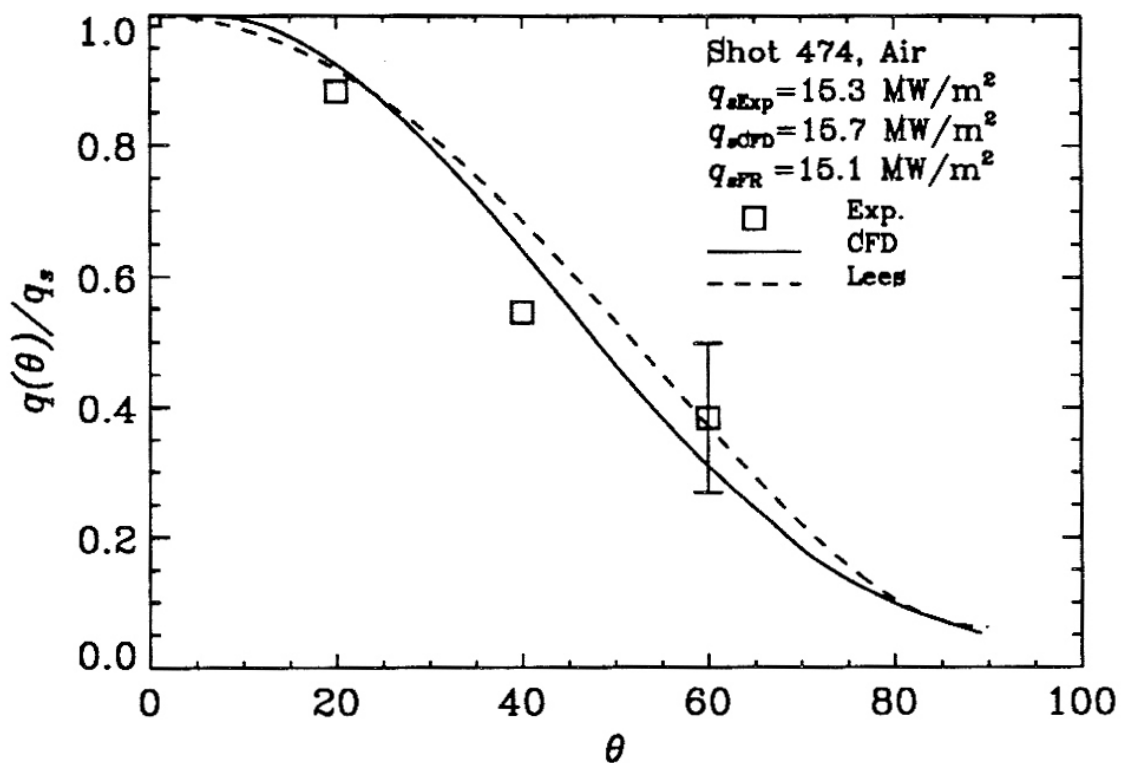


Figure 4.54: Heat flux distribution for Shot 471 (reproduction of fig. 4.29 from Wen).

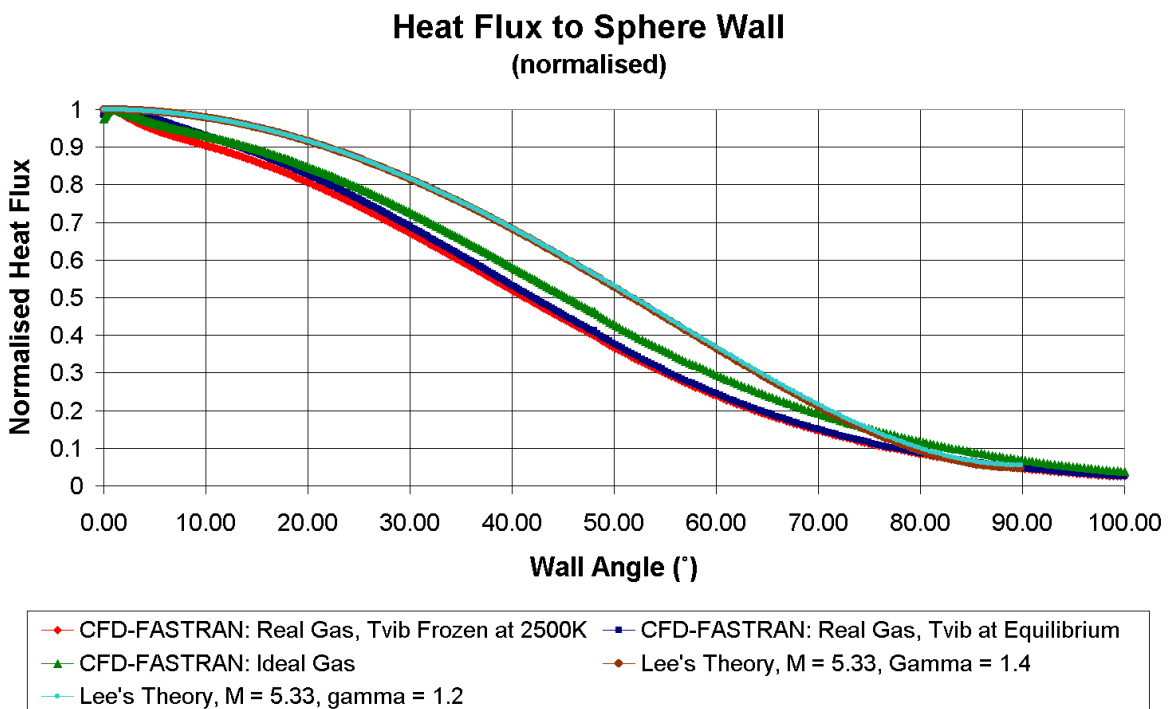
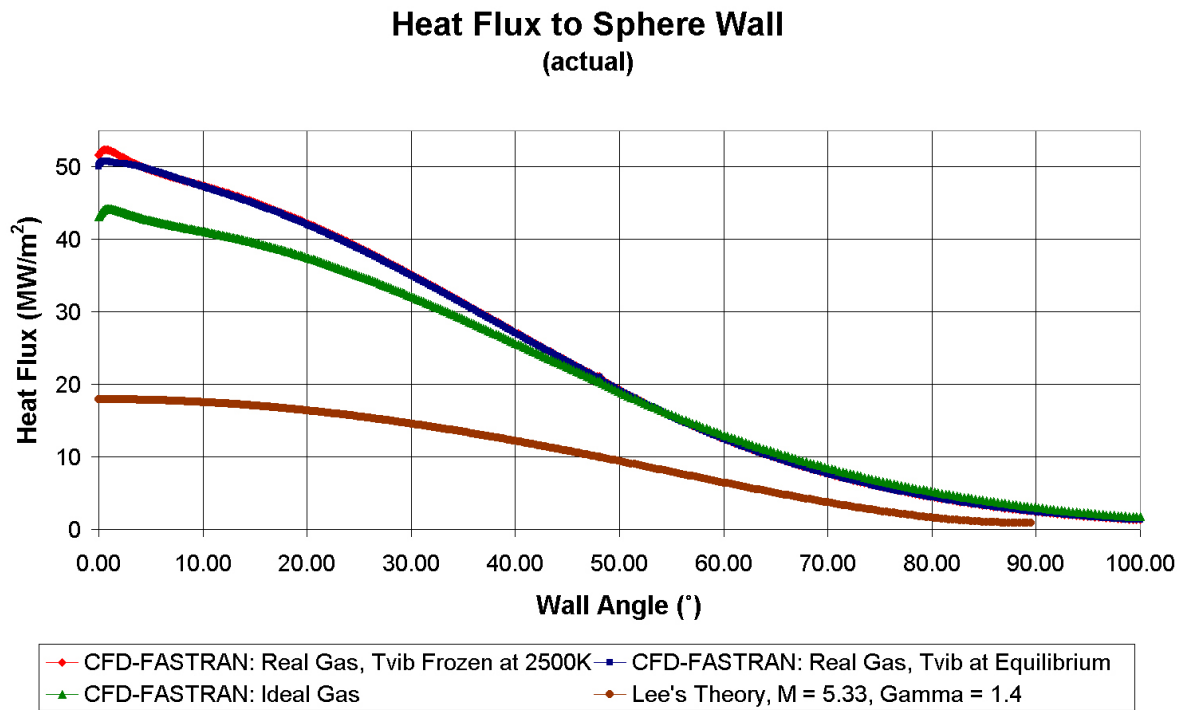


Figure 4.55: Predictions of heat flux distribution across the sphere for Shot 491.



## Conclusions

---

The complexity of modern CFD software codes is commonly hidden from users by easy to use graphical interfaces. Newcomers to CFD can sometimes be given the impression that CFD is no harder than mastering a series of simple interfaces. Whilst mastering the interface of a CFD package is undoubtedly helpful, it will not ensure the user is equipped with the right skills to obtain meaningful answers from that package. It is therefore important for a newcomer to the field of CFD to have some background knowledge before rushing to construct complex models.

In this thesis, the software package CFD-FASTRAN was used to construct and analyse CFD models. CFD-FASTRAN is a commercial software package which solves the compressible Navier-Stokes equations using a density based method. The first three chapters of this thesis were aimed at providing the CFD newcomer with guidance in applying CFD-FASTRAN to supersonic and hypersonic flow problems. When combined with the software manuals [15], [16], [17] and [18] the newcomer should have enough information to model some challenging hypersonic problems. For users of other comparable CFD software, these chapters should provide insight into the tasks required for a successful CFD analysis. Chapter 4 of this thesis was dedicated to presenting six validation cases involving either supersonic or hypersonic flow. The experimental results for these validation cases were obtained from various papers published in AIAA, JFM, the Shock Waves Journal and for Case 4, from the proceedings of the 17th International Symposium on Shock Waves and Shock Tubes. The six cases were selected based on the range of results presented and wherever possible the inclusion of graphical results such as Schlieren images and interferograms. The cases also had to meet the criteria of being planar or axisymmetric flow and were required to exhibit a range of flow phenomena which would be challenging to model.

Cases 1 - 4 examined issues of shockwave dynamics such as the unsteady interaction of shockwaves with vortices, boundary layers, contact surfaces and other shockwaves. These four experiments involved flow at Mach numbers of 3 or less placing them in the mid supersonic range. Cases 5 and 6 focused on the high temperature and nonequilibrium

aspects of high speed flow with Mach numbers in the hypersonic range. The supersonic test cases showed excellent agreement between experiment and simulation. The results of the hypersonic cases also showed good agreement but some discrepancies did arise. These include the location of the boundary layer reattachment point in Case 5 and the estimation of the stagnation point heat transfer in Case 6. A grid dependency study was performed for Case 5 which showed that the reattachment location was reasonably well resolved with respect to the grid, eliminating the grid as a source of error in this case. Such a study was not performed for Case 6 so firm conclusions regarding the nature of the error cannot be made. Possible causes of error include a lack of cells in the boundary layer (the maximum  $Y^+$  value of 5.78 is quite high for heat transfer calculations) and the inability of the solver to account for dissociation-vibration coupling. The incorporation of a more modern flux limiter such as AUSM or one of its variants may have provided a more stable solution with superior accuracy in the boundary layer.

Generally the code performed well overall and particularly well in capturing unsteady shockwave phenomena. However, further studies are required to fully evaluate the scope of hypersonic problems which can be successfully modelled using CFD-FASTRAN.

## 5.1 Suggestions for Future Study

The validation exercises undertaken in this thesis have shown that the area of high temperature gas modelling requires further study. A larger range of validation problems at hypersonic speed is required in order to thoroughly assess the scope of hypersonic problems for which CFD-FASTRAN can be used. This finding is not unexpected as the hypersonic test cases require all of the effects of the supersonic flow in addition to modelling the complex behaviour of high temperature gas. It is therefore likely that any CFD code will be more challenging to validate at hypersonic speeds than at supersonic speeds for a given model.

Figure 5.1 shows the setup of a hollow cylinder extended flare (HCEF) model, a good candidate for another hypersonic validation study. Most researchers who attempted the sharp double cone model presented in Case 5 of this thesis also attempted the HCEF model. Many results are therefore available for comparison. When constructing a CFD model for the HCEF experiment it should be noted that the hole bored into the center of the HCEF model is for the purpose of preventing a bow shock from forming. The flow in this region is not of interest to the study and not required to be modelled.

Figure 5.2 shows a  $25^\circ - 60^\circ$  blunt double cone model for which experimental results are available. The model was investigated using air and Nitrogen at enthalpies of 5 and

10 MJ/kg. The results are presented together with numerical results from two research groups in a paper from Candler and Nompelis [14]. This model is also a good candidate for future research as the paper notes that numerical modelling of the configuration is very sensitive to chemical effects.

In regards to the general direction of future research, there are several different paths which could be explored. One path is to continue to validate relatively simple planar or axisymmetric geometries but explore higher speed flows which require the consideration of more comprehensive thermodynamic models than those considered in this thesis. This path will require the use of a different code to CFD-FASTRAN unless later versions are updated to include more complex thermodynamic models. Such studies might consider validating flows where the exchange of radiative energy into and out of the gas is important. Radiation is particularly intensive to compute as energy can jump cells and so each cell needs to consider not only its neighbouring cells but also every other cell in the model. Radiative energy exchange also occurs across a range of frequencies and is strongly coupled to the nonequilibrium exchange of internal energy and to chemical reaction rates. In models where radiation is important, ionisation may also require consideration and, if a significant portion of the gas is ionised, the effects of the electric and magnetic fields on the flow must also be considered.

Another option for further study would be to investigate validating the effects of turbulence in supersonic and hypersonic flow. Many experimental results are available on this topic which would be ideal for the basis of a validation study. CFD-FASTRAN could be used for this research as there are a number of turbulence models available within the software.

Lastly, this thesis has concentrated on planar and axisymmetric flows so that the computational requirements could be kept to a minimum. There have however been a number of experimental results published which provide examples of true three dimensional flow. One such example which would provide an excellent starting point for a validation study is a paper from Jiang, Onodera and Takayama [43]. This paper compares experimental interferograms with numerical results for the vortex formation which occurs as supersonic flow is discharged out of a square nozzle. Holden also provides many sets of experimental results for three dimensional supersonic and hypersonic flow [36], [33], [34], [32]. Experiments involving transition and turbulence at supersonic and hypersonic speeds are also discussed in these papers.

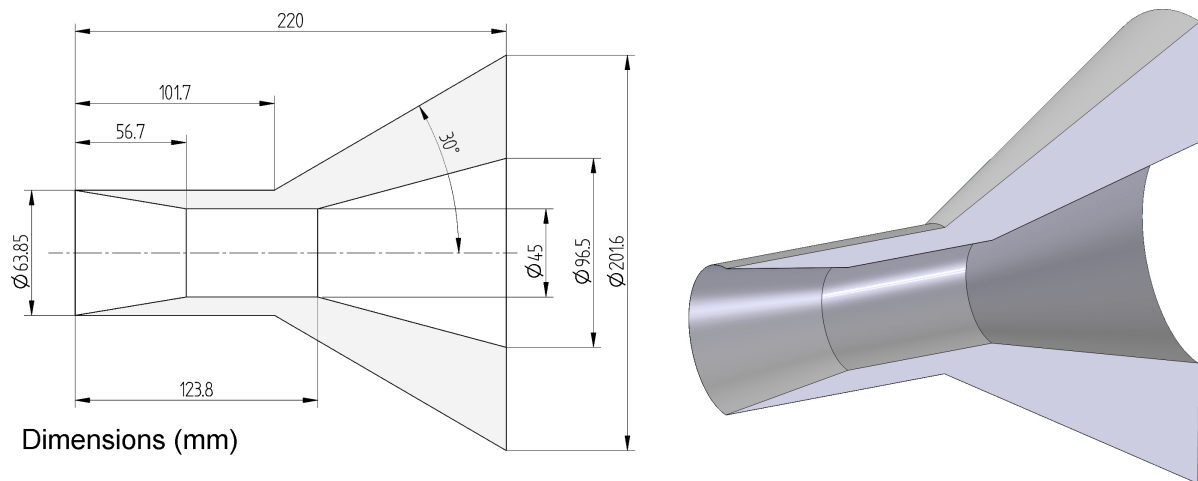


Figure 5.1: Hollow cylinder extended flare (HCEF) model.

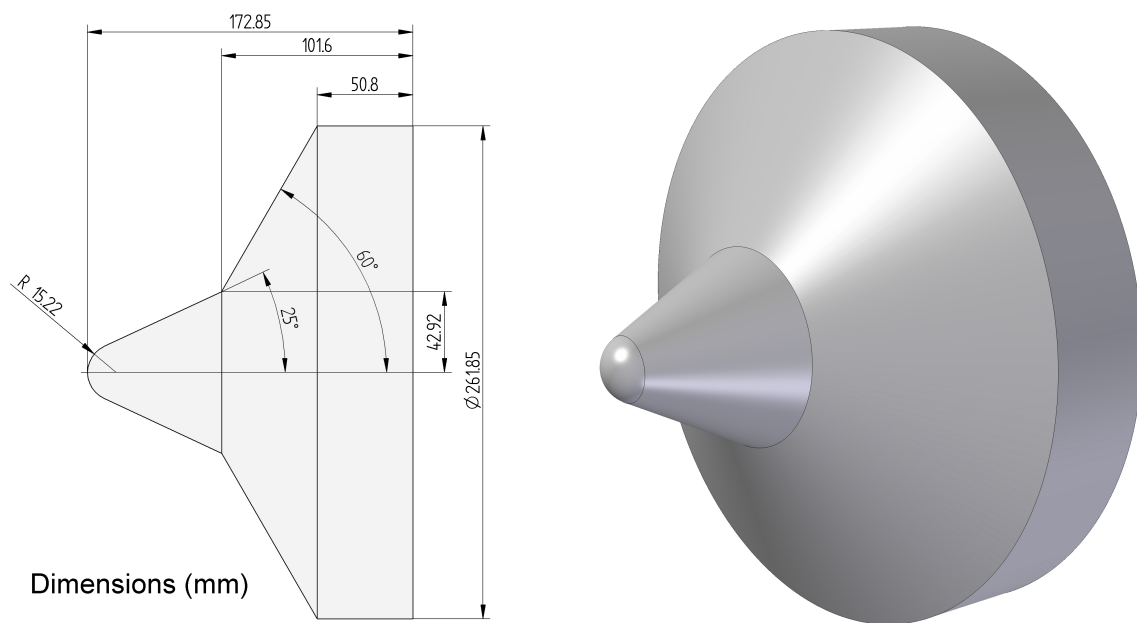


Figure 5.2:  $25^\circ - 60^\circ$  blunt double cone model.

---

## Review of Equations

---

The theoretical equations used by CFD-FASTRAN are presented here for reference. The purpose of this Appendix is to present the equations which are documented in the CFD-FASTRAN v2002 Theory Manual [15] in a form which is specific to this thesis. This Appendix aims to:

- present the theoretical equations from the CFD-FASTRAN Theory Manual in a clear and logical manner
- augment the material with relevant equations from alternative sources
- simplify the equations by removing terms relating to turbulence
- make modifications such that the nomenclature is consistent across all equations
- identify and correct any relevant errors in the existing CFD-FASTRAN documentation

Each equation or set of equations presented in this appendix has been referenced to the source on which it is based, though many equations were edited to keep the nomenclature consistent. Equations from the CFD-FASTRAN Theory Manual [15] which were believed to contain errors have been marked accordingly. Equations sourced from documents other than the CFD-FASTRAN Theory Manual which use different nomenclature are noted. The material presented here is for reference purposes only and no derivation of the equations is presented. Comprehensive derivations of such equations can be found in Anderson's Texts [8], [7] or in Hirsch's Texts [29], [30]. The GASP User Manual also provides useful reference material [5]. Note that all nomenclature is defined at the beginning of this thesis. Finally, the equations presented here are in tensor notation  $\left(\frac{\partial u_i}{\partial x_j} \text{ etc.}\right)$ . Those not familiar with tensor notation might wish to consult the text "Transportation Phenomena" [9] which contains a comprehensive appendix on vector and tensor notation in the context of gas dynamics. The text itself also contains many derivations related to the material presented in this appendix.

## A.1 Conservation Equations

The conservation equations describe the balance of mass, momentum and energy which occur in fluid dynamics. The form of the conservation equations presented here is for the laminar flow of compressible gases. The equations of inviscid flow can be obtained by removing the diffusion terms ( $J, \mu$  and  $\kappa$ ) from the equations.

### Conservation of Mass

For a single species flow:

$$\frac{\partial}{\partial t}(\rho) + \frac{\partial}{\partial x_j}(\rho u_j) = 0$$

CFD-FASTRAN Theory Manual [15], Page 2-3

For each species in a multiple species flow:

$$\frac{\partial}{\partial t}(\rho_s) + \frac{\partial}{\partial x_j}(\rho_s u_j) = -\frac{\partial}{\partial x_j}(J_{sj}) + \omega_s$$

CFD-FASTRAN Theory Manual [15], Page 2-4

Where the total density is the sum of species densities:

$$\rho = \sum_{s=1}^n (\rho_s)$$

CFD-FASTRAN Theory Manual [15], Page 2-5

### Conservation of Momentum

For a single or multiple species flow:

$$\frac{\partial}{\partial t}(\rho u_i) + \frac{\partial}{\partial x_j}(\rho u_i u_j) = \frac{\partial}{\partial x_j}(\tau_{ij} - p\delta_{ij})$$

CFD-FASTRAN Theory Manual [15], Page 2-4

### Conservation of Energy

For a single species flow:

$$\frac{\partial}{\partial t}(E_t) + \frac{\partial}{\partial x_j} [(E_t + p)u_j] = \frac{\partial}{\partial x_j}(q_j) + \frac{\partial}{\partial x_i}(u_j\tau_{ij})$$

Adapted from CFD-FASTRAN Theory Manual [15], Page 2-4

For a multiple species flow:

$$\frac{\partial}{\partial t}(E_t) + \frac{\partial}{\partial x_j} [(E_t + p)u_j] = \frac{\partial}{\partial x_j}(q_j) + \frac{\partial}{\partial x_i}(u_j\tau_{ij}) - \frac{\partial}{\partial x_j} \left[ \sum_{s=1}^n h_s J_{s,j} \right]$$

CFD-FASTRAN Theory Manual [15], Page 2-4

Note  $E_t$  denotes the total energy per unit volume whereas  $e_t$  denotes the total energy per unit mass.

### Conservation of Internal Energy (thermal nonequilibrium flow only)

For a single species flow:

$$\frac{\partial}{\partial t}(E_{\text{int}}) + \frac{\partial}{\partial x_j} [E_{\text{int}}u_j] = \omega_{\text{int}} - \frac{\partial}{\partial x_j}(q_{\text{int},j})$$

Adapted from the CFD-FASTRAN Theory Manual [15], Page 2-5

For a multiple species flow:

$$\frac{\partial}{\partial t}(E_{\text{int}}) + \frac{\partial}{\partial x_j} [E_{\text{int}}u_j] = \frac{\partial}{\partial x_j} \left[ \sum_{s=1}^n (e_{\text{int},s} J_{s,j} - q_{\text{int},j}) \right] + \omega_{\text{int}}$$

CFD-FASTRAN Theory Manual [15], Page 2-5

Where  $\omega_{\text{int}}$  is the internal energy source term as defined in section A.4.

## A.2 Equations of State

The equations of state are a set of constitutive relations which link together variables which describe the state of matter. These variables include the physical attributes of a gas such as pressure ( $p$ ), temperature ( $T$ ) and density ( $\rho$ ) as well as the less tangible quantities such as enthalpy ( $h$ ) and entropy ( $S$ ).

### Single Species Calorically Perfect Gas

$$p = \frac{\rho R_U T}{\mathcal{M}}$$

CFD-FASTRAN Theory Manual [15], Page 3-1

$$E_t = \rho C_V T + \frac{1}{2} \rho (u_j \cdot u_j)$$

CFD-FASTRAN Theory Manual [15], Page 3-2

$$C_V = \frac{R_U}{\mathcal{M}(\gamma - 1)}$$

CFD-FASTRAN Theory Manual [15], Page 3-3

$$C_P = \frac{R_U}{\mathcal{M}\gamma(\gamma - 1)}$$

Derived from the previous equation and  $\gamma = \frac{C_P}{C_V}$

### Multiple Species Thermal Equilibrium and Nonequilibrium

$$p = \sum_{s=1}^n \left( \frac{\rho_s R_U T}{\mathcal{M}_s} \right)$$

CFD-FASTRAN Theory Manual [15], Page 3-2

and as noted in section A.1:

$$\rho = \sum_{s=1}^n (\rho_s)$$

CFD-FASTRAN Theory Manual [15], Page 2-5

$$C_V = \sum_{s=1}^n ([Y_s] C_{V,s})$$

CFD-FASTRAN Theory Manual [15], Page 3-5

$$C_P = \sum_{s=1}^n ([Y_s] C_{P,s})$$

CFD-FASTRAN Theory Manual [15], Page 3-5

## Total Energy

THERMAL EQUILIBRIUM USING THE LOW TEMPERATURE DATABASE OPTION:

$$E_t = \sum_{s=1}^n \rho_s \left( h_s - \frac{R_U T}{\mathcal{M}_s} \right) + \frac{1}{2} \rho (u_j \cdot u_j)$$

CFD-FASTRAN Theory Manual [15], Page 3-3

Where  $h_s$  is the sensible enthalpy per unit mass for species “s”:

$$h_s = \int_{T_{\text{ref}}}^T C_{P,s}(T) dT + \Delta h_{f,s,T_{\text{ref}}}^0$$

CFD-FASTRAN Theory Manual [15], Page 3-3

THERMAL NONEQUILIBRIUM USING LOW TEMPERATURE DATABASE OPTION:

Note that for thermal nonequilibrium CFD-FASTRAN assumes a two temperature model. A standard temperature ( $T$ ) which is proportional to translational-rotational molecular energy is used together with an internal temperature  $T_{\text{int}}$ , which is proportional to the vibrational-electronic molecular energy (internal energy). This temperature is purely vibrational if the molecular database is used. The internal energy equation is enabled only when using a two temperature model. CFD-FASTRAN allows one internal energy equation per model whereas a more precise (but more computationally intensive) method would involve a separate internal energy equation for each species. The expression for total energy per unit volume for a nonequilibrium model using the low temperature database is:

$$E_t = \sum_{s=1}^n \rho_s \left( (C_{V,Trans} + C_{V,Rot})(T - T_{\text{ref}}) + \Delta h_{f,s,T_{\text{ref}}}^0 + T_{\text{ref}} \frac{R_U}{\mathcal{M}_s} \right) + E_{\text{int}} + \frac{1}{2} \rho (u_j \cdot u_j)$$

CFD-FASTRAN Theory Manual [15], Page 3-3

THERMAL EQUILIBRIUM OR NONEQUILIBRIUM USING MOLECULAR DATABASE OPTION:

$$E_t = \sum_{s=1}^n \rho_s \left( (C_{V,Trans} + C_{V,Rot})T + \Delta h_{f,s,T_{\text{ref}}}^0 \right) + E_v + \frac{1}{2} \rho (u_j \cdot u_j)$$

Adapted CFD-FASTRAN Theory Manual [15], Page 3-2

$E_v$  is the vibrational energy per unit volume:

$$E_v = \sum_{s=1}^n (\rho_s e_{Vib,s})$$

Where  $e_{Vib,s}$  is the total vibrational energy for species “s” as defined in section A.4.

### The Low-Temperature Database Option

This option instructs CFD-FASTAN to use polynomials fitted from experimental data when evaluating the specific heat ( $C_{P,s}$ ), sensible enthalpy ( $h_s$ ) and entropy ( $S_s$ ) for a species. The valid range for this data is stated as 300 K - 6,000 K<sup>1</sup>, however temperatures outside this range are handled using the method described on Page 3-14 of the CFD-FASTAN Theory Manual [15]. The polynomial constants  $a_1 - a_6$  are from curve fits to experimental data published by Svehla and McBride [73]. These curves are commonly known as NASA Lewis Research Center (LeRC) curve fits for thermodynamic data. Curve fits for many typical species are included in the file “low\_temp.dat”, which is supplied with the CFD-FASTAN solver. This file also includes the species molecular weight ( $\mathcal{M}_s$ ) and the heat of formation at STP ( $\Delta h_{f,s,T_{ref}}^0$ ). The following set of equations are used when the low temperature database option is enabled:

$$h_s \approx \frac{R_U T}{\mathcal{M}_s} \left( a_1 + \frac{a_2 T}{2} + \frac{a_3 T^2}{3} + \frac{a_4 T^3}{4} + \frac{a_5 T^4}{5} + \frac{a_6}{T} \right)$$

CFD-FASTAN Theory Manual [15], Page 3-4

$$C_{P,s} \approx \frac{R_U}{\mathcal{M}_s} (a_1 + a_2 T + a_3 T^2 + a_4 T^3 + a_5 T^4)$$

CFD-FASTAN Theory Manual [15], Page 3-4

$$S_s \approx \frac{R_U T}{\mathcal{M}_s} \left( a_1 \ln T + a_2 T + \frac{a_3 T^2}{2} + \frac{a_4 T^3}{3} + \frac{a_5 T^4}{4} + a_7 \right)$$

CFD-FASTAN Theory Manual [15], Page 3-5

### The Molecular Database Option

The Molecular Database option instructs CFD-FASTAN to use spectroscopic data for each species which is located in the file “fastran\_molecular.dat”. The spectroscopic data was obtained from McBride et al. [56] with the exception of data on the species H<sub>2</sub>,OH, HNO, HO<sub>2</sub> and H<sub>2</sub>O<sub>2</sub> which was obtained from Wilson [83]. Using the Molecular Database option, the specific heat ( $C_V$ ) is separated into translational, rotational and vibration components. Note that this option neglects electronic modes of internal

<sup>1</sup>This range is quoted as 300 K - 5,000 K in the GASP User Manual [5].

energy. The internal temperature is therefore equal to the vibrational temperature with this option. The total specific heat for species “s” can be expressed as follows:

$$C_{V,s} = C_{V,Trans,s} + C_{V,Rot,s} + C_{V,Vib,s}$$

Based on Anderson [7], Page 440

The translational component of the specific heat is constant across all species. The rotational component of the specific heat is determined from the rotational degrees of freedom in the molecule ( $\varepsilon$ ). Monatomic gases such as Helium (He) have no rotational degrees of freedom, diatomic and linear polyatomic gases such as Nitrogen ( $N_2$ ) have two and non-linear polyatomic gases such as steam ( $H_2O$ ) have three. The translational and rotational components of specific heat are calculated as follows:

$$C_{V,Trans,s} = \frac{3R_U}{2\mathcal{M}_s}$$

CFD-FASTRAN Theory Manual [15], Page 3-9

$$C_{V,Rot,s} = \frac{\varepsilon R_U}{2\mathcal{M}_s}$$

CFD-FASTRAN Theory Manual [15], Page 3-9

For the vibrational component of specific heat, the value depends on whether the thermal equilibrium option or the two temperature nonequilibrium option is chosen. In the more general case of thermal nonequilibrium the vibrational temperature can differ from the physical (translational-rotational) temperature. In this case, CFD-FASTRAN uses separate equations to model the conservation of energy and the conservation of internal energy. In this case both the temperature and a vibrational temperature are considered and the specific heat is described by the equation:

$$C_{V,Vib,s} = \sum_{m=1}^N \left( \frac{R_U}{\mathcal{M}_s} \left( \frac{\Theta_{V,s}^{(m)}}{T_{Vib}} \right)^2 \frac{e^{\left( \frac{\Theta_{V,s}^{(m)}}{T_{Vib}} \right)}}{\left( e^{\left( \frac{\Theta_{V,s}^{(m)}}{T_{Vib}} \right)} - 1 \right)^2} \right)$$

Adapted from Gasp User Manual [5], Page 493

For the case of equilibrium the two temperatures are equal and only one energy equation is modelled. In this case the equation is the same as the previous equation but with T in the place of  $T_{Vib}$  (the asterisk denotes equilibrium):

$$C_{V,Vib,s}^* = \sum_{m=1}^N \left( \frac{R_U}{\mathcal{M}_s} \left( \frac{\Theta_{V,s}^{(m)}}{T} \right)^2 \frac{e^{\left( \frac{\Theta_{V,s}^{(m)}}{T} \right)}}{\left( e^{\left( \frac{\Theta_{V,s}^{(m)}}{T} \right)} - 1 \right)^2} \right)$$

Gasp User Manual [5], Page 493

Lastly, CFD-FASTRAN assumes all molecules are harmonic oscillators such that:

$$\Theta_{V,s}^{(m)} = \frac{\hbar \nu^{(m)}}{k}$$

GASP User Manual [5], Page 492

## A.3 Diffusion and Transport Properties

Diffusion is the exchange of mass, momentum and energy on a molecular level. Diffusion is considered only in viscous flow. CFD-FASTRAN allows for the diffusion of mass, momentum and energy when a laminar or turbulent flow model is selected. If the nonequilibrium flow option is selected then CFD-FASTRAN also considers diffusion of internal energy. Each mode of diffusion relates to a conservation equation:

- Mass Diffusion (conservation of mass)
- Momentum Diffusion (conservation of momentum)
- Thermal Diffusion (conservation of energy)
- Internal Energy Diffusion (conservation of internal energy)

These diffusive processes are characterised by their corresponding transport properties:

- Mass Diffusivity ( $D_s$ )
- Absolute Viscosity ( $\mu$ )
- Thermal Conductivity ( $\kappa$ )
- Internal Energy Conductivity ( $\kappa_{\text{int}}$ )

### Mass Diffusion

$$J_s = -\rho D_s \frac{\partial [Y_s]}{\partial x_j}$$

CFD-FASTRAN Theory Manual [15], Page 3-7

The mass diffusivity is evaluated using one of the following methods:

A) FICK'S LAW:

$$D_s = \frac{\mu}{\rho S c}$$

CFD-FASTRAN Theory Manual [15], Page 3-10

Where  $\mu$  is the mixture viscosity evaluated using Wilke's Law

B) EFFECTIVE BINARY DIFFUSION

For a mix of species "s" and "r":

$$D_s = \frac{1 - [\mathcal{X}_s]}{\sum_{r=1}^n \left[ \frac{[\mathcal{X}_r] P_{atm} \sigma_{sr}^2 \Omega_{D_{sr}}}{1.8583 \times 10^{-7} \sqrt{T^3 \left( \frac{1}{\mathcal{M}_s} + \frac{1}{\mathcal{M}_r} \right)}} \right]}$$

Where:

$$\sigma_{sr} \approx \frac{1}{2}(\sigma_s + \sigma_r)$$

Anderson [7], Page 597

(Note:  $d_{AB} \equiv \sigma_{sr}$ )

### Momentum Diffusion

The CFD-FASTRAN solver assumes all gases obey Stoke's hypothesis and are Newtonian fluids such that the viscosity ( $\mu$ ) is linearly proportional to the velocity gradient:

$$\tau_{ij} = \mu \begin{pmatrix} \frac{2}{3} \left[ 2 \frac{\partial u_1}{\partial x_1} - \frac{\partial u_2}{\partial x_2} - \frac{\partial u_3}{\partial x_3} \right] & \left[ \frac{\partial u_1}{\partial x_2} + \frac{\partial u_2}{\partial x_1} \right] & \left[ \frac{\partial u_1}{\partial x_3} + \frac{\partial u_3}{\partial x_1} \right] \\ \left[ \frac{\partial u_1}{\partial x_2} + \frac{\partial u_2}{\partial x_1} \right] & \frac{2}{3} \left[ 2 \frac{\partial u_2}{\partial x_2} - \frac{\partial u_1}{\partial x_1} - \frac{\partial u_3}{\partial x_3} \right] & \left[ \frac{\partial u_2}{\partial x_3} + \frac{\partial u_3}{\partial x_2} \right] \\ \left[ \frac{\partial u_1}{\partial x_3} + \frac{\partial u_3}{\partial x_1} \right] & \left[ \frac{\partial u_2}{\partial x_3} + \frac{\partial u_3}{\partial x_2} \right] & \frac{2}{3} \left[ 2 \frac{\partial u_3}{\partial x_3} - \frac{\partial u_1}{\partial x_1} - \frac{\partial u_2}{\partial x_2} \right] \end{pmatrix}$$

Adapted from GASP Manual [5], Page 510

The viscosity is evaluated using one of the following methods:

A) CONSTANT VISCOSITY (SINGLE SPECIES):

$$\mu = \text{constant}$$

CFD-FASTRAN Theory Manual [15], Page 3-7

B) SUTHERLAND'S LAW (SINGLE SPECIES):

$$\mu = \frac{C_1 T^{\frac{3}{2}}}{C_2 + T}$$

CFD-FASTRAN Theory Manual [15], Page 3-7

Where  $C_1$  and  $C_2$  are empirical constants derived from experimental data.

For air:

$$C_1 \approx 1.4605 \times 10^{-6} \frac{kg}{m \cdot s \cdot \sqrt{K}}$$

$$C_2 \approx 110K$$

CFD-FASTRAN User Manual [16], Page 5-4

Note there is an alternative form of Sutherland's Equation:

$$\mu = \mu_0 \left( \frac{T}{T_0} \right)^{\frac{3}{2}} \left( \frac{T_0 + S}{T + S} \right)$$

GASP Manual [5], Page 525

The constants can be mapped from one form of the equation to the other:

$$C_1 = \frac{\mu_0(T_0 + S)}{T_0^{\frac{3}{2}}}$$

$$C_2 = S$$

Derived

### C) WILKE'S LAW (MULTIPLE SPECIES)

For a mixture of species "s" and "r":

$$\mu = \sum_{s=1}^n \left[ \frac{[\mathcal{X}_s] \mu_s}{\sum_{r=1}^n \left[ [\mathcal{X}_r] \left( 1 + \sqrt{\frac{\mu_s}{\mu_r}} \left( \frac{\mathcal{M}_r}{\mathcal{M}_s} \right)^{\frac{1}{4}} \right)^2 \left( \sqrt{8 \left( 1 + \frac{\mathcal{M}_s}{\mathcal{M}_r} \right)} \right)^{-1} \right]} \right]$$

Where:

$$\mu_s = 2.6693 \times 10^{-6} \frac{\sqrt{\mathcal{M}_s T}}{\sigma^2 \Omega_\mu}$$

CFD-FASTRAN Theory Manual [15], Page 3-8

The molecular weights ( $\mathcal{M}_s, \mathcal{M}_r$ ) come from the chosen database (curve-fit or molecular). The characteristic molecular diameter  $\sigma$  is based on Lennard-Jones potentials obtained from Svehla [72] and this information is supplied in a file named “`fastran_trans.dat`”. A reduced temperature  $T^*$  is calculated and this is used to determine the viscosity collision integral  $\Omega_\mu$  via a look up table. This method is based on Hirschfelder [31].

### Thermal Diffusion and Internal Energy Diffusion

FOR FLOWS IN THERMAL EQUILIBRIUM:

$$q_j = -\kappa \frac{\partial T}{\partial x_j}$$

CFD-FASTRAN Theory Manual [15], Page 3-6

OR FOR FLOWS IN THERMAL NONEQUILIBRIUM:

$$q_j = -\kappa \frac{\partial T}{\partial x_j}$$

CFD-FASTRAN Theory Manual [15], Page 3-6

and

$$q_{\text{int},j} = -\kappa_{\text{int}} \frac{\partial T_{\text{int}}}{\partial x_j}$$

CFD-FASTRAN Theory Manual [15], Page 3-6

(Note:  $T_j$  should be  $x_j$  in the manual)

The thermal conductivity  $\kappa$  is evaluated using one of the following methods:

A) CONSTANT PRANDTL NUMBER (THERMAL EQUILIBRIUM):

$$\kappa = \frac{\mu C_P}{Pr}$$

CFD-FASTRAN Theory Manual [15], Page 3-9

Where  $Pr$  is the Prandtl number and is usually taken to be around 0.7 for laminar flows.

B) EUCKEN'S ASSUMPTION (THERMAL NONEQUILIBRIUM):

$$\kappa_s = \mu_s \left( \frac{5}{2} C_{V_{Trans,s}} + C_{V_{Rot,s}} \right)$$

CFD-FASTRAN Theory Manual [15], Page 3-9

$$K_{int,s} = \mu_s C_{Vib,s}$$

CFD-FASTRAN Theory Manual [15], Page 3-9

## A.4 Thermochemical Source Terms

The source term ( $\omega_s$ ) for species “s” is defined by:

$$\omega_s = \frac{\partial \rho_s}{\partial t} = \mathcal{M}_s (\nu''_{sr} - \nu'_{sr}) \left[ \sum_{r=1}^R \beta_{sr} \left( \frac{\rho_s}{\mathcal{M}_s} \right) \right] \left[ K_{f,r} \prod_{s=1}^n \left[ \frac{\rho_s}{\mathcal{M}_s} \right]^{\alpha'_{sr}} - K_{b,r} \prod_{s=1}^n \left[ \frac{\rho_s}{\mathcal{M}_s} \right]^{\alpha''_{sr}} \right]$$

Adapted from CFD-FASTRAN Theory Manual [15], Page 3-11 and the GASP User Manual [5], Page 498

The terms  $\nu'_{sr}$  and  $\nu''_{sr}$  are stoichiometric coefficients of the reactants and products respectively,  $\beta_{sr}$  is the third body coefficient for a given reaction and  $\alpha'_{sr}$  and  $\alpha''_{sr}$  are concentration powers for the forward and backwards rates respectively. CFD-FASTRAN assumes that the concentration powers are equal to the stoichiometric coefficients:

$$\begin{aligned} \nu'_{sr} &= \alpha'_{sr} \\ \nu''_{sr} &= \alpha''_{sr} \end{aligned}$$

CFD-FASTRAN Theory Manual [15], Page 3-11

$K_{f,r}$  and  $K_{b,r}$  are the reaction rate equations for the forwards and backwards reactions respectively. CFD-FASTRAN assumes a modified Arrhenius reaction rate model which includes a pre-exponential temperature factor. The equation for the forward reaction rate of reaction “r” is:

$$K_{f,r} = A_{f,r} T^{\eta_{f,r}} e^{-\left[ \frac{E_{a,f,r}}{R_U T} \right]}$$

CFD-FASTRAN Theory Manual [15], Page 3-11

and for the backwards reaction rate of reaction “r”:

$$K_{b,r} = A_{b,r} T^{\eta_{b,r}} e^{-\left[ \frac{E_{a,b,r}}{R_U T} \right]}$$

CFD-FASTRAN Theory Manual [15], Page 3-12

Or if equilibrium is assumed the backwards reaction rate is:

$$K_{b,r} = \frac{K_{f,r}}{K_{eq,r}}$$

$A$ ,  $\eta$  and  $E_a$  are empirical constants which must be obtained from experimental data for each particular reaction. Typically a lot of variability is present in this rate data.

$K_{eq,r}$  is the equilibrium chemical reaction rate for reaction “r”:

$$K_{eq,r} = \frac{P_0}{RT} \left( \sum_{r=1}^R (\nu''_{sr} - \nu'_{sr}) \right) e^{-\left( \frac{\sum_{r=1}^R (\nu''_{sr} - \nu'_{sr}) \bar{G}_s^0}{RT} \right)}$$

### Generation of Internal Energy in Nonequilibrium Flow

If a two temperature model is used then a source term ( $\omega_{int,s}$ ) arises from an imbalance between the internal energy and the equilibrium internal energy of the system:

$$\omega_{int,s} = \frac{\partial e_{int,s}}{\partial t} = \sum_{s=1}^n \left[ \frac{e_{int,s}^*(T) - e_{int,s}(T_{int})}{\tau_{vib,s}} \right] + \sum \omega_s e_{int,s}$$

The term  $\tau_{vib,s}$  is the Milikan-White characteristic vibrational relaxation time. This is the time required to reach vibrational equilibrium and is different for each species. The relaxation time is also a function of both the local pressure and the local temperature:

$$\tau_{vib,s} = \frac{c_1 e^{\left( \sqrt[3]{\frac{C_2}{T}} \right)}}{p}$$

Table A.1 shows values for  $C_1$  and  $C_2$  taken from Page 489 of Anderson [7] for several pure gases. As with the rate data for chemical reactions, significant variability is also present in the vibrational relaxation rate data. It should also be noted that the time taken for other internal energy modes to come to equilibrium is not considered by the CFD-FASTRAN solver.

Table A.1: Constants for the vibrational relaxation time equation.

Species	$C_1$ (atm · $\mu s$ )	$C_2$ (K)
O <sub>2</sub>	$5.42 \times 10^{-5}$	$2.95 \times 10^6$
N <sub>2</sub>	$7.12 \times 10^{-3}$	$1.91 \times 10^6$
NO	$4.86 \times 10^{-3}$	$1.37 \times 10^5$

The term  $e_{int,s}^*(T)$  is the temperature dependent equilibrium internal energy level. Ignoring the electronic mode of internal energy (as is the case with the Molecular Database option), this energy can be defined as purely the vibrational energy:

$$e_{int,s}^*(T) \equiv e_{Vib,s}^* = \frac{R_U}{\mathcal{M}_s} \sum_{m=1}^N \left[ \frac{\Theta_{V,s}^{(m)}}{e^{(\Theta_{V,s}^{(m)}/T)} - 1} \right]$$

Gasp User Manual [5], Page 505

The term  $e_{int,s}(T_{int})$  is the internal energy level which is dependent on the internal temperature. Ignoring the electronic mode of internal energy again, this energy can be defined as purely the vibrational energy:

$$e_{int,s}(T) \equiv e_{Vib,s} = \frac{R_U}{\mathcal{M}_s} \sum_{m=1}^N \left[ \frac{\Theta_{V,s}^{(m)}}{e^{(\Theta_{V,s}^{(m)}/T_{Vib})} - 1} \right]$$

Gasp User Manual [5], Page 505

## Simulation Results in Video Format

---

This appendix consists of a CD which is attached to the back of this thesis. The appendix contains video files created from CFD-FASTRAN results data. For each file, CFD-VIEW was used to process CFD-FASTRAN results data into a series of bitmap images. The program "VideoMach" was then used to compile the images into video, in compressed AVI format. Note that some videos are quite large and will require a screen resolution of  $1,600 \times 1,200$  and a graphics card with 128 MB or more of RAM to run. A digital copy of this thesis in PDF form is also included on the CD. Table B.1 shows a list of files included on the CD.

Table B.1: Listing of files included on Appendix B CD.

directory and file	brief description
<b>Transient</b>	
1_schliren.avi	Numerical Schlieren video for Case 1.
2A_schliren.avi	Numerical Schlieren video for Case 2A.
2B_schliren.avi	Numerical Schlieren video for Case 2B.
3A_schliren.avi	Numerical Schlieren video for Case 3A.
3A_schliren_cyl.avi	As above with close up view of cylinder.
3B_schliren.avi	Numerical Schlieren video for Case 3B.
3B_schliren_cyl.avi	As above with close up view of cylinder.
4A_schliren.avi	Numerical Schlieren video for Case 4A.
4B_schliren.avi	Numerical Schlieren video for Case 4B.
<b>Other</b>	
1_odd_even.avi	Schlieren animation showing odd-even decoupling for Case 1.
3B_vortex.avi	Schlieren and streamline animation showing complex Mach reflection in Case 3B which results in the formation of a vortex.
3B_vortex_slow.avi	As above with less frames per second.
3B_roe.avi	Schlieren animation showing spurious wave formations when using Roe's scheme in Case 3B.
3B_roe_cyl.avi	As above with close up view of cylinder.
4B_shock_BL.avi	Velocity vectors and flooded contours of speed showing shock boundary layer interaction (magnified view)
5B_temperature.avi	Convergence history for temperature variable in Case 5B.
<b>PDF</b>	
Thesis.pdf	This thesis in PDF format

---

## Bibliography

---

- [1] The U.S. Standard Atmosphere (1962). U.S. Government Printing Office, Washington, D.C., 1962.
- [2] CFD Validation Bibliography. internet site, 2005.  
[www.grc.nasa.gov/WWW/wind/valid/tutorial/bibliog.html](http://www.grc.nasa.gov/WWW/wind/valid/tutorial/bibliog.html).
- [3] Merriam-Webster's Online Dictionary. internet site, 2005. [www.m-w.com](http://www.m-w.com).
- [4] Adams, V. and Askenazi, A. *Building Better Products with Finite Element Analysis*. Onword Press, 1999.
- [5] Aerosoft, Inc., Blacksburg, Virginia. *GASP v4 User Manual*.
- [6] Aerosoft, Inc., Blacksburg, Virginia. *GUST v2 User Manual*.
- [7] Anderson, J. D. Jr. *Hypersonic and High Temperature Gas Dynamics*. McGraw Hill, 1989.
- [8] Anderson, J. D. Jr. *Computational Fluid Dynamics: The Basics with Applications*. McGraw Hill, 1995.
- [9] Bird, R. B., Stewart, W. E. and Lightfoot, E. N. *Transport Phenomena*. John Wiley and Sons Inc., 2nd edition, 2002.
- [10] Blondin, J. M. and Lufkin, E. A. The Piecewise-Parabolic Method in Curvilinear Coordinates. *The Astrophysics Journal Supp.*, (88), 1993.
- [11] Boris, J. P. and Book, D. L. Flux Corrected Transport I. SHASTA, a Fluid Algorithm That Works. *Journal of Computational Physics*, 11:38–69, 1973.
- [12] Breazeale, M. A. From Monochromatic Light Diffraction to Colour Schlieren Photography. *Journal of Optics A: Pure and applied optics*, 3(S1-S7), 2001.
- [13] Bryson, A. E. and Gross, R.W.F. Diffraction of Strong Shocks By Cones, Cylinders and Spheres. *Journal of Fluid Mechanics*, 10(1):1–16, July 1960.
- [14] Candler, G. V. and Nompelis, I. CFD Validation for Flight: Real Gas Flows. *AIAA*, (2002-0434), 2002.

- [15] CFDRC. *CFD-FASTRAN v2002 Theory Manual*, 2002.
- [16] CFDRC. *CFD-FASTRAN v2002 User Manual*, 2002.
- [17] CFDRC. *CFD-FASTRAN Validation Manual*, 2002.
- [18] CFDRC. *CFD-GEOM v2003 User Manual*, 2003.
- [19] Colella, P. and Woodward, P. R. The Piecewise Parabolic Method (PPM) for Gas-Dynamical Simulations. *J. Comp. Phys.*, (54), 1984.
- [20] Courant, R., Friedrichs, K. O. and Lewy, H. Uber die Partiellen Differenzengleichungen der Mathematischen Physik. *Mathematische Annalen*, (100):32–74, 1928. Translated into English as “On the Partial Differential Equations of Mathematical Physics”, IBM Journal of Research and Development, 11, pp. 215-234, 1967.
- [21] Dunn, M. G. and Kang, S. W. Theoretical and Experimental Studies of Reentry Plasmas. Technical Report CR-2232, NASA, April 1973.
- [22] Elford, M. C. Cone Shock Interaction. Submitted to K. Takayama in response for the for the call for papers announced in Vol 13. of the *Journal Shock Waves*, July 2003.
- [23] Fox, R. W. and McDonald, A. T. *Introduction to Fluid Mechanics*. John Wiley & Sons Inc., 4th edition, 1994. SI Version.
- [24] Frey, P. J., Borouchaki, H. and George, P. Delaunay Tetrahedralization using an Advancing-Front Approach. In *5<sup>th</sup> International Meshing Roundtable*, pages 31–46, Sandia National Laboratories, October 1996.
- [25] Gerhold, T., Friedrich, O., Evans, J. and Galle, M. Calculation of Complex Three-Dimensional Configurations Employing the DLR-TAU-Code. *AIAA*, (97-0167), 1997.
- [26] Glass, I.I., Kaca, J., Zhang, D.L., Glaz, H.M., Bell, J.B., Trangenstein, J.A. and Collins, J.P. Diffraction of Planar Shock Waves Over Half Diamond and Semicircular Cylinder: An Experimental and Numerical Comparison. In Y.W. Kim, editor, *17<sup>th</sup> International Symposium On Shock Waves and Shock Tubes*, American Institute of Physics Conference Proceedings, New York, 1989.
- [27] Godunov, S. K. Finite Difference Methods for the Computation of Discontinuous Solutions of the Equations of Fluid Dynamics. *Matematicheskii Sbornik*, (47):271–306, 1959.
- [28] Harvey, J. K. A Review of a Validation Exercise on the Use of the DSMC Method to Compute Viscous / Inviscid Interactions in Hypersonic Flow. *AIAA*, (2003-3643),

2003. presented at the 36<sup>th</sup> AIAA thermophysics conference, Orlando FL, June 23-36, 2003.
- [29] Hirsch, C. *Numerical Computation of Internal and External Flows*, volume 1. John Wiley & Sons, July 1990.
- [30] Hirsch, C. *Numerical Computation of Internal and External Flows*, volume 2. John Wiley & Sons, July 1990.
- [31] Hirschfelder, J. O., Curtiss, C. F. and Bird, R. B. *Molecular Theory of Gases and Liquid*. John Wiley and Sons, 1954.
- [32] Holden, M. S. A Review of Experimental Studies for DSMC and Navier-Stokes Code Validation in Laminar Regions of Shock / Shock and Shock / Boundary Layer Interaction Including Real Gas Effects. *AIAA*, (2003-3641), 2003.
- [33] Holden, M. S., Wadhams, T. P., Candler, G. V. Experimental Studies and Numerical Predictions for Hypervelocity Vehicle Design and Code Validation. *AIAA*, (2003-6905), 2003. presented at the 41<sup>st</sup> AIAA Aerospace Sciences Meeting and Exhibit, Reno NV, January 6-9, 2003.
- [34] Holden, M. S., Wadhams, T. P., Candler, G. V. and Harvey, J. K. Measurements in Regions of Low Density Laminar Shock Wave / Boundary Layer Interaction in Hypervelocity Flows and Comparison with Navier Stokes Predictions. *AIAA*, (2003-1131), 2003. presented at the 41<sup>st</sup> AIAA Aerospace Sciences Meeting and Exhibit, Reno NV, January 6-9, 2003.
- [35] Holden, M. S., Wadhams, T. P., Harvey, J. K. and Candler, G. V. Comparison between DSMC and Navier-Stokes Solutions and Measurements in Region of Laminar Shock Wave / Boundary Layer Interaction in Hypersonic Flows. *AIAA*, (2002-0435), 2002. presented at the 40<sup>th</sup> AIAA Aerospace Sciences Meeting and Exhibit, Reno NV, January 14-17, 2002.
- [36] Holden, M.S. and Wadhams, T. P. A Database of Aerothermal Measurements in Hypersonic Flows in “Building Block” Experiments for CFD Validation. *AIAA*, (2003-1137), 2003. presented at the 41<sup>st</sup> AIAA Aerospace Sciences Meeting and Exhibit, Reno NV, January 6-9, 2003.
- [37] Izumi, K., Aso, S. and Nishida, M. Experimental and Computational Studies Focusing Processes of Shock Waves Reflected from Parabolic Reflectors. *Shock Waves*, (3):213–222, 1994.
- [38] Jacobs, P. A. MBCNS: A Computer Program for the Simulation of Transient Compressible Flows. Technical Report 10, Department of Mechanical Engineering, The University of Queensland, Brisbane, Dec 1996.

- [39] Jacobs, P. A. MBCNS: A Computer Program For the Simulation of Transient Compressible Flows; 1998 Update. Technical Report 7, Department of Mechanical Engineering, The University of Queensland, Brisbane, June 1998.
- [40] Jacobs, P. A. Axisymmetric Shock Wave Interaction with a Cone: Benchmark Submission. Submitted to K. Takayama in response for the for the call for papers announced in Vol 13. of the Journal *Shock Waves*, July 2003.
- [41] Jacobs, P. A. and Goozee, R. J. Implementation of a Workstation Cluster for Compressible Flow Simulation. HPC Conference Asia 2001, 2001.
- [42] Jenkins, D. R. *Hypersonic! The Story of the North American X-15*. Specialtypress, 2003.
- [43] Jiang, Z., Onodera, O. and Takayama, K. Evolution of Shock Waves and the Primary Vortex Loop Discharged from a Square Cross-Sectional Tube. *Shock Waves*, 9(1):1–10, February 1999.
- [44] Johnston, I. A. *Simulation of Flow Around Hypersonic Blunt Nosed Vehicles for the Calibration of Air Data Systems*. PhD thesis, University of Queensland, January 1999.
- [45] Kang, S. W., Dunn, M. G. and Jones W. L. Theoretical and Measured Electron-Density Distributions for the RAM Vehicle at High Speeds. *AIAA*, (72-689), June 1972. AIAA 5<sup>th</sup> Fluid and Plasma Dynamics Conference.
- [46] Krist, E., Biedron, R. and Rumsey C. *CFL3D User's Manual (Version 5.0)*. National Aeronautics and Space Administration, June 1998. 1998-20844.
- [47] Lanis, T. R. and Jenkins, D. R. *X-15 Photo Scrapbook*. Specialtypress, 2003.
- [48] LeVeque, R. J. *Finite Volume Methods for Hyperbolic Problems*. Cambridge University Press, 2002.
- [49] Leyland, P. mini-CFD course. University of Queensland Lecture Notes.
- [50] Liever, P. A., Habchi, S. D., Burnell, S. I. and Lingard, J. S. CFD Prediction of the Beagle 2 Aerodynamic Database. *AIAA*, (2002-0683), 2002.
- [51] Lin, H. C. Dissipation additions to flux-difference splitting. *AIAA*, (CP-91-1544), 1991.
- [52] Liou, M.S. and Steffen, C. J. Development of a New Flux Splitting Scheme. In *Tenth Computational Fluid Dynamics Conference*, pages 967–968. AIAA, June 1991.

- [53] Liou, M.S. and Steffen, C. J. A New Flux Splitting Scheme. *Journal of Computational Physics*, 107(1):23–39, July 1993.
- [54] Macrossan, M. N. The Equilibrium Flux Method for the Calculation of Flows with Non-Equilibrium Chemical Reactions. *Journal of Computational Physics*, 80(1):204–231, February 1989.
- [55] Marvin, J. G. Perspective on Computational Fluid Dynamics Validation. *AIAA*, 33(10), Oct 1995.
- [56] McBride, B. J., Heimil, S., Elhers, J. G. and Gordon, S. Thermodynamic Properties to 6000K for 210 Substances Involving the First 18 Elements. Technical Report SP-3001, NASA, 1963.
- [57] Mehta, U. B. Credible Computational Fluid Dynamics Simulation. *AIAA*, 36(5), May 1998.
- [58] Oberkampf, W. L. and Blottner, F. G. Issues in Computational Fluid Dynamics Code Verification and Validation. *AIAA*, 36(5), May 1998.
- [59] Olejniczak, J. *Computational and Experimental Study of Nonequilibrium Chemistry in Hypersonic Flows*. PhD thesis, University of Minnesota, April 1997.
- [60] Park, C. On Convergence of Computation of Chemically Reacting Flows. *AIAA*, (85-0247), 1985. 23<sup>rd</sup> AIAA Aerospace Sciences Meeting, January 14-17, 1985.
- [61] Park, C. *Nonequilibrium Hypersonic Aerothermodynamics*. Wiley, New York, 1990.
- [62] Park, C. Review of Chemical-Kinetic Problems of Future NASA Missions, I: Earth Entries. *Thermophysics and Heat Transfer*, 7(3):9–23, July - Sept. 1993.
- [63] Patankar, S. V. *Numerical Heat Transfer and Fluid Flow*. Taylor & Francis, 1980.
- [64] Peery, K. M. and Imlay, S. T. Blunt Body Flow Simulations. *AIAA*, (88-2904), 1988.
- [65] Post, D. E. and Votta, L. G. Computational Science Demands a New Paradigm. *Physics Today*, Jan 2005.
- [66] Pullin, D. I. Direct Simulation Methods for Compressible Inviscid Ideal-Gas Flow. *Journal of Computational Physics*, 34(2):231–244, February 1980.
- [67] Quirk, J. A Contribution to the Great Riemann Solver Debate. Technical Report 92-64, Institute for Computer Applications in Science and Engineering, NASA Langley Research Center, Nov. 1992.
- [68] Roache, P. J. Verification of Codes and Calculations. *AIAA*, 36(5), May 1998.

- [69] Roe, P. L. Approximate Riemann Solvers, Parameter Vectors and Difference Schemes. *Journal of Computational Physics*, 43:357–372, 1981. Springer Verlag.
- [70] Roe, P. L. The Use of the Riemann Problem in Finite Difference Schemes. *Lecture Notes in Physics*, 141:354–359, 1981. Springer Verlag.
- [71] Roy, C. J., Gallis, M. A., Payne, J. L. and Bartel, T. J. Navier-Stokes and DSMC Simulations for Hypersonic Laminar Shock / Shock Interaction Flows. *AIAA*, 2002. presented at the 40<sup>th</sup> AIAA Aerospace Sciences Meeting and Exhibit, Reno NV, January 14-17, 2002.
- [72] Svehla, R. A. Estimated Viscosities and Thermal Conductivities of Gases at High Temperatures. Technical Report R-132, National Aeronautics and Space Administration, 1962.
- [73] Svehla, R. A. and McBride, B. J. FORTRAN IV Computer Program for Calculation of Thermodynamic and Transport Properties of Complex Chemical Systems. Technical Report NASA TN D-7056, NASA, 1973.
- [74] Takayama, K. A Benchmark Test: Axisymmetric Shock Wave Interaction with a Cone. Call for Papers, 2003.
- [75] Thompson, M. O. *At the Edge of Space: The X-15 Flight Program*. Smithsonian Institute, 1992.
- [76] Van Leer, B. Flux-Vector Splitting for the Euler Equations. In E. Krause, editor, *Eighth International Conference on Numerical Methods in Fluid Dynamics*, volume 170 of *Lecture Notes in Physics*, pages 507–512. Springer-Verlag, 1982.
- [77] Vatsa, V. N. and Wedan, B. W. Development of an Efficient Multigrid Code for 3-D Navier-Stokes Equations. *AIAA*, (CP-89-1791), 1989.
- [78] Vatsa, V. N., Sanetrik, M. D. and Parlette, E. B. Development of a Flexible and Efficient Multigrid-Based Multi-Block Flow Solver. *AIAA*, (CP-93-0677), January 1993.
- [79] Wada, Y. and Liou, M.S. A Flux Splitting Scheme with High-Resolution and Robustness for Discontinuities. *AIAA*, 107(94-0083):23–39, January 1994.
- [80] Wen, C. *Hypervelocity Flow Over Spheres*. PhD thesis, Graduate Aeronautical Laboratories California Institute of Technology, 1994.
- [81] Wen, C.Y. and Hornung, H.G. Non-Equilibrium Dissociating Flow Over Spheres. *Journal of Fluid Mechanics*, 299:389–405, 1995.

- 
- [82] White, J. A. and Morrison, J. H. A Pseudo-Temporal Multi-Grid Relaxation Scheme for Solving the Parabolized Navier-Stokes Equations. *AIAA*, (99-3360), 1999.
- [83] Wilson, G. J. *Computation of Steady and Unsteady Shock-Induced Combustion over Hypervelocity Blunt Bodies*. PhD thesis, Department of Aeronautics and Astronautics, Stanford University, 1991.
- [84] Wright, M.J., Candler, G.V. and Bose, D. Data-Parallel Line Relaxation Method for the Navier-Stokes Equations. *AIAA*, 36(9):1603–1609, September 1998.